Atomic Scale Investigation of Structures and Functionalities in Quantum Matter Heteroepitaxy

Wang, Hongguang

(2020)

MAX PLANCK INSTITUTE FOR
SOLID STATE RESEARCH

Atomic Scale Investigation of Structures and Functionalities in Quantum Matter Heteroepitaxy

Hongguang Wang

Dissertation submitted as a requirement for the degree of Doctor of Philosophy
September 2020 – Technical University of Darmstadt (TUD) – D17

Darmstadt, 2020

Atomic Scale Investigation of Structures and Functionalities in Quantum Matter Heteroepitaxy

Dissertation submitted to the Department of Materials and Earth Sciences at Technische Universität Darmstadt

in Fulfillment of the Requirements for the Degree of
Doctor of Philosophy (Dr. rer. nat.)

By

Hongguang Wang
Max Planck Institute for Solid State Research

Born in Shandong, China

Referee: Prof. Dr. Ralf Riedel
Co-referee: Prof. Dr. Peter A. van Aken

Date of Submission: 18.09.2020
Date of Oral Examination: 16.11.2020

TECHNISCHE
UNIVERSITÄT
DARMSTADT

Darmstadt, 2020

Hongguang Wang: Atomic Scale Investigation of Structures and Functionalities in Quantum Matter Heteroepitaxy

Darmstadt, Technische Universität Darmstadt
Publication Year of Dissertation at TUprints: 2020
URN: urn:nbn:de:tuda-tuprints-172227
Date of Oral Examination: 16.11.2020

Darmstadt, 2020

THESIS SUPERVISORS

Prof. Dr. Ralf Riedel

Professor of Materials Science
Materials Science Department
Technical University of Darmstadt

Prof. Dr. Peter A. van Aken

Professor of Geo-Material Science
Max Planck Institute for Solid State Research
Stuttgart Center for Electron Microscopy (StEM)

THESIS COMMITTEE

Prof. Dr. Ralf Riedel

Referee
Professor of Materials Science
Materials Science Department
Technical University of Darmstadt

Prof. Dr. Peter A. van Aken

Co-referee
Professor of Geo-Material Science
Geo- and Material Sciences Department
Technical University of Darmstadt

Prof. Dr. Hans-Joachim Kleebe

Examiner
Professor of Geo-Material Science
Geo- and Material Sciences Department
Technical University of Darmstadt

Prof. Dr. Christoph T. Koch

Examiner
Professor of Physics
Department of Physics
Humboldt University of Berlin

Atomic Scale Investigation of Structures and Functionalities in Quantum Matter Heteroepitaxy

By

Hongguang Wang

Submitted to the Department of Materials and Earth Sciences on 18.09.2020 in Partial Fulfillment of the Requirements for the Degree of Doctor of Philosophy in Geo-Material sciences

ABSTRACT

"…whether, ultimately---in the great future---we can arrange the atoms the way we want; the very atoms, all the way down! What would happen if we could arrange the atoms one by one the way we want them…" Richard Feynman described the exciting blueprint of nanotechnology in his famous lecture entitled "There's plenty of room at the bottom" in 1959. He devoted a significant part of electron microscopy in his lecture, underlining the possible breakthroughs in many research fields, if we are able to look at the atomic scale. With explosive advances in nanoscience and nanotechnologies, since then, especially after the 1980s, Feynman's visions have arguably been realized. So far, the arrangement of the atoms can be artificially manipulated with advanced synthesis methods and microscopy techniques, whilst they can be visualized using microscopy techniques with high resolution. The latest generation of electron microscopes is capable of resolutions of 0.39 Å. The work in this thesis is dedicated to studying "plenty of room at the bottom" from two perspectives. On the one hand, we fabricated quantum matter heterostructures by arranging the atoms using pulsed laser deposition (PLD) with atomic-layer precision and studied caused physical behaviors. On the other hand, we visualized the actual arrangement of atoms in quantum matter heterostructures, in particular at the heterointerface, using state-of-the-art scanning transmission electron microscopy (STEM) and spectroscopy. The underlying mechanisms of physical behaviors were explained accordingly.

Firstly, $SrRuO_3$ (SRO) artificial atoms (AAs) were fabricated by electron beam lithography (EBL) patterning of the epitaxial-grown SRO thin films with atomic layer precision using PLD. The size of AAs is down to 15 nm, which is the smallest size reported so far. Due to the spatial confinement of the electron system, interesting magnetic phenomena occur with decreasing the size of AAs, showing a gradual increase of magnetic Curie temperature and a reorientation of the easy axis towards the in-plane direction. Based on the optimization of TEM sample preparation, we performed atomically resolved STEM observations of the atomic arrangements in different samples. It was found that the chemical distribution keeps unchanged, while the epitaxial strain is gradually relieved as the size of AAs decreases. The strain relaxation leads to the Curie temperature variations, whilst the strain relaxation induces the change of magnetocrystalline anisotropy that results in a rotation of the magnetic easy-axis.

The hetero-interface between $SrMnO_3$ (SMO) and $SrTiO_3$ (STO) is then studied atomic column by atomic column using STEM and spectroscopy. We found that the electronic charges accumulate close to the interface layer, reaching the maximum charge density at the first SMO monolayer. A fundamental understanding of the charge accumulation was elaborated with a combination of STEM investigations and numerical calculations. STEM offers atomic-scale information in terms of strain fields in out-of-plane and in-plane directions and two-dimensional distribution of constituent elements. The SMO layer close to the

interface is demonstrated to have the largest tensile strain and the strongest intermixing of Mn and Ti than other regions away from the interface. The role of tensile strain, elemental intermixing, charge transfer, and space-charge effects are intensively discussed, proving a comprehensive perspective of the interfacial charge distribution.

We also studied the atomic structure and functionality of cracks formed around the heterointerface due to thermal strain relaxations. The atomic arrangement of crack tips was clearly visualized by STEM imaging. Quantitative analyses of STEM images revealed a large strain gradient around the tip of deep crack that is extended into the STO substrate. With the STEM-based lattice displacement analysis, we determined the displacements between the negative center and the positive center unit cell by unit cell and thereby obtained the flexoelectric polarization around crack tips with atomic resolution. The averaged polarization around the tip of the deep crack is about $62 \pm 16\ \mu C \cdot cm^{-2}$, which is the largest flexoelectric polarization measured so far. The flexoelectric polarization is screened by the electronic charge with a density of $0.7 \pm 0.1\ e^-$/uc localized within one unit cell. We suggest that the flexoelectricity plays an essential role in the propagation of cracks, because the flexoelectric energy density was found to be ~3% of that of the elastic energy.

Benefited from the unique advantages of STEM in terms of high spatial resolution, this thesis presents three applications about studying the atomic worlds “at the bottom” visioned by Feynman sixty years ago, providing an atomic-scale understanding of structure and properties of quantum matter heterostructures. In the near future, the atomic arrangement in quantum matter heterostructures will be better controllable. Furthermore, the capacity of STEM will undoubtedly be more versatile to explore atomic worlds, such as direct visualization of the electric and magnetic fields on the atomic scale. Many mysterious phenomena in the atomic-scale world are about to be revealed.

ZUSAMMENFASSUNG

"...Ob wir letztendlich - in weit entfernter Zukunft – dazu in der Lage sind, die Atome so anordnen zu können, wie wir es uns vorstellen. Was würde passieren, wenn wir die Atome einzeln anordnen könnten, wie wir es wollen ..." Richard Feynman beschrieb die aufregende Blaupause der Nanotechnologie 1959 in seinem berühmten Vortrag mit dem Titel „*There's plenty of room at the bottom*". In seinem Vortrag widmete er einen bedeutenden Teil der Elektronenmikroskopie und unterstrich die möglichen Durchbrüche in vielen Forschungsbereichen, wie z.B. in der Nanowissenschaft und der Nanotechnologie, wenn wir eines Tages dazu in der Lage sein werden, atomar aufgelöste Bilder aufzunehmen. Seitdem, insbesondere nach den 1980er Jahren, wurden Feynmans Visionen durchaus verwirklicht. Heute sind wir dazu in der Lage, die Anordnung von Atomen mit fortschrittlichen Synthesemethoden und Mikroskopietechniken künstlich zu manipulieren, während man die Atome mittels hochauflösender Mikroskopie visualisieren kann. Die neueste Generation von Elektronenmikroskopen kann Auflösungen von bis hinunter zu 0,39 Å erreichen. Inhaltlich soll in dieser Dissertation „der große Spielraum nach unten" beleuchtet werden. Einerseits wurden Quantenmaterie-Heterostrukturen hergestellt, indem wir die Atome mithilfe der gepulsten Laserabscheidung (PLD) mit atomarer Schichtgenauigkeit angeordnet und das physikalische Verhalten untersucht haben. Andererseits wurde die Anordnung von Atomen in Quantenmaterie-Heterostrukturen, insbesondere an der Hetero-Grenzfläche, unter Verwendung modernster Raster-Transmissionselektronenmikroskopie (STEM) und -spektroskopie untersucht. Die zugrundeliegenden Mechanismen des physikalischen Verhaltens werden entsprechend erläutert.

Zunächst wurden künstliche $SrRuO_3$ (SRO)-Atomstrukturen (AAs) durch Elektronenstrahl-lithographiemusterung der epitaktisch gewachsenen SRO-Dünnfilme mit atomarer Schichtgenauigkeit unter Verwendung von PLD hergestellt. Die Größe der untersuchten AAs beträgt 15 nm, was die kleinste bisher erreichte Größe darstellt. Aufgrund der räumlichen Begrenzung des Elektronensystems treten interessante magnetische Phänomene mit abnehmender Größe der AAs auf. Diese Phänomene verzeichnen einen allmählichen Anstieg der magnetischen Curie-Temperatur und eine Neuorientierung der in der Ebene liegenden magnetischen Vorzugsrichtung. Basierend auf der Optimierung von TEM-Probenvorbereitungen, wurden STEM-Aufnahmen der atomaren Anordnungen in verschiedenen Proben durchgeführt. Es wurde festgestellt, dass die chemische Verteilung unverändert bleibt, während die epitaktische Belastung bei abnehmender Größe der AAs abnimmt. Die Dehnungsrelaxation führt zu einer Variation der Curie-Temperatur. Hierbei kommt es zu einer Änderung der Magnetokristalline Anisotropie, was zu einer Drehung der magnetischen Vorzugsrichtung führt.

Die Hetero-Grenzfläche zwischen $SrMnO_3$ (SMO) und $SrTiO_3$ (STO) wurde dann Atomsäule für Atomsäule unter Verwendung von Raster-Transmissionselektronenmikroskopie und -spektroskopie atomar untersucht. Dabei wurde herausgefunden, dass sich die elektronischen Ladungen nahe der Grenzflächenschicht ansammeln und die maximale Ladungsdichte an der ersten SMO-Monoschicht erreicht ist. Ein tieferes Verständnis der Ladungsakkumulation wurde mit einer Kombination aus STEM-Untersuchungen und numerischen Berechnungen erhalten. STEM liefert Informationen auf atomarer Ebene in Bezug auf Dehnungsfelder in Richtungen außerhalb der Ebene und in der Ebene sowie eine zweidimensionale Verteilung der Elemente. Es wird aufgezeigt, dass die SMO-Schicht nahe der Grenzfläche die größte Zugspannung und die stärkste Vermischung von Mn und Ti aufweist. Die verschiedenen Rollen der Zugspannung, der elementaren Vermischung, des Ladungstransfers und der Raumladungseffekte werden intensiv diskutiert, was zu einem umfassenden Verständnis der Ladungsverteilung an der Grenzfläche führt.

Ebenfalls wurde die atomare Struktur und Funktionalität von Rissen, die sich aufgrund thermischer

Dehnungsrelaxationen um die Hetero-Grenzfläche gebildet haben, untersucht. Die atomare Anordnung der Rissspitzen wurde durch STEM-Bildgebung deutlich sichtbar gemacht. Die quantitative Analyse von STEM-Bildern ergab einen großen Dehnungsgradienten um die Spitze des tiefen Risses, welcher in das STO-Substrat eindringt. Mit der STEM-basierten Gitterverschiebungsanalyse wurden die Verschiebungen zwischen dem negativen Zentrum und dem positiven Zentrum Einheitszelle für Einheitszelle bestimmt. Dadurch konnte die flexoelektrische Polarisation um die Rissspitzen mit atomarer Auflösung erhalten werden. Die gemittelte Polarisation um die Spitze des tiefen Risses beträgt etwa 62 ± 16 μCcm^{-2}, was die größte bisher gemessene flexoelektrische Polarisation darstellt. Diese flexoelektrische Polarisation wird durch die elektronische Ladung mit einer Dichte von 0,7 ± 0,1 e^-/uc abgeschirmt, die innerhalb einer Einheitszelle lokalisiert ist. Hier wird vorgeschlagen, dass die Flexoelektrizität aufgrund des Flexoelektrikums eine wesentliche Rolle bei der Ausbreitung von Rissen spielt, weil die Energiedichte ~ 3% der elastischen Energie beträgt.

Vorliegende Arbeit zeigt deutlich die einzigartigen Vorteile von STEM bezüglich einer hohen räumlichen Auflösung auf und präsentiert drei Anwendungen zur Untersuchung der Welt der Atome „*at the bottom*", die vor 60 Jahren von Feynman vorhergesagt wurde. Durch bahnbrechende Fortschritte in der Mikroskopie konnten wesentliche Lücken im atomaren Verständnis der Struktur und der Eigenschaften von Quantenmaterie-Heterostrukturen gefüllt werden. In naher Zukunft wird die atomare Anordnung der Quantenmaterie-Heterostrukturen noch besser kontrollierbar sein. Darüber hinaus wird die Fähigkeit von STEM zweifellos vielseitiger sein, um die atomare Welt noch besser zu erforschen (*e.g.* die direkte Visualisierung der elektrischen und magnetischen Felder auf atomarer Ebene). Zahlreiche mysteriöse Phänomene in der Atomwelt werden in naher und ferner Zukunft entschlüsselt werden.

Dedicated to my beloved ones …

“Persistence guarantees that results are inevitable.”

人要有毅力，否則一事無成

ACKNOWLEDGMENTS

None of this work would be possible without the support, guidance, help, and efforts of numerous people. First and foremost, I would like to express my utmost gratitude to my thesis supervisor, Prof. Dr. Peter A. van Aken, and Prof. Dr. Ralf Riedel. It was a tough time, when I decided to shift my Ph.D. research field from advanced material synthesis to electron microscopy. I gratefully thank the support, understanding, and encouragement from both supervisors. My special thanks to Prof. Dr. Peter A. van Aken for offering me the opportunity for a Ph.D. study in his group. Peter introduced me to the fascinating field of electron microscopy and provided tremendous support for my Ph.D. project. He has been kindly preparing me to be a scientist by helping me improve scientific writing, teaching me to refine physical information from experimental results, and offering me numerous chances for attending international conferences. I am also very grateful for his caring and support for my little family. I would like to thank Prof. Dr. Ralf Riedel for accepting me as a Ph.D. student at the Technical University of Darmstadt.

I would also like to express my gratitude to Prof. Hans-Joachim Kleebe and Prof. Christoph T. Koch for serving on my examination committee and their valuable comments.

I sincerely thank my daily supervisor Dr. Vesna Srot for her full support and regular instructions for my Ph.D. work. Vesna has been taught me the STEM-related techniques and data processing, and spent much time correcting my papers. Her rigorous working style and diligent working attitude are profoundly affecting me. I also owe my sincere thanks to Dr. Yi Wang for his generous help and very beneficial advice. Yi has shared with me his expertise in STEM-related techniques and his DM scripts. I deeply appreciate Dr. Wilfried Sigle for his insightful guidance and very useful and timely help. I feel honored to work with and learn from all of them during my Ph.D. study.

I would like to thank my great collaborators for their indispensable contributions. I have been fortunate to collaborate with colleagues, Prof. Dr. Jochen Mannhart, Dr. Hans Boschker, and Dr. Gennady Laskin, from Solid State Quantum Electronics Department, Max Planck Institute for Solid State research. I am grateful to Prof. Dr. Jochen Mannhart for the fruitful discussions, and many insights into my work. I sincerely thank Dr. Gennady Laskin for growing beautiful SRO/STO nanostructures and perform the magnetic measurement; Dr. Hans Boschker for preparing interesting SMO/STO heterostructures and answering my countless questions about interfacial physics. I would also like to acknowledge Prof. Dr. Robert W. Stark and Xijie Jiang from the Technical University of Darmstadt for the help in AFM; Prof. Joachim Meyer and Dr. Lei Jin from Ernst Ruska-Centre, Juelich, Germany for the access to the NanoMill system; Bernhart Fenk from the Nanostructuring Lab of the institute for the help in TEM sample preparation with FIB.

I would like to express my sincere gratitude to the entire StEM group for bringing me a pleasant learning time. I firstly want to thank the StEM administrative assistant, Caroline Heer, for her warm care and great assistance to me and my family. I gratefully thank Kersten Hahn and Peter Kopold for teaching me electron microscopy techniques; Ute Salzberger and Marion Kelsch for tutoring me TEM sample preparation; Felicitas Predel for helping me at the SEM. I would also like to thank the members of StEM group, who have made my Ph.D. time colorful and enjoyable: Surong Guo, Nilesh Vats, Robin Lingstädt, Xu Chen, Yu-Mi Wu, Xuejiao Zhang, Chao Yang, Nicolas Bonmassar, Julia Deuschle, Eren Suyolcu, Chen Li, Timothy Pennycook, Dan Zhou, Pouya Moghimian.

Last but not least, I indebted a great deal to the support and love of my family. My parents spent tremendous effort to ensure me receiving the best education possible and continuously concern about my well-being and health. My sisters always understand me, inspire me, and support my decisions. My wife and my son have been bringing the greatest happiness of my life.

BIOGRAPHICAL NOTE

EDUCATION

Ph.D.	Max Planck Institute for Solid State Research (MPI-FKF) Technical University of Darmstadt (TUD) *Material sciences*	2016–2020 *Supervised by,* Prof. Dr. Peter A. van Aken Prof. Dr. Ralf Riedel
M.Sc.	University of the Chinese Academy of Sciences *Material Physics and Chemistry*	2012–2015 *Supervised by,* Prof. Dr. Jinbao Xu
B.Eng.	University of Jinan *Materials Science and Engineering*	2006–2010 *Supervised by,* Prof. Dr. Xianqin Hou Prof. Dr. Qi Wang

LIST OF JOURNAL PUBLICATIONS

Publications Related to the Present Thesis:

A. Hongguang Wang, Vesna Srot, Xijie Jiang, Min Yi, Hans Boschker, Rotraut Merkle, Robert W. Stark, Jochen Mannhart, Peter A. van Aken. "Probing Charge Accumulation at $SrMnO_3/SrTiO_3$ Hetero-Interfaces *via* Advanced Electron Microscopy and Spectroscopy." *ACS Nano*, 2020, Accepted.

B. Hongguang Wang, Xijie Jiang, Yi Wang, Robert W. Stark, Peter A. van Aken, Jochen Mannhart, and Hans Boschker. "Direct observation of huge flexoelectric polarization around crack tips." *Nano Letters* 20, 1(2020): 88–94.

C. Gennadii Laskin*, Hongguang Wang*, Hans Boschker, Wolfgang Braun, Vesna Srot, Peter A. van Aken, and Jochen Mannhart. "Magnetic Properties of Epitaxially Grown $SrRuO_3$ Nanodots." *Nano letters* 19, 2 (2019): 1131-1135. (***Equal Contribution**)

D. Hongguang Wang, Vesna Srot, Gennadii Laskin, Jochen Mannhart, Peter A. van Aken. "Aberration-corrected STEM Observations on the Interfacial Structure and Strain Fields of Patterned $SrRuO_3$ Artificial Atoms." *Microscopy and Microanalysis* 25 (S2)(2019): 964-965.

E. Hongguang Wang, Vesna Srot, Gennadii Laskin, Bernhard Fenk, Lei Jin, Jochen Mannhart, Peter A. van Aken. "TEM Sample Preparation of Patterned Quantum Dots". *Microscopy and Microanalysis* 25 (S2)(2019): 790-791.

Other Publications:

A. Honglei Wang, Wenzhen Lv, Jun Shi, Hongguang Wang, Dexu Wang, Lu Jin, Jie Chao, Peter A. van Aken, Runfeng Chen, and Wei Huang. "Efficient Liquid Nitrogen Exfoliation of MoS_2 Ultrathin Nanosheets in the Pure 2H Phase." *ACS Sustainable Chemistry & Engineering* 8, 1 (2019): 84-90.
B. Hongguang Wang, Lei Wang, PengFei Hu, Wei Ren, Jinbao Xu, Pengjun Zhao, and Aimin Chang. "Strong optical absorption of $LaMn_{0.6}Al_{0.4}O_3$ thin films in the mid-infrared atmospheric window." *RSC Advances* 6, 58 (2016): 53389-53392
C. Hongguang Wang, Jinbao Xu, Pengjun Zhao, Chao Ma, Lei Wang, Liang Bian, and Aimin Chang. "Optical Character of Barium Titanate Based Thin Films around the Phase Transition." *Ferroelectrics* 491, 1 (2016): 8-14.
D. Hongguang Wang, Xinqian Xiong, Jinbao Xu, Lei Wang, Liang Bian, Wei Ren. "Complex impedance analysis on orientation effect of $LaMn_{0.6}Al_{0.4}O_3$ thin films." *Journal of Materials Science: Materials in Electronics* 26, (2015): 369–376
E. Hongguang Wang, Jinbao Xu, Chao Ma, Pengjun Zhao, Lei Wang, Liang Bian, Wei Ren, and Aimin Chang. "Infrared optical properties of ferroelectric $0.5BaZr_{0.2}Ti_{0.8}O_3$–$0.5Ba_{0.7}Ca_{0.3}TiO_3$ thin films." *Ceramics International* 41, 1(2015): 475-480.
F. Pengjun Zhao, Jinbao Xu, Hongguang Wang, Lei Wang, Wenwen Kong, Wei Ren, Liang Bian, and Aimin Chang. "Calcium manganate: A promising candidate as buffer layer for hybrid halide perovskite photovoltaic-thermoelectric systems." *Journal of Applied Physics* 116, 19 (2014): 194901.
G. Chao Ma, Hongguang Wang, Pengjun Zhao, Jinbao Xu, Aimin Chang, Lei Wang, and Liang Bian. "Temperature dependence of $Mn1_{.56}Co_{0.96}Ni_{0.48}O_4$ thin films optical properties by spectroscopic ellipsometry." *Materials Letters* 136 (2014): 225-228.
H. Hongguang Wang, Jinbao Xu, Chao Ma, Fanglong Xu, Lei Wang, Liang Bian, and Aimin Chang. "Spectroscopic ellipsometry study of $0.5BaZr_{0.2}Ti_{0.8}O_3$–$0.5Ba_{0.7}Ca_{0.3}TiO_3$ ferroelectric thin films." *Journal of alloys and compounds* 615 (2014): 526-530

Submitted manuscripts:

A. Hongguang Wang, Vesna Srot, Bernhard Fenk, Wilfried Sigle, Gennadii Laskin, Jochen Mannhart, Peter A. van Aken. "An optimized TEM specimen preparation method of quantum nanostructures". *Micron* (2020), Under review.

CONFERENCE CONTRIBUTIONS

A. Hongguang Wang, Vesna Srot, Gennadii Laskin, Jochen Mannhart, Peter A. van Aken. "Aberration-corrected STEM Observations on the Interfacial Structure and Strain Fields of Patterned $SrRuO_3$ Artificial Atoms". (***Oral lecture***), Microscopy and Microanalysis, August 4-8, 2019, Portland, OR, USA.
B. Hongguang Wang, Vesna Srot, Gennadii Laskin, Bernhard Fenk, Lei Jin, Jochen Mannhart, Peter A. van Aken. "TEM Sample Preparation of Patterned Quantum Dots". (***Poster presentation***), Microscopy and Microanalysis, August 4-8, 2019, Portland, OR, USA.
C. Hongguang Wang, Vesna Srot, Gennadii Laskin, Jochen Mannhart, Peter A. van Aken. "STEM investigations of strain relaxation in $SrRuO_3$ artificial atoms". (***Oral lecture***), European Materials Research Society (E-MRS) Spring Meeting, May 27–31, 2019, Nice, France.
D. Hongguang Wang, Vesna Srot, Gennadii Laskin, Jochen Mannhart, Peter A. van Aken "STEM investigations of $SrRuO_3$ quantum dots". (***Invited lecture***), 2018 International Workshop at Ringberg Castle. December 9–12, 2018, Tegernsee, Bavaria, Germany.

E. Hongguang Wang, Vesna Srot, Yi Wang, Hans Boschker, Jochen Mannhart and Peter A. van Aken "Oxygen deficiency evolution in defect-engineered epitaxial $SrMnO_3$ thin films" (***Mini-talk***), Material Science and Engineering Conference. September 26-28, 2018, Darmstadt, Germany.

F. Hongguang Wang, Vesna Srot, Yi Wang, Hans Boschker, Jochen Mannhart and Peter A. van Aken. "Interfacial phenomena at manganite heterointerface" (***Poster presentation***), Advanced Topics in

G. Cs-corrected STEM and Spectroscopy: Theory meets Experiment. June 29–July 4, 2018, SciTech Daresbury Campus, United Kingdom

H. Hongguang Wang, Vesna Srot, Yi Wang, Hans Boschker, Jochen Mannhart and Peter A. van Aken. "Strain-induced defect phase in $SrMnO_3$ thin film" (***Oral lecture***), European Materials Research Society (E-MRS) Spring Meeting. June 18–22, 2018, Strasbourg, France.

I. Hongguang Wang, Vesna Srot, Yi Wang, Hans Boschker, Jochen Mannhart and Peter A. van Aken "Atomically-resolved investigations of local structure and cationic intermixing at $SrMnO_3$-$SrTiO_3$ heterointerfaces by aberration-corrected analytical transmission electron microscopy" (***Invited mini-talk***), Interfaces in Energy Materials conference. April 10-12, 2018, University of Cambridge, United Kingdom.

J. Hongguang Wang, V. Srot, Yi Wang, H. Boschker, J. Mannhart and P. A. van Aken. "Atomic-scale observations of microstructure and local chemistry at $SrMnO_3$-$SrTiO_3$ heterointerfaces". (***Poster presentation***) DPG (German Physical Society) Spring Meeting, March 11-16, 2018, Berlin, Germany.

Table of Contents

List of figures

Abbreviations and Symbols

Abbreviations

TEM - Transmission Electron Microscopy

STEM - Scanning Transmission Electron Microscopy

CTEM - Conventional TEM

4D-STEM - Four-Dimensional Scanning Transmission Electron Microscopy

HAADF - High-Angle Annular Dark-Field

ABF - Annular Bright-Field

EELS - Electron Energy-Loss Spectroscopy

ELNES - Electron Energy Loss Near-Edge Structure

EDS - Energy-Dispersive X-ray Spectroscopy

SEM - Scanning Electron Microscopy

GPA - Geometric Phase Analysis

TP&IM - Tripod Polishing Followed by Subsequent Argon Ion Milling

FIB&NM - Focused Ion Beam Followed by Subsequent NanoMill

PLD - Pulsed Laser Deposition

MBE - Molecular Beam Epitaxy

EBL - Electron Beam Lithography

AFM - Atomic Force Microscopy

MFM - Magnetic Force Microscopy

UHV - Ultra-High Vacuum

SQUID - Superconducting Quantum Interference Device

RHEED - Reflection High-Energy Electron Diffraction

XRD - X-ray Diffraction

RSMs - Reciprocal Space Maps

PMMA - Poly(methyl methacrylate)

TMOs - Transition Metal Oxides

AAs - Artificial Atoms

STO - $SrTiO_3$

SRO - $SrRuO_3$

SMO - $SrMnO_3$

MSA - Multivariate Statistical Analysis

PCA - Principal Component Analysis

DOS - Density of States

TDS - Thermal Diffuse Scattering

QEP - Quantum Excitation of Phonons

FFT - Fast Fourier Transform

Symbols

e - Electron Charge

n - Refractive Index

λ_l - Wavelength of Light

λ_e - Wavelength of Electrons

d_s - Minimum Confusion due to Spherical Aberration

C_s - Spherical Aberration Coefficient

d_{tot} - Total Confusion

E - Kinetic Energy of Electrons

d - Beam Diameter

I - Beam Current

α - Convergence Angle

β - Collection Angle

T - Tolerance Factor

t - Sample Thickness

λ - Mean Free Path

a_f - Film Lattice Constant

a_s - Substrate Lattice Constant

E_F - Fermi Energy

ε - Strain

D - Lattice Displacement

E_{form} - Oxygen Vacancy Formation Energy

μ - Flexoelectric Coefficient

P - Electric Polarization

Chapter 1. Introduction

In this chapter, the motivation of applying electron microscopy-related techniques to study quantum matter heteroepitaxy is presented. Hereafter, a brief introduction to the background and progress of quantum matter heterostructures and related research topics that are focused on in this dissertation is described. Finally, an overview of the dissertation will be provided.

1.1 Motivation

In quantum matter, electrons behave in unconventional and usually surprising ways, giving rise to exciting properties on their own. An important class of quantum matter is the complex transition metal oxides (TMOs) with strongly correlated electron systems, because most transition metals have partially filled d or f electron shells and narrow bandwidths. The complex oxides display a broad spectrum of physical properties, including dielectricity, semiconductivity, (super)conductivity, piezoelectricity, (anti)ferromagnetism, ferroelectricity, photocatalytic, and metal-insulating transition behavior.[1, 2]

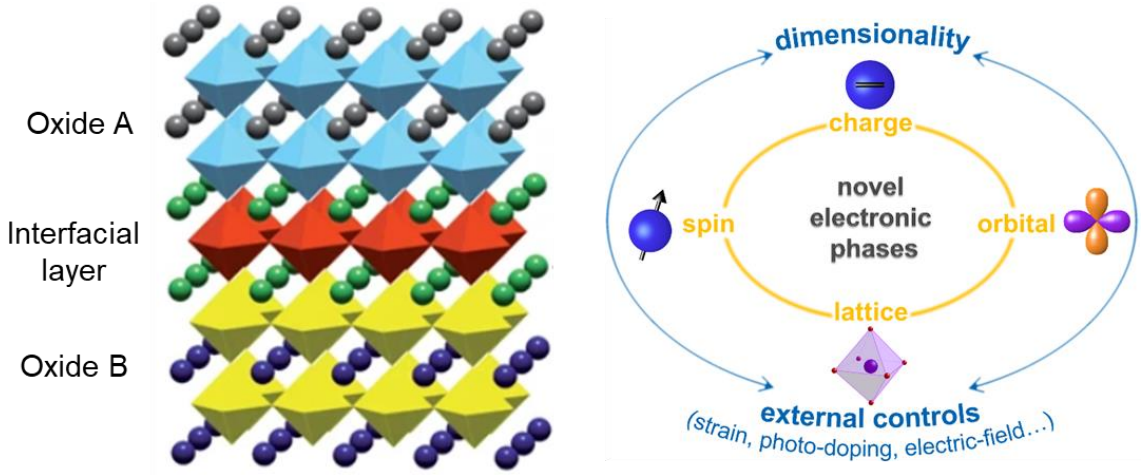

Figure 1-1. The schematic showing the heteroepitaxy[3] (left side) and the factors for controlling electronic states (right side, figure courtesy of Liyuan Zhao from University of Michigan).

When joining two oxides into heterostructures, coupling various phases in heterostructures may lead to a large variety of novel electronic states, especially at the heterointerface, resulting in the unprecedented properties that are usually absent in the constituent materials (Figure 1-1, left panel). Furthermore, the quantum matter heterostructures provide a unique opportunity to tailor their fascinating behaviors (Figure 1-1, right panel). On the one hand, one can engineer electronic states through manipulating the interplay among the charge, spin, orbital, and lattice degrees of freedom during the growth (intrinsic factors), which mostly depend on the characteristics of the composing atoms and the crystal structure of the materials. The electronic states, on the other hand, can be tailored by controlling the dimensionality, electric, magnetic, and force fields (external factors). Famous examples include high-temperature superconductivity in copper oxides, two-dimensional electron gas at the interface between insulating materials, colossal magnetoresistance in manganites.[1, 2] The central goal of this dissertation is to study the lattice structure,

electronic structure, and functionalities of quantum matter heterostructures on the atomic scale and understand their linking to emergent properties.

As a powerful tool for nanoscience, scanning transmission electron microscopy (STEM) was utilized for studying quantum matter heterostructures, because it allows for imaging at significantly high resolution and precision. Especially with the addition of an aberration corrector, atomic resolution can be routinely reached. In STEM, the electron probe is focused on sub-angstrom diameters and raster-scanned over the sample, allowing to identify individual atomic columns with unprecedented clarity. Combined with electron energy-loss spectroscopy (EELS), STEM enables us to not only visualize the structure and elemental distribution, but also extract the bonding states at the interface and defects at atomic resolution. Additionally, quantitative analysis of atomically-resolved STEM images offers the opportunity to measure local strain fields, lattice anisotropy, octahedral rotations, and even nanoscale functionalities like electrical polarization.

In this thesis, epitaxial quantum matter heterostructures are grown with atomic layer precision by pulsed laser deposition (PLD). STEM is devoted to three applications in quantum matter heterostructures: (i) explaining the exotic magnetic properties of $SrRuO_3$ (SRO) artificial atoms (AAs); (ii) probing the charge accumulation at $SrMnO_3/SrTiO_3$ (SMO/STO) interfaces; (iii) visualizing the flexoelectricity around crack tips. Besides, for achieving high-quality STEM results, a pathway for preparing TEM specimens of quantum matter nanostructures is proposed. First, I will stimulate the work by giving a brief overview of quantum matter heteroepitaxy.

1.2 Quantum matter heteroepitaxy

The physical description of all materials is rooted in quantum mechanics, which describes, how atoms bond and electrons interact at a fundamental level.[4, 5] Typically, the quantum behavior can be approximated by a classical description at the macroscopic level, in which atoms become balls that stick together in well-defined arrangements *via* simple forces and vibrate much like balls on springs.[6] In some materials, however, quantum effects remain manifest over a broader range of energy and length scales, and the only path to fully understand, how the material behaves, is to keep the quantum behavior in view. Quantum materials is a broad term in condensed matter physics,[7] defined as "solids with exotic physical properties, arising from the quantum mechanical properties of their constituent electrons" by the US Department of Energy.[6] The properties of quantum material surpass incoherent and mean-field behaviors and often are collective and emergent.[8, 9] Canonical quantum materials are superconductors, graphene, topological insulators, Weyl semimetals, quantum spin liquids, and spin ices. [8, 10]

Unprecedented properties can emerge, when joining quantum materials in heteroepitaxy, resulting from the interplay between spin, charge, orbital, lattice degrees of freedom and can be tailored by controlling parameters such as strain and electric fields imposed by gates.[11-13] Many of them derive their properties from reduced dimensionality, in particular from the confinement of electrons to two-dimensional sheets. The development of quantum-matter heterostructures is exemplified by the development of transition-metal oxide heterostructures with strongly correlated electrons and the intriguing behavior of transition-metal oxide interfaces. One famous example is the formation of a 2-dimensional electron liquid at the interface between insulating STO and $LaAlO_3$ (LAO) with perovskite structure (Figure 1-2).[14, 15] In this thesis, I focus on the studies of the quantum matter heteroepitaxy fabricated with perovskite oxides.

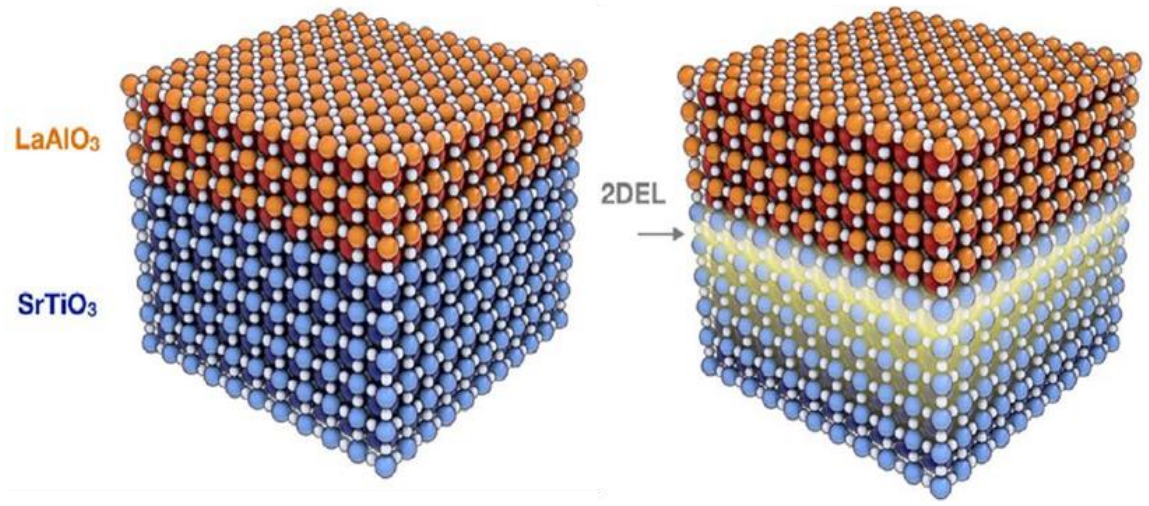

Figure 1-2. Schematic drawings showing a 2D electron liquid (2DEL) (yellow) generated at the interface between two insulators (STO and LAO), if the LAO layer is thicker than 3 unit cells. (figure courtesy of Jochen Mannhart)[16]

1.2.1 Perovskite oxides

Perovskite oxides, which are structurally similar to the mineral $CaTiO_3$, have been well studied due to their rich physical characteristics, such as high-temperature superconductivity, ferroelectricity, ferromagnetism, catalysis, and electro-optical effects.[17, 18] The typical chemical structural formula for perovskite oxides is ABO_3, which is displayed in Figure 1-3. A-site ions are large rare-earth, alkaline-earth, alkali, or large ions such as Bi^{3+} or Pb^{2+}, which coordinate to 12 oxygen atoms. B-site ions are 3*d*, 4*d*, or 5*d* transition metal ions, which occupy oxygen octahedrons. The 'A' atoms are generally larger than the 'B' atoms. A large number of chemical elements and different cations can successfully be incorporated on the A- or B-sites in the crystal lattice. For the material studied in this thesis, the A sites are occupied by alkaline-earth element Sr; B sites are occupied by 3*d* transition metal Ti, Mn, and the 4*d* transition metal Ru, respectively. [19]

The relative ion radii requirements for stability of the perovskite structure can be characterized by the

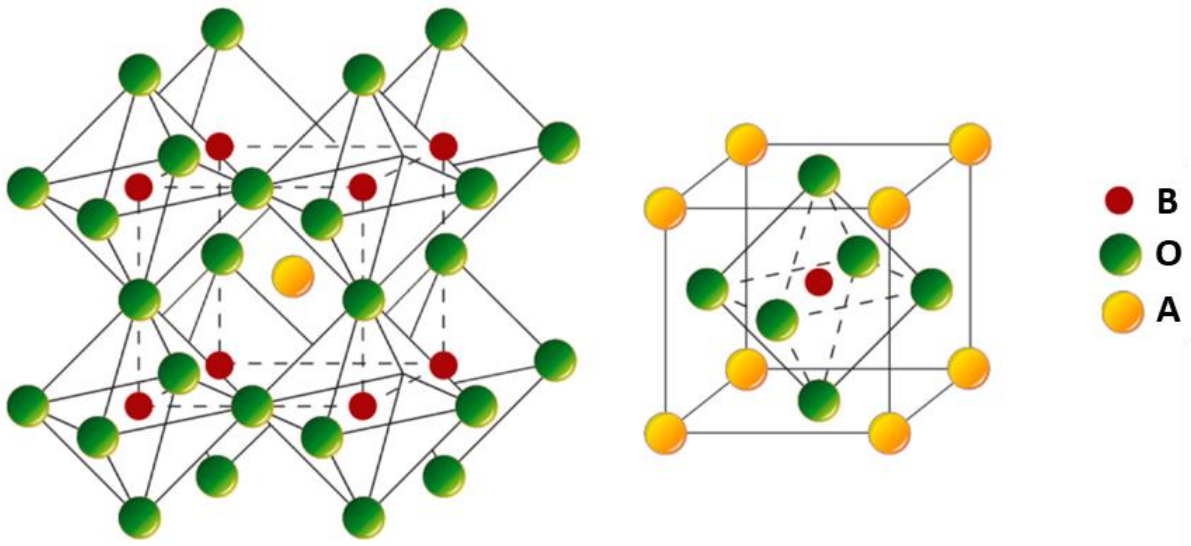

Figure 1-3. The ideal cubic structure of an ABO_3 perovskite. O refers to the oxide ion O^{2-}, A is a large 12-fold coordinated cation, and B is a small 6-fold (octahedral) coordinated cation (modified from ref. [20]).

tolerance factor (T), which was introduced by Goldschmidt in the 1920s.[21] The Goldschmidt tolerance factor is based on the correlation between structural geometry and the ionic radii of the cations:

$$T = \frac{R_A + R_O}{\sqrt{2}(R_B + R_O)} \tag{1-1}$$

where R_A, R_B, and R_O are the ionic radii of A and B site elements and oxygen, respectively. Note that the covalent character of the perovskite oxides is ignored in this formula. All cations in the structure should meet the restriction of $0.75 < T < 1.0$.[22] The ideal cubic perovskite structure appears in a few cases for T-values very close to 1 and at high temperatures. In most cases, T-values deviate from unity, inducing an increased tendency for structural distortions in the lattice. Distortions lower the symmetry from cubic to orthorhombic, rhombohedral, tetragonal, monoclinic or triclinic.[23] The distortion of perovskite oxides usually takes the form of octahedral deformation, tilt, or rotation, which is related to spontaneous symmetry breaking, like the Jahn-Teller effect, the motion of cations, non-stoichiometry like oxygen vacancies, and cation doping.[24] Furthermore, some external factors, such as pressure and temperature, are also expected to induce distortions of the perovskite structure.

Consider a transition-metal atom in a crystal with perovskite structure. It is surrounded by six oxygen ions, which produce a crystal field acting on this transition metal atom with cubic symmetry, hinders the free rotation of the electrons, and quenches the orbital angular momentum by introducing the crystal field splitting of the *d* orbitals.[25] Consequently, the originally five-fold degenerate *d* orbitals are split into three-fold degenerate t_{2g} orbitals (*xy*, *yz*, *zx* orbitals), and two-fold degenerate e_g orbitals (x_2-y_2, $3z_2-r_2$ orbitals) (see Figure 1-4). e_g orbitals pointing toward O^{2-} ions have higher energy in comparison with t_{2g} orbitals pointing between e_g orbitals. The energy difference between e_g and t_{2g} states is characterized by the crystal-field splitting energy, which varies between ~1-2 eV depending on the system and the extent of the distortion. These orbitals have a different sign for the wave function depending on the radial direction, which sometimes results in the cancellation of the overlap integrals with the *p* orbitals of the O ions between two neighboring transition metal ions. In TMOs, the orbital degree of freedom of the *d* electrons is proven to play an important role, not only in the prominent case of the colossal magnetoresistance of manganese oxides, but also in anisotropic electronic and magnetic properties of many transition-metal oxides.[26, 27]

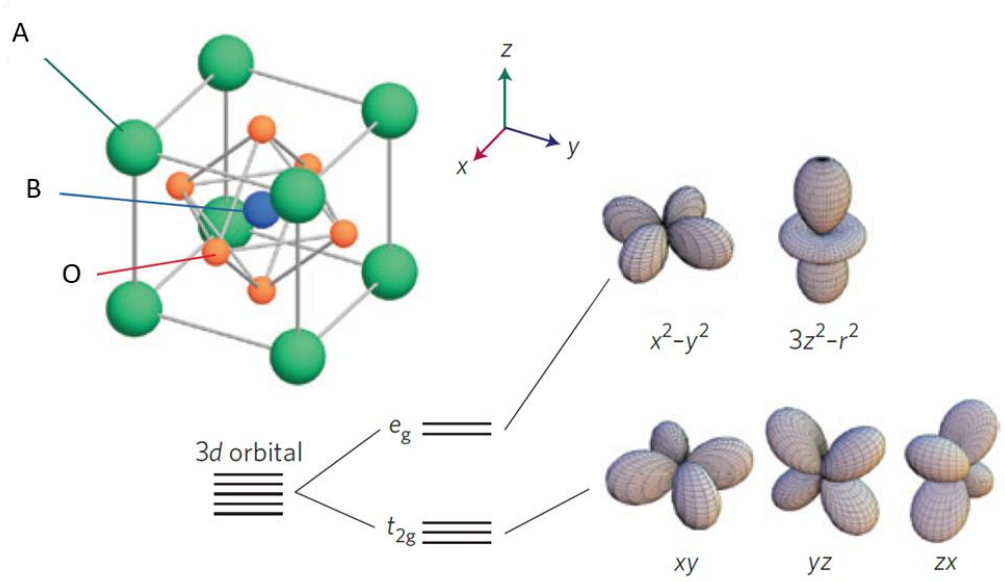

Figure 1-4. Sketch of the 3*d*-electron orbitals in a cubic crystal field (modified from ref. [13]).

1.2.2 Unprecedented phenomena at the heterointerface

Herbert Kroemer emphasized the importance of the interface in heterostructures by stating, "*Often, it may be said that the interface is the device*." in his Nobel lecture.[28] With remarkable advances in epitaxial growth techniques, in particular molecular beam epitaxy (MBE) and PLD, one could grow high-quality material with complex structure with atomic layer precision.[29] Atomic-level control of heterointerfaces has become feasible.[30] Subtle atomic structures that are not energetically favored in 3D bulk can be fabricated, leading to unprecedented phenomena characterized by interface conductivity, magnetoelectric coupling, and quantum transport effect at oxide heterointerfaces.[13] The abundant physical behaviors at the heterointerface of TMOs arise from the complex interactions between their charge, orbital, spin, and lattice degree of freedoms. These interactions can be tailored by the epitaxial strain, local symmetry breaking, charge transfer, electrostatic coupling, *etc.* Considering the relevance to the results in this thesis, the effects of epitaxial strain, and charge distribution will be briefly introduced.

Epitaxial strain. The crystal structure of grown layers is changed due to the matching of in-plane lattice constant to that of the substrate. The matching results in strain in layers and the magnitude of the strain field can be controlled with the use of different substrates. When the lattice constant of a film (a_f) is dissimilar to the lattice constant of a substrate (a_s), compression or elongation occurs within the film's crystal structure. Thus an elastic strain is induced in the film. For cases of different lattice constants ($a_f \neq a_s$), the structure of the thin film tries to take the structure of the substrate, causing structural changes (mainly the change of rotation, tilting, and distortion in BO_6 octahedron, and/or the change in B-O bond length) to occur from the original atomic position.[31] Quantitatively, the amount of strain (ε) induced in a film is defined as:

$$\varepsilon = \frac{a_s - a_f}{a_f} \tag{1-2}$$

where a_s is the substrate lattice constant and a_f is the film lattice constant. The compressive strain is induced in a film, when $a_f > a_s$, whereas a tensile strain is induced in a film, when $a_f < a_s$ (Figure 1-5). Strain engineering has become a very popular way to control lattice distortions, which, in return, affect the electronic degrees of freedom, and thus adjusting materials' properties and stabilizing novel electron states.[32-34] One example is the strain engineering of the multiferroic effect in SMO thin films, showing that the epitaxial SMO thin films yield a ferroelectric polarization under >1% epitaxial tensile strain imposed by the substrate.[35] Investigations of SRO thin films demonstrate that the magnetic anisotropy is tunable by epitaxial strain.[36] In this thesis, I carefully consider the strain effect during the studies of SRO/STO and SMO/STO heterostructures in Chapter 4, Chapter 5, and Chapter 6. Based on STEM results, the strain field in epitaxial layers is quantitatively analyzed with high spatial resolution.

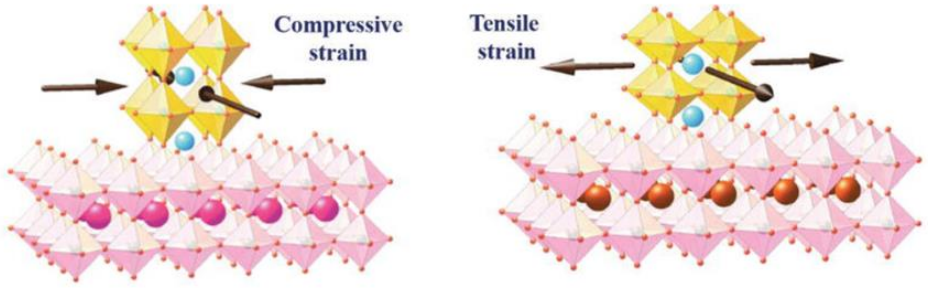

Figure 1-5. The in-plane epitaxial strain imposed by the substrate in perovskite oxide heteroepitaxy.[34]

Charge distribution. The charge distribution is one of the cornerstone mechanisms at the heterointerface, leading to a wide range of phenomena such as interfacial conductivity of LAO/STO heterostructures [15] and interfacial ferromagnetism of $CaMnO_3/CaRuO_3$ heterointerfaces.[37] Since the Fermi energy (E_F) must be constant all through the heterostructure in equilibrium, a charge transfer occurs between oxide layers, which have a mismatch of their Fermi level. Electrons move from the material with high E_F to that with low E_F to line up the E_F at the interface, modifying the local potential and electronic structures. The charge transfer in SMO is suggested to have a sensitive impact on the magnetic transition.[38] By growing an appropriate heterostructure, the provoked doping into Mn *d* states may trigger a transition from a G-type antiferromagnetic ground state to a ferromagnetic ground state.

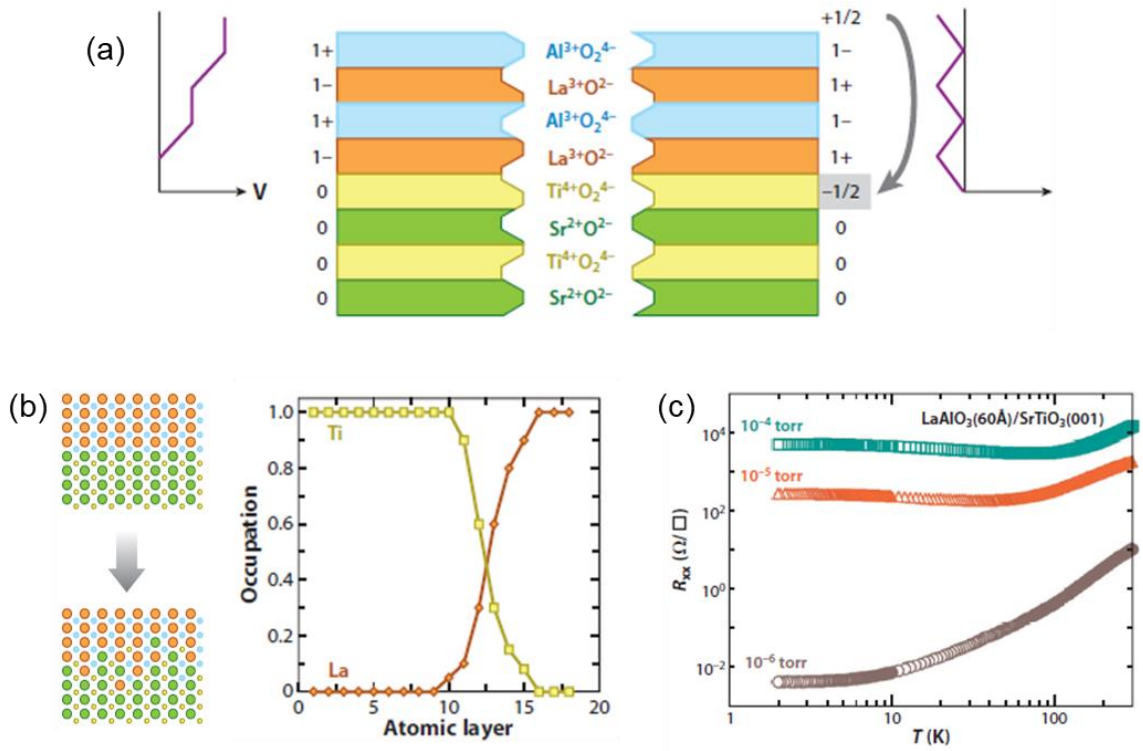

Figure 1-6. The possible origin of the electron gas at the LAO/STO interface. (a) The polar discontinuity triggers a potential build-up across the LAO layer as a function of its thickness (left). Above a critical thickness, an electronic reconstruction occurs, resulting in electron accumulation at the interface (right). (b) The sketch shows an interfacial layer with cationic intermixing (La/Sr and Ti/Al) (left). The depth profiles for the Ti and La ions are measured by EELS. (c) The electrical characteristics of the LAO/STO system depend on the oxygen pressure during the growth. R_{xx} represents the resistance at a certain temperature (modified from ref.[11]).

The charge accumulation at the interface is an essential point for the interpretation of the metallic states in LAO/STO heterostructures. Both compounds are band insulators (E_{gap}=5.6 eV for bulk LAO and E_{gap} = 3.2 eV for bulk STO); yet, when a LAO film is deposited layer by layer on top of a TiO_2-plane-terminated (001)-oriented STO substrate, the interface switches to a metallic state, when the film thickness exceeds 3 unit cells.[14, 39] As shown in Figure 1-6(a), the polar discontinuity at the interface is a possible driver. In detail, the LaO and AlO_2 layers are polar and carry a positive and negative charge of +1 *e* and -1 *e* per unit cell, respectively, forming a formal polarization in LAO. The electric potential across the LAO film increases as the LAO layer gets thicker and breaks down at a critical thickness, which is suggested to be around 3–4 unit cells.[40] Above the critical thickness, holes form in the O *2p* valence band of the surface LAO layer and electrons accumulate at the interface in the Ti *d* orbitals (t_{2g}), leading to the formation of

the observed metallic interface layers.[41] The carrier density is expected to rise from $n_{2D} = 0$ before the breakdown to $n_{2D} = 3.3 \times 10^{14}$ cm^2 (*i.e.*, half an electron per unit cell) for thick layers.[11] The effect of the interfacial chemical environment on the charge carrier is another important factor. As illustrated in Figure 1-6 (b), if the interface is not chemically sharp, with some La/Sr and Ti/Al intermixing, the doped interfacial layer could induce carriers at the interface, which is evidenced by STEM [42] and X-ray diffraction (XRD)[43]. It has been demonstrated that oxygen vacancies introduced during the growth could be an alternative doping mechanism for the carrier formation. As shown in Figure 1-6(c), at the same temperature, the carrier density increases with the decrease of the oxygen pressure during the deposition because of the formation of oxygen vacancies. Furthermore, when the interface region yields charged ionic defects such as oxygen vacancies, space-charge effects on the charge accumulation should not be ignored. In chapter 5 on the SMO/STO interface, the role of charge transfer, elemental intermixing, oxygen vacancies and the space-charge effects on the charge accumulation will be discussed.

1.2.3 Quantum confinement of electron system

Quantum confinement effects describe the change of electronic energy level, when materials' size and dimensions continuously decrease, closely relating to their electric, magnetic and optical properties. The first evidence of quantum confinement effects in clusters came from crystalline CuCl clusters grown in silicate glasses.[45] Figure 1-6 shows, how the DOS is modified under different types of confinement in general. The dimensions of confinement increase with the decrease of the dimension of the material, resulting in a gradual transition from the continuous the DOS in 3D materials to a set of discrete energy levels in 0D quantum dots.[46] Because of the shell structure of the electron states and their coherency across the dots, quantum dots are appropriately described as "artificial atoms".[47-49] Experimentally, confining electrons in one or more dimensions can be realized by varying the material structure or applying external

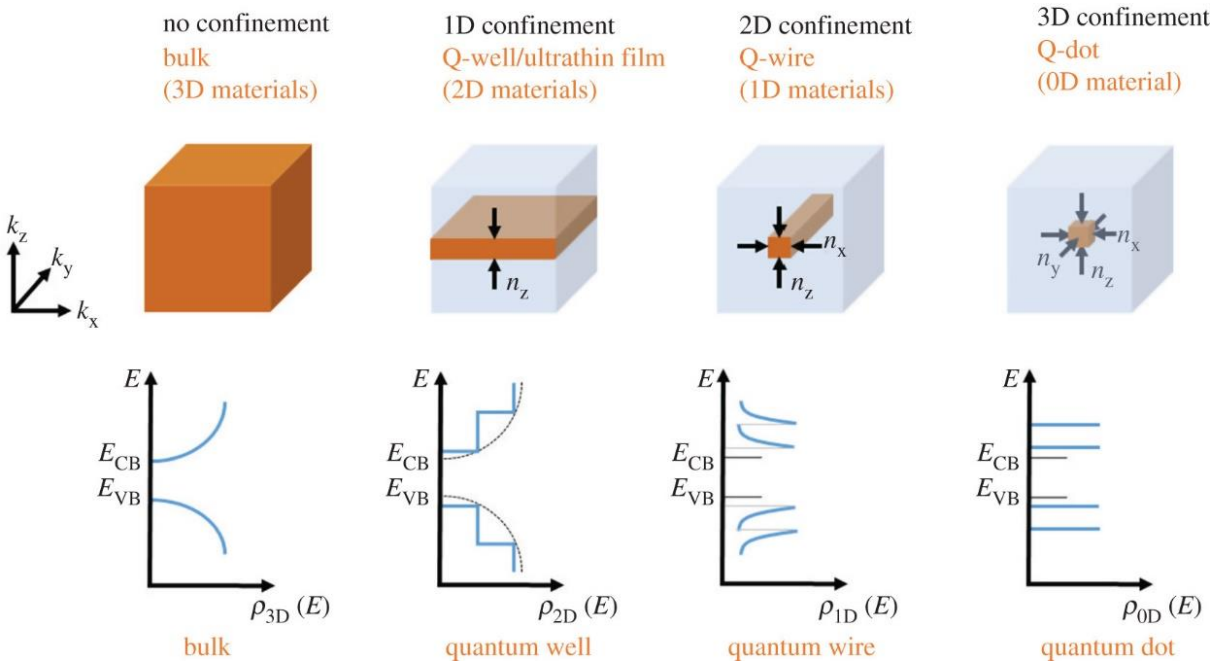

Figure 1-7. Schematic illustration of the density of states (DOS) in a material as a function of dimension.[44]

conditions through electromagnetic fields or patterning. It allows to reduce the number of degrees of freedom effectively available for electrons and to modify the properties of the electron systems significantly. In semiconductors, size effects may substantially affect the DOS, the size of the bandgap, the behavior of excitons, phonon distributions, and many other characteristics.[50] Examples of spatial confinement effects are 1D confinement in thin films[51] and at the interface[52], 2D confinement in nanolines[53], and 3D confinement in quantum dots[54]. These confined electron systems have already found widespread applications, including quantum-well laser diodes,[55] quantum dot displays,[56] biological imaging systems,[57] and quantum computing[58]. For a mean-field system, interactions between electrons in conventional semiconductors are negligible compared to their kinetic energy. Thus, the interaction of a single electron with the other electrons can be described as a movement in an average, mean potential. However, this concept no longer works in correlated materials such as TMOs with *d* electrons due to their strong electron-electron interactions, which is even more pronounced in their bulk form. From this perspective, quantum confinement of correlated materials presumably form more complex electronic states and thereby produce more intriguing behaviors than relatively simple mean-field materials.

To date, most published works on confined correlated materials are focused on the 1D confinement, such as 2D electron gases, and rarely go beyond the 1D case. The obstacle is the high complexity of correlated materials in terms of their lattice structure and chemical composition. Furthermore, it remains a challenge to fabricate high-quality patterning of correlated materials to small dimensions and small size down to the nanoscale. The smallest size of patterned correlated material systems reported in the literature is about 80 nm, which is shown in Figure 1-8. TEM images in Figures 1-8 (a-c) show the even spacing of 80 nm-sized single-crystalline SRO dots and the atomically sharp interface between SRO and STO. Magnetic force microscopy (MFM) measurements of dots at room temperature (Figure 1-8 (e)) and 77K (Figure 1-8(g)) demonstrated that the magnetic properties of the large-area SRO thin films are preserved in the nanodot arrays with the dot diameter down to 80 nm.[59] However, it remains unclear, how the magnetic properties change for even smaller dot arrays. In chapter 4, I will present the fabrication and study of AAs down to 15 nm fabricated with intrinsically correlated and ferromagnetic SRO.

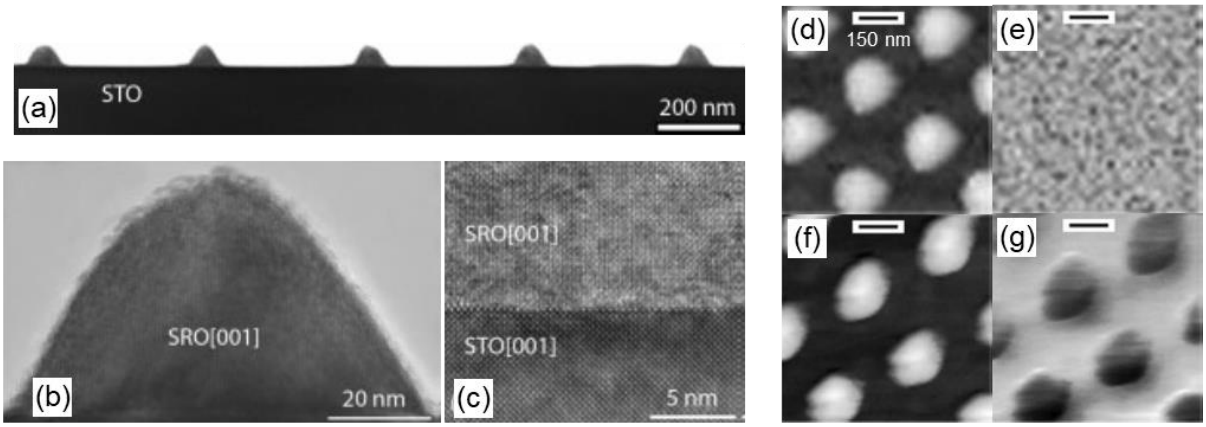

Figure 1-8. TEM images for the cross-section of 80 nm-sized SRO dots on STO substrate including dots array profile (a), an individual nanodot (b), the interfacial structure between SRO and STO (c). Atomic force microscopy (AFM) and MFM images of SRO nanodots at room temperature (d, e) and 77 K (f, g). (modified from ref. [59])

1.2.4 Nanoscale flexoelectricity

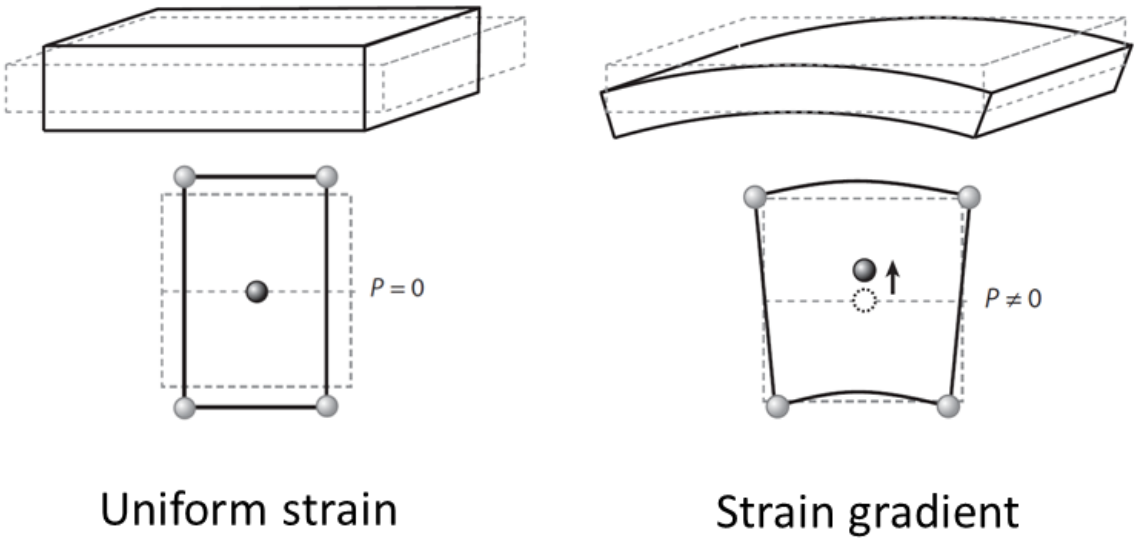

Figure 1-9. Schematic illustration of flexoelectricity. Left panel: the absence of polarization under uniform strain. Right panel: the appearance of electric polarization under strain gradient. (modified from ref.[60])

The flexoelectric effect, as a universal electromechanical coupling effect, describes the response of electric polarization to a mechanical strain gradient. Since the flexoelectric effect was first identified theoretically by Mashkevich and Tolpygo [61, 62] based on their studies of lattice dynamics in crystals, this effect has been found to exist in a wide variety of materials including solid dielectrics, liquid crystals, and biological systems, *etc.*[60] Based on a simple ionic model, the theory of the flexoelectric effect was proposed by Tagantsev[63]. Unlike piezoelectric materials, which become electrically polarized, when subjected to mechanical stress, the flexoelectric coupling is between polarization and strain gradient, rather than between polarization and homogeneous strain. Therefore, flexoelectricity even appears in centrosymmetric materials. As illustrated in Figure 1-9, when a centrosymmetric material is subjected to a homogeneous deformation (left panel), no polarization appears because of the absence of preferred directions of the polar vector. By comparison, the strain gradient breaks the local centrosymmetric and induces a vertical gradient of in-plane strain (right panel). The central cation is squeezed up. The centers of gravity of the negative ions (large circles) and the positive ions (small circles) no longer coincide, which results in a non-zero net dipole moment in the directions indicated by the arrow. The piezoelectric effect can only be observed in 20 non-centrosymmetric crystal point groups[64], while the flexoelectric effect can exist in all 32 point groups. In general, the total electric polarization of materials (P) can result from both flexoelectric and piezoelectric effects.[65] The polarization can be described as:

$$P_i = d_{ijk}\sigma_{jk} + \mu_{ijkl}\frac{\partial \varepsilon_{jk}}{\partial x_l} \tag{1-3}$$

where d_{ijk}, σ_{jk}, μ_{ijkl}, ε_{jk}, and x_l are the piezoelectric constant, applied stress, flexoelectric constant, strain, and position coordinate, respectively.[66] $\frac{\partial \varepsilon_{jk}}{\partial x_l}$ represents the strain gradient. As discussed above, due to the absence of piezoelectricity, the polarization in a centrosymmetric material can be simplified as:

$$P_i = \mu_{ijkl}\frac{\partial \varepsilon_{jk}}{\partial x_l} \tag{1-4}$$

The flexoelectric tensor μ_{ijkl} is a fourth-rank tensor, which guarantees the existence of flexoelectricity in all crystals with any symmetry. It has 54 independent components for most general cases. For cubic crystals, it has only three independent components, known as the longitudinal coefficient μ_{11}, transverse coefficient μ_{12}, and shear coefficients μ_{44}.[67] Pioneer work by Zubko *et al.*[60] experimentally investigated the flexoelectricity of STO single crystals and obtained its three flexoelectric coefficients for the first time. Furthermore, the flexoelectric coefficient scales with the dielectric susceptibility of the material.

Following its discovery in the last several decades, studies of flexoelectricity in solids did not draw much attention because of the rather small magnitude of this effect in bulk samples with common scales due to the small strain gradient. The order of magnitude of the flexoelectric coefficients is estimated as $\sim e/a$ (10^{-9}C/m), where e is the electron charge, and a is the lattice constant. However, flexoelectricity is a size-dependent effect, because large strain gradients are often present at the nanoscale and lead to strong flexoelectric effects.[68] Examples are flexoelectricity at extreme temperature by tuning cation diffusion in core-shell nanoparticles[69] and flexoelectric polarization at dislocation cores of STO.[70] With the development of nanotechnologies, oxide heterostructures can be fabricated with high precision, stimulating the research interest on nanoscale flexoelectricity. Catalan *et al.*[71] found that nano-twins in a thin layer of $PbTiO_3$/STO heterostructures generate strong lateral strain gradients, inducing corresponding flexoelectric polarization. Such polarizations are comparable to the size of the spontaneous ferroelectric polarization, and thus the magnitude and orientation of the total polarization in $PbTiO_3$ are substantially changed.

Generally, cracks in materials yield the most substantial strain gradients that a material can withstand and thus leads to a significant flexoelectricity effect around crack tips. Cracks are, therefore, a natural ground to search for flexoelectric effects. The role of flexoelectricity in fracture physics is an interesting topic for investigations. Using a self-consistent model of flexoelectricity, Abdollahi *et al*[72] evidenced that, in the presence of flexoelectricity, fracture toughening significantly increases in a size-dependent manner, and this toughening is asymmetric concerning the sign of the polarization. This prediction has been verified in recent work by Cordero-Edwards *et al.*[73] As shown in Figure 1-10, based on nanoindentation testing on a Rb-doped $KTiOPO_4$ single crystal with in-plane polarization, they demonstrate that the crack length parallel to the polarization is always larger than the crack length antiparallel to the polarization, irrespective of the polarity of the domain. However, the study of flexoelectricity around crack tips on smaller scales down to nanometer is not yet available. In chapter 6, I will present a direct observation of flexoelectricity around crack tips in SMO/STO heterostructures.

1.3 Dissertation overview

This thesis, consisting of 7 chapters, is dedicated to the study of quantum heteroepitaxy based on perovskite oxides on the atomic scale *via* aberration-corrected STEM and spectroscopy. The motivation and subjects of this thesis are introduced in chapter 1.

Chapter 2 is devoted to the overview of experimental methodologies used in this thesis. I start with a brief introduction of the epitaxial growth process for oxide heterostructures and the fabrication of AAs with a pattering technique. Afterwards, I present the microscopy techniques employed in this thesis, focusing on STEM and EELS. The last part describes the basic principles for STEM-related data processing and simulation methods.

Chapter 3 presents an optimized TEM specimen preparation method for quantum nanostructures. Through the use of a combination of existing techniques (focused ion beam (FIB) & NanoMill), I succeed in making high-quality TEM specimens out of quantum nanostructures by optimizing the preparation process. Compared to the conventional method (tripod polishing (TP) & ion milling (IM)), the presented approach

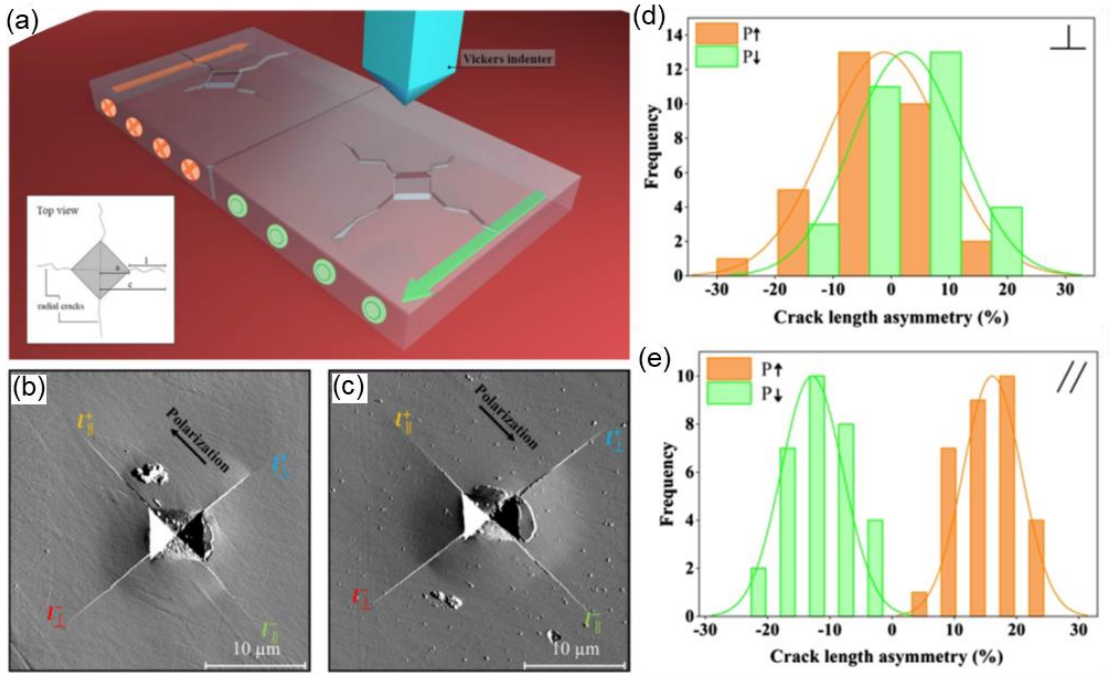

Figure 1-10. (a) Schematic illustration of the Vickers indentation test showing the top view of typical radial crack propagation in case of ferroelectric polarization. (b), (c) is the AFM topography of the radial crack propagation for materials with up and down polarization, respectively. (d), (e) is crack length asymmetry perpendicular and parallel to the polar axis, respectively (the asymmetry coefficient is defined as %Asy =100(l^+-l^-)/<l>, where l^+ is the crack length parallel to the polarization, l^- is the crack length antiparallel to the polarization, and <l> is average crack length (l^+-l^-)/2.) (modified from ref.[73]).

enables us to make higher quality TEM specimens more efficiently. This method will be used for preparing the AA TEM specimen in chapter 4.

Chapter 4 focuses on the study of SRO AAs, which are periodically arranged on top of STO substrates *via* patterning with electron-beam lithography. The magnetic behaviors of patterned AAs compared to the unpatterned thin films are investigated, which are mainly about the magnetic transition and the magnetic anisotropy. For the sake of probing underlying mechanisms, I make detailed STEM observations in terms of lattice structure (strain), interfacial chemistry and oxygen octahedral rotation.

Chapter 5 explores the charge distribution at SMO/STO interfaces. STEM-EELS results on Mn-$L_{2,3}$ and Ti-$L_{2,3}$ edges evidence that electronic charges accumulate at the SMO side close to the interface. Taking this interface as a model, I make a comprehensive discussion about the possible contributions to the charge accumulation, including charge transfer, epitaxial strain, ionic defects, and space-charge effects.

Chapter 6 is dedicated to studying the flexoelectricity around crack tips. Cracks occur due to the thermal stress relief and are mainly divided into two types: shallow cracks and deep cracks. Based on atomic displacement measurements with STEM images, I find a large strain gradient around the tip of the deep crack, together with a huge flexoelectric polarization that is screened by extra charge at the crack tip. The role of flexoelectricity on crack propagation is discussed.

Chapter 7 summarizes the obtained results, followed by an outlook for future directions.

Chapter 2. Experimental methodology

This chapter aims to give a brief introduction to the experimental methods used in the thesis. I will start with the growth and fabrication of quantum matter heterostructures. Next, the basic principles of microscopy techniques will be introduced. In particular, theory and function of aberration-corrected STEM methods are presented. Last but not least, the data processing of TEM results and relating theoretical calculations are described.

2.1 Sample growth and fabrication

Heterostructures studied in this thesis are grown using PLD by collaborators from the Solid State Quantum Electronic Department of Max Planck Institute for Solid State Research (MPI-FKF). SRO AAs are fabricated using a hard mask patterned with EBL.

2.1.1 Epitaxial growth of oxide heterostructures using pulsed laser deposition

As one of the physical vapor deposition techniques, PLD has been demonstrated a very powerful tool for growing thin films. Combined with a stoichiometry transfer between target and substrate and the possibility of working in ultra-high vacuum (UHV) as well as in different reactive and inert gas atmospheres, PLD allows depositing all kinds of different materials, *e.g.*, high-temperature superconductors, oxides, nitrides, carbides, semiconductors, metals, and even polymers or fullerenes can be grown with high deposition rates.[74] Because of their high melting points, PLD is especially suited for growing thin oxide films. Besides, the molecular oxygen gas, present in the chamber during deposition, helps not only reduce the kinetic energy of the ablated species in the plume and prevent the surface damage, but also provides the reactivity necessary for oxidation processes.

Prior to deposition, the surface of the substrate and the target is required to be clean enough for the growth of high-quality epitaxial layers. The substrate is wiped with lens paper at first and consecutively cleaned in acetone (10 min), isopropanol (10 min), and ultrapure water (10 min) using an ultrasonic bath. Afterwards, substrates are annealed and terminated in a UHV chamber using a CO_2 laser system with a wavelength of 9.27 μm at low molecular oxygen background pressure.[75] Atomically flat single-phase surfaces of substrates can be obtained. The target is first polished by a gradation SiC paper to remove visible defects on the surface and then sonicated in isopropanol to remove dust and other contaminants. Afterwards, the target is annealed at low temperature (about 80 °C) to dry and degas it. Finally, the target surface was pre-ablated in the PLD chamber directly before the growth to remove possible residual contaminants and provide a smooth homogeneous surface for the ablation.

The sketch of the PLD process is displayed in Figure 2-1. The substrate is mounted to a tantalum sample holder and then placed on a heating stage directly under the target. The chamber is then filled with molecular oxygen, after which the substrate is annealed at a high temperature (1300°C) gradually cooled to the deposition temperature at a rate of 1 K/s. For the deposition, the target is ablated using a KrF excimer laser with a wavelength of 248 nm, forming a plasma plume. The target-substrate distance is set to 56 mm. After every laser pulse, the target is shifted laterally according to a pre-defined path to use a large surface area of the target. Two consequent ablation spots may overlap with each other by a defined value. The substrate temperature during growth is measured and controlled using a pyrometer on its back surface. The pressure in the chamber can be adjusted by varying the gas flow and the pumping speed using a variable shutter in front of the turbopump. During the deposition, reflection high-energy electron diffraction (RHEED) has been used to monitor the growth of oxide thin films.[76]

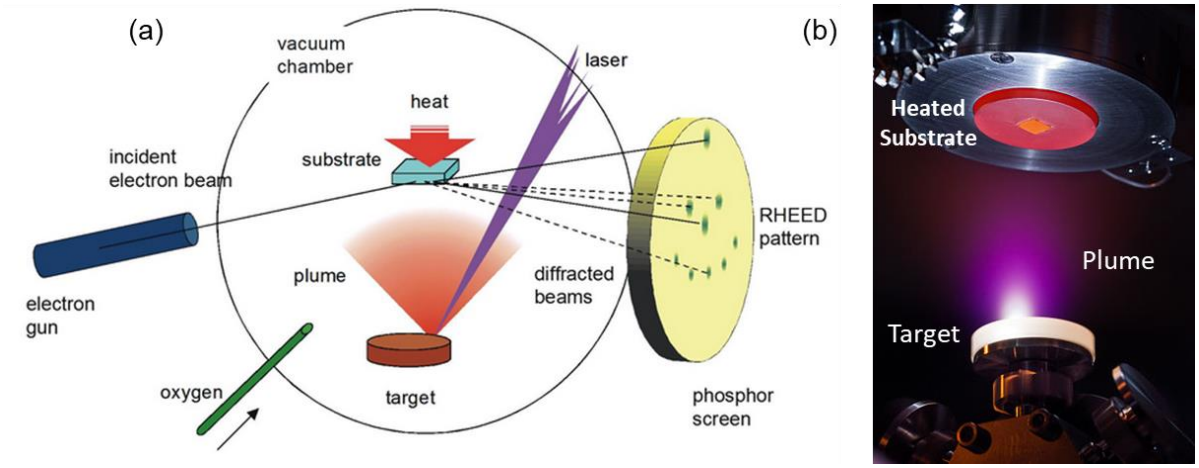

Figure 2-1. (a) Schematic illustration of the PLD process (image courtesy from Jin San Choi from University of Ulsan). (b) Photograph for the deposition of the ablation material on the substrate. The heated substrate, a plasma plume, and the target material are indicated (image courtesy from Wikipedia).

A successful deposition requires the careful control of the parameters, including substrate temperature during deposition, type of gas and its pressure, energy density of the laser beam on a target, and laser pulses repetition rate. Detailed parameters for the grown thin films in this thesis are presented as following.

SMO thin film. The epitaxial SMO thin film was grown on TiO_2-terminated (001)-oriented STO substrates (Shinkosha) by PLD using a stoichiometric, polycrystalline target (Lesker). For making the single terminated TiO_2 surface of STO substrates, the STO substrates were prepared by ultrasonification in water, and then treated by a combination of etching with a buffered HF solution and *ex-situ* annealing at 1050°C.[77] The growth temperature was 800 °C, the oxygen pressure was 0.05 mbar, the laser fluency was 2 J cm^{-2}, the laser frequency was 1 Hz, and the growth rate was 0.04 monolayer per pulse. The wavelength of the KrF laser was 248 nm. The growth mode is a layer-by-layer growth as evidenced by the observation of RHEED oscillations.

SRO thin film. The epitaxial SRO thin film was grown with the same PLD system with that of SMO thin films under similar conditions. The growth temperature was 680 °C, the oxygen pressure was 0.08 mbar, the laser fluency was 2.5 J cm^2, the laser frequency was 1 Hz, and the growth rate was 0.05 monolayer per pulse. The growth process was also observed using RHEED.

2.1.2 Fabrication of $SrRuO_3$ artificial atoms

Based on the growth of high-quality single-crystalline SRO thin films, the SRO AAs in this thesis are patterned with electron-beam lithography (EBL). The EBL technique enables us to make custom shapes by the irradiation of a suitably sensitive resist material with a focused beam of electrons.[78] In general, the electron beam of the EBL setup can be focused to several nanometers in diameter. However, the final resolution of the exposure is limited. Electrons can be scattered into a large volume during the etching process.[79] Besides, *e*-beam resists that consist of long polymer molecules introduces additional limitation of the resolution depending on the size of these molecules.[80] Therefore, the parameters for patterning should be uniquely optimized for the specific structure and material systems.

As shown in Figure 2-2, starting with a high-quality SRO thin film, the fabrication of SRO AAs consists of the following steps:

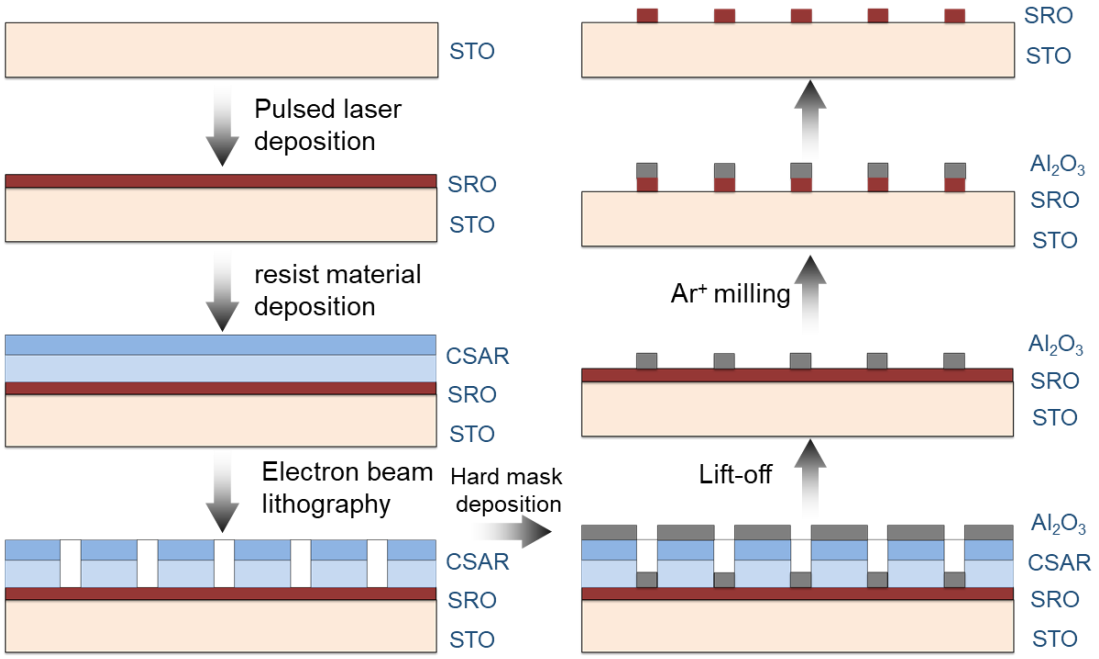

Figure 2-2. Schematic illustration for the fabrication process of SRO AAs.

- Depositing *e*-beam resist on the top of SRO layer by spin coating. The resist material used in this work is poly(*α*-methyl styrene-co-*α*-chloroacrylate methylester) (CSAR, Allresist GmbH, Germany). This resist provides superior resolution and requires a smaller exposure dose than the resist poly(methyl methacrylate) (PMMA) and, therefore, is more suitable for small-scale structures. Since the STO substrate is insulating, it is necessary to coat an additional layer of conducting polymer Espacer 300Z (Showa Denko, USA) on top of the resist to reduce the charging effect and thus improve the stability during exposure.

- Loading the sample into a UHV chamber and exposing it by an electron beam according to the design layout to remove parts of the resist layer. Exposures were performed in a 100 kV electron beam lithography system JEOL JBX6300. The rather high voltage renders electrons to penetrate deeper into the substrate, which reduces the amount of secondary radiation absorbed by the resist, improving the resolution. After the exposure, resists are developed by immersing into a developer liquid. Here, a proper layout should be selected to make the area covered with arrays as large as possible to provide an adequate amount of material for the magnetic measurement.

- Deposition of a hard mask of a thin layer of amorphous Al_2O_3 on the top by PLD. Al_2O_3 is used, because it has a low ion milling rate and thus allows to reduce the thickness of the hard mask and of the resist.[81] Additionally, it can also be easily dissolved in many bases or acids.

- Lift-out the resist layer and leaving the only hard mask on the top of the SRO layer. This step is done by chemically dissolving it in a remover solution. Low-power ultrasound and moderate heating can be used to facilitate the process. To remove the residuals of the resist, the sample is additionally cleaned in acetone and isopropanol and exposed to an oxygen plasma.

- Dry etching with a flux of ionized argon to pattern the SRO layer. This is done using an Ar^+ milling set-up connected to the radial transport line of the epitaxy system. The set-up consists of a UHV chamber equipped with a Kaufman ion source (KDC 40), powered with a source controller (Model KSC1202). The acceleration voltage of the ion beam is 600 V. No cooling condition is applied.

2.2 Microscopy techniques

2.2.1 Aberration-corrected scanning transmission electron microscopy

A brief introduction. The last 80 years have seen a growing trend for the development and applications in TEM. Based on prior technical and theoretical advances, the first TEM was presented by Max Knoll and Ernst Ruska in 1931 in Germany.[82-84] Since then, the instrument has steadily developed from a microscope that barely matched the resolution of an optical microscope to a sophisticated sub-nanometer-resolution imaging technique, which is an indispensable tool for biology, geology, and materials research as well as nanoscience and nanotechnology. With the development of TEM, the first STEM was built in 1938 by Manfred von Ardenne[85] and the model of a modern STEM was invented by Albert Crewe in the 1970s, who developed the field emission gun and demonstrated the ability to image atoms using the STEM with an annular dark field detector.[86] With the invention of the aberration corrector in the 1990s [87] and its addition to the probe-forming and image-forming lenses, the state-of-the-art (S)TEM has been developed with a sub-angstrom resolution, enabling to identify individual atomic columns with unprecedented clarity. Historically, TEM has been developed due to the limited resolution in light microscopes, which is imposed by the wavelength of the visible light (400-700 nm). According to the classic Rayleigh criterion for the light microscope, the smallest distance can be resolved given approximately by:

$$r_d = \frac{0.61\lambda_l}{n \sin \alpha} \tag{2-1}$$

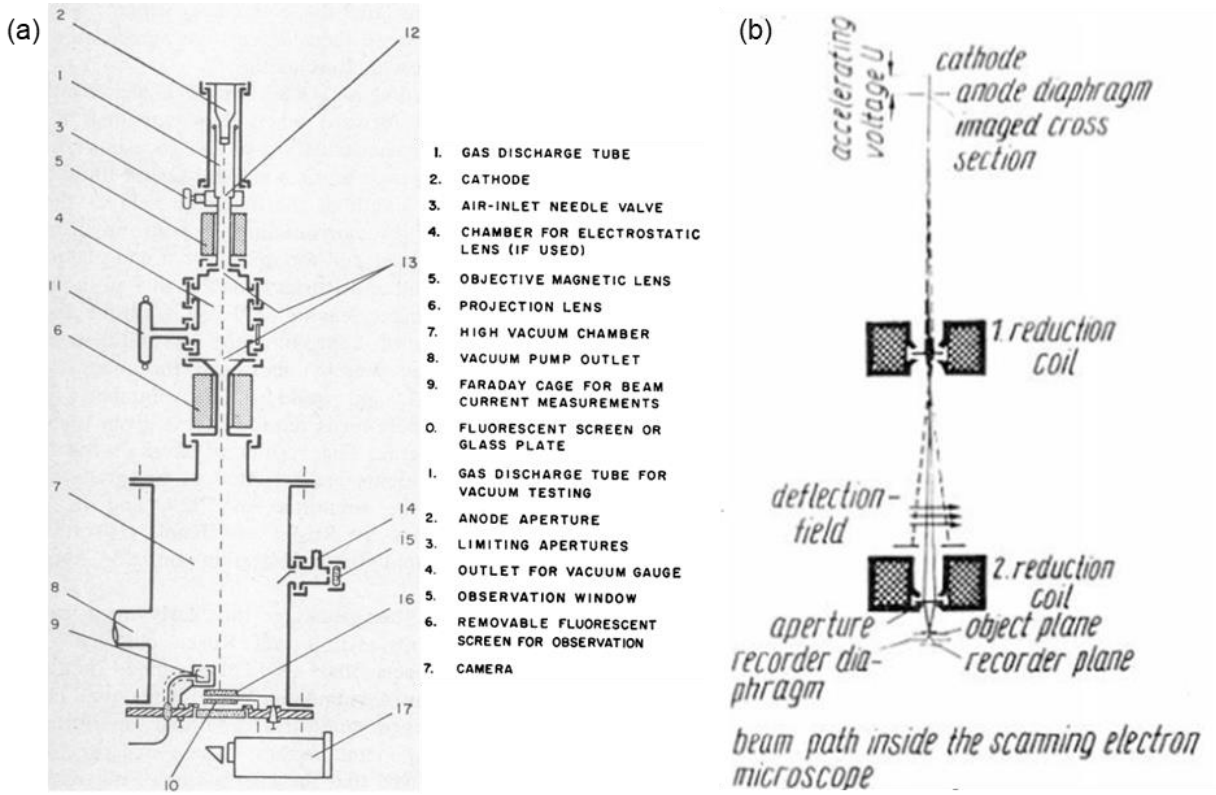

Figure 2-3. Schematic diagrams of the first electron microscope (a) demonstrated by Max Knoll and Ernst Ruska in 1931[83] and the first STEM (b) built by Manfred von Ardenne[85].

where λ_l is the wavelength of light, n the refractive index of the intervening medium, α is the collection semi-angle of the magnifying lens and $n\sin\alpha$ is known as the numerical aperture of the lens. This equation shows that the smaller the wavelength, the better is the resolution. The resolution limit for a visible light microscope is about 200 nm.

In 1924, Louis de Broglie theorized the wave and particle characteristics of electrons, unveiling that electrons can be diffracted and focused like light.[88] His famous equation shows that the wavelength of electrons is related to their energy. Their relation can be simplified as (ignoring the relativistic effects and the inconsistency in units):

$$\lambda_e = \frac{1.22}{E^{1/2}} \tag{2-2}$$

where λ_e is the wavelength of the electrons in nm and E is the kinetic energy in electron volts (eV). Therefore, for 100 keV electrons, λ is about 0.004 nm, which is much smaller than the wavelength of visible light. Thus, the electron microscope, in principle, has the potential to deliver a much higher resolution than the optical microscope. In a TEM, since n of Equation 2-1 can be assumed to be unity (vacuum) and $\sin\alpha=\alpha$ (α less than a few degrees), the best resolution can be approximated as:

$$r_d = \frac{0.61\lambda_e}{\alpha} \tag{2-3}$$

From the combination of Equation 2-2 and 2-3, it is clear that, at higher electron kinetic energy, the wavelength is shorter and, therefore, the resolution of the TEM is higher. However, one cannot build a perfect TEM, of which the resolution approaches the wavelength-based limit, because we cannot build a perfect lens without aberrations.

Lens aberrations. In an ideal optical system, electron rays that are very close to the optic axis form an image of the object with the correct position, shape, and size. However, in reality, the electron rays that are inclined to the optic axis usually do not come to focus at the correct location, causing a blur in the image, which is called aberration. There are many kinds of aberrations. Among them, the most important ones are the spherical and chromatic aberrations as well as astigmatism.

Spherical aberration describes that the electron trajectories away from the optic axis are bent more strongly by the magnetic field than those near the axis, and thereby off-axis rays are not brought to a focus at the same point as paraxial rays (Figure 2-4(a)). With longitudinal spherical aberration, the different crossovers still lie on the optic axis, but transverse spherical aberration can also occur. Electrons of different wavelengths are focused at various points on the optical axis, leading to distortion to the TEM image, which is called chromatic aberrations (Figure 2-4 (b)). In reality, the high-tension power supplies cause variation of the electron energy smaller than one part per million. These fluctuations are small enough, and they do not cause significant problems in the microscopes.[88] In the case of astigmatism (Figure 2-4(c)), the cross-over of the off-axis rays is displaced along the optic axis, and the degree of displacement varies with the azimuthal angle of the beam.

The disc of minimum confusion with a diameter d_s due to spherical aberration is defined as:

$$d_s = \frac{1}{2} C_s \alpha^3 \tag{2-4}$$

where C_s is the spherical aberration coefficient, α is the collection semi-angle of the lens. This equation indicates that the resolution will degrade as α becomes larger, which competes with the Rayleigh criterion

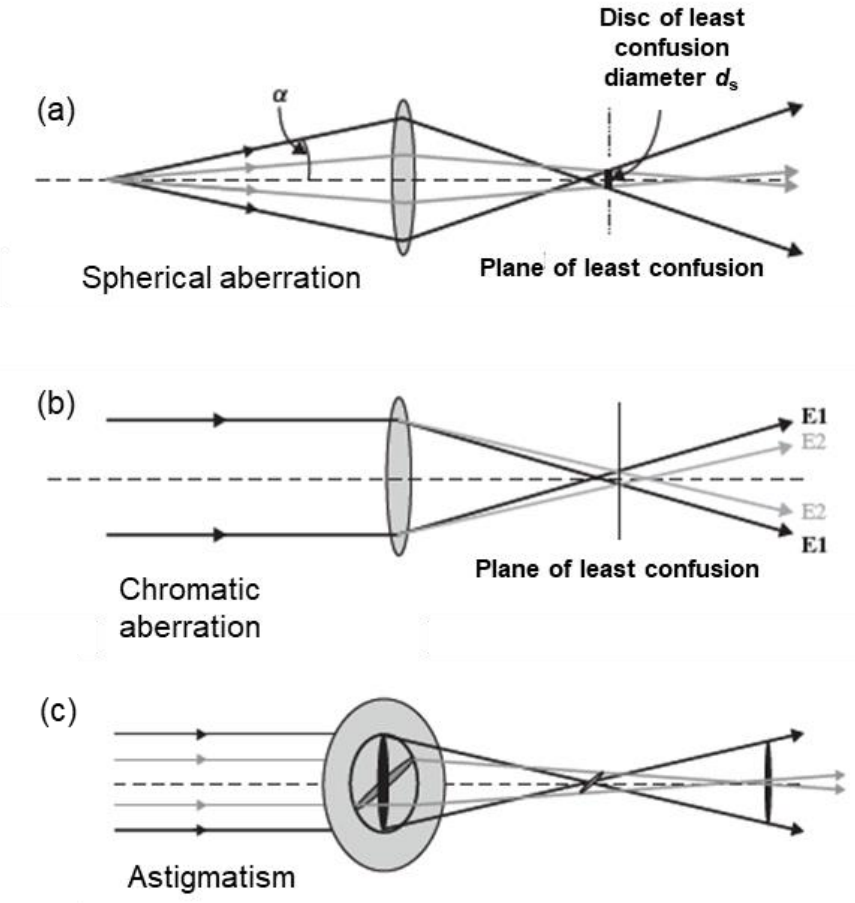

Figure 2-4. Schematic illustration of the spherical aberration, chromatic aberration and astigmatism. α is the collection semi-angle of the lens and d_s is the diameter of the disc of least confusion (modified from ref. [89]).

(Equation 2-3), suggesting that the resolution improves as α increases. Combined with both equations, the total confusion (d_{tot}) is given as:

$$d_{\mathrm{tot}} = 0.91\lambda_e^{\,3/4} C_{\mathrm{s}}^{\,1/4} \qquad (2\text{-}5)$$

This equation is often quoted as a simple guide to microscope resolution, when only taking theoretical lens resolution and the spherical aberration into consideration.[90]

Based on the principles outlined by Scherzer[91] in 1947 that non-round lenses can correct the aberrations, the breakthrough of aberration correctors took place in the 1990s. Multipole lenses are used to generate a negative value of C_s and thus cancel the positive C_s of the round lens. With the use of a set of multiple lenses, rays scattered at high angles to the optic axis are now brought to the correct focus, and the resolution limit is improved.[92] There are two basic designs of the corrector, the octupole/quadrupole assembly,[93] and the hexapole assembly[94]. For the TEMs used in this work (JEM-ARM200F, JEOL Ltd.), C_s-correctors with the latter design are installed.

Structure of the TEM. The TEM works similarly to an optical microscope used in transmission mode, which typically consists of five parts: The light source, the condenser lens, a transparent sample, the objective lens, and the magnifying lens(es). A TEM can be divided into similar sections. As is shown in Figure 2-5. The five sections of a TEM are (from top to bottom): the electron gun, the illumination stage (condenser lenses), the objective lens, with an electron transparent sample immersed into its magnetic field,

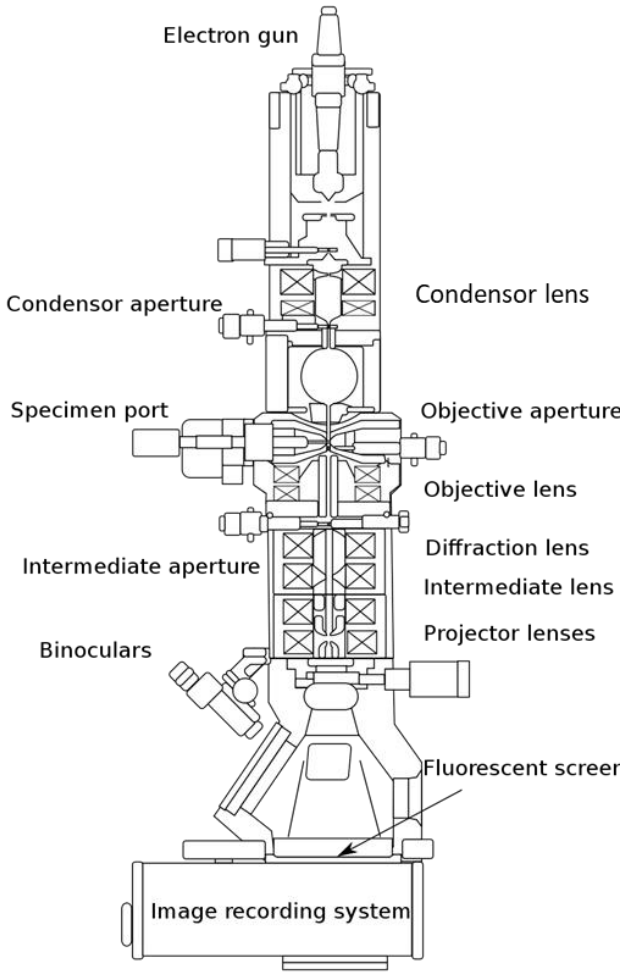

Figure 2-5. Sketch of essential components in a basic TEM (image courtesy from Wikipedia).

the magnification (intermediate lenses) and projection system (projective lenses), often with three or more lenses, and the detector (a viewing screen, photographic camera, charge-coupled device (CCD) camera, *etc.*)

The model of a modern TEM is typically divided into two types, conventional TEM (CTEM) and scanning TEM (STEM), depending on the way they address the specimen.[89] As sketched in Figure 2-6, in the CTEM, a close-to-parallel electron beam floods the whole area of interest and a TEM image is collected in parallel, which is formed by the post-specimen lenses. The magnified image is generated by simultaneous interaction of the electron beam with a large area of the specimen. Unlike CTEM, the STEM technique scans a very finely focused beam of electrons across the sample in a raster pattern. Interactions between the beam electrons and sample atoms generate a serial signal stream, which is correlated with the beam position to build an image. The image resolution in CTEM is primarily determined by the imperfections or aberrations in the objective lens. In contrast, in a STEM instrument, the resolution of the STEM image is mostly determined by the beam diameter generated by the probe-forming lens, which is also limited by aberrations. The modern CTEM and STEM system can routinely reach the image resolution better than an angstrom. Compared to CTEM, STEM has been recognized to be more suitable for analytical works, because it possesses a superior control over the positioning of the beam and simultaneous acquisition of all available signals for making spectroscopy.[95] STEM allows for a direct correlation of microscopy and spectroscopy data. Therefore, I mainly use the STEM technique for our studies.

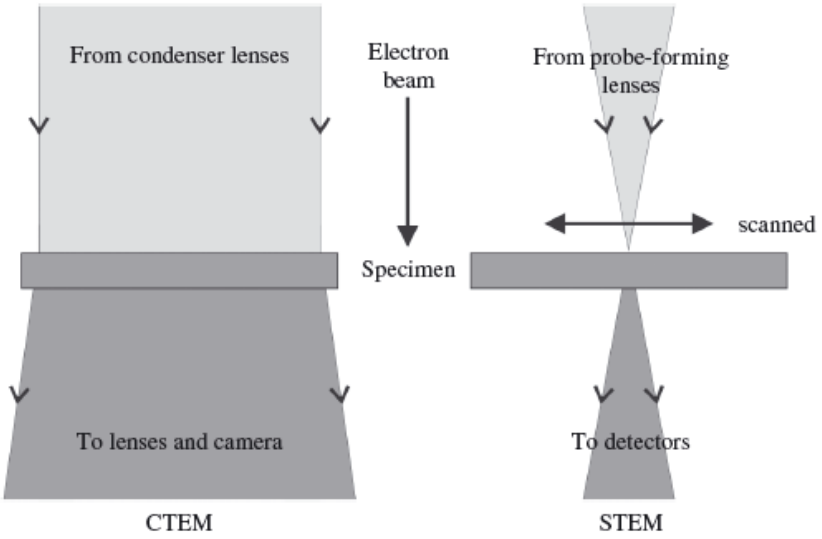

Figure 2-6. Schematic diagrams of the electron beam pathway for CTEM and STEM.[89]

Electron-material interaction. In STEM, an electron beam is focused on the electron-transparent sample. Electrons are scattered by the sample, either elastically or inelastically, giving rise to a large variety of secondary signals, including elastically scattered electrons, X-rays, back-scattered electrons, light, Auger electrons, secondary electrons, inelastically scattered electron, electron-hole pairs, *etc*. (Figure 2-7). Electron signals after interaction carry the information on structure, topology, morphology, and composition of a material. Many kinds of microscopy and spectroscopy techniques have been developed to collect different signals and thus to extract specific information of materials. Generally speaking, STEM imaging mainly makes use of the elastic signals, providing structural information of material. Inelastic signals are exploited in analytical techniques such as EELS and energy-dispersive X-ray spectroscopy (EDS) to chemical information of material.[96]

In the following parts, I will emphasize STEM imaging, EELS, and EDS techniques, which are used in this thesis.

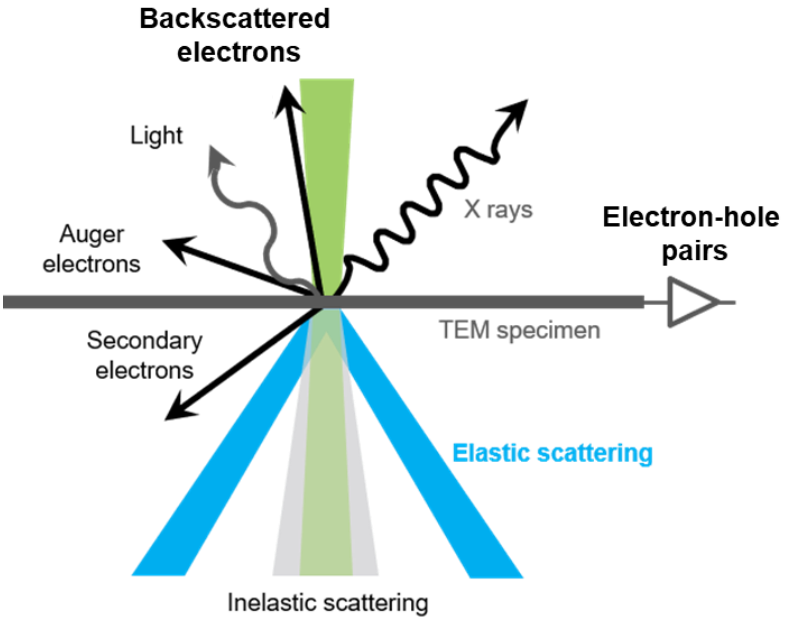

Figure 2-7. Scheme of electron-matter interactions in a STEM (Modified image courtesy of GATAN website).

2.2.2 STEM imaging

In STEM, transmitted beam electrons that have been scattered through different angles are collected using angular detectors. The total scattered intensity to the detector is plotted as a function of the probe position during its two-dimensional raster scan across the sample, thereby forming a STEM image. Figure 2-8 shows the schematic for the STEM imaging. Depending on the size of the collection semi-angle, various STEM images can be obtained corresponding to different contrast mechanisms. Practically, the condenser aperture in the probe-forming optics determines the convergence angle (α) of STEM imaging. The use of a large convergence angle minimizes the problems of channeling enhanced X-ray emission and electron channeling in EELS measurements. A convergence angle of 20.4 mrad is employed in this thesis. The collection angle (β) is related to the selected camera length and the relative position of detectors. To improve the signal-to-noise ratio (SNR) and to minimize the image distortion of HAADF and ABF images, ten serial frames were acquired with a short dwell time (2 μs/pixel), aligned and added afterwards.

Annular dark-field imaging. In general, the electrons scattered to high angles larger than the convergence angle of the probe are the signal source of annular dark-field imaging (ADF), which is usually divided into high-angle ADF (HAADF), medium-angle ADF (MAADF) and low angle ADF (LAADF) modes, depending on the range of the collection angle (right panel of Figure 2-8).[97] Since the HAADF image is mostly contributed by the incoherently Rutherford scattered electrons from the nucleus of the atoms, the signal intensity of the HAADF image is proportional to Z^2, where Z is the atomic number of the illuminated atom, which is also named Z-contrast image.[98] In this thesis, HAADF images are acquired with the collection angle of 70-300 mrad, offering an intuitive judgment about the interfacial sharpness by observing the image contrast between materials consisting of different atoms. Furthermore, I will use STEM images to analyze the strain fields as well as lattice deformation and displacement of perovskite crystals.

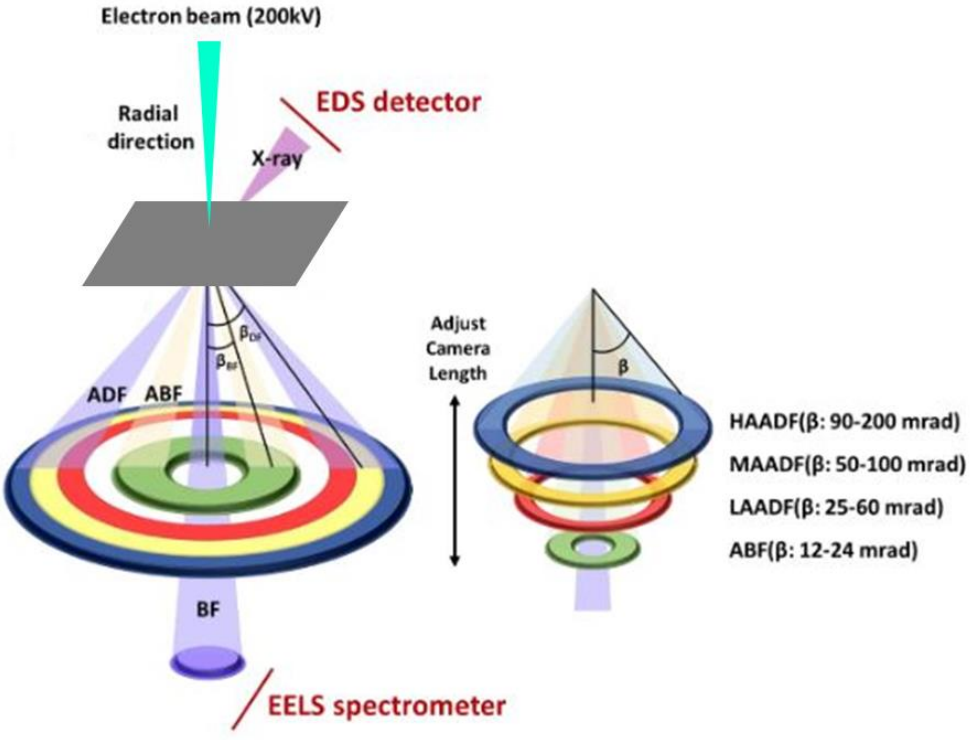

Figure 2-8. Schematic diagram of the imaging, analytical EELS, and EDS modes in a STEM (left panel). Different STEM imaging modes for corresponding collection angles (right panel).

Annular bright-field (ABF) imaging. Compared to HAADF-STEM imaging, which is considered as a robust, direct interpretable imaging mode, the bright-field (BF) images formed with a small, on-axis disk detector is not robust owing to the sensitivity to sample thickness and probe defocus. However, the ABF image is demonstrated to be interpretable. The combination of forward-focusing by light element columns and high-angle scattering by heavy-element columns reduce the electron intensity in the outer area of the bright-field region relative to its value, when the probe is between columns, making both light and heavy atomic columns appear consistently as dark spots in ABF images.[99] ABF imaging has reduced dependence of the atomic number Z, approximately $Z^{1/3}$ compared to Z^2 in HAADF, and thereby shows a unique advantage for studying light elements, *e.g.*, oxygen atoms in perovskite oxides.[100] Furthermore, ABF-STEM images can be simultaneously acquired with HAADF-STEM images as well as some spectroscopic images. A collection of 11-22 mrads is used for simultaneous ABF imaging in this thesis. I will use ABF images to study the rotation of oxygen octahedron and its linking to the magnetic properties near the oxide interface.

2.2.3 Electron energy-loss spectroscopy

EELS is a powerful analytical method measuring the change in the kinetic energy of electrons after the interaction with the specimen. The change of the energy of the electron is closely related to the structure and the substance of materials.[101, 102] Through analyzing the energy distribution of scattered electrons, EELS allows to not only probe the lattice structure, but also to analyze the chemical composition.[103] The modern STEM-EELS enables us to measure the structural and chemical information at the atomic level.

As shown in Figure 2-9(a), the EELS spectrum is usually separated into three regions: zero loss, low loss, and core loss. The zero-loss region comprises the elastically scattered electrons and electrons with minor energy losses, *e.g.*, phonons. Recent developments push the energy resolution of EELS below 10 meV, making the observation of phonon modes possible.[104, 105] In this thesis, the thickness of samples (t/λ, where t is the absolute sample thickness and λ the inelastic mean free path) are estimated using the zero-loss spectrum together with the low-loss spectrum *via* the log-ratio method.[106]

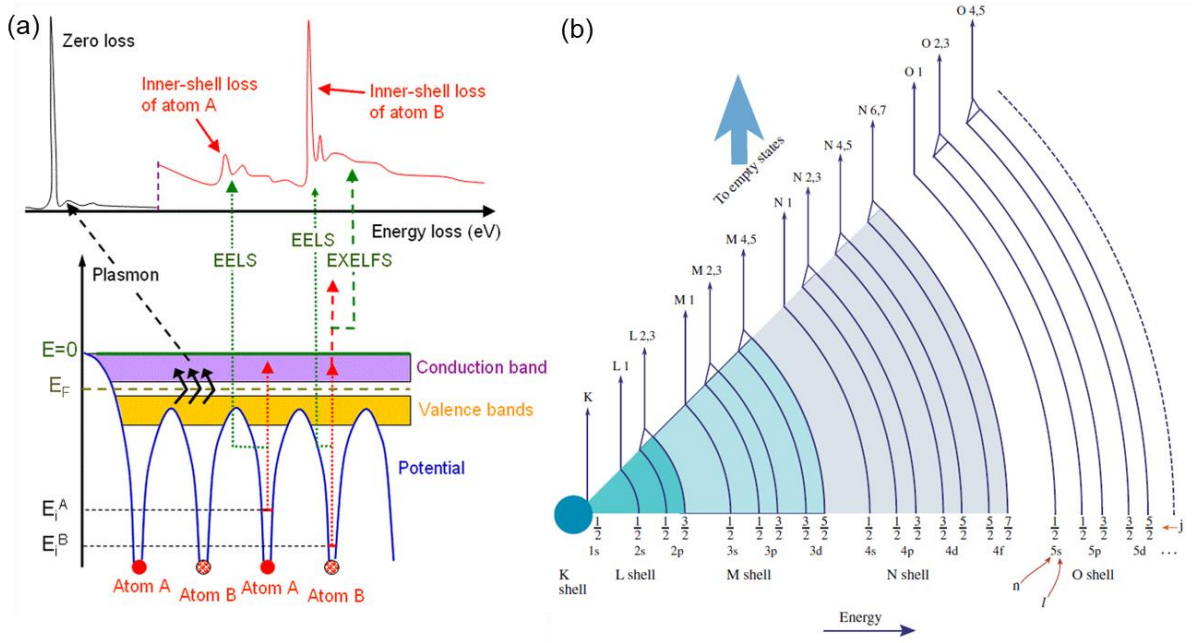

Figure 2-9. (a) Schematic diagram of the EELS spectrum and formation mechanisms for main peaks (from http://www.globalsino.com). (b) EELS core-loss edges and their correspondence to the core-shell ionization.[107]

The low-loss region corresponds to the energy from 0 to 50 eV and corresponds to the inelastic scattering by outer-shell (valence or conduction) electrons. This scattering can take the form of a collective oscillation (resonance) of many outer-shell electrons, known as a plasmon excitation. The low-loss spectrum contains information about the band structure and the dielectric properties of materials. The low-loss spectrum has been successfully used to characterize the electronic and optical properties of nanoparticles and nanostructures.[108]

The core-loss region with an energy larger than 50 eV gives the information about the inelastic excitation of inner-shell electrons. Because this ionization energy is characteristic of a particular chemical element, the core-loss edges indicate the elements present in materials (Figure 2-9(b)). In this thesis, core-loss EELS is employed to identify different elements as well as their distributions in heterostructures, in particular at the interface. The electron energy-loss near-edge structure (ELNES) of core-level EELS reflects corresponding electronic excitations from core electronic states to unoccupied states of selected atoms.[109] Therefore, ELNES provides useful information on the local atomic arrangement, such as coordination environment, symmetry, and electronic structures, including valence, spin state, and chemical bonding of target atoms.[2, 110] For perovskite oxides composed of oxygen and multi-valence transition metals, the ELNES analysis is especially useful. Since this method is used for the study of the SMO in chapter 5, I will introduce the ELNES analysis for manganite oxides, which has been reported in literature.[111, 112]

The O-K edge of manganite oxides stems from electron transitions between oxygen 1*s* core levels to unoccupied states in the 2*p* band hybridized with the Mn 3*d* band. Three main features are found in the near-edge fine structure of O-K edges in Figure 2-10(a). A pre-peak right at the onset around 530 eV is related to the Mn 3*d* bands. A second peak around 535 eV is attributed to hybridization with La 5*d* and/or Ca 3*d* bands. Moreover, the third peak around 540 eV is mainly contributed to Mn 4*sp* type bands.[113] Among these peaks, the pre-peak is extremely sensitive to the variation of Mn oxidation states by showing

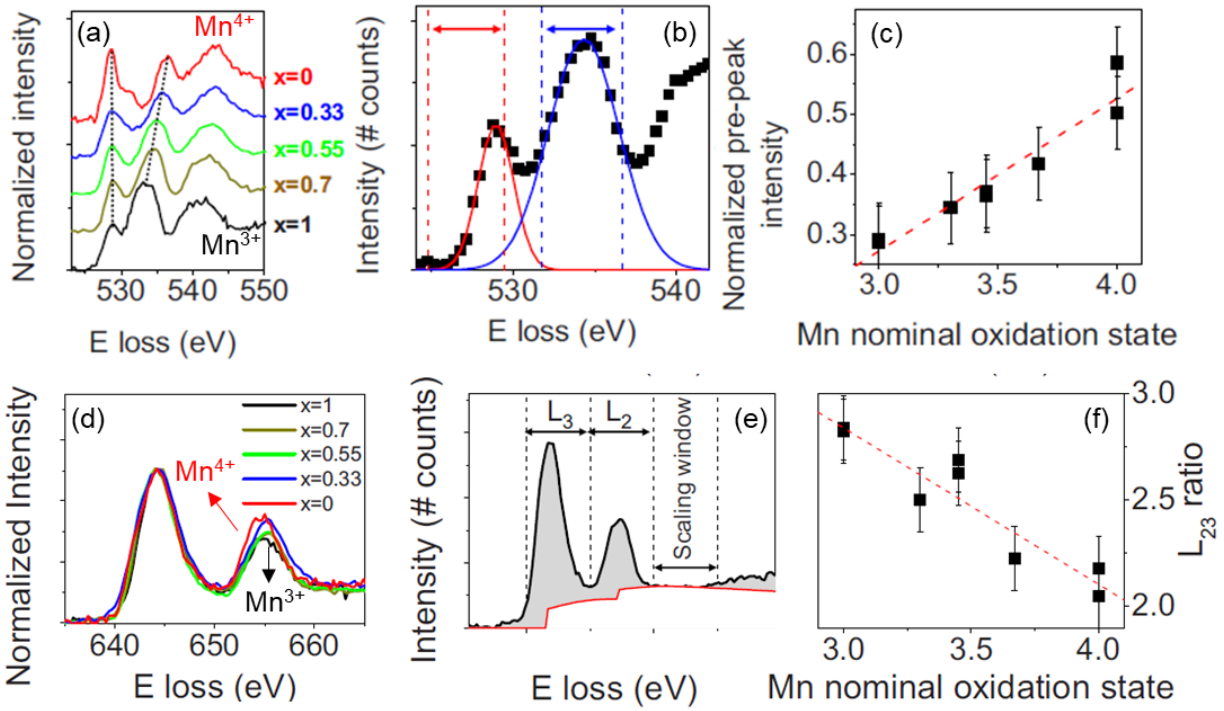

Figure 2-10. ELNES analysis of O-K edges (a, b, c) and Mn-$L_{2,3}$ edges (d, e, f) for a series of $La_xCa_{1-x}MnO_3$ compounds with x=1 (black), x=0.7 (dark yellow), x=0.55 (green), x=0.33 (blue), and x=0 (red) as modified from ref.[114]

significant changes in shape and position of the peak. Figure 2-10(a) shows that the intensity of the pre-peak is gradually reduced as the Mn valence varies from 4^+ to 3^+. To quantify valence variations, both the pre-peak (red line) and the main peak (blue line) are fitted by Gaussians to determine the peak intensity and position (Figure 2-10(b)). The normalized pre-peak intensity is found to be approximately linear to the oxidation state (Figure 2-10(c)).

Moreover, the difference in peak positions between the pre-peak and the adjacent main peak shows a clear linear correlation to the nominal Mn oxidation state, which is attributed to an energy shift of the initial core and the final states of the ejected electron.[115] Thus, ELNES analysis of the O-K edge provides a robust way to study the oxidation state of Mn. In this thesis, the fine structure of the O-K edge will be used to unveil the interfacial states in the SMO/STO heteroepitaxy.

Another popular method is the analysis of the fine structure of core-loss edges such as Mn-$L_{2,3}$ and Ti-$L_{2,3}$ edges. $L_{2,3}$ white lines originate from transitions from the spin-orbit split $2p_{3/2}$ and $2p_{1/2}$ levels to the available states in the 3*d* bands. Based on the $2j+1$ degeneracy of the initial core state in a one-electron model, the L_3/L_2 intensity ratio of white lines should be two.[114] However, the ratio often deviates from 2 due to the 3d band occupancy and interactions, the core-hole and the excited electron.[116] Figure 2-10(d) shows that the intensity ratio for Mn changes when the Mn oxidation state varies from +3 to +4. As shown in Figure 2-10(e), the intensity of L_3 and L_2 edges is integrated after removing the background below the Mn $L_{2,3}$ edge using a power-law fit and then removing the continuum contribution by scaling a step function and subtracting it from the Mn $L_{2,3}$ edges. There exist other methods in the literature for calculating the white line ratio.[117, 118] The calculated intensity ratio also shows a linear trend to the nominal Mn oxidation state, which is frequently used to estimate the valence state of Mn in manganese oxides.

Additionally, the multiple linear least-squares (MLLS) fitting method is usually applied to determine the valence states. For example, the experimental Ti-$L_{2,3}$ edges are fitted with the MLLS method using reference Ti-$L_{2,3}$ spectra of Ti^{4+} and Ti^{3+}. Thus, the oxidation state of Ti is figured out by determining the relative portion of the individual valence states.[70] Of course, this MLLS fitting method is also applicable to analyze Mn-$L_{2,3}$ edges. These methods will be used to determine the valence states of Mn and Ti in the following chapters. It is worth noting that some other features of white lines, such as chemical shift and the change of peak shape, are adopted to figure out the bonding state of transition metals as well.[119]

In this thesis, EELS acquisition was performed by a Gatan GIF Quantum ERS imaging filter with dual-EELS acquisition capability with a convergent semi-angle of 20.4 mrad and a probe size of 1 Å (5C), which is larger than that of STEM imaging 0.8 Å (8C). While the spatial resolution becomes worse as the probe size increases, the probe current rises, allowing for enhanced EELS analysis with a higher signal-to-noise ratio. With the 1.5 cm camera length and 5 mm entrance aperture of the image filter, a collection semi-angle of 111 mrad was used for EELS acquisition.

Energy-loss near-edge structure analysis was carried out with a dispersion of 0.1 eV/channel, where the energy resolution is 0.7 eV measured as the full-width at half-maximum of the zero-loss peak. For the study of SMO/STO interfaces, dual EELS spectrum imaging (SI) was performed with a dispersion of 1 eV/channel and 510 eV drift tube energy with a 2048 pixel wide detector for the simultaneous acquisition of the Sr, Ti, and Mn spectrum image. The elemental maps were extracted using a standard multiple linear least square fitting method, and the integration windows for Sr, Mn and Ti maps are (1871-2093) eV, (629-654) eV, and (443-478) eV, respectively. For the study of SRO/STO interfaces, integration windows for Sr, Ru and Ti maps are (1900-2100) eV, (2800-3000) eV, and (443-512) eV by using a dispersion of 1 eV/channel and a drift tube energy of 1600 eV. The SI survey image was simultaneously acquired using

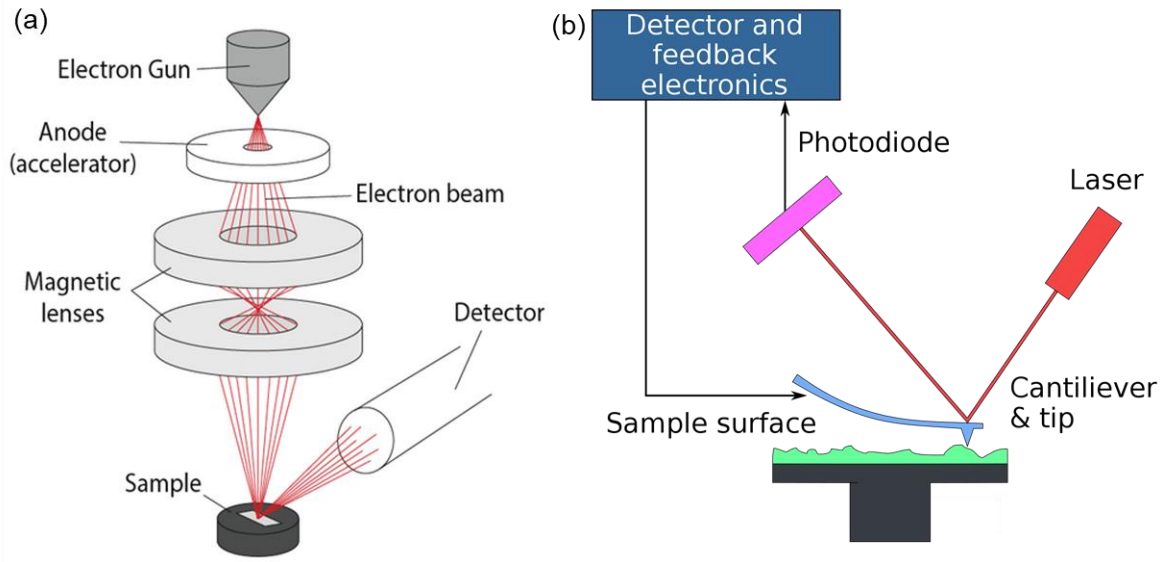

Figure 2-11. Schematic diagrams of SEM (a) and AFM (b) (image courtesy from Wikipedia).

the Gatan ADF detector at an inner collection semi-angle of 111 mrad. The raw spectrum image data were firstly denoised by applying principal component analysis (PCA) with a MSA plugin (HREM Research Inc.) in Gatan DigitalMicrograph and then smoothed using a spatial filter in Gatan DigitalMicrograph. The PCA process may introduce some artifacts to the maps, making the atomic columns sharper than expected.[120]

2.2.4 Energy-dispersive X-ray spectroscopy

As a kind of emission spectroscopy, EDS measures the energy of X-rays produced as a result of the interaction of the incident electron with the sample. The incident electron beam may excite an electron in an inner shell, ejecting it from the shell, while creating an electron hole, where the electron was. Then an electron from the outer, high-energy shell drops into the hole, releasing an X-ray. This process favored by heavier elements involves the emission of an X-ray. The energy of this emitted X-ray is characteristic of the atom and allows for elemental identification, whilst the X-ray intensity can be used for quantification of the elemental concentration. The function of EDS is quite similar to that of EELS, while it has respective advantages. The spectral resolution in EELS is significantly better than that in EDS typically by a factor of 100 or more. While the EDS has a considerably greater spectral range (some ten to twenty times larger) than in EELS, which shows an advantage to make elemental identification for material with many heavy elements.[121] Practically, we can run the EDS and EELS measurement simultaneously and thus characterize materials in a complementary manner. Here, EDS results on AAs were obtained by acquiring area scans using a 100 mm^2 JEOL Centurio SDD-EDS detector and the Thermo Noran System 7 EDS system (Thermo Fischer Scientific Inc.) in the ARM-DCOR microscope.

2.2.5 Other microscopy techniques

Scanning electron microscopy. Scanning electron microscopy **(**SEM) has been a versatile tool for the characterization of all materials. Unlike the TEM, which detects electrons that pass through a very thin specimen, SEM uses the electrons that are reflected or knocked off the near-surface region of a sample to create an image (Figure 2-11(a)). SEM can achieve resolution better than 1 nm.[122] In the most common SEM mode, secondary electrons (SEs) (about 50 eV) emitted by atoms are used for imaging materials. Besides, backscattered electrons (BSEs) are also used for imaging. Because BSEs come from deeper

regions of the sample, whereas SEs originate from surface regions, two imaging modes carry different types of information. BSE images show high sensitivity to differences in atomic number and sample thickness. SE imaging can provide information about the surface, *e.g.*, the surface topography of materials.[123] In this work, I will use the SEM in SE mode to image cracks on the surface of thin films and use the BSE signal to monitor the process of TEM specimen preparations.

Atomic force microscopy. Since invented in 1986, AFM has been developed into a useful instrument for a variety of research fields, including physics, chemistry, and biology, and engineering. The spatial resolution for a modern AFM system is on the order of fractions of a nanometer. The primary operation mode for AFM is the topography mode. As sketched in Figure 2-11(b), a cantilever scans the surface of samples in a raster way. The sharp tip on the end of the cantilever contacts the surface, bending the cantilever and changing the amount of laser light reflected into the photodiode. Using a feedback system, the height of the cantilever is then adjusted to restore the response signal resulting in the measured cantilever height tracing the surface. An AFM image showing the topography of the sample surface is finally obtained. For thin-film technology, this technique is popular for checking the surface cleanness and the quality of growth. I will use this method to check the surface cracks of as-grown SMO thin films and the morphology of fabricated nanostructures.

2.3 Data processing and simulations

High-resolution TEM images indeed provide much information beyond the intuitive observation. For example, *Z*-contrast HAADF-STEM images intuitively show the distribution of different elements, whilst one could get the information on the lattice structure, strain states, and even functionalities, if these images are carefully processed and analyzed. Additionally, corresponding simulations for TEM results are necessary to verify and figure out the information from TEM images. Here, I will introduce the data processing method and simulations used in this thesis.

2.3.1 Geometric phase analysis

As discussed in chapter 1, strain is a crucial factor in understanding and tailoring physical phenomena in quantum matter heterostructures. Geometric phase analysis (GPA), which was developed by Martin Hytch[124], can quantify the lattice displacement and strain fields in crystalline materials by analyzing high-resolution TEM images with Fourier filtering.[125] This method has been widely used to analyze the strain of semiconductors and heterostructures. For the sake of precision, the GPA method requires atomic resolution images without scan distortion. Therefore, I acquired multi-frame images (usually 8-10 frames) during the STEM and aligned them for minimizing scan distortions.

The GPA approach is based on combining real space and reciprocal space information. The intensity in an image (*I(r)*) is written as

$$I(r) = \sum_{\mathrm{g}} I_{\mathrm{g}}(r)\, e^{2\pi i g \cdot r} \tag{2-6}$$

where g is the reciprocal lattice vector describing the undistorted lattice. In this formula, $I_g(r)$ is the local Fourier component obtained by filtering in Fourier space and can be described as:

$$I_{\mathrm{g}}(r) = A_g(r) e^{iP_{\mathrm{g}}(r)} \tag{2-7}$$

where the amplitude $A_g(r)$ and the phase $P_g(r)$ correspond to the local contrast and position of the fringes.

The phase $P_g(r)$ and the displacement field $u(r)$ have the following relation:

$$P_g(r) = -2\pi g \cdot u(r) \tag{2-8}$$

Since two reciprocal lattice vectors g_1 and g_2 are usually selected, corresponding to two phase images $P_{g1}(r)$ and $P_{g2}(r)$, the two-dimensional displacement field can be written as:

$$u(r) = -\frac{1}{2\pi}\left[P_{g1}(r)a_1 + P_{g2}(r)a_2\right] \tag{2-9}$$

where a_1 and a_2 are the basis vectors for the lattice in real space corresponding to the reciprocal lattice defined by g_1 and g_2. The mask size for selecting reciprocal vectors determines the spatial resolution of strain maps.

The local distortion of the lattice is given by the gradient of the displacement field and can be described by the 2×2 matrix, e, defined as[124]:

$$e = \begin{pmatrix} e_{xx} & e_{xy} \\ e_{yx} & e_{yy} \end{pmatrix} = \begin{pmatrix} \frac{\partial e_{xx}}{\partial x} & \frac{\partial e_{xy}}{\partial y} \\ \frac{\partial e_{yx}}{\partial x} & \frac{\partial e_{yy}}{\partial y} \end{pmatrix} \tag{2-10}$$

In this thesis, the misfit strain can be calculated using $\varepsilon_{xx} = e_{xx}$, and $\varepsilon_{yy} = e_{yy}$. The shear strain field map is calculated using $\varepsilon_{xy} = (e_{xy} + e_{yx})/2$. The rotation map is calculated by $\varepsilon_{rot} = (e_{xy} - e_{yx})/2$. A commercial GPA plugin (HREM Research Inc.) in Digital Micrograph is used for strain analysis. Detailed procedures for GPA are outlined on the official website: https://www.hremresearch.com/Eng/plugin/GPAEng.html.

2.3.2 Lattice deformation determination

Simultaneously acquired HAADF and ABF images allow us to resolve all kinds of atoms in perovskite oxides. The relative positions of these atoms carry tremendous information about the structure, such as lattice constant, octahedral rotation, and even functionality like ferroelectricity. It essentially requires a precise measurement of the position of every atom. The standard technique for sub-pixel estimation of atom positions from atomically resolved STEM images relies on fitting intensity maxima or minima with a two-dimensional Gaussian function. Based on 2D Gaussian fitting, several specialized algorithms have been reported to quantify the atom positions in TEM data, such as the oxygen octahedra picker,[126] StatSTEM,[127] Atomap,[128] mpfit[129], and others[130]. Among them, oxygen octahedra picker, developed by Dr. Y. Wang from MPI-FKF, is specialized in identifying the STEM data of the ABO_3 perovskite oxides, exhibiting an impressive accuracy of as small as 3 pm for HAADF images. I used the oxygen octahedra picker tool in Digital Micrograph to analyze the atomically resolved STEM images of heterostructures in this thesis.

In the oxygen octahedra picker tool, positions of atomic columns are determined by an iterative process of two methods: center-of-mass or 2D Gaussian fitting. The center of mass method works faster than 2D Gaussian fitting, which is useful for analyzing large quantities of data, while 2D Gaussian fitting is more precise. The center of an atomic column is first located by the center-of-mass method. Then the program takes the results of the center-of-mass process as the initial input for 2D elliptical Gaussian fitting:

In the center-of-mass method (also referred to the moment method or the centroid method), the peak center of an atomic column is given by:

$$C_x = \frac{\sum_i \sum_j (x_i \cdot I_{ij})}{\sum_i \sum_j I_{ij}} \text{ and } C_y = \frac{\sum_i \sum_j (y_i \cdot I_{ij})}{\sum_i \sum_j I_{ij}} \tag{2-11}$$

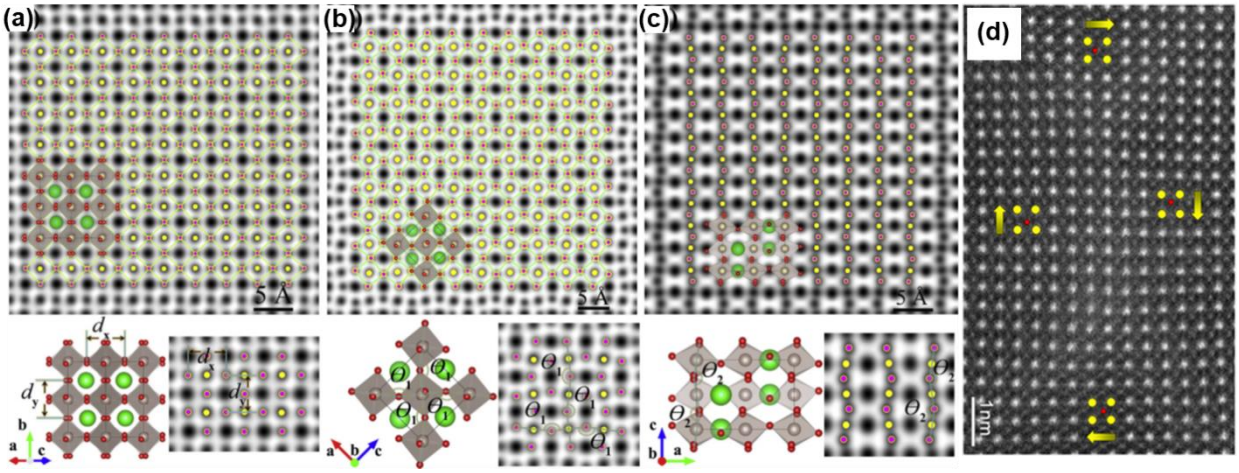

Figure 2-12. Locating atomic columns for measuring the lattice constants (a) and octahedral distortion (b, c) in orthorhombic SRO[126] and lattice displacement-induced ferroelectric polarization (d) in $PbTiO_3$ (modified from ref.[135]).

where x_i and y_j are the positions along the x and y axes, and I_{ij} is the image intensity of the pixel(i, j).[131] For the 2D Gaussian fitting, the intensity of each atomic column is defined as:

$$I(x,y) = I_0 + \mathrm{A} * \exp\left\{-\frac{1}{2(1-c^2)}\left[\left(\frac{x-x_0}{x_w}\right)^2 + \left(\frac{y-y_0}{y_w}\right)^2 - \frac{2c(x-x_0)(y-y_0)}{x_w y_w}\right]\right\} \qquad (2\text{-}12)$$

where I_0 is the intensity of background, A is the Gaussian amplitude, x_w and y_w are the atomic column widths, and x_0 and y_0 are the atomic column position.[131, 132] The optimized 2D Gaussian function finally fits each atomic column in the TEM image. Based on the positions of atomic columns, the interatomic distance in different orientations can be obtained, representing lattice constants in corresponding directions, as shown in Figure 2-12(a). In perovskites, through measuring the relative positions of neighboring oxygen atoms of TEM images taken from different directions, the 3D rotation pattern for the oxygen octahedron can be revealed (Figure 2-12(b) and (c)). Furthermore, *via* the determination of the displacement vectors of B atoms relative to the mass center of four nearest A neighbours, the electrical polarization states, including the direction and magnitude, can be achieved. Figure 2-12(d) shows the 4-fold domain-wall junctions in $PbTiO_3$ unveiled by the quantification of HAADF images. This method has become a popular way to investigate the local electrical polarization on the atomic scale.[133, 134]

2.3.3 QSTEM simulation

QSTEM developed by Prof. Dr. Christoph T. Koch from the Department of Physics, Humboldt University of Berlin enables us to make the quantitative simulation of HAADF-STEM, BF-STEM, and BF-TEM images and diffraction patterns of arbitrarily large structures, *e.g.*, dislocations or interfaces.[136] This software is based on the multi-slice algorithm with frozen phonon modeling, including thermal diffuse scattering and scattering (TDS) factors for atoms of arbitrary charge. The lens aberrations can be considered up to the 5th order.[137] Right now, one can run the QSTEM code with a self-installed package or with Matlab and Python, all from a friendly graphic user interface (GUI). In this thesis, I perform QSTEM simulation of the HAADF-STEM and ABF-STEM images at the heterointerface with a self-installed package on a computer. The simulation process typically contains the following steps:

- Creating a data file containing the coordinates of the model in the .cfg format. There are mainly two ways to create the input file. A convenient way is to use the QSTEM Model Builder from a GUI, which can build superstructures containing arbitrarily many crystalline grains. One can load images (.dm3, .img, .tif, .jpg, *etc.*) and build the atomic model to match the atomic columns in the

image. I use this method to build the atomic model to match the atomic columns around interfaces. Alternatively, a code called Convert2CFG can convert crystal structure data in .xtl or .xyz format to the .cfg format.

- Loading the structural model. The model needs to be carefully checked by viewing from different directions. The size and orientation of the supercell are defined.
- Setting up the scan region and the probe array. The scan region is selected by dragging a rectangle with the mouse. The pixel numbers in scan directions and sampling and size of the probe array are defined.
- Slicing the structural model. When viewing the supercell from the front, one slice contains one atomic layer, and the atomic layers are in the center of slices.
- Setting up microscopy parameters, including the voltage, defocus, aberrations, convergence angle, and collection angles for STEM imaging. Please note that for quantitative simulation, TDS should be turned on. Otherwise, calculations only use simple Debye-Waller attenuation of Bragg beams. Intermediate images can be generated by selecting the "slices between outputs."
- Double-checking all settings and run the simulation.

Detailed introductions for the code and running procedures can be found on this website: https://www.physics.hu-berlin.de/en/sem/software/software_qstem.

2.3.4 µSTEM simulation

µSTEM is a microscopy simulation suite that was developed mainly at the University of Melbourne. The µSTEM suite is based on the multislice algorithm implemented using fast Fourier transforms and is available for both GPU and CPU computing models. µSTEM is capable of simulating various imaging modes based on inelastic scattering in both STEM and CTEM. In particular, µSTEM is able to model elemental mapping using EELS and EDS analysis based on inner-shell ionization.

For µSTEM simulations, thermal scattering is accounted for with one of two models: the absorptive model and the quantum excitation of phonons (QEP) model.[138] The absorptive model permits a rapid calculation, but only considers, how thermal scattering attenuates the elastic wave function. This model is less accurate for thicker specimens, because thermal scattering cross-sections are calculated in a single inelastic scattering approximation. Channeling of the thermally scattered electrons is also ignored. While the QEP model (also called TDS) includes all thermal scattering effects, which provides overall results numerically equivalent to the frozen phonon method. With the QEP model, one can keep track of electrons that have been elastically scattered and thermally scattered separately. It means that the contribution to EELS and EDS due to both elastically and thermally scattered electrons can be evaluated independently .[139]

The experimental STEM-EELS and STEM-EDS maps are quite complicated due to the complex electron-material interaction process, such as beam broadening and channeling effects.[140] Great care should be taken for atomic-scale studies of interface chemistry to get rid of misinterpretations. Previous work has revealed that on-axis maps of even perfectly abrupt interfaces exhibit significant signal delocalization, emphasizing the need for both extremely thin samples and supporting simulations to interpret experimental data accurately.[141] In this thesis, I will quantify the STEM-EELS chemical maps around oxide interfaces with the help of corresponding µSTEM simulations.

The step-by-step introduction for running the μSTEM code is described in the official manual (http://tcmp.ph.unimelb.edu.au/mustem/dist/muSTEM_v5.0_manual.pdf).

Chapter 3. An optimized TEM specimen preparation method of quantum nanostructures*

3.1 Abstract

Electron transparent TEM lamella with unaltered microstructure and chemistry is the prerequisite for successful TEM explorations. Currently, TEM specimen preparation of quantum nanostructures, such as AAs, remains a challenge. In this chapter, I optimize the sample-preparation routine for achieving high-quality TEM specimens consisting of SRO AAs grown on STO substrates. It shows that a combination of ion-beam-milling techniques can produce higher-quality specimens of quantum nanostructures compared to TEM specimens prepared by a combination of TP followed by Ar^+ ion milling. In the proposed method, simultaneous imaging in a focused ion-beam device enables accurate positioning of the AA regions and assures the presence of dots in the thin lamella by cutting the sample inclined by 5° relative to the AAs array. Furthermore, the preparation of TEM lamellae with several large electron-transparent regions that are separated by thicker walls effectively reduces the bending of the specimen and offers broad thin areas. The final use of a NanoMill efficiently removes the amorphous layer without introducing any additional damage.

Graphical abstract: A secondary electron image of a prepared FIB lamella (left) and an HAADF-STEM image of the cross-section of a single artificial atom with a diameter of 30 nm (right).

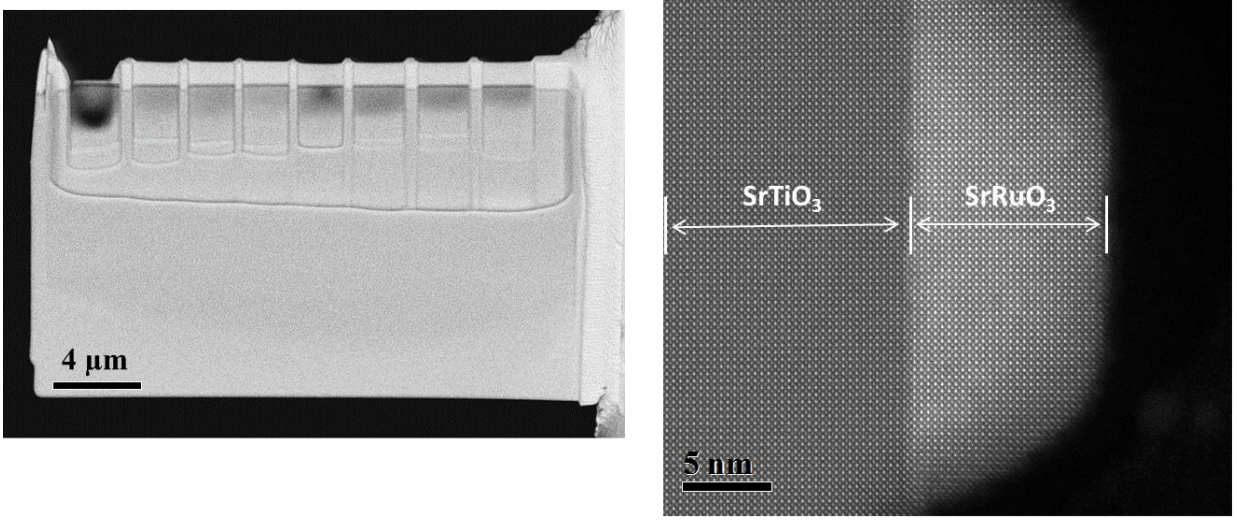

*Part of this chapter has been submitted to *Micron*

3.2 Introduction

Quantum matter nanostructures offer possibilities for artificial manipulation of novel electron systems [142, 143], which have been playing an important role in applications like quantum computing and sensing [58]. Among them, zero-dimensional electron systems, also known as quantum dots or AAs, attract great attention due to their size confinement [16, 46], which splits the electron energy levels and generates intriguing quantum phenomena. It has been reported that the magnetic Curie temperature of SRO AA nanostructures increases, if the dot size is reduced to 30 nm [144]. Atomically resolved investigations of their structure and chemistry are crucial for the understanding of their fundamental physical mechanisms.

A transmission electron microscope (TEM) is a superior tool used for nanoscale characterization of AAs. Particularly after the invention of aberration correctors, TEM enables the observation of microstructure, electronic structure, and local chemistry at the atomic scale [145]. However, the quality of TEM specimens is often a major limiting factor [90, 146]. Uniformly thin TEM specimens with a clean surface and a thickness of up to 50 nm are prerequisites for TEM observations [147]. Due to the small size of AAs (down to 15 nm) [144, 148], it is particularly challenging to obtain electron transparent lamellae, where the AAs have been cut through their central part. TEM investigations of 80 nm SRO AAs were reported [59], displaying an extensive amorphous layer covering the SRO AAs and a noticeable shape change caused by the TEM specimen preparation procedure. Due to technological advancements, the size of the AAs has been decreasing over the years, making TEM specimen preparation even more challenging and demanding.

In this chapter, by utilizing aberration-corrected STEM, I compare the quality of TEM specimens that were prepared by (i) tripod polishing followed by Argon ion milling (TP&IM) and (ii) focused ion beam cutting with subsequent low-energy milling and cleaning in a Fischione NanoMill (FIB&NM).

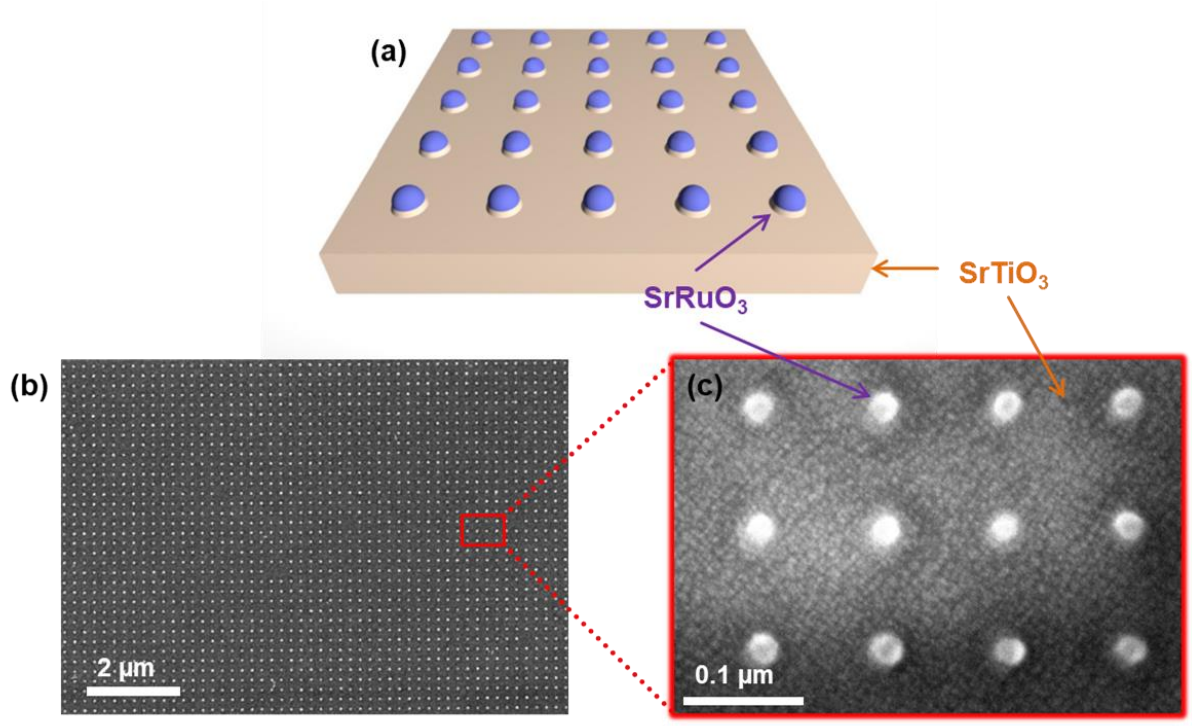

Figure 3-1. (a) Sketch of a SRO AAs array on a STO substrate. (b) SEM image of the SRO AAs nanostructure studied in our work. (c) Magnified SEM image of the region within the rectangle marked in (b).

3.3 Specimen preparation methods and TEM characterization

The SRO AA nanostructures were obtained by patterning an epitaxial SRO thin film grown on a STO substrate by EBL (JEOL JBX6300) with an electron-beam energy of 100 keV. Detailed procedures are introduced in chapter 2. The dot size and spacing are controlled during the patterning process. Figure 3-1(a) shows a sketch of the SRO AA nanostructures. SEM images of the patterned SRO AAs on STO substrates are shown in Figure 3-1(b, c). Here, SRO AAs with 30 nm diameter are periodically arranged with a spacing of about 100 nm.

In this work, I have prepared electron-transparent TEM lamellae by two combinations of methods, TP&IM and FIB&NM. All prepared cross-sectional samples were observed by (S)TEM along the [100] direction of the STO substrates.

3.3.1 Tripod polishing with a subsequent argon Ar^+ ion milling

As shown in Figures 3-2(a-c), samples were cut into slabs of 0.5 mm width and 1.5 mm length with a diamond wire saw cutting system (Well, Model 3242), which is displayed in Figure 3-2(e). The diamond saw cutting used a wire with a diameter of 150 µm, impregnated with diamond dust of the size of 20 µm. Due to the high hardness of diamonds, this cutting technique can cut through almost any material that is

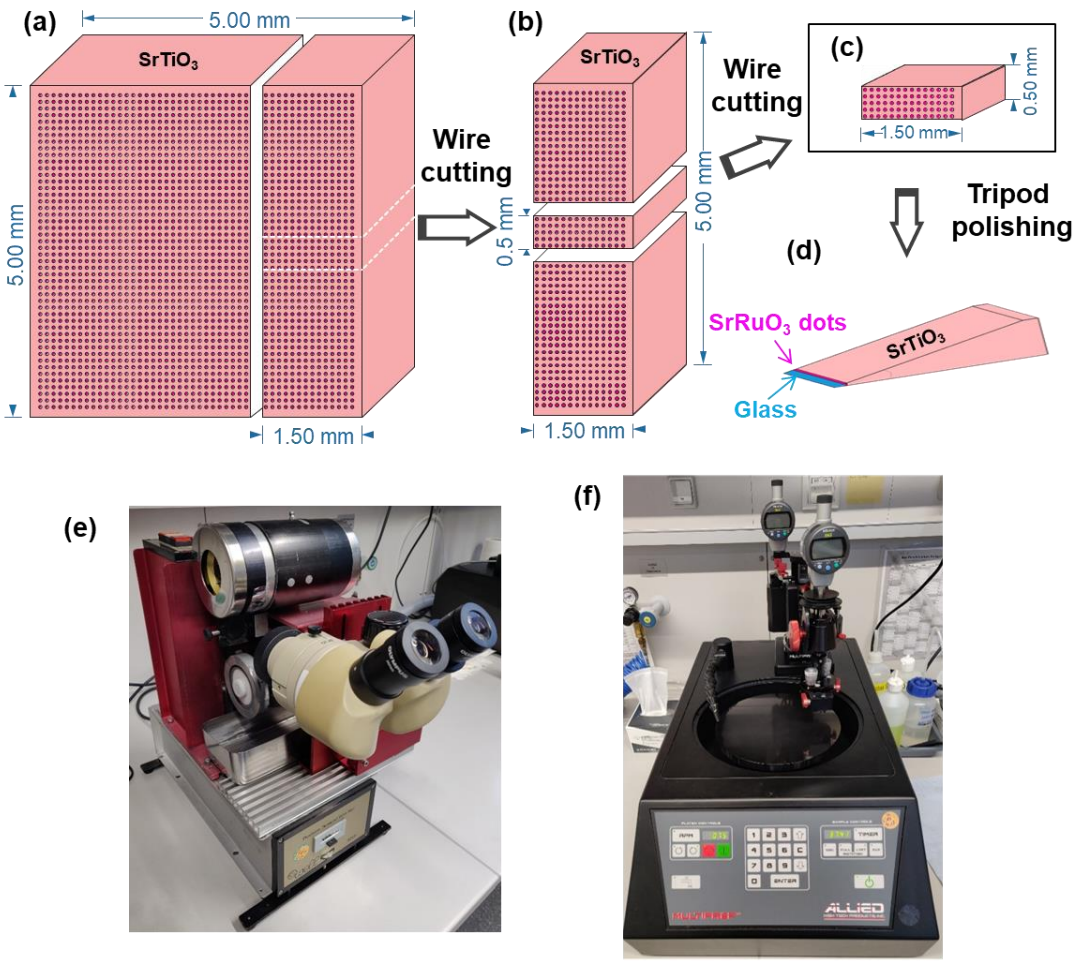

Figure 3-2. Schematic diagram of TEM sample preparation by TP&IM. (a–c) Cutting slabs of 1.5 mm width and 0.5 mm thickness using a wire saw. (d) Preparation of the wedge-shaped specimen by tripod polishing. (e) The diamond wire saw cutting system. (f) The Allied MultiPrep system used for grinding and wedge polishing.

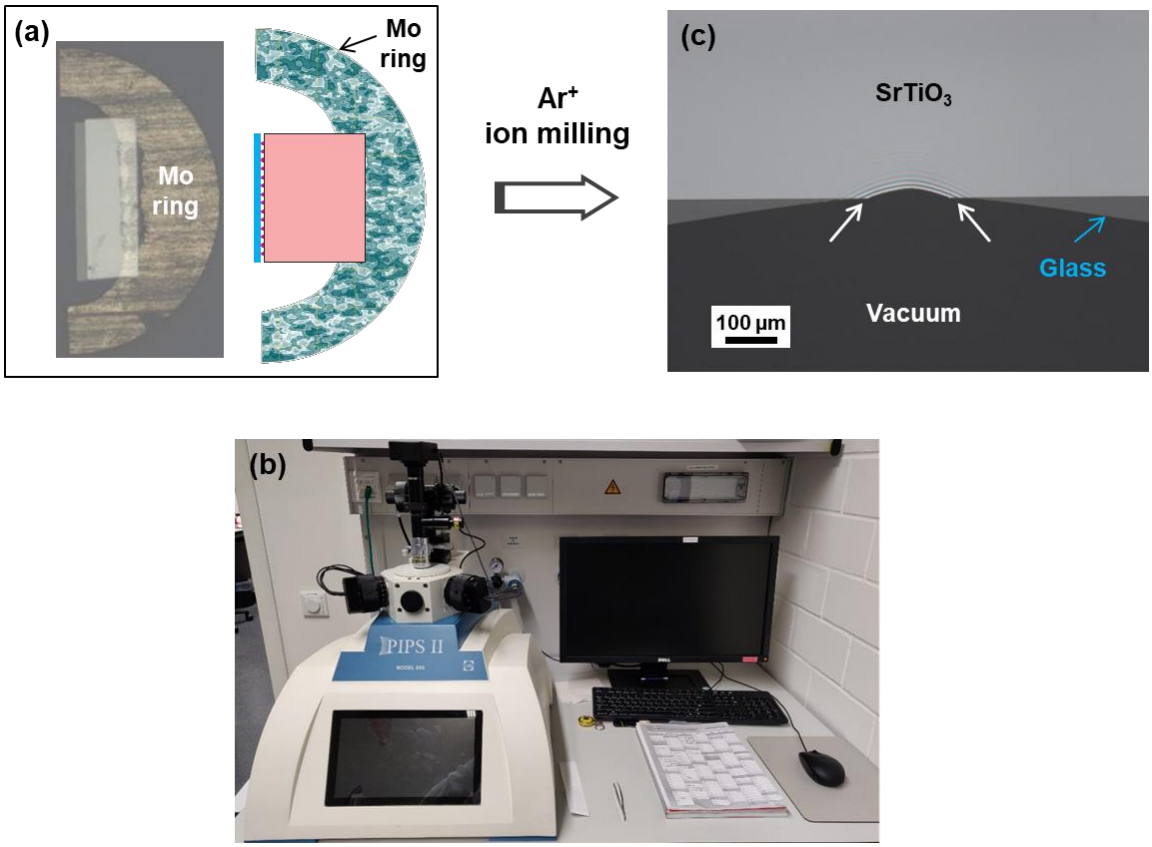

Figure 3-3. (a) Attaching a tripod-polished sample to a molybdenum half ring. The left image is the real experimental setup, and the right image is the corresponding sketch. (b) The Gatan Precision Ion Polishing System (PIPS II, Model 695) used for Ar^+ ion milling. (c) Apparent thickness fringes in the central region of the thin part of the wedge milled by Ar^+ ion milling as observed by a light microscope. The white arrows mark the areas of interest; the blue arrow marks the glass layer.

softer than the diamond abrasive. A thin layer of glass was mounted to the surface of the slab with glue (Epoxy bond 110) to protect the surface structure from contamination and damage during further processing. Then, the samples were attached to a Pyrex specimen holder using Crystal Bond thermoplastic wax for mechanical polishing. An Allied MultiPrep System (Figure 3-2(f)) was used for automated tripod polishing of the samples in cross-sectional geometry [146, 149]. Diamond lapping films (DLF) with grain sizes of 3.0, 1.0, 0.5, and 0.1 µm were used. Firstly, one side was flatly polished, until the sample thickness was below 250 µm. During the polishing of the second side, a wedge angle of 1° was introduced as the thin part of the wedge was below 70 µm. Finally, by using a 0.1 µm DLF, the thin part of the wedge was polished down to about 10 µm (Figure 3-2(d)). During the mechanical polishing process, the sample thickness was regularly checked with an optical microscope.

The tripod-polished samples were removed from the holder and glued to a molybdenum half-ring with M-Bond 610 epoxy (Figure 3-3(a)). A Gatan Precision Ion Polishing System (PIPS II, Model 695) (Figure 3-3(b)) was used for Ar^+ ion milling of the samples at liquid N_2 temperature. To thin the sample and to reduce the ion-beam-induced damage, the acceleration voltage during Ar^+ ion milling was progressively lowered from 3.3 kV to 2.0 kV and 0.3 kV. The central region of the thin part of the wedge was milled using the ion beam at an angle of 8° with a single modulation. An optical microscopy image (Zeiss AxioCam HRc) of the final TEM specimen is shown in Figure 3-3(c). Optical interference fringes indicate that the thickness close to the curved region is thin enough for TEM observation [150]. The edges marked by arrows in Figure. 3-3(c) are the regions of interest, where (S)TEM investigations were performed.

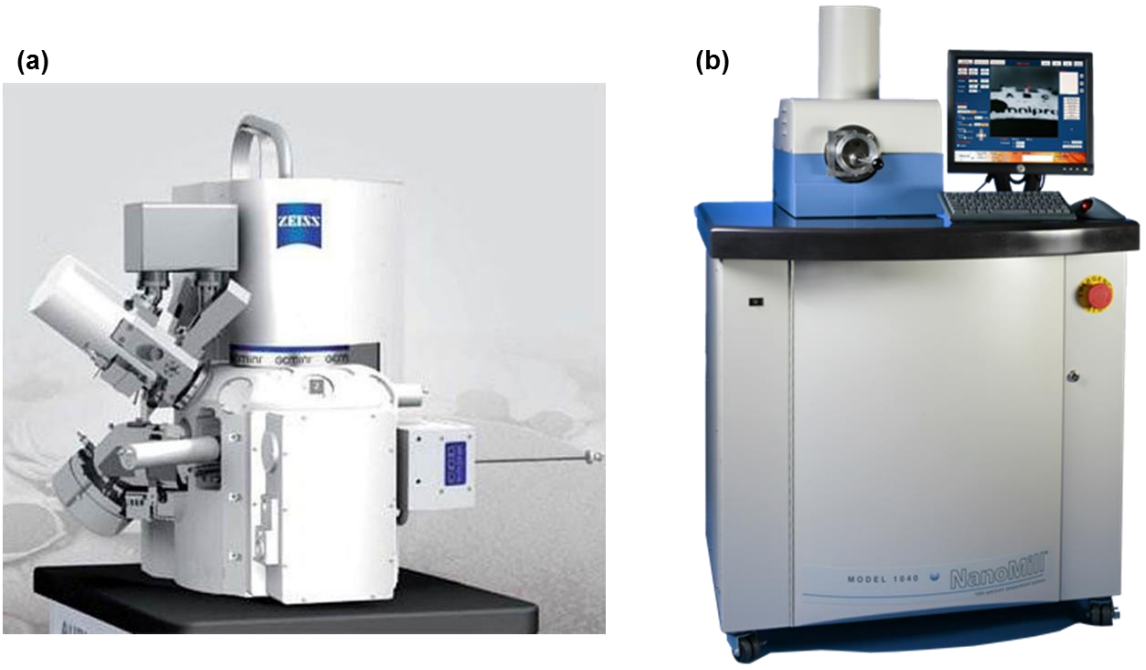

Figure 3-4. (a) The focused ion beam system used for cutting the lamella. (c) The NanoMill system used for final thinning and polishing of the FIB lamella.

It is necessary to note that the above-described TP&IM method is well-established in the Stuttgart Center for Electron Microscopy, and we can routinely prepare high-quality TEM specimens out of most samples with this method. In this thesis, all the studied TEM samples apart from the SRO AAs are prepared with this method.

3.3.2 Focused ion beam cutting followed by Ar^+ ion thinning and polishing in a Fischione NanoMill system

The focused ion beam system (Zeiss CrossBeam XB 1540) (Figure 3-4(a)) makes use of a combination of a focused ion beam (FIB) and an electron beam for SEM. This combination allows for site-specific preparation of the samples [151, 152], and thus is ideally suited for TEM specimen preparation of quantum nanostructures. To ensure the presence of central-cut SRO AAs in the electron transparent lamellae, the cutting direction needs to be precisely determined. In this work, a cutting angle of 5° between the cutting direction and the parallel rows of QDs was used. The spacing between the dots is 130 nm, and the final sample thickness is ca. 20 nm

Before FIB preparation, the SRO AAs nanostructure was pretreated. The surface of the sample was firstly wiped by an organic solvent (acetone) to clean possible surface contaminations, which is necessary to reduce artifacts of preferential milling [153]. Then, the sample was coated with carbon by thermal evaporation (Leica EM ACE 600 coater system) to protect the surface of the sample and make it conductive for reducing charging effects [154]. Next, a Pt protection layer was deposited by electron-beam induced deposition (EBID) and ion-beam induced deposition (IBID), successively. This protection layer with a size of 30 µm × 2 µm is inclined by 5° with respect to the SRO AAs rows. As shown in Figure 3-5(a), a Pt strap was deposited on the surface of the sample. Two trenches on both sides of the Pt strap were milled with the Ga^+ ion beam at 30 kV and 10 nA followed by milling at 30 kV and 2 nA (Figure 3-5(b)). An U-shaped undercut separated the lamella from the bulk. Thereafter, the *in-situ* micromanipulator needle (Kleindiek MM3A) was attached to the edge of the lamella (Figure 3-5(c)) and the sample was lifted out

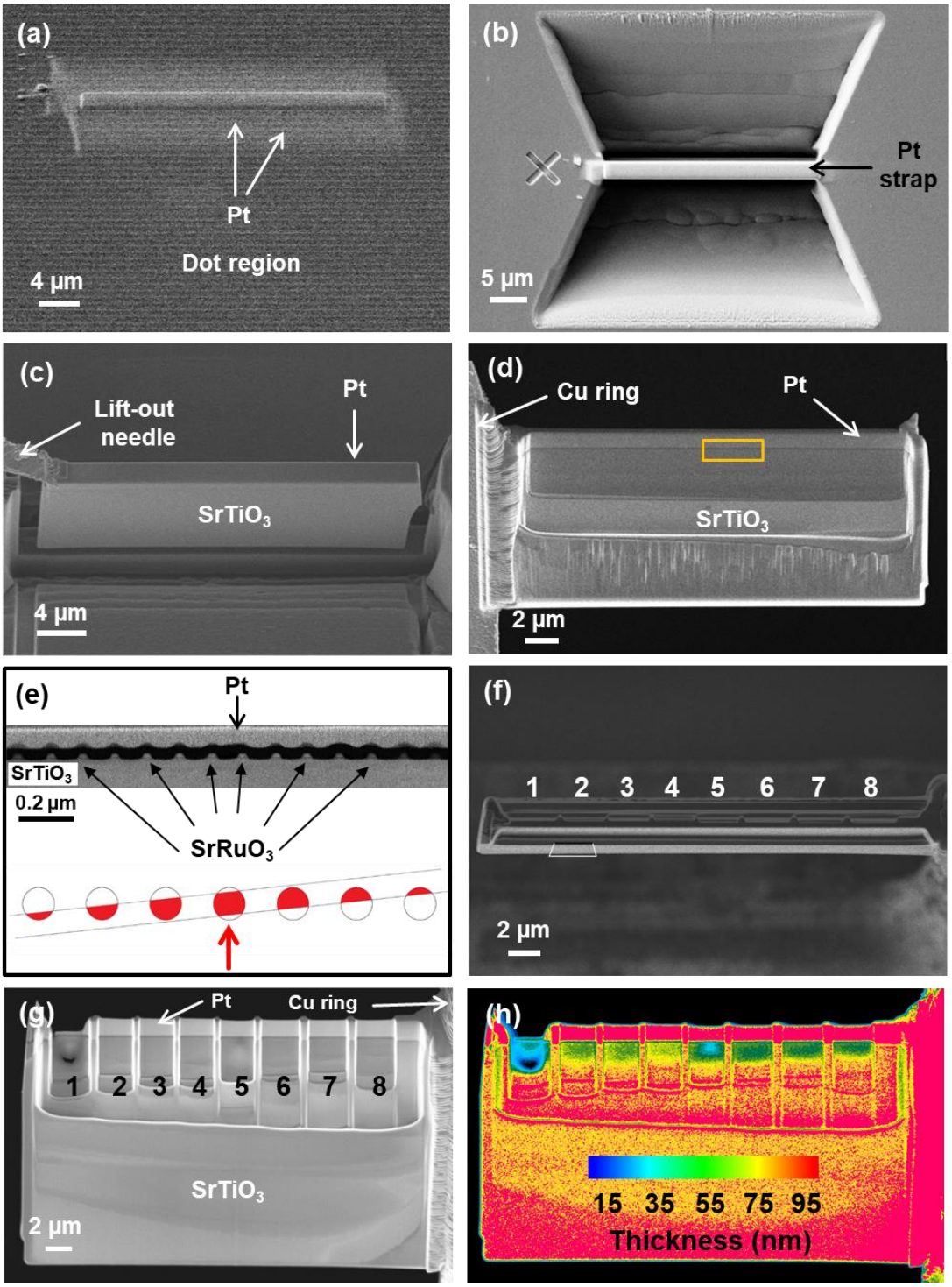

Figure 3-5. TEM sample preparation with A focused ion beam (FIB). (a) Deposition of a Pt protective layer on the bulk surface *via* electron-beam and ion-beam induced deposition. The straight Pt strap is deposited at an angle of 5° with respect to the AA rows. (b) Cutting of two trenches on both sides of the Pt strap with a Ga^+ ion beam leaving a thin section of material isolated at the center. (c) Separation of the lamella from the bulk with a U-shaped undercut by an in-situ lift-out of the specimen with a micromanipulator (Kleindiek MM3A). (d) Attaching of the FIB lamella to a half-moon-shaped copper (Cu) grid (Omniprobe 3 post lift-out grid) using Pt. (e) Upper part: Imaging of the AAs by HAADF-STEM imaging within the yellow box region marked in (d). Bottom part: A sketch of the cutting geometry of AAs at different positions. (f) Thinning of the FIB lamella from two sides (top view). Eight regions of interest were set for fine thinning. (g) Backscattered electron image of the final FIB lamella that was thinned from both sides. 8 regions are separated by thicker walls. (h) Thickness map of the lamella based on the backscattered electron signal, where STO was used as a reference for the thickness evaluation.

	PIPS	FIB	NM
Ion beam	Ar^+	Ga^+	Ar^+
Energy (kV)	3.3 / 2.0 / 0.3	30 / 3	0.9 / 0.7 / 0.4
Angle (°)	8	±(2-1.2) (30 kV) / ±5 (3 kV)	±10
Direction of the ion beam	S-D	D-S	D-S
Beam current density	~10 mA/cm^2	~(5-16) A/cm^2	up to 1 mA/cm^2
Cooling condition	Liquid-N_2	No cooling	Liquid-N_2

Table 1. Experimental details for the different ion milling processes. D (dot) – S (substrate) represents the ion beam direction from the dot to the substrate and vice versa. The current density (current per unit area) of the electron beam has been calculated using the formula $I/\pi(d/2)^2$, where I is the beam current and d is the beam diameter.

moon-shaped copper (Cu) grid using Pt. The SEM image of the obtained FIB lamella is shown in Figure 3-5(d). The geometry of AAs in the obtained FIB lamella appears different due to the applied cutting angle, as shown in the ADF-STEM image and the sketch in Figure 3-5(e). According to the gradual variation of the geometry of AAs in this row, one can easily find the central-cut AA, which periodically appears in different areas of the FIB lamella. Red-colored regions (the sketch in Figure 3-5(e)) indicate the remaining part of AAs. This FIB lamella was additionally milled by Ga^+ ion from both sides (Figures 3-5(f-g)). Then FIB milling was performed at an acceleration voltage of 30 kV by using a beam current of 200 pA for coarse milling, which was gradually reduced to 50 pA for fine thinning with the milling angle reduced from 2° to 1.2°. Eight regions were set for fine thinning, and thick walls lie in-between, which is beneficial to minimize bending effects during TEM characterization. Among them, region 1 was further milled at an acceleration voltage of 3.0 kV using a beam current of 50 pA at a milling angle of 5°. The thickness map of the finalized FIB lamella (Figure 3-5(h)) was obtained by the Zeiss SmartEPD software package *via* analyzing the backscattered intensity using STO as a reference[155, 156]. The thickness of region 1 is about 30 nm. The thickness of regions 2 to 8 ranges from 50 nm to 70 nm. Region 2 to 8 were additionally thinned and cleaned using a Fischione Model 1040 NanoMill TEM specimen preparation system (E.A. Fischione Instruments, Inc.) (Figure 3-4(b)) at liquid nitrogen temperature. This sample treatment using the NanoMill is ideal for post-FIB processing [157-160], since it efficiently removes amorphized material and implanted Ga^+ ions caused by FIB preparation using a highly focused Ar^+ ion beam (as small as 1 µm in diameter). With the Nanomill, the FIB lamella was milled from both sides, starting with an ion-beam acceleration voltage of 900 V, which was gradually reduced to 700 V for thinning and finally to 400 V for cleaning with a beam starting from 100 pA and being reduced to 50 pA.

In this work, three different ion-milling machines (NM, FIB, and PIPS) were employed. The experimental conditions, including the ion energy, the angle between the ion beam and specimen, the direction of the ion beam, the ion current density, and the specimen temperature, determine the ion-beam-induced damage. The resulting details of our experiments are displayed in Table 1. Their effects on the quality of the final TEM specimen will be discussed in the following parts.

3.4 Results and discussions

Figure 3-6(a) displays the low-magnification HAADF-STEM image of SRO AAs on a STO substrate acquired from the TEM specimen prepared by TP&IM, showing a regular arrangement of AAs. The HAADF-STEM image of a single SRO AA is shown in Figure 3-6(b). It can be seen that an amorphous layer is present on the top of the dot, which may result from a surface damage layer induced by the patterning process. EDS measurements performed from 3 regions marked in Figure 3-6(b) are shown in Figure 3-6(c). The chemical composition measured from regions 1 and 2 is from the STO substrate. Since the signal intensity of the HAADF image in the same material is proportional to the thickness, the difference in image contrast between these two areas is attributed to the thickness differences of the TEM specimen. Since the etching process during the AA preparation extends to the STO substrate, either the TEM specimen thickness is larger than the dot size (30 nm) or the thickness difference between region 1 and region 2 originates from a non-central cutting of the dot. As expected, in the AA (position 3), only the elements Sr, Ru, and O are detected.

For the TEM sample preparation of AA nanostructures, TP&IM has certain technical drawbacks that cannot be overcome:

1. Only a limited number of AAs are present in areas that are thin enough for TEM observations. Therefore, the possibility of finding a complete AA structure that was sliced through its center is significantly reduced.

2. Since the AAs cannot be located during the TEM sample preparation process, their presence in the final TEM lamellae is by mere chance.

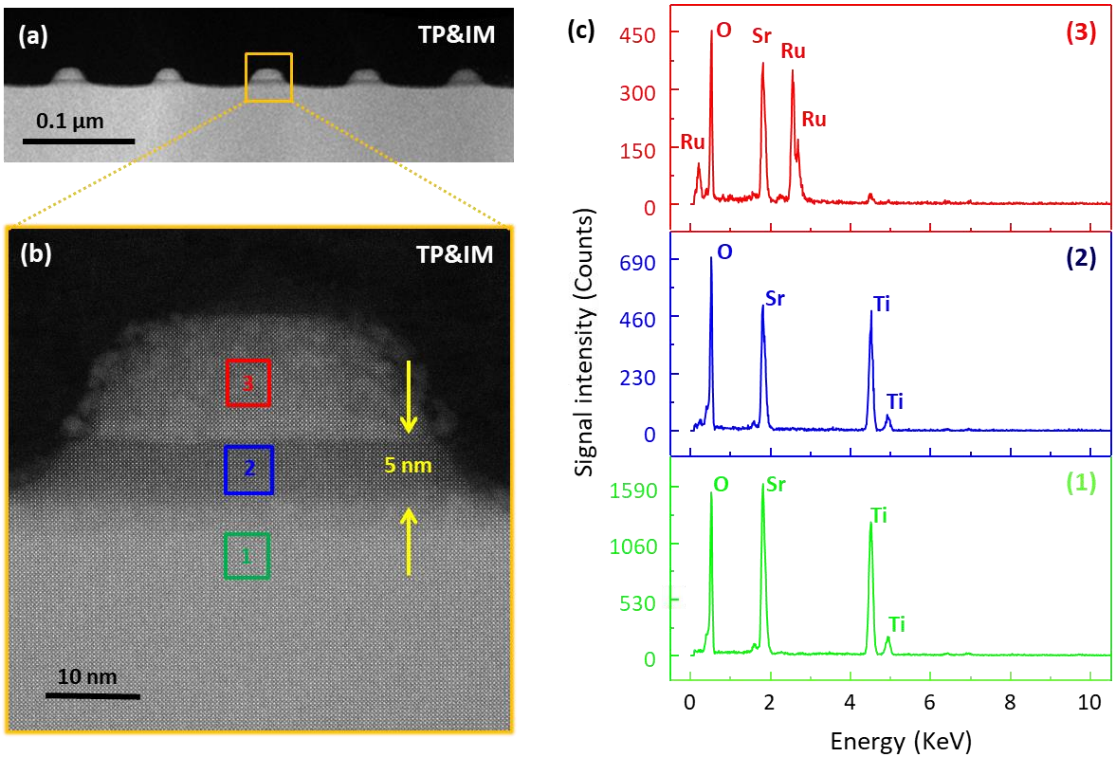

Figure 3-6. (a) Low-magnification HAADF-STEM image of the nanostructure cross-section prepared by tripod polishing followed by Ar^+ ion milling. (b) HAADF-STEM image of an individual SRO AA with a relative thickness of $t/\lambda \approx 0.25$ (c) Corresponding EDS spectra measured from regions (1-3) marked in (b). Normalized atomic ratios of Sr, Ti and Ru in region 1: 50±3.3 %, 49±1.2 %, 0.5±0.3 %; in region 2: 47.8±3.9 %, 51.2±1.1 %, 1.0±0.5 %.

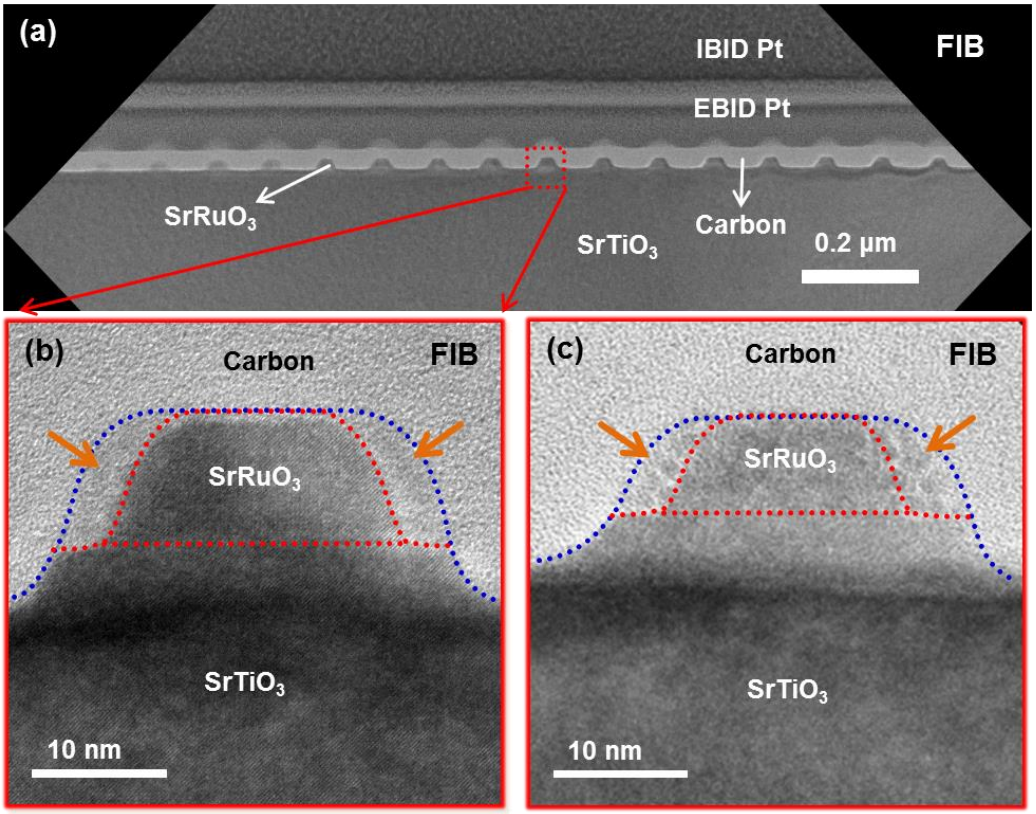

Figure 3-7. (a) Low-magnification BF-TEM image of a thick region ($t/\lambda \approx 0.7$) in a FIB-prepared lamella. (b), (c) are the close-up images of a single SRO AA acquired from thick ($t/\lambda \approx 0.7$) and thin regions ($t/\lambda \approx 0.3$) in a FIB-prepared lamella, respectively. Red dotted curves circle the regions of SRO AA and the blue dotted curves circle the SRO AAs surrounded by damaged SRO material (marked by orange arrows).

Figure 3-7(a) shows a bright-field (BF)-TEM image of a thick region (region 2 to region 8 in Figure 3-5(g)) in the FIB lamella. The close-up image of a single SRO AA is displayed in Figure 3-7(b). Shadows appear at the right and left sides of the SRO AA. One area of the FIB lamella (marked as region 1 in Figure 3-5(g)) was further thinned by Ga^+ ions to obtain a thickness below 30 nm. The TEM image of a single SRO AA acquired from the thin region is shown in Figure 3-7(c). It can be seen that shadows are still present, which are in similar shape as the shadow in Figure 3-7(b). As shown in Figure 3-7(b) and Figure 3-7(c), both AAs are inside the carbon protection layer, revealing that shadows mostly result from the patterning process during the fabrication of AAs nanostructures. The NanoMill was employed to further thin and fine polish the FIB-prepared lamella. The measured relative sample thickness t/λ of the Nanomill-processed FIB lamella is 0.25, which is similar to the thickness of the specimen prepared by TP&IM. The estimated mean free path λ of SRO is about 80 nm [161, 162], giving an absolute thickness (t) of SRO of around 20 nm. With the combination of FIB and NM, one can easily find the locations of the central-cut dots and produce the high-quality TEM specimen for high-resolution STEM studies with high accuracy and high precision.

Next, the quality of TEM specimens obtained with different TEM specimen preparation methods are compared using atomically resolved HAADF-STEM images, as shown in Figures 3-8(a) and (b). As discussed before, the different contrast in the STO region of Figure 3-8(a) is attributed to a thickness step in the STO substrate during the specimen prepared by TP&IM (Figure 3-8(a)). Such a step is absent for the QD cut through its center, which has been prepared by FIB&NM, as shown in Figure 3-8(b). Furthermore, the signal intensity of the STO substrate in Figure 3-8(b) is more homogeneous than in Figure 3-8(a).

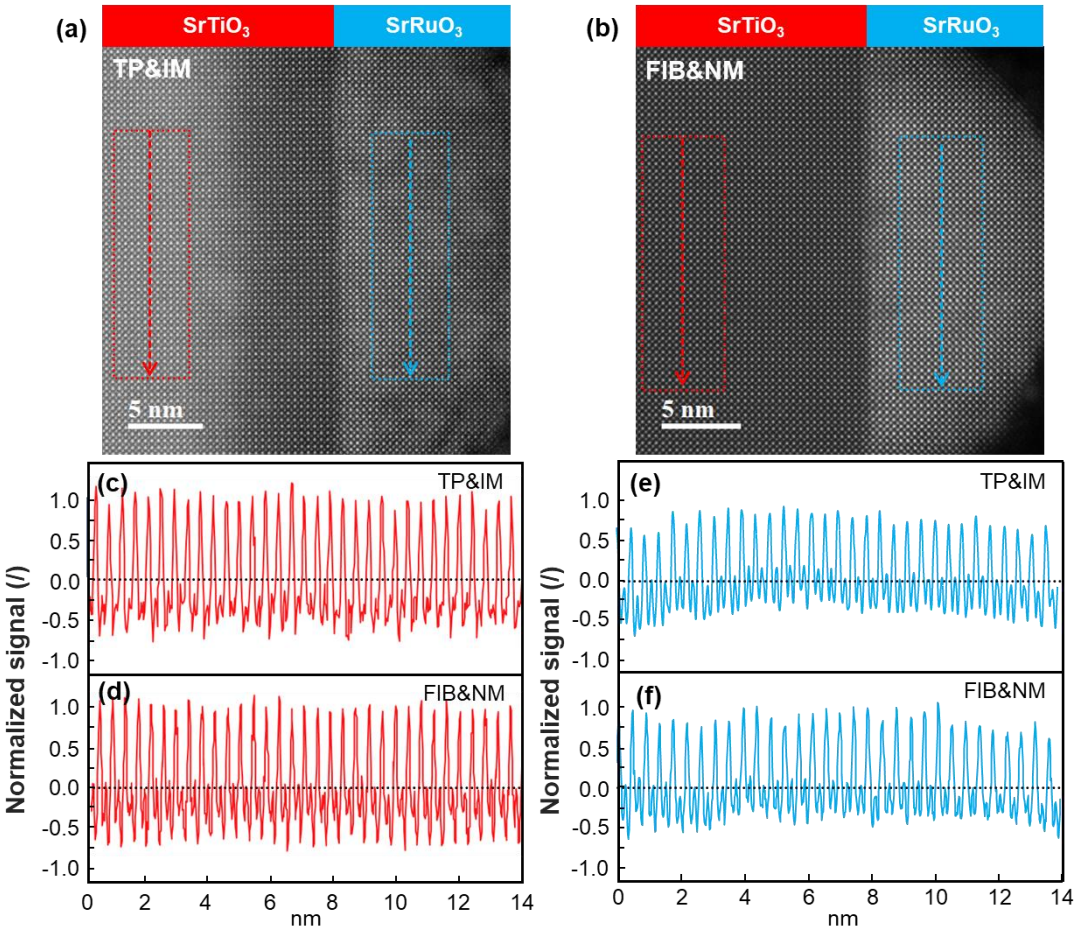

Figure 3-8. HAADF-STEM images of individual SRO AAs prepared by (a) TP&IM and by (b) FIB&NM. The corresponding normalized intensity profiles of a region (14 nm ×5 nm) of STO substrates (12 nm to the interface) marked with red boxes in (a, b) are shown in ((c) TP&IM, (d) FIB&NM). The corresponding normalized intensity profiles ((e) TP&IM, (f) FIB&NM) of a SRO region (14 nm ×5 nm) of SRO located at 4 nm to the interface marked with blue boxes in (a, b).

In order to compare the quality of TEM specimens, the signal intensities of two images are normalized according to the formula: $I_{normalized}=2\cdot(I-I_{mean})/(I_{max}-I_{min})$, where I_{mean} is the mean value, I_{max} is the maximum and I_{min} is the minimum value of the signal intensity. Using this formula, the HAADF signal is normalized between 1 and -1. The quality of the TEM specimen can be evaluated by observing the signal oscillation around 0 in the normalized signal intensity profiles. Figure 3-8(c) and Figure 3-8(d) represent the normalized intensity profile of a region in the STO substrate (12 nm to the interface) marked with the red box in Figure 3-8(a) and 3-8(b). It shows that the signal oscillations in Figure 3-8(d) are more uniform than those of Figure 3-8(c). The average maximum values are 1.00±0.08 and 1.00±0.04 for Figure 3-8(c) and Figure 3-8(d), respectively. Besides, the corresponding minima are -0.61±0.08 and -0.69±0.03, respectively. In contrast to Figure 3-8(c), the signal deviation in Figure 3-8(d) is smaller, revealing that the TEM specimen prepared by FIB&NM has a better quality compared to that by TP&IM. The SRO part of Figure 3-8(b) appears cleaner without obviously damaged regions compared to Figure 3-8(a). Figures 3-8(e) and (f) correspond to the normalized intensity profiles extracted from a region (4 nm to the interface) marked with blue boxes in Figures 3-8(a) and (b), respectively. The averaged maximum for Figure 3-8(e) and Figure 3-8(f) are 0.87±0.11 and 0.90±0.08, respectively. Moreover, the corresponding averaged minimum is -0.52±0.12 and -0.45±0.10. In contrast to Figure 3-8(e), the standard deviation of the signal intensity in Figure 3-8(f) is smaller, revealing a better specimen quality in the SRO part. The proposed sample preparation by FIB&NM enables us to find the central-cut dots in the FIB lamella and thus

minimizes the influence of the dead surface layer on the image contrast during the TEM characterization. The NanoMill can substantially reduce the beam damage and produce a sample with clean surfaces using a focused argon-ion beam with a low beam-current density (Table 1). The presented data demonstrate that the optimized procedures through a combination of FIB and NM can indeed produce high-quality TEM specimens of QD nanostructures.

3.5 Summary and conclusions

In this chapter, I report two methods, TP&IM and FIB&NM, for the preparation of TEM specimens of AA nanostructures. It is demonstrated that our optimization of the combination of FIB&NM has several advantages that can be applied for efficiently preparing high-quality and damage-free TEM specimens consisting of AAs:

1. A FIB lamella offers large thin regions and therefore enhances the probability of finding a complete dot structure in TEM specimens. Thinning of multiple regions effectively reduces the bending of the sample, which is beneficial for TEM characterization.

2. The probability for the presence of AA structures cut through their centers is increased, when cutting the lamella at an angle of 5° with respect to the dot arrays, where the ideal cutting angle is closely correlated to the size and spacing of the dots and needs to be adjusted accordingly.

3. The Fischione NanoMill was used to additionally thin and polish the thick FIB lamellae from both sides. The surface contamination and amorphous layer were gently removed by using Ar^+ ions at a low current density, resulting in a flat and clean TEM specimen consisting of SRO AAs on the STO substrate.

With the obtained high-quality TEM specimen, one can carry out more precise structural and chemical studies of AA nanostructures for unraveling the underlying mechanism of their emergent phenomena. The reported settings are practically useful for TEM sample preparations with TP, IM, FIB, and NM. I believe that the optimization of the combined methods (FIB&NM) has significant implications not only for preparing TEM specimens of AAs, but also for other emerging quantum nanostructures.

Contributions to this chapter:

Hongguang Wang carried out the TEM specimen preparation, TEM data acquisition, and TEM-related data processing. Part of this chapter has been submitted to the journal *Micron*. H.G. Wang and Vesna Srot (MPI-FKF) conceived this work. Bernhard Fenk (MPI-FKF) contributed to the preparation of the FIB lamella. Gennadii Laskin (MPI-FKF) performed the fabrication of the AAs and the related SEM measurement. Wilfried Sigle (MPI-FKF) contributed to the discussion part of this chapter. Lei Jin from Ernst Ruska-Centre, Juelich, Germany offered help for the preparation of TEM lamellae by NanoMill. Peter A. van Aken (MPI-FKF), Jochen Mannhart (MPI-FKF) supervised and oversaw this work. The work in this chapter also got support during TEM sample preparation by Ute Salzberger (MPI-FKF) and Marion Kelsch (MPI-FKF), and the TEM support by Kersten Hahn (MPI-FKF) and Peter Kopold (MPI-FKF).

Chapter 4. Quantitative STEM study of strongly-correlated $SrRuO_3$ artificial atoms*

4.1 Abstract

Spatial confinement of correlated systems in 2D, *e.g.*, at interfaces, in thin films, or superlattices, promises a variety of exciting advantages over their mean-field counterparts. Although novel electronic properties are expected, if correlated systems are confined in more dimensions, *i.e.*, to 1D and 0D, such systems have been explored only marginally. In this chapter, arrays of 0D AAs of SRO with sizes between 500 and 15 nm are fabricated and explored regarding their magnetic properties. Then I studied the microstructure and chemistry of AAs by STEM. Cross-sectional STEM imaging shows the high-quality epitaxial growth of the samples with the absence of any visible defects. Down to the smallest AA-size explored, the samples were found to be magnetic with a maximum Curie temperature T_C achieved by AAs of 30 nm diameter. This peak in T_C is associated with a dot-size-induced relief of the epitaxial strain, as evidenced by quantitative STEM analysis. Furthermore, the easy axis of the SRO rotates toward the in-plane direction by decreasing the size of AAs, which is correlated to the magnetocrystalline anisotropy of the SRO.

Graphical abstract: Surface morphology and cross-sectional structure of the unpatterned SRO thin film and patterned arrays of SRO AAs with different sizes (200 nm / 80 nm / 30 nm).

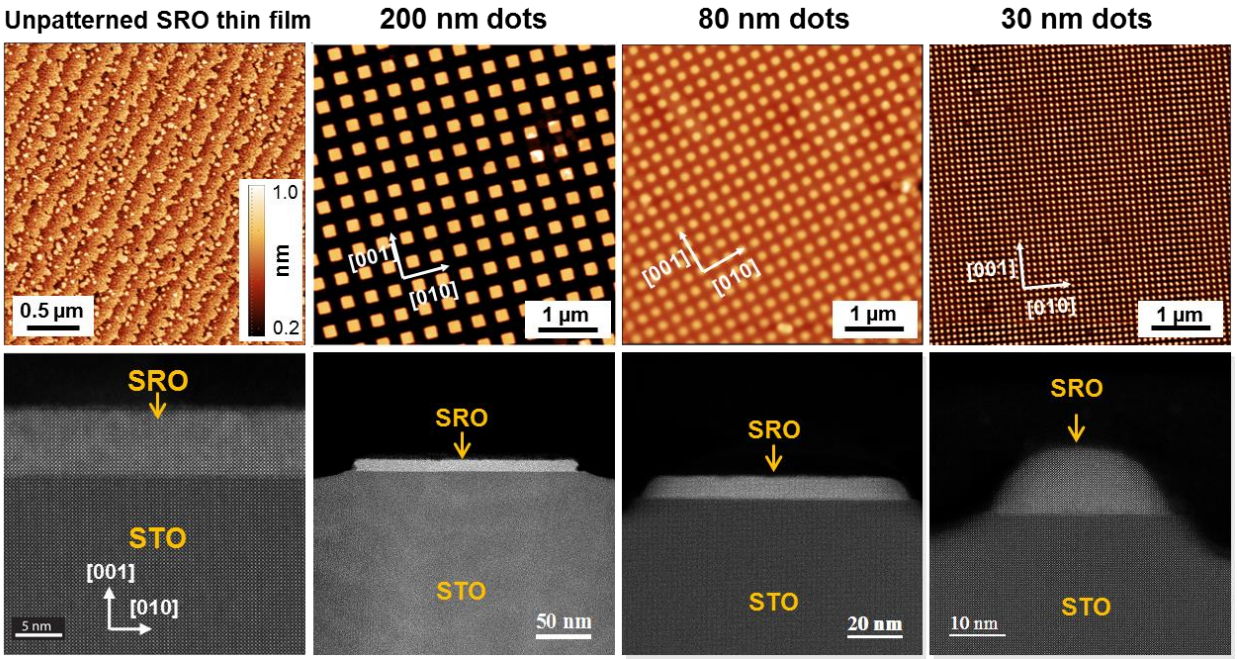

*Part of this chapter has been published in Ref. [144]

4.2 Introduction

Artificial atoms (AAs), also known as quantum dots and zero-dimensional electron systems, describe the shell structure of the electron states and their coherency across the material[16, 47, 48]. It mimics the electron states of natural atoms by a coherent many-body wave function with one macroscopic phase[49, 163]. As the characteristic size of AAs approaching to the de Broglie wavelength of electrons, holes, and excitons, quantum confinement effects will manifest, leading to discrete energy states[46, 54]. The exotic electronic structure thus brings about unexpected optical, electrical and magnetic properties that have been applied in biological system imaging [164], quantum dot monitor [165], photon emitter for quantum computing [58], *etc.* Till now, most of the work was focused on self-assembled AAs of uncorrelated mean-field type semiconductors such as III-V compounds (GaAs, InP) [166, 167], II-IV compounds (CdS, CdSe) [168], and group IV compounds (Si, Ge) [169]. However, due to difficulties in the fabrication, only a few examples of strongly correlated systems were reported,[59, 170, 171] whose properties are very susceptible to their size, geometry, strain and interfacial states. It is still a big challenge to synthesize a highly pure material with low defect density, and to fabricate AAs with small size that allows the formation of a coherent many-body electron wave function with the top-down etching approach. Furthermore, it is well-known that the patterning process causes local material damage and dead layers, which can significantly reduce the mean free path of the electrons.[172]

SRO is a correlated conducting perovskite oxide with strong itinerant ferromagnetism (bulk Curie temperature $T_C \approx 160$ K).[173] It exhibits orthorhombic symmetry at room temperature, and its ferromagnetic properties highly depend on the material quality as well as on the film thickness.[174, 175] Even slight variations of the stoichiometry or lattice parameters may lead to a significant change of magnetic properties. Hence, SRO is a model system to study the relevance of dead-layer creation and how materials behave upon confinement. In this work, strongly-correlated SRO AAs with the diameter of tens of nanometer were firstly fabricated by EBL of epitaxially-grown SRO thin film. Then, the superconducting quantum interference device (SQUID) was employed to explore how the magnetic properties of the material behave between the thin film and the AAs with different diameters.

Microscopic structure and chemistry for the AAs and the heterointerface between SRO and STO play a crucial role in affecting the magnetic properties.[173, 176] In order to study the underlying mechanisms of observed magnetic phenomena, it is significant to make intensive microscopic explorations of the AAs with TEM at high spatial resolution and accuracy. In this work, based on the acquired high-resolution (S)TEM images, I quantitatively analyzed the strain fields, the lattice anisotropy, and the oxygen octahedral rotations in SRO on the nanoscale to the atomic-scale. The atomically resolved elemental distributions at the interface between SRO and STO were studied as well with EELS.

4.3 Epitaxial-grown $SrRuO_3$ thin films and patterned $SrRuO_3$ artificial atoms

4.3.1 Microstructure of $SrRuO_3/SrTiO_3$ thin films

The SRO thin films were epitaxially grown by PLD on (100)-oriented STO substrates for patterning AAs samples. The quality of the thin films largely determines the quality of patterned nano-devices. Therefore, it is critical to ensure the high-quality of SRO thin films before patterning.

As a powerful technique to study the crystalline structure, XRD was used to confirm the epitaxial growth of SRO thin films. Figure 4-1(a) shows a wide range $\theta/2\theta$ scan of epitaxial grown SRO thin film. The first four STO peaks from the (h00) family are well visible. The peaks correspond to the diffraction maxima of λ =1.541 Å on a cubic crystal with the lattice periodicity of 3.905 Å matching the lattice parameter of STO. The positions of SRO peaks are close to the left of the corresponding STO ones. Figure 4-1 (b) displays a close-up view on the (004) STO and the corresponding (440) SRO peaks. The SRO peak is shifted by ≈ 0.9° towards smaller angles, indicating a larger out-of-plane lattice parameter of SRO. That fits the out-of-plane lattice elongation caused by the Poisson effect and the bi-axial in-plane compressive strain applied to the film from the substrate. The broadening of SRO peaks results from the small thickness of the thin film. The thickness and the out-of-plane lattice parameter of the film can be extracted from the Laue intensity oscillations.[177] The calculated thickness and out-of-plane lattice parameter are 10 nm and 3.943 Å, respectively. The measured thickness oscillations decay faster as compared to the simulated Laue curve in Figure 4-1 (b). This is ascribed to the roughness of the film surface.

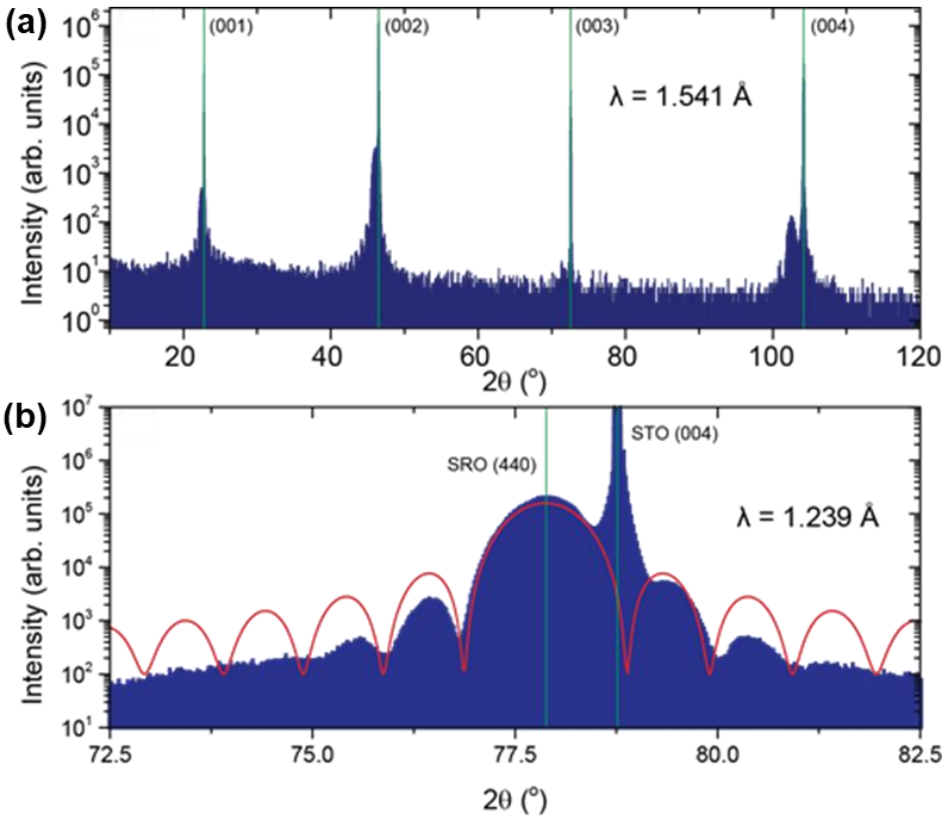

Figure 4-1. (a) Large scale θ/2θ scan of a 10-nm-thick SRO film grown on STO (100) performed with the wavelength λ = 1.541 Å. (b) θ/2θ scan close to the (004) STO peak performed at the ANKA synchrotron facility (λ = 1.239 Å). Green lines mark peak positions, and the red curve depicts the calculated Laue oscillations.

Figure 4-2(a) shows four reciprocal space maps (RSMs) of the SRO thin films at different ϕ angle orientations of the STO substrates. The intense central maximum in the upper part of the maps corresponds to the $(\bar{1}03)$ STO diffraction peak. The vertically elongated peaks correspond to SRO. These peaks are shifted to smaller Q_Z, indicating a larger out-of-plane lattice parameter of SRO than STO. The in-plane lattice parameters along Q_X are identical, confirming that the epitaxial SRO thin films are fully strained. Figure 4-2(b) shows the line-by-line averaged intensity profiles along the Q_Z direction extracted from the RSM maps in Figure 4-2(a). It shows that the SRO peak positions are shifted in the Q_Z direction by a small value, which depends on the ϕ angle, revealing that the SRO has a distorted orthorhombic structure. The profiles for SRO peak along $\phi = 0°$ and $\phi = 180°$ coincide, implying that no orthorhombic distortion can be observed in these directions. In contrast, the peaks at $\phi = 90°$ and $\phi = 270°$ are shifted relative to the central ones ($\phi = 0°$ and $\phi = 180°$). These peak shifts allow us to determine the degree of the orthorhombicity. The distorted orthorhombic unit cell can be approximated as a tilted pseudocubic unit cells with the tilt angle $\alpha = \arctan(\Delta Q_Z / \Delta Q_X)$, where ΔQ_Z and ΔQ_X are distances in reciprocal space along x and z between SRO peaks for different ϕ angle orientations. The evaluation from the $\phi = 90°$ and $\phi = 270°$ peaks gives a tilt angle value of $\alpha = 0.49°$, which is in good agreement with the literature data.[178, 179]

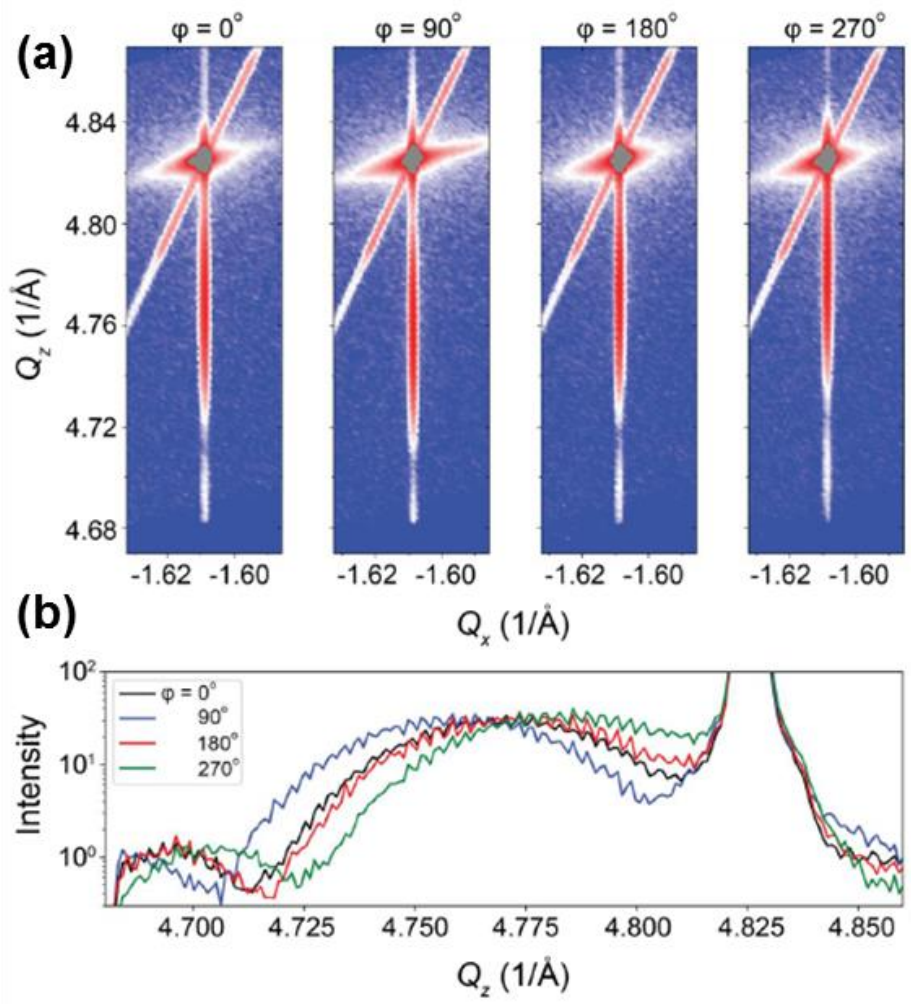

Figure 4-2. (a) RSMs for the SRO thin films measured around the $(\bar{1}03)$ peak of STO at four different ϕ angle orientations of the substrate. (b) line-by-line averaged intensity profiles along the Q_z direction for different ϕ angles.

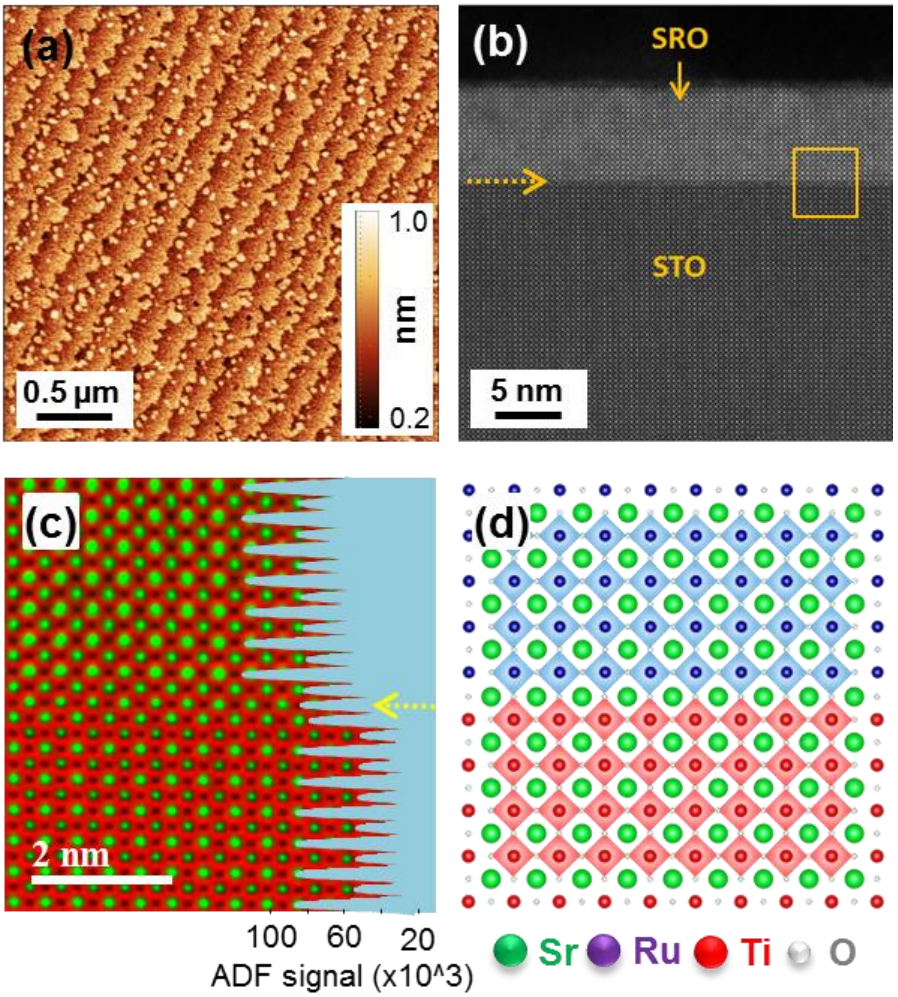

Figure 4-3. (a) Surface morphology of the epitaxial SRO thin film by AFM. The surface terrace structure is clear. (b) HAADF-STEM imaging of the cross-section of the epitaxial SRO thin film. The horizontal yellow arrow marks the interface between SRO and STO. The yellow box marks one region at the interface. (c) Overlay of simultaneously acquired HAADF (blue) and ABF (red) images of the box region showing the cationic (Sr, Ru, Ti) and anionic (O) positions. The right side is the laterally averaged intensity profile of the HAADF signal and the yellow arrow indicates the interface. (d) The corresponding sketch of (c). Positions of atomic columns are presented.

Figure 4-3(a) shows the topographic AFM image of the epitaxial SRO thin film right after the growth to avoid the artefacts due to the contamination of the surface by hydrocarbons and air dust, when exposed to the ambient environment. The terrace structure with the height of about one unit cell of the SRO lattice is well visible, showing a smooth surface of the SRO thin film. Surface defects, like cracks, are invisible. It indicates a good epitaxial quality of the SRO thin film. The cross-sectional TEM specimen of the SRO thin film was prepared by a combination of TP and NM described in Chapter 3. Figure 4-3(b) displays the HAADF-STEM image of the cross-section of the SRO thin film. The SRO thin film is grown on top of STO by perfect layer-by-layer stacking. Since signal intensities of the HAADF image are proportional to the mass of the constituent atoms, the interface between SRO and STO is self-explanatory. There exist no visible defects in the thin film and at the interface. An enlarged image of the interface between SRO and STO is shown in Figure 4-3(c). The oxygen octahedron of SRO and STO are well connected through the corner-sharing modus. The corresponding sketch of the interfacial structure is displayed in Figure 4-3(d).

The microstructure studies by XRD, AFM, and STEM confirm the high epitaxial quality of the SRO thin films with a single crystalline structure, flat surface, and clean interface.

4.3.2 Microstructure of patterned $SrRuO_3$ artificial atoms

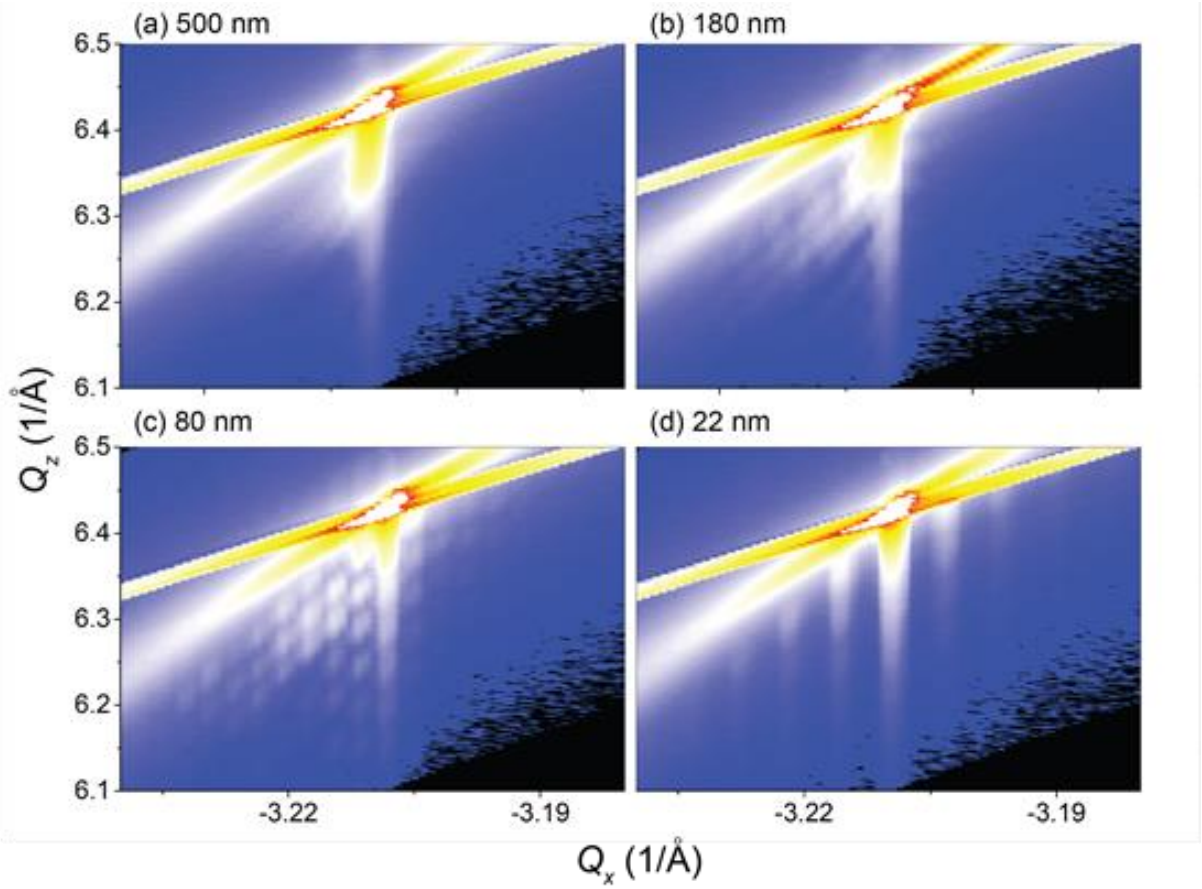

Figure 4-4. Reciprocal space maps close to the (204) peak of STO for the array of SRO AAs of different diameters: (a) 500 nm, (b) 180 nm, (c) 80 nm, (d) 22 nm. The diffraction on the large scale structure of the arrays corresponding to different AA periodicities can be observed.

Figure 4-4 shows RSMs measured close to the (204) reflection of STO for the array of AAs with different diameters. RSMs for AA arrays also show an elongated SRO peak located under the STO one. Also, depending on the array periodicity, additional diffraction peaks appear on the sides of the main one, which originates from XRD on the large scale structure of the arrays. The distance between the peaks in reciprocal space increases with decreasing real space periodicity of AA arrays. This distance describes the correct value of the AA spacing in the arrays. Due to the small amount of SRO in these nanostructures, the counting statistics of the XRD measurement is low, and a solid conclusion about the structure of the patterned arrays cannot be drawn.

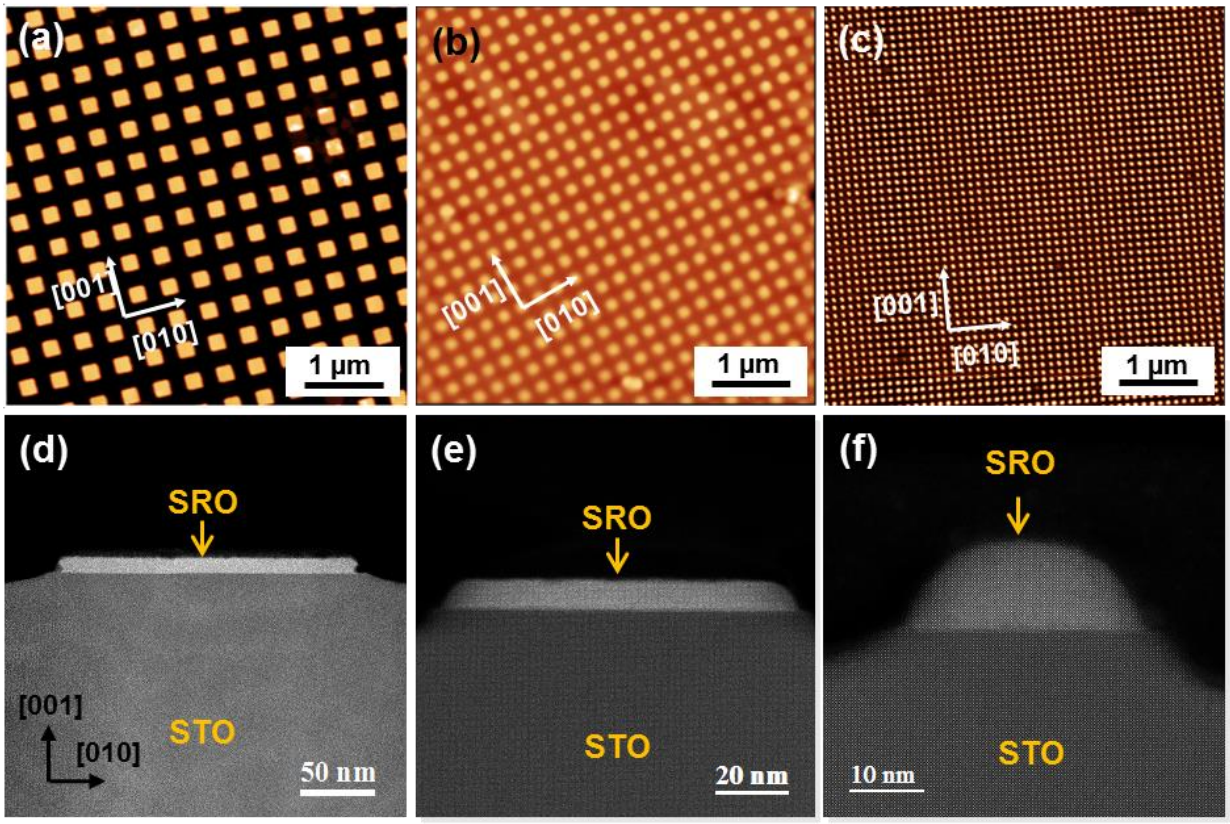

Figure 4-5. The topographic AFM image for the array of AAs with different diameters: (a) 200nm, (b) 80 nm, (c) 30 nm. The HAADF-STEM images for the cross-section of AAs with different diameters: (d) 200 nm, (e) 80 nm, (f) 30 nm.

Figures 4-5 (a), (b), (c) show the topography of the array with AAs size of 200 nm, 80 nm, and 30 nm, respectively. AAs are well arranged on top of the STO substrate, and the shape of AAs deviates from rectangle to circle as the size is smaller than 200 nm. The number of AAs increases with the decrement of the AA size. For the 20 nm-sized AA arrays, the number of SRO AAs is on the order of magnitude of 10^9. Due to inhomogeneity during patterning, *i.e.*, resist thickness variations and substrate charging, defects, such as missing or distorted AA, may appear in the resulting structure (Figure 4-5(c)). Figures 4-5 (d), (e), (f) display the cross-section of single AA with a diameter of 200 nm, 80 nm, and 30 nm, respectively. The probability of such effects increases with reducing AA size and spacing, but typically does not exceed several percents of the total number of AA. It shows that the samples after patterning still keep a high epitaxial quality with a clean interface without any visible defects, revealing that the crystalline structure keeps nearly unchanged during the patterning process. Due to technical limits, the side edge of the AAs inevitably becomes curved as the AA size decreases. During the sample preparation for TEM, the AA was cut through its center with a lamella thickness of ≈ 20 nm. Therefore, the cross-section provides a projection through almost the entire AA. The curved shape of the substrate near the AA and the shape of the AA itself are caused by non-uniform removal of material during dry etching with Ar ions.

4.4 Magnetic properties of the $SrRuO_3$ thin films and patterned $SrRuO_3$ artificial atoms

4.4.1 Magnetic Curie temperature

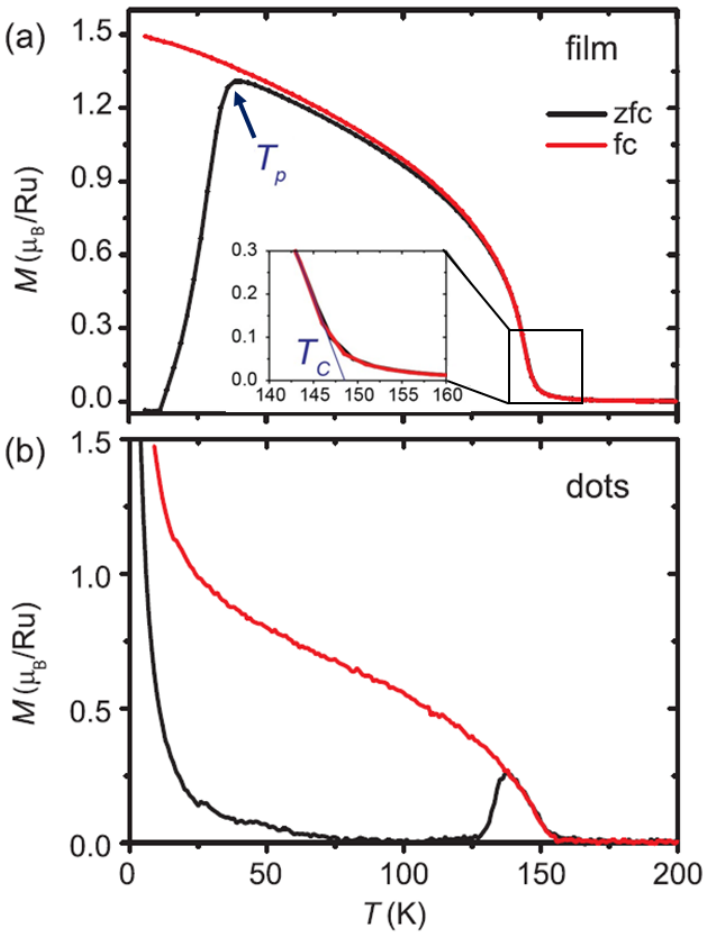

Figure 4-6. The temperature-dependent magnetization of (a) an unpatterned SRO thin film and (b) an array of 20 nm diameter AAs patterned from the same film, measured with zero-field cooling (zfc) and field-cooling (fc) in the out-of-plane oriented magnetic field of 0.1 T. *Tp* denotes the magnetic peak temperature of the zero-field-cooled magnetization, T_C means the magnetic Curie temperature by extrapolation. The black and red lines correspond to zero-field-cooled and field-cooled measurements, respectively. The diamagnetic contribution of the STO substrate has been subtracted.

In order to determine the ferromagnetic properties of the epitaxial SRO thin film, two types of measurements were performed: the magnetization versus temperature *M (T)*, and the magnetic hysteresis loop *M (B)*.

Figure 4-6(a) shows the magnetization of SRO thin films as a function of temperature under zero-field-cooled (zfc) and field-cooled (fc) processes. For the zfc curve, a sample is firstly cooled to low temperature in the absence of the external magnetic field. Ideally, magnetic moments remain randomly oriented across the ferromagnetic transition, and the net magnetization remains zero. Then a small magnetic field (usually ~ 0.1 T) is applied, and then the sample is heated. The magnetic peak temperature T_p is about 39 K. The sample is cooled again in the same magnetic field as soon as surpassing the ferromagnetic transition, yielding the fc curve. The shape of the curve and the saturation magnetization of 1.5 μ_B/Ru are in good agreement with the literature data.[180, 181] The Curie temperature T_C is determined by linear extrapolation of the transition curve to $M = 0$ (the inset of Figure 4-6(a)). However, a finite magnetic moment exists above this temperature, attributed to the domain structure and film reorientation.[182] For all films, the transition has been found at a $T_C = 149 \pm 1$ K, which is comparable to the T_C values reported in the literature for equally thick films deposited by PLD.[183, 184]

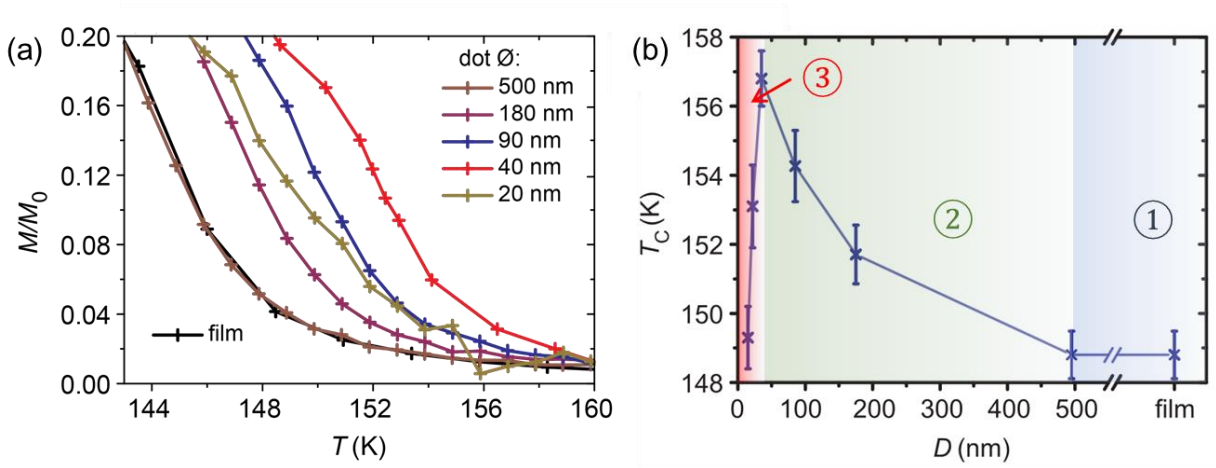

Figure 4-7. (a) Measured temperature dependence of the magnetization of several samples with different AA sizes in the temperature range close to T_C. All magnetization curves were normalized. (b) Curie temperature of the samples plotted as a function of the AA diameter. Zone ①: SRO thin films to the AA diameter of 500 nm, zone ②: the AA diameter of 500 nm to the AA diameter of 30 nm, zone ③: the AA diameter below 30 nm.

Figure 4-6(b) shows an example of the magnetic transition curve for a patterned sample with a diameter of 20 nm. Considerably different is the behavior of the magnetic response at low temperatures, where a significant increase of the magnetization is observed. This is due to the paramagnetism inherent in STO[185], which causes difficulties for measuring the AA magnetization, because of the minimal SRO volume compared to the STO substrate. However, this contributes only to the low-temperature properties and does not affect the magnetization close to the ferromagnetic transition region, in which we are primarily interested here. After patterning, the sample remains ferromagnetic with a T_C = 153 ± 1 K, *i.e.*, 4 K higher than that of the film.

To clarify the size effects on the magnetic Curie temperature, a series of samples with different AA sizes (from 500 to 15 nm) was fabricated and systematically studied for their T_C variations. The measured *M (T)* curves for the samples are shown in Figure 4-7(a), and the Curie temperatures extracted from the curves are plotted in Figure 4-7(b). Since the saturation magnetization and the shape of the *M (T)* curves depend on the AA size, all curves in Figure 4-7(a) have been normalized to the magnetization level of the film. The observed variation of the T_C in Figure 4-7(b) is divided into three zones. In zone ①, at AA diameters larger than 500 nm, T_C remains the same as in the unpatterned film. In zone ②, T_C increases with reducing the AA size. T_C attains a maximum ($T_C \approx 157$ K) with AA sizes of ≈ 30 nm, which is close to the T_C of bulk SRO (≈ 160 K [47]). At this point, the increase of T_C is ≈ 8 K. In zone ③, T_C drops as soon as the AA size is below 30-40 nm, which is more rapid than the rise, presumably due to surface defects and dead layers. A decrease of T_C with shrinking feature size is well known for thin films[186] and has been observed in nanoparticles of other perovskites[187] and also for metals.[188] This reduction of T_C is generally attributed to the reduced number of neighbors and the corresponding destabilization of the magnetic ordering.[188] Even for the smallest AA sizes, however, the Curie temperature exceeds that of the unpatterned film.

4.4.2 Magnetic easy-axis rotation

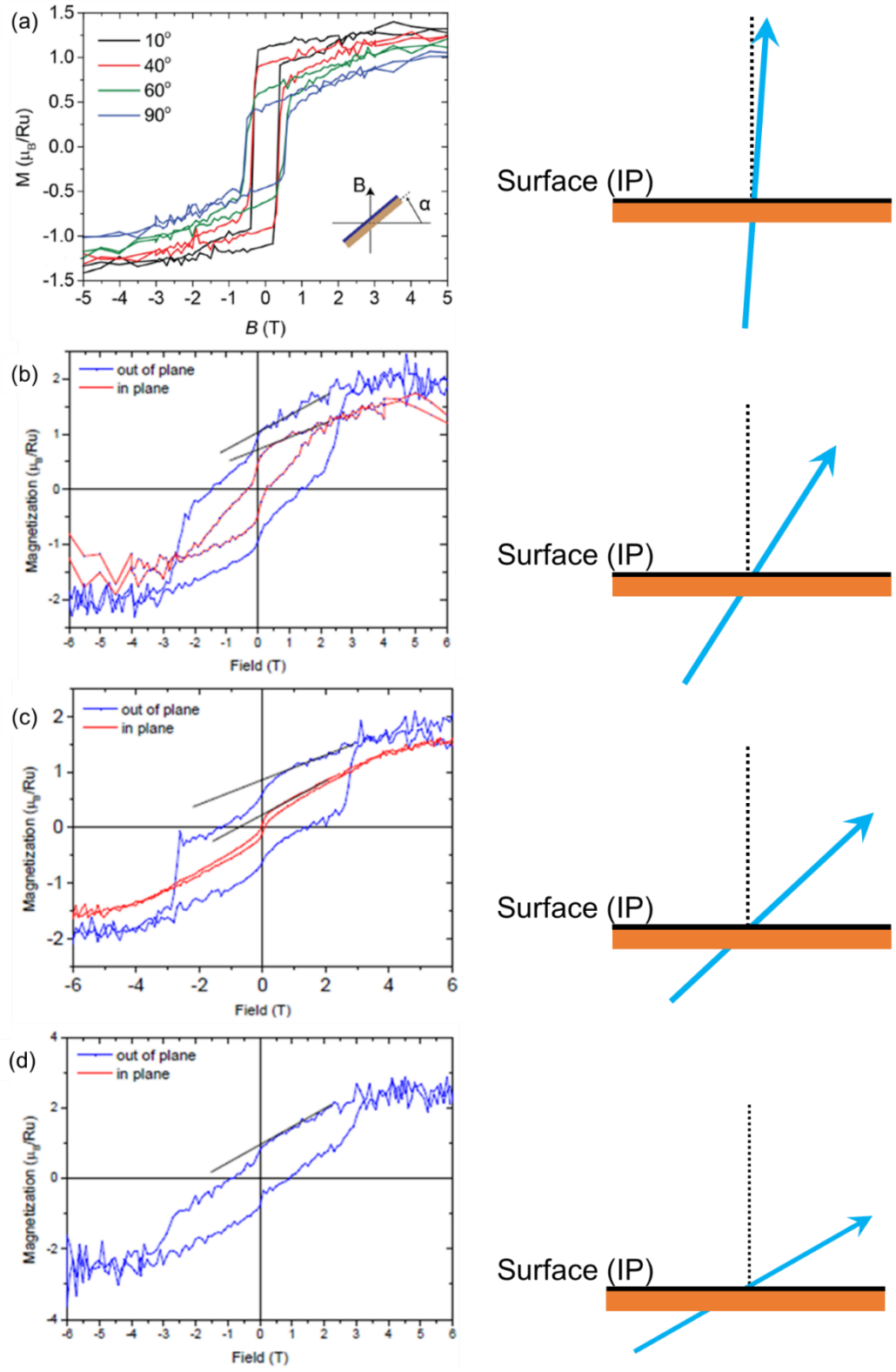

Figure 4-8. (a) Magnetic hysteresis *M(B)* measurements of an epitaxial SRO film performed at several substrate orientations and T = 15 K. Magnetic hysteresis *M(B)* measurements of an array of (b) 200 nm, (c) 80 nm and (d) 30 nm diameter AAs patterned from the same film. The blue curve and the red curve are measured in the out-of-plane and in-plane (IP) orientations, respectively. The sketch on the right side illustrates the direction of the magnetic easy-axis (lines with arrow) in the material.

The magnetic hysteresis loop enables us to extract the ferromagnetic properties of materials. The characteristic values, *e.g.*, saturation magnetization M_{sat}, remnant magnetization $M_{rem,}$ and coercive field B_C, respectively, and the overall shape of the hysteresis loop can give valuable information about the magnetic anisotropy and domain structure. A measurement of a hysteresis loop starts at the magnetic field $+B$ above the magnetic saturation. After that, the field is swept to $-B$ and back to $+B$ again, measuring a closed loop. When sweeping the magnetic field, the measured magnetic moment is the projection of the magnetization vector to the magnetic field axis. In the absence of the magnetic field, the magnetization orients along the crystallographically defined magnetic easy axis of the material. If the angle between the easy axis and the measurement axis is small, the remnant magnetization M_{rem} tends to be close to the saturation magnetization M_{sat}, making the shape of hysteresis loop rectangular-like.

Figure 4-8(a) shows the hysteresis loops, when the magnetic easy-axis of the unpatterned SRO thin film rotates relative to the magnetic field *(B)*. Four different orientations (10°, 40°, 60°, 90°) of the substrate were applied for the measurement of *M(B)* curves. The shape of loops changes as the direction of the magnetic easy-axis deviates further from the magnetic field axis. The shape at 10° is more "rectangle" than others, indicating that the easy axis is oriented relatively close to the 10° to film normal. Unfortunately, the construction of the magnetometer does not allow precise control of the magnified direction and the substrate angle. The angle measurement error is ≈ 10°. Furthermore, for a uniaxial magnetic system like SRO, the orientation with the largest ratio of the remanent to the saturation magnetization M_{rem}/M_{sat} indicates the magnetic easy-axis. From the image it can be seen that the ratio decreases from $(M_{rem}/M_{sat})_{\perp}$=0.85 to $(M_{rem}/M_{sat})_{//}$=0.34 with an increasing angle from α=10° to α=90°, indicating that the magnetic easy axis is oriented close to the film normal. Figure 4-8(b, c, d) corresponds to the magnetic hysteresis *M(B)* loops of an array of 200 nm, 80 nm, and 30 nm diameter AAs patterned from the same film, measured in the out-of-plane and in-plane orientations, respectively. For the hysteresis loop of 200 nm-sized AA arrays in Figure 4-8(b), the M_{rem}/M_{sat} changes from $(M_{rem}/M_{sat})_{\perp}$=0.51 in the out-of-plane to just $(M_{rem}/M_{sat})_{//}$=0.32 in the in-plane orientation. For the hysteresis loop of 80 nm-sized AA arrays in Figure 4-8(c), the value $(M_{rem}/M_{sat})_{\perp}$=0.44 and $(M_{rem}/M_{sat})_{//}$=0.12. For the array of even smaller AAs down to 30 nm, the magnetic signal of AAs becomes much weaker. Here, only the hysteresis loop in the out-of-plane direction was obtained reproducible. The corresponding value $(M_{rem}/M_{sat})_{\perp}$ amounts 0.39. For these calculations, the region of the coherent magnetization rotation is extrapolated to the intersection with the B=0 axis to ignore the rapid magnetization drop in small fields, which is not related to anisotropy. The $(M_{rem}/M_{sat})_{\perp}$ drops gradually as the decrease of the AA size, revealing that the magnetic easy-axis rotates from the out-of-plane direction toward the in-plane direction, which is sketched in the right panel. Other researchers have found similar phenomena.[36, 189]

4.5 Interfacial structure and elemental distribution

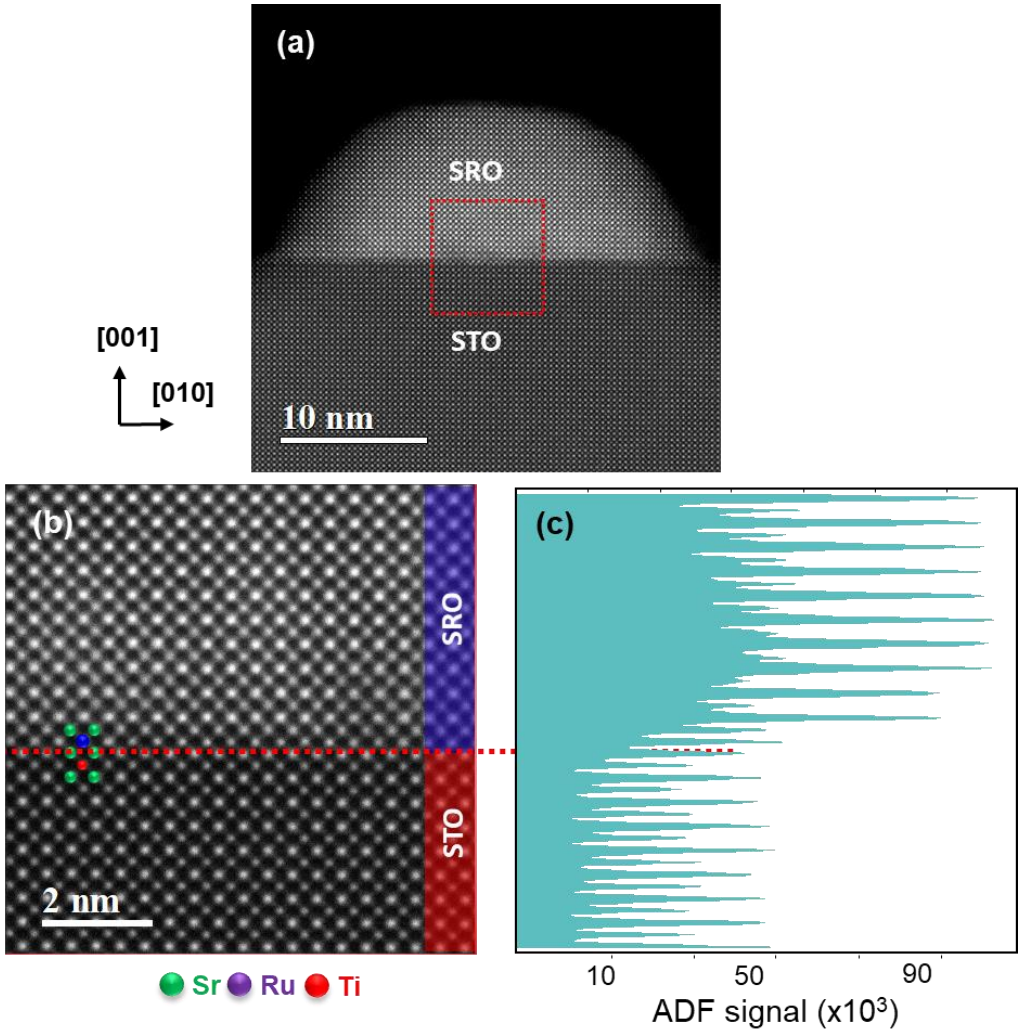

Figure 4-9. STEM observation of the interfacial structure of the AA with a diameter of 30 nm. (a) The HAADF-STEM image of the cross-section of the AA. (b) HAADF-STEM image of the interfacial region between SRO and STO. (c) The laterally averaged signal intensity of (b). The red dotted line denotes the interfacial Sr-O monolayer.

Novel electronic states may occur at oxide interfaces due to the interplay of charge, spin, orbital and lattice degrees of freedom and be responsible for the emergent phenomena of the fabricated materials.[13] To explore the effects of interfaces on the magnetic properties of the AAs, I made a detailed study of their interfacial structure and local chemistry. Figure 4-9(a) shows the HAADF-STEM image of the cross-section of a single AA with a diameter of 30 nm, indicating a bright contrast between the SRO AA and the STO substrate material with a sharp interface. HAADF-STEM images in Figure 4-9(b) displays a close-up view of the interfacial zone. The mismatched SRO and STO lattices are patched up in high quality and form a unified interface. The horizontally-averaged intensity profile of the HAADF image in Figure 4-9(c) depicts that the intensity of the first Ru-O monolayer is between that of the Ti-O layer and Ru-O layer in their "bulk" regions. A similar result also emerges in the intensity profile of the SRO thin film in Figure 4-3(c). It illustrates that the interface may not be uniformly-terminated, but keeps unchanged during the patterning process. The terminations at the interface involve intricate and non-trivial phenomena that affect the overall band structures in oxide heterostructures.[190, 191]

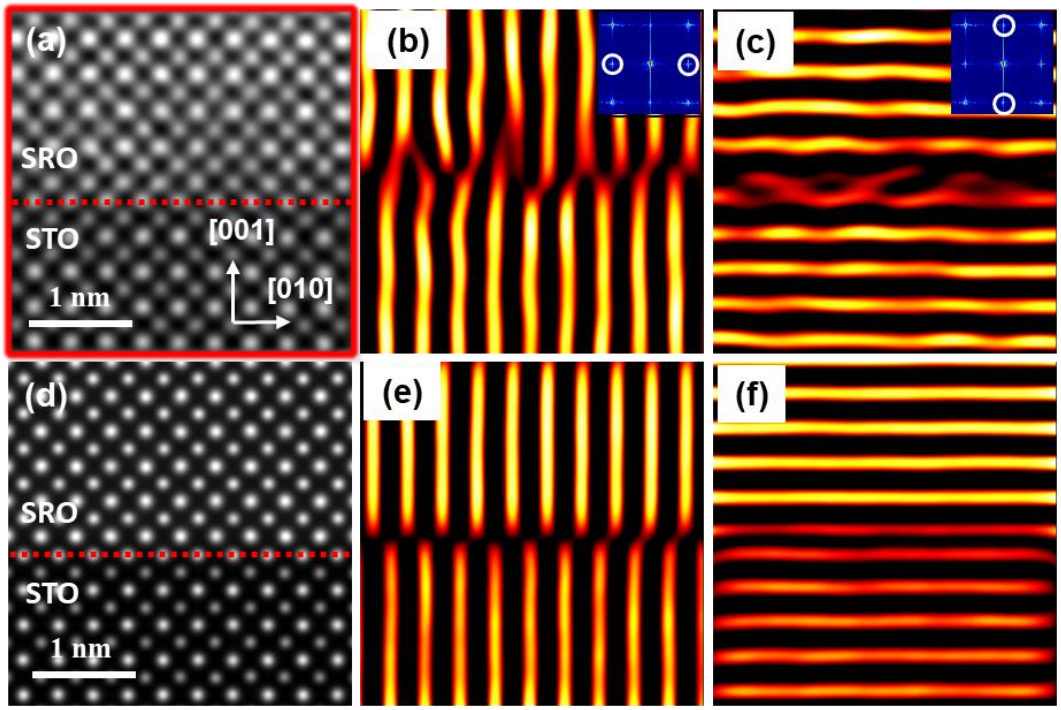

Figure 4-10. The sharpness of the interface between SRO and STO. (a) The HAADF-STEM image of a 10 uc × 10 uc zone at the interface between SRO and STO. The red dotted line denotes the interface. (b), (c) corresponds to the inverse fast Fourier transform (FFT) image with the reflections of (010) and (001), respectively. The inset in (b) and (c) are the FFT image of (a), where the white circles indicate the selected reflections. (d) The corresponding simulated image of (a) in case that the interface is uniformly-terminated. (e) and (f) correspond to the inverse FFT image of (d) with the reflections of (010) and (001), respectively.

To study the sharpness of the interface in more detail, the inverse FFT image of the experimental and simulated HAADF image of the interface are compared in Figure 4-10. For the inverse FFT images with the reflection of (010) in Figure 4-10(b) and (e), the bright lines represent the RuO plane in the upper SRO part and SrO plane in the bottom STO part. The bright lines in Figure 4-10(e) are uniformly terminated at the interface between SRO and STO. However, in Figure 4-10(b), the bright lines extend to both sides of the interface, revealing that the interface in the experiment may not be atomically sharp, where minor intermixing may occur. A similar message can be obtained from the inverse FFT images with the (001). reflection. The two lines close to the interface in Figure 4-10(c) are not as straight as those of Figure 4-10(f). Since the grown SRO thin films have a surface terrace structure with the height of about one unit cell, the projected STEM image may include the terrace, which then deviates from a sharp interface.

Figure 4-11 displays a STEM-EELS study of the elemental distribution around the interface between SRO and STO in 30 nm-sized SRO AAs at the atomic scale. The experimental HAADF-STEM image is shown in Figure 4-11(a). The Sr-L_3 map (Figure 4-11(b)) visualizes the homogeneous distribution of Sr around the interface. The Ti-$L_{2,3}$ (Figure 4-11(c)) and Ru-$L_{2,3}$ (Figure 4-11(d)) maps indicate the region of STO and SRO, respectively. The signal intensities of the first TiO monolayer and the first RuO monolayer close to the interface seem to drop, revealing a weak intermixing of Ti and Ru signals around the interface. The composite image (Figure 4-11(e)) of Sr-L_3, Ti-$L_{2,3,}$ and Ru-$L_{2,3}$ maps show a direct visualization of the elemental distribution around the interface. When plotting the signal intensity profiles of Ru and Ti around the interface in Figure 4-11(f), we find that the cationic intermixing between Ru and Ti occurs at a width of one unit cell on both sides of the interface, showing the same interfacial chemical distribution as the interface of SRO thin films (See Appendix A). STEM-EELS results are in good agreement with the inverse FFT analysis. Similar results have been reported at the interface of PLD-grown STO-SRO superlattices.[192]

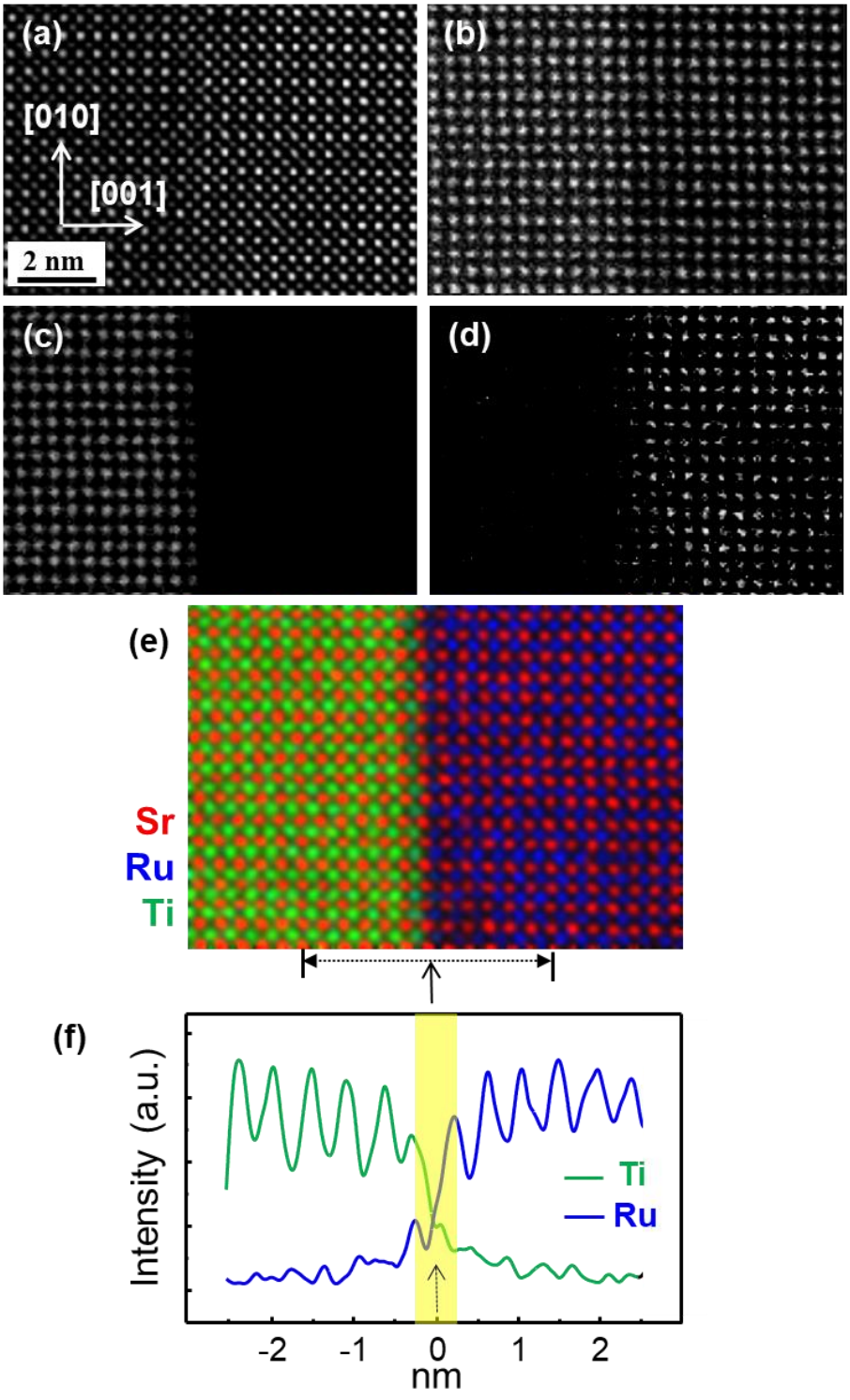

Figure 4-11. Elemental distribution at the interface. (a) the HAADF-STEM image of one region close to the interface. Elemental maps for (b) Sr from Sr-$L_{2,3}$ edge signal, (c) Ti from Ti-$L_{2,3}$ edge signal and (d) Ru from Ru-$L_{2,3}$ edge signal. (e) The composite map with Sr (red), Ru (blue) and Ti (green). (f) The corresponding signal intensity of Ti and Ru in the interfacial region. The yellow shaded region indicates the interdiffusion of the Ti and Ru signals.

STEM investigations show that the interfacial structure and chemical distribution at the interface are the same for SRO thin films and the AAs with different diameters, demonstrating that the interfacial chemical distribution is not responsible for the observed magnetic Curie temperature variation.

4.6 Quantitative study of strain fields

Due to the lattice mismatch between SRO and STO, epitaxially grown SRO layers naturally yield strain fields, which are crucial for their physical properties. As discussed above, by naked-eye observation of HAADF-STEM images, there exists no apparent difference between the SRO thin film and patterned AAs. However, quantitative analysis of the HAADF images can highlight subtle variations and extract more detailed information out of images. Here, STEM-based GPA has been used for determining the strain fields by measuring interatomic distances.[124] This method not only enables to visualize the 2-dimensional strain distribution in thin films and AAs, but also allows to calculate the strain filed on the nanoscale resolution.[125] The in-plane and out-of-plane strain states are analyzed with the lattice constants of STO substrates as the reference.

Figure 4-12 shows the strain fields of an unpatterned SRO thin film grown on a (100) STO substrate. The color scales in the SRO part and STO part are different in the out-of-plane strain map (Figure 4-12(b)), but remain unchanged in the in-plane strain map (Figure 4-12(c)). The horizontally averaged intensity profiles are displayed in the right panel of strain maps. It shows that the lattice constant in the in-plane direction does not change across the interface, while, for the out-of-plane direction, it is elongated by a constant value of ≈ (1.4 ± 0.3) % compared to STO. The strain results demonstrate that the STO substrate fully strains the SRO thin film.

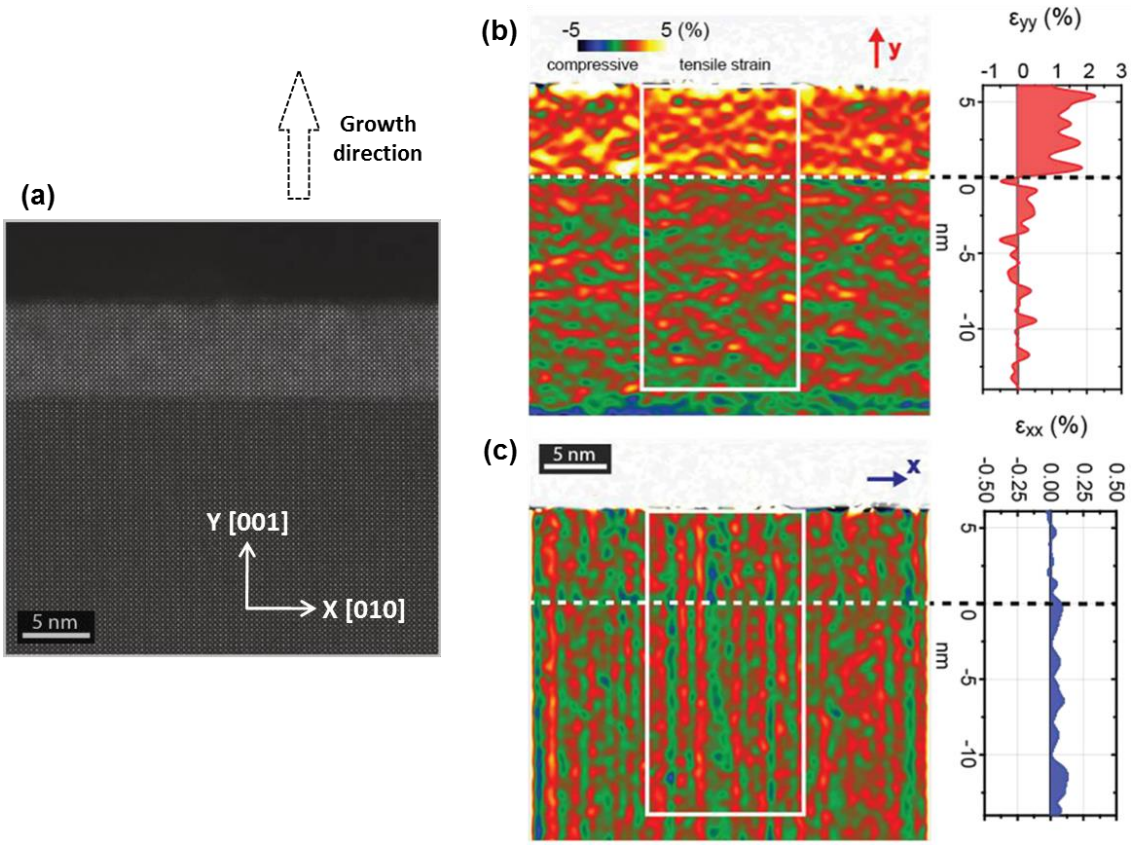

Figure 4-12. The strain fields of an unpatterned SRO thin film. (a) The HAADF-STEM image of the cross-section of the unpatterned SRO thin film. (b) and (c) correspond to the out-of-plane ε_{yy} and in-plane ε_{xx} components of the strain obtained from STEM-based GPA. The graphs on the right side are extracted from the horizontally averaged regions marked by the boxes.

Figure 4-13 shows the strain fields of a patterned AA with a diameter of 80 nm. The color scale in the in-plane (Figure 4-13(c)) strain map looks the same to that of the thin film (Figure 4-12(c)). However, the corresponding intensity profile in the right panel appears different. It shows that the in-plane lattice constant of SRO increases gradually while moving away from the interface. The strain value reaches 0.35 ± 0.10 % at 8 nm away from the interface. For the out-of-plane direction, the lattice elongation is not constant like the thin film anymore, showing a maximum of the elongation close to the interface. The elongation drops as moving away from the interface, resulting from the in-plane lattice relaxation.

Figure 4-14 displays the strain fields of a patterned AA with a diameter of 30 nm. Compared with the 80 nm-sized AA, the lattice elongation in the out-of-plane direction (Figure 4-14(b)) reduces more swiftly and the in-plane lattice (Figure 4-14(c)) has a stronger and faster relaxation. In the out-of-plane direction, the strain in the first two unit cells of SRO at the interface is similar to that of the film. It then decays quickly together with the in-plane strain to approach a three-dimensionally relaxed structure close to the surface. Similar mechanisms have been reported in patterned semiconductor nanostructures, *e.g.*, in Si,[193] InGaN/GaN,[194] or (Ga, Mn)As[195]. The in-plane strain value reaches 0.75 ± 0.10 % at 8 nm away from the interface, matching fully relaxed SRO.

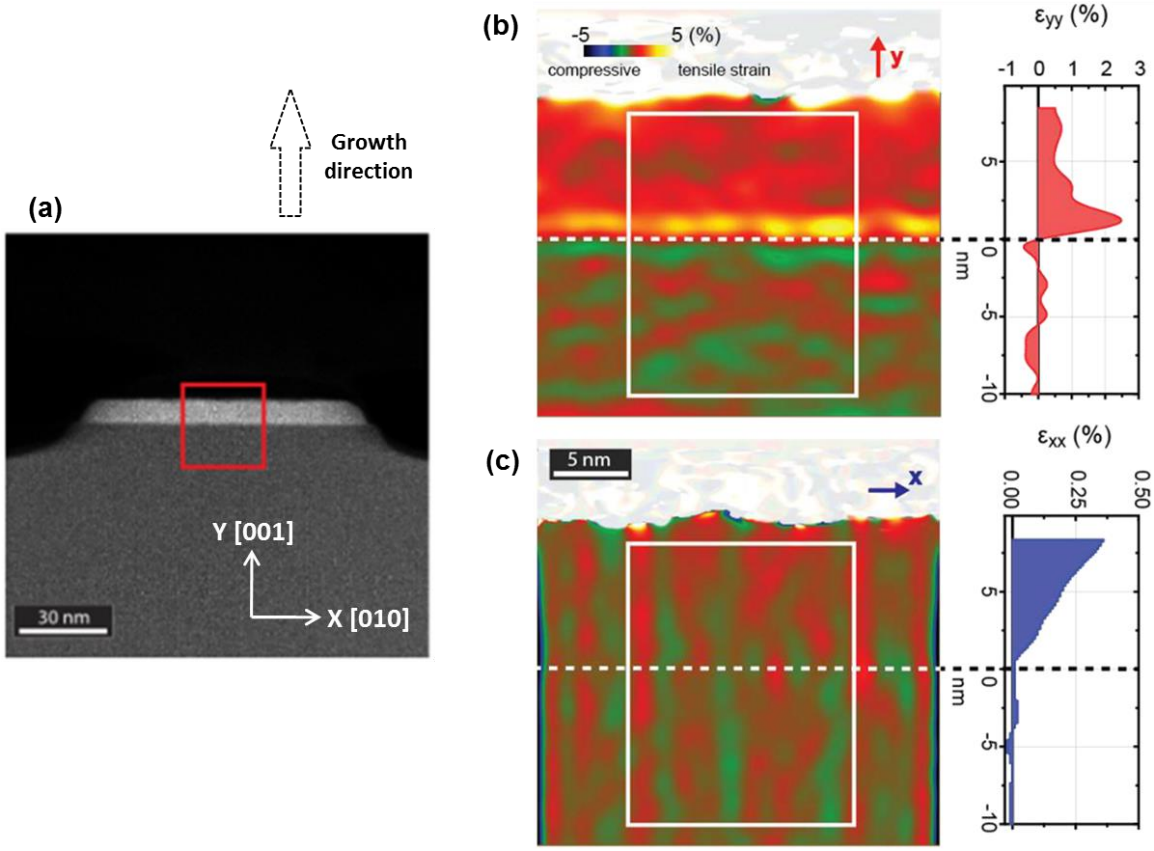

Figure 4-13. The strain fields of the AA with a diameter of 80 nm. (a) The HAADF-STEM image of the cross-section of the 80 nm-sized AAs. (b) and (c) correspond to the out-of-plane ε_{yy} and in-plane ε_{xx} components of the strain in the central region of the AA (red rectangle) obtained from STEM-based GPA. The graphs on the right-side graphs are extracted from the horizontally averaged areas marked by the boxes.

I unambiguously demonstrate that the patterning process relaxes the misfit strain and changes the structure of SRO layers through a quantitative analysis of HAADF-STEM images of samples. Except for the above-mentioned strain analysis of unpatterned films, 80-nm sized AAs, and 30 nm-sized AAs, I also analyzed further samples, *e.g.*, 500 nm-sized and 200 nm-sized AAs. The strain relaxation for all samples is summarized and displayed in Figure 4-15. Since previous work has proved that the magnetic properties of SRO are closed-related to the strain states[196-198], the observed Curie temperature variation in Figure 4-7 is linked to the patterning-induced misfit-strain relaxation. Zone ①: SRO thin films to 500 nm-sized AAs. The strain keeps almost unchanged, resulting in the same T_C value. Zone ②: AAs with diameters from 500 nm to 30 nm. The degree of the strain relaxation of SRO increases with the shrinkage of the sizes of AAs, leading to the increment of T_C values. Zone ③: AAs with a diameter below 30 nm. For AAs with a diameter

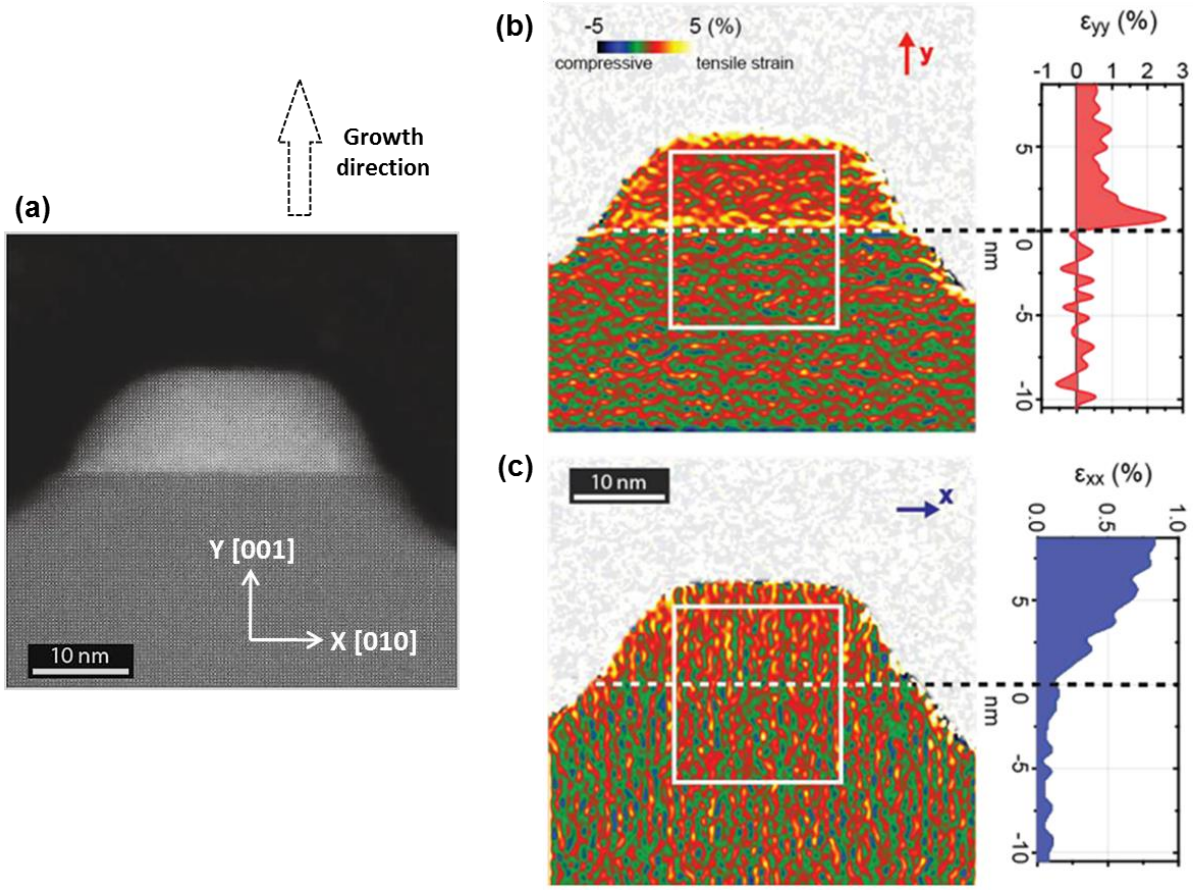

Figure 4-14. The strain fields of the AA with a diameter of 80 nm. (a) The HAADF-STEM image of the cross-section of the 30 nm-sized AAs. (b) and (c) correspond to the out-of-plane ε_{yy} and in-plane ε_{xx} components of the strain obtained from STEM-based GPA. The graphs on the right side are extracted from the horizontally averaged regions marked by the boxes.

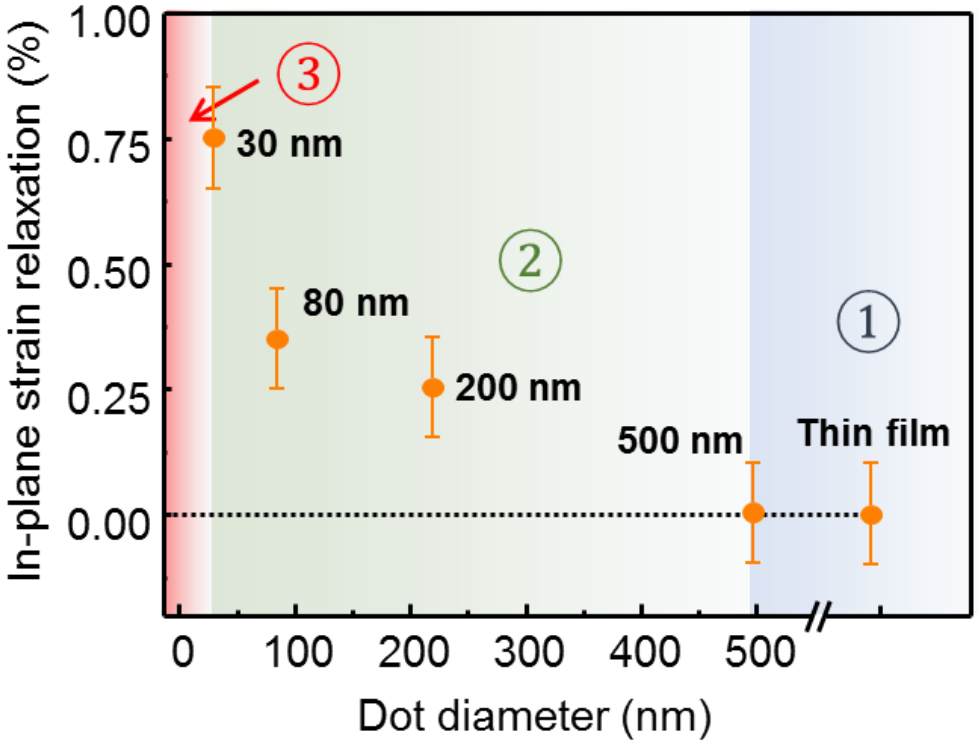

Figure 4-15. The in-plane strain relaxation of the patterned SRO thin films and the patterned array of the AA of different diameters (500 nm, 200 nm, 80 nm, 30 nm). The strain values are extracted from the region that is 8 nm away from the interface.

below 30 nm, the strain states are the same and not responsible for the T_C variations. The effects of the surface defect and dead layer become more predominant as the AAs become smaller, causing the decrease of the T_C.

4.7 Quantitative study of the lattice anisotropy and oxygen octahedral rotation

The orientation of the magnetic easy axis is closely related to the magnetic anisotropy, which could be caused by multiple contributions, *e.g.*, magnetocrystalline anisotropy, shape anisotropy, stress anisotropy, and exchange anisotropy.[199] For AAs with a complicated shape, a non-uniform crystal lattice, and interactions with each other, a thorough understanding of rotations of the magnetic easy axis would be challenging. Nevertheless, SRO belongs to the hard magnetic materials with an extremely high intrinsic anisotropy energy, making the analysis more straightforward than expected. The magnetocrystalline anisotropy is assumed to be the dominating factor for easy-axis rotation in the AAs system. The patterning-induced strain relaxation may modify the magnetocrystalline anisotropy from two perspectives: the lattice anisotropy and oxygen octahedral rotation, which can be studied through quantitative analysis of high-resolution STEM images.

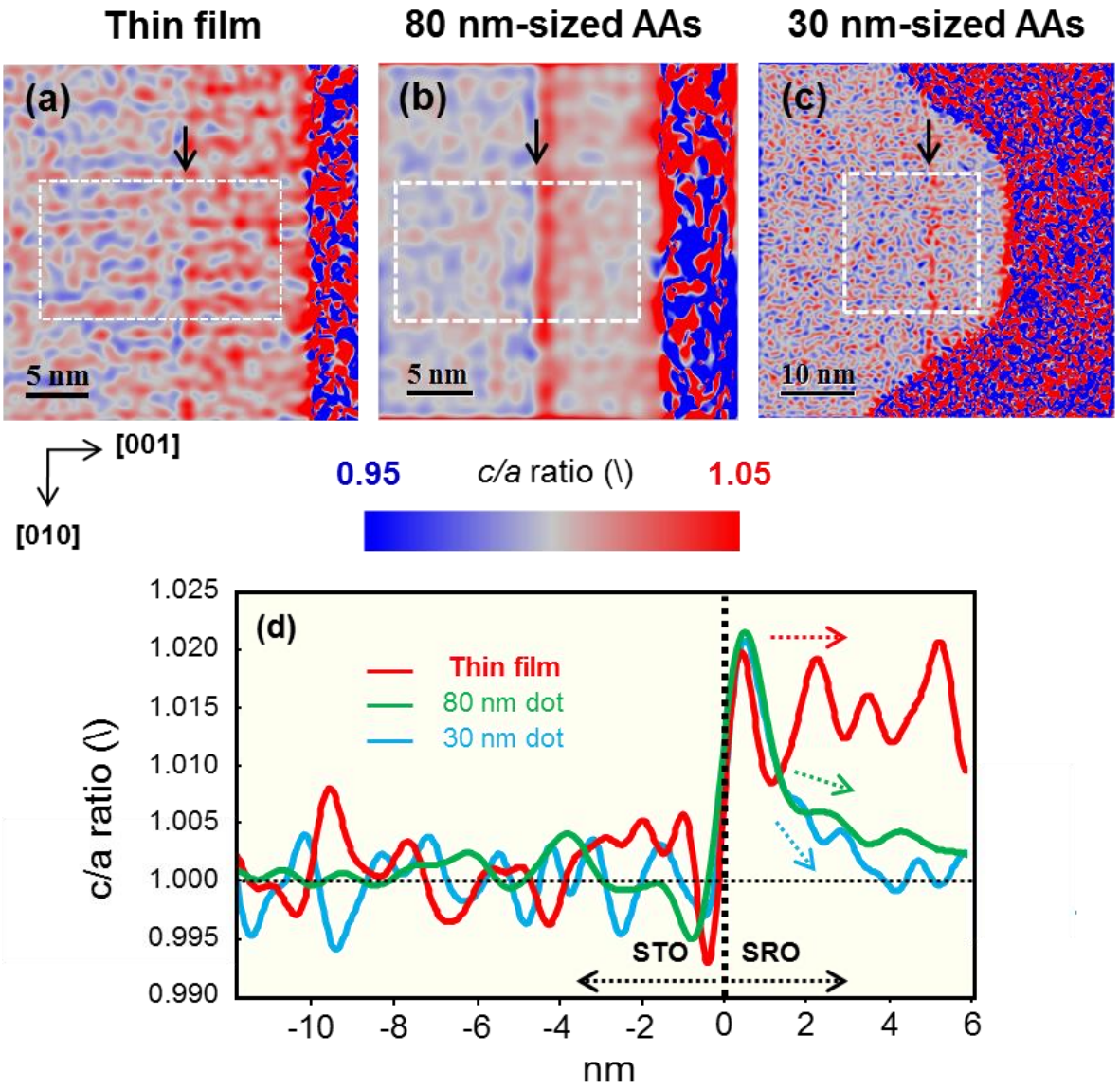

Figure 4-16. The lattice anisotropy (*c/a*) of samples. (a) The 2D *c/a* map of the unpatterned SRO thin film. (b) The 2D *c/a* map of the 80 nm-sized AAs. (c) The 2D *c/a* map of the 30 nm-sized AAs. The vertical arrows denote the interface between SRO and STO. (d) The vertically averaged *c/a* values of the regions are marked by boxes.

The obtained interatomic distances in the in-plane (*a*) and out-of-plane directions (*c*) enable us to study the lattice anisotropy (*c/a*) of materials. The 2D *c/a* maps of the unpatterned SRO thin film, the 80 nm-sized AAs, and the 30 nm-sized AAs are displayed in Figure 4-16(a), (b), and (c) with the same color scale, respectively. In the SRO part of unpatternted thin films, the color is evenly distributed red. In contrast, the red color in AAs has the maximum intensity for SRO close to the interface. Concrete speaking, the plots in Figure 4-16(d) describe that the *c/a* value is 1 in STO substrates for all samples. In the SRO part, the *c/a* value is identical, with a magnitude of 1.015 ± 0.005 in thin films. The *c/a* value attains the maximum in the SRO part close to the interface. Moreover, it gradually drops as moving away from the interface toward the surface in AAs. The smaller the AA size, the faster the *c/a* value decrease. Since the geometry phase analysis of STEM images has a spatial resolution on the nanometer scale, this method is not adequate to address the interfacial conditions at the atomic scale. It is necessary to study *c/a* value at interfaces at the atomic resolution.

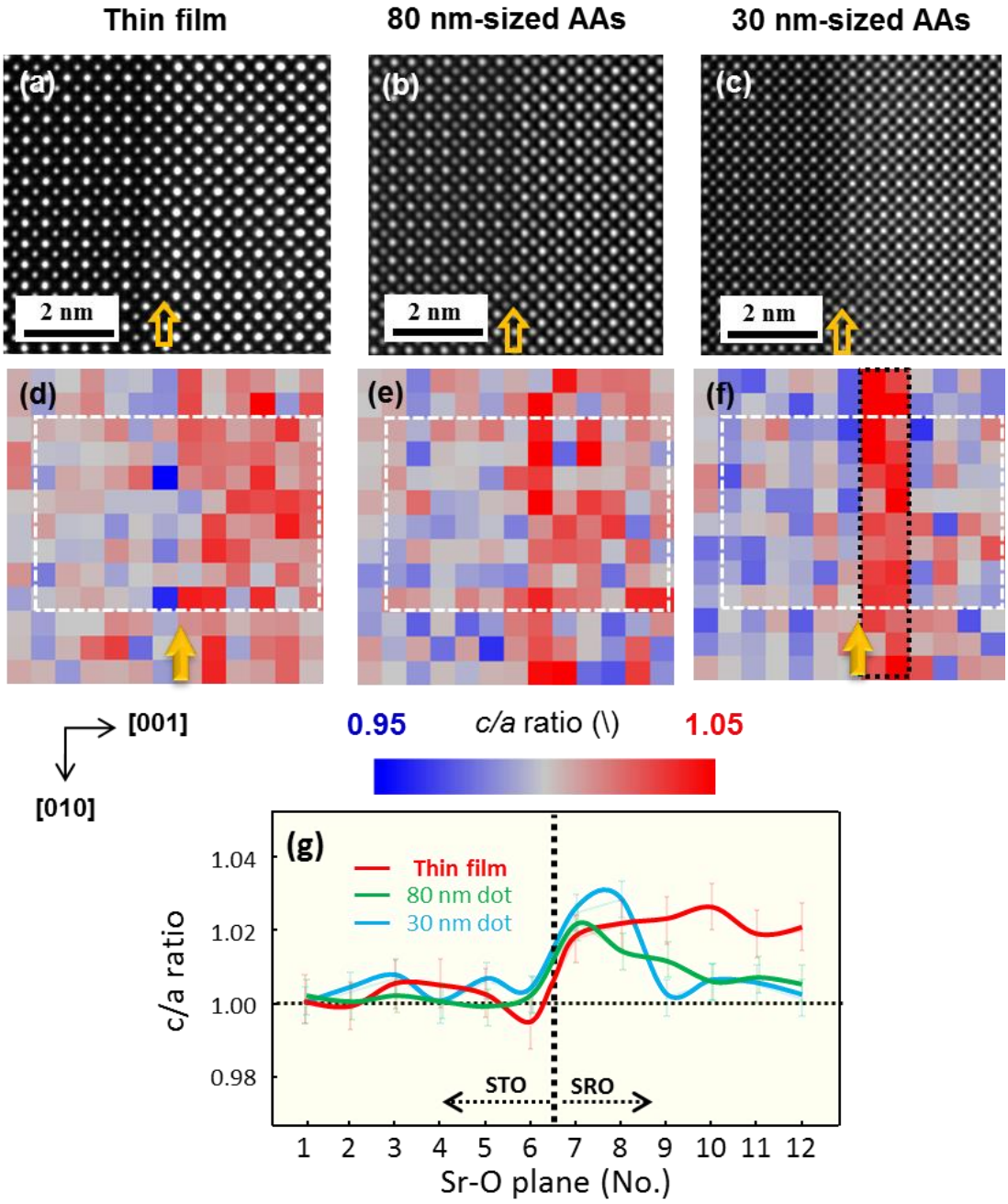

Figure 4-17. The atomically resolved lattice anisotropy (*c/a*) of interface regions. (a-c) correspond to the HAADF-STEM images of the unpatterned SRO thin film, the 80 nm-sized AAs and the 30 nm-sized AAs, respectively. Images are denoised using a bandpass filter. (d-f) represent the 2D *c/a* maps of the unpatterned SRO thin film, the 80 nm-sized AAs and the 30 nm-sized AAs, respectively. (g) The vertically averaged *c/a* values of the regions marked by white boxes.

The atomic columns of HAADF-STEM images around the interface were fitted by Gaussian functions and their coordinate positions can, therefore, be determined.[126] The fitting results allow us to calculate the interatomic distances at atomic resolution. Figures 4-17 (a-c) show the interfacial HAADF-STEM images of the unpatterned SRO thin film, the 80 nm-sized AAs and the 30 nm-sized AAs. The images are denoised by a bandpass filter to improve the fitting efficiency. The calculated 2D *c/a* maps are displayed in Figures 4-17 (d-f), where one pixel corresponds to one unit cell. They convey similar information with

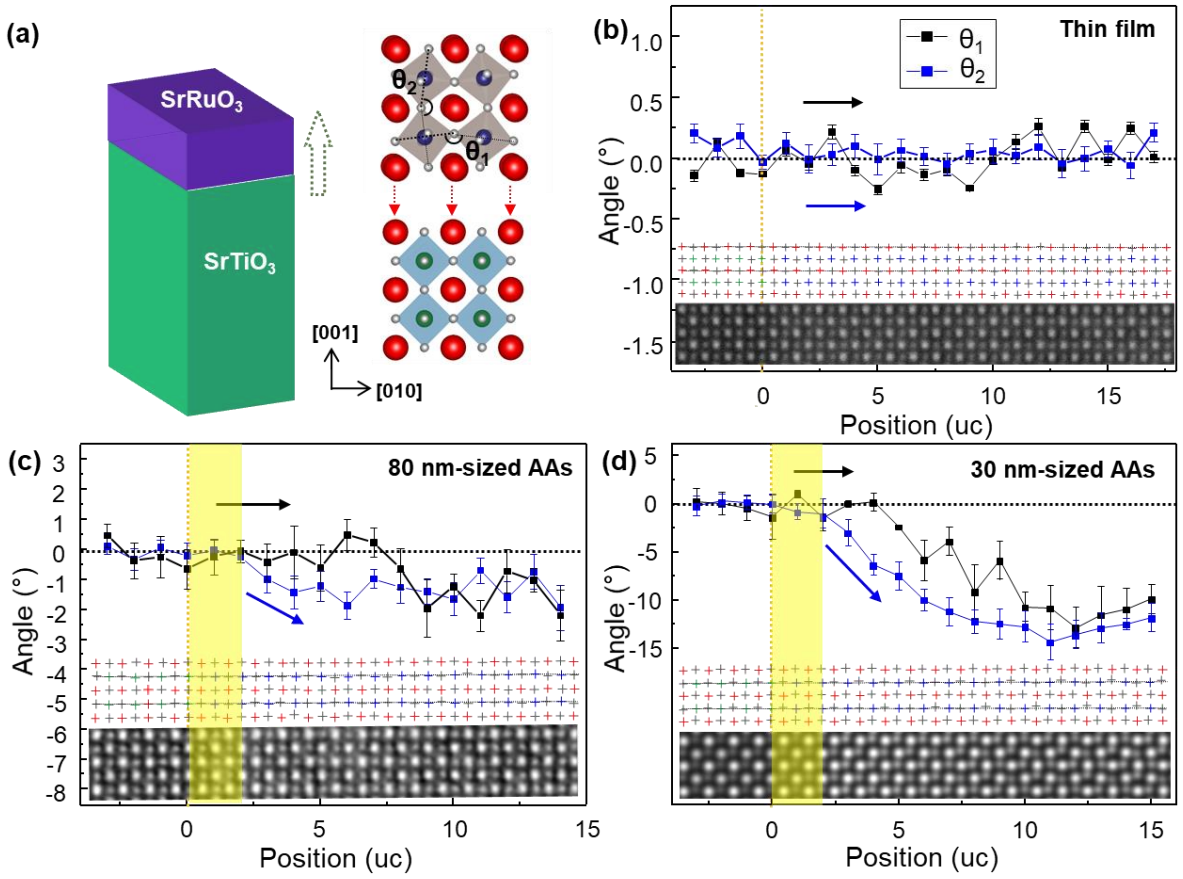

Figure 4-18. Oxygen octahedral rotation in the SRO layer. (a) The sketch of the SRO/STO heterostructure (left panel) and the epitaxial growth of pseudocubic SRO on cubic STO (right panel). θ_1 and θ_2 represents the rotation angle along in-plane [010] and out-of-plane [001], respectively. (b), (c), (d) correspond to the rotation angles of the unpatterned SRO thin film, 80 nm-sized AAs and 30 nm-sized AAs. The insets are the inversed ABF images of the lattice structures denoised using a bandpass filter, and their fitted coordinate positions of Sr (red), Ti (green), Ru (blue), and O (grey).

the 2D *c/a* maps in Figure 4-16. Nevertheless, the interfacial *c/a* value is presented unit cell by unit cell. The *c/a* value is nearly identical at the SRO part of thin films with a magnitude of 1.02 and gradually decreases as moving away from the interface for 80 nm-sized AAs. The *c/a* value of the 30 nm-sized AAs only rises in the first two unit cell and quickly decreases to 1. It indicates that the overall magnetic moment tends to orient towards in-plane direction as the size of AAs becomes smaller, inducing the observed rotation of the magnetic easy axis.

The coordinate positions of the oxygen columns can additionally be extracted by Gaussian fitting of ABF images. In order to make a comprehensive understanding of the octahedral rotation, the STEM analysis was performed along two different orientations. Figures 4-18(a) shows the sketch of the SRO/STO heterostructure. Due to the difference of symmetry between SRO and STO, the rotation of oxygen octahedra in SRO couples with the epitaxial strain imposed by the STO substrate. As indicated in the right panel of Figures 4-18(a), the angles θ_1 and θ_2 couple with in-plane strain and out-of-plane strain, respectively. Figures 4-18(b), (c), (d) correspond to the rotation angles of the unpatterned SRO thin film, the 80 nm-sized AAs and the 30 nm-sized AAs. For the unpatterned SRO thin film, the angles θ_1 and θ_2 remain unchanged in SRO at a value of 180°, because SRO lattices are fully strained by the STO substrate. The rotation of oxygen octaheda appears in SRO part of the patterned AAs due to the strain-relaxation effect. The angle θ_1 deviates from 180° as moving away from the interface. Since the in-plane strain

relaxation is more prominent in small AAs, the corresponding octahedral rotation in 30 nm-sized AAs is more obvious than in 80 nm sized ones. The angle θ_2 also deviates from 180° after the second unit cell of SRO in AAs, which fits with the trend of the out-of-plane strain relaxation. The distortion of oxygen octahedra in SRO can alter the orientation of the magnetic moment and thus control the magnetic anisotropy of the SRO layer. Interestingly, the presented results show that the oxygen octahedra of the first 2 SRO monolayers are too robust to be changed by the patterning process.

4.8 Summary and conclusions

In summary, SRO AAs were fabricated to the diameter ranging from several hundred nanometers down to 15 nm by using *e*-beam lithography of high-quality SRO thin films. XRD and STEM investigations verified the single crystalline structure of the SRO layers, which still keep a high quality without any visible defects after the patterning process. The heterointerface between SRO and STO is found to have minor mixing between Ru and Ti in 1 uc at both sides of the interface.

SRO shows ferromagnetism even in the smallest AAs. The M (T) measurement reveals that the magnetic properties are enhanced for AA sizes below 500 nm and the Curie temperature depends on the size of the AAs, increasing gradually from 149 K in thin films and AAs larger than 500 nm to 157 K at 30 nm AA size. The STEM-based strain analysis unambiguously demonstrate that the misfit strain of SRO is gradually relaxed as the size of AAs shrinks. This strain relief is attributed to the removal of lateral constraint around the AA, which is responsible for the variation of Curie temperature. The strain environment is the same for AAs with a size smaller than 30 nm, where the Curie temperature variation is mostly owing to the surface defects and dead layer.

The M (B) measurement unveils that the magnetic easy axis of SRO rotates from an angle close to the out-of-plane direction in thin films towards the in-plane direction as the size of AAs decreases. STEM results indicate that the easy axis rotation is attributed to the changed lattice anisotropy and oxygen octahedral rotation due to the strain relaxation in AAs. This work paves a pathway to tune the magnetic properties of the material by lithography.

Contributions to this chapter:

Hongguang Wang carried out the TEM specimen preparation, TEM data acquisition, and TEM-related data processing. Part of this chapter has been published in Ref.[144]. Gennadii Laskin (MPI-FK) performed the fabrication of the AAs, XRD test, AFM measurement, and magnetic measurement. Hans Boschker (MPI-FKF) contributed to the discussion part of this chapter. Peter A. van Aken (MPI-FKF), Jochen Mannhart (MPI-FKF) supervised and oversaw this work. The work in this chapter also got support during TEM sample preparation by Ute Salzberger (MPI-FKF) and Marion Kelsch (MPI-FKF), and the TEM support by Vesna Srot (MPI-FKF), Yi Wang (MPI-FKF), Kersten Hahn (MPI-FKF) and Peter Kopold (MPI-FKF).

Chapter 5. Charge Accumulation at $SrMnO_3/SrTiO_3$ Interfaces*

5.1 Abstract

The last three decades have seen a growing trend towards studying the interfacial phenomena in complex oxide heterostructures. Of particular concern is the charge distribution at interfaces, which is a crucial factor in controlling the interface transport behavior. The study of the charge distribution is very challenging due to the limitation in characterization techniques and the complexity at interfaces. Here, by a combination of aberration-corrected STEM and spectroscopy techniques, I identify the charge accumulation on the SMO side of SMO/STO hetero-interfaces and find that the charge density attains the maximum of 0.13±0.07 e^-/unit cell (uc) at the first SMO monolayer. Based on quantitative atomic-scale STEM analyses and first-principle calculations, I explore the origin of interfacial charge accumulation in terms of epitaxial strain-favored oxygen vacancies, cationic interdiffusion, interfacial charge transfer, and space-charge effects. This study, therefore, provides a comprehensive description of the charge distribution and related mechanisms at the SMO/STO hetero-interfaces, which is beneficial for the functionality manipulation *via* interface engineering.

Graphical abstract: Electronic charge density together with interfacial epitaxial strain and cationic interdiffusion

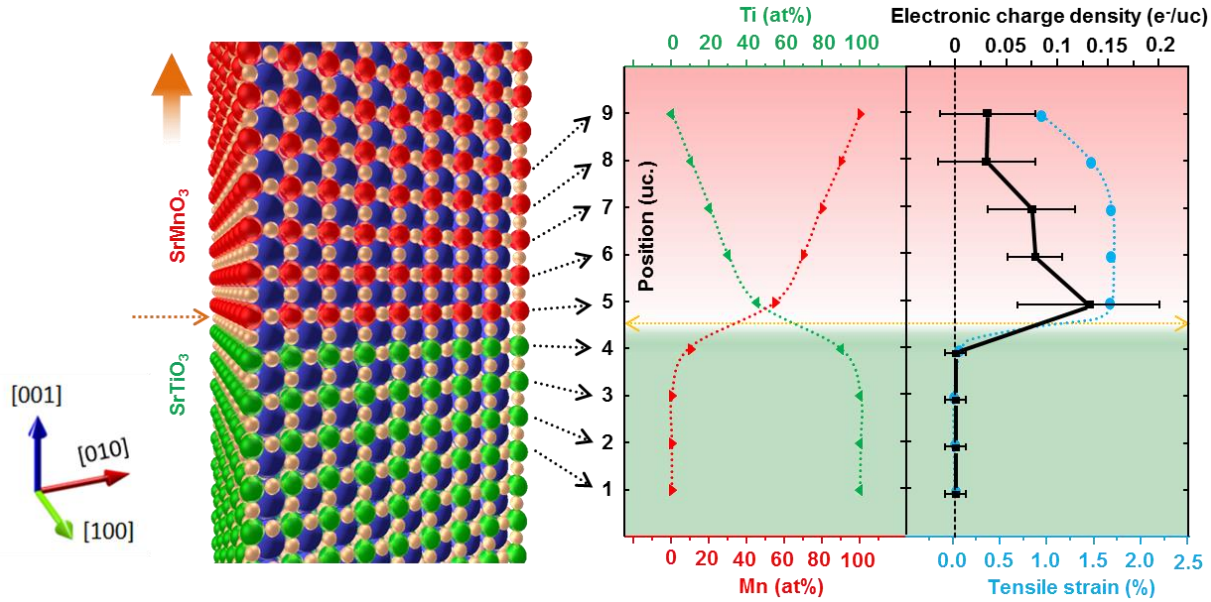

*This chapter has been accepted for the publication in *ACS Nano*.

5.2 Introduction

Hetero-interfaces in complex metal oxides promote unprecedented physical phenomena that are not found in their bulk constituents due to the often-cited interplay of charge, spin, orbital, and lattice degrees of freedom.[13, 52, 200-202] One of the cornerstone mechanisms is the charge distribution at a hetero-interface.[13, 203, 204] Previous researchers have demonstrated that the concentration and distribution of charge can produce intriguing phenomena, *e.g.*, enhanced ionic conductivity,[205] metallicity,[42] two-dimensional electron gases (2DEGs),[15, 206] and ferromagnetism.[207] For example, the provoked charge transfer has been found to trigger a transition of the SMO heterostructure from a G-type antiferromagnetic state to a ferromagnetic state.[38, 208, 209] Therefore, a comprehensive understanding of the charge distribution and their formation mechanisms at the interface is necessary for engineering the functionalities of complex oxide heterostructures.

To date, many efforts have been devoted to figuring out the interfacial charge state and its impact on the properties of materials. However, this task is still technically challenging, (i) because the characteristic scale for oxide interfaces is at the nanometer level, which makes direct observation of interface effects demanding, and (ii) because structural rearrangements and chemical environments at oxide interfaces are very complex. Therefore, it is difficult to extract the interfacial charge conditions by bulk-based characterization techniques.[210] With the advancement of methodologies and instrumentation, analytical STEM has become a highly-suitable method to study the distribution of charges at the interface, because it can reveal the charge density and ordering at the atomic scale by EELS,[110, 134, 211-213] electron holography,[190, 214] and electron diffraction.[215-217] Recently, Gao *et al.* reported the visualization of the real-space charge density at sub-Angstrom resolution by four-dimensional STEM (4D-STEM).[218] However, there still does not exist a routine capability to measure the charge distributions at interfaces. Numerous studies have attempted to explore the charge environments at the interface of manganite heterostructures with STEM-based techniques. In a recent study, Cheng *et al*. identified, by core-loss EELS analysis, a new type of charge-ordering at an interfacial MnO layer, which contributes to the polarization of thin films.[219] Likewise, Garcia-Barriocanal and coworkers examined the charge density at a manganite/titanate (LMO/STO) interface and reported a charge-leakage process.[220] Meanwhile, researchers also succeeded in revealing the charge distribution on the atomic scale through quantifying high-resolution TEM images.[215-217, 221] However, most microscopic and spectroscopic studies were mainly focused on observations of the charge profiles and the induced properties. The formation mechanism and its association with the local structure and chemistry are still lacking clarification.

In this chapter, epitaxial SMO thin films were grown on TiO_2-terminated (001)-oriented STO substrates by PLD. By using aberration-corrected STEM, I studied the structure and chemistry of the SMO films at the atomic scale and found charge accumulation at the SMO side of the interface between SMO and STO. Using STEM-based observations and first-principle calculations, the underlying formation mechanism of charge accumulation are discussed, considering the oxygen vacancies, charge transfer, and interfacial space-charge effects. This study advances the understanding of the charge distribution at manganite interfaces, which is instructive for the fabrication of nano-devices by interfacial charge engineering.

5.3 Results and Discussions

5.3.1 Microstructure of $SrMnO_3/SrTiO_3$ thin films

AFM measurements performed directly after growth (Figure 5-1(a)) show a flat surface of the epitaxial SMO thin film devoid of cracks. However, surface cracks appear, when the surface morphology of the SMO thin film was again measured after more than 4 weeks, which is shown in Figure 5-1(b) and Figure 5-1(c). The vertical-averaged height profile in Figure 5-1(b) indicates the apparent fluctuation of the surface height, where the minima denote the positions of cracks. In contrast, the phase map in Figure 5-1(c) more clearly displays the surface cracks. Phase imaging highlights edges and is not affected by large-scale height differences, and could provide for more explicit observation of fine features, which

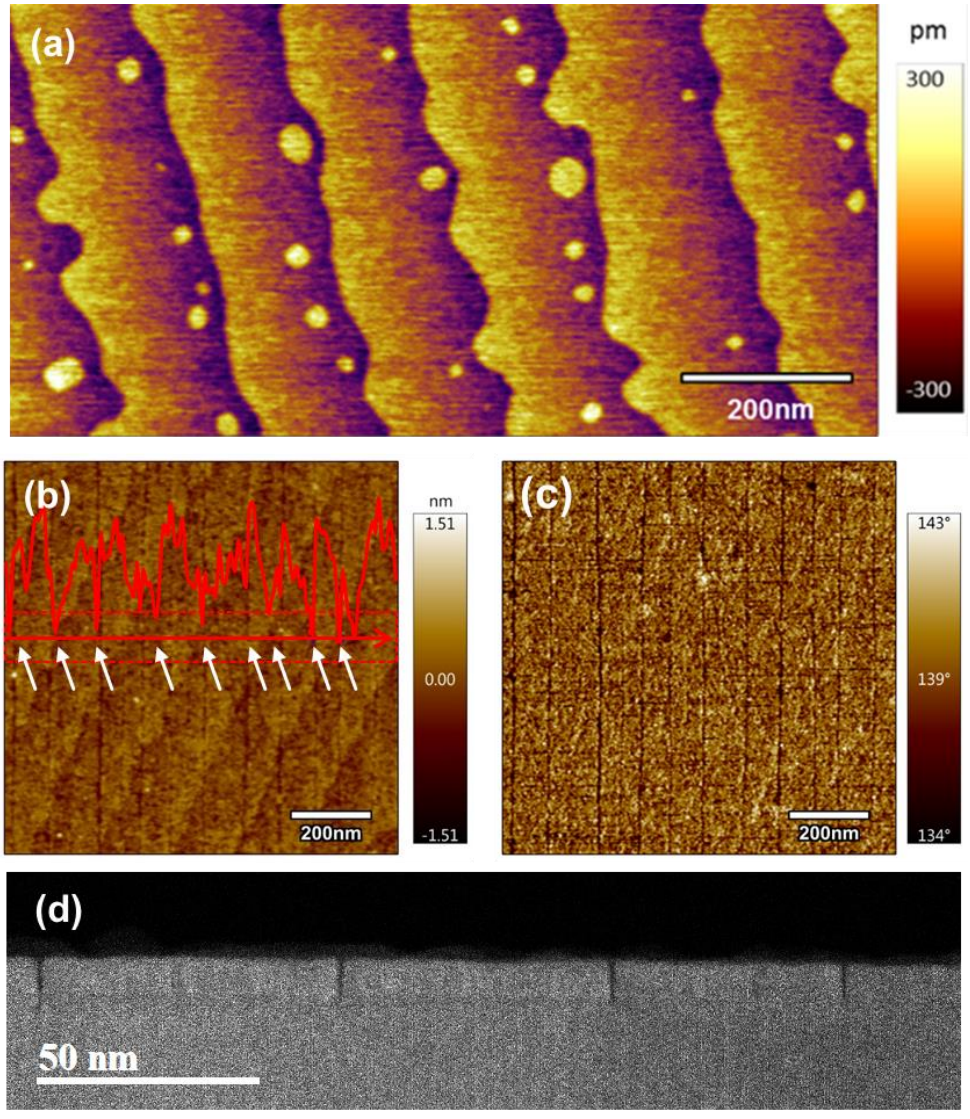

Figure 5-1. Surface morphology and low-magnification STEM images of a SMO/STO heterostructure. (a) Surface-height map of the epitaxial SMO thin film directly after growth. (b) Surface-height map of the SMO surface after more than 4 weeks. The inset is the vertical-averaged height profile. The white arrows mark the cracks. (c) The corresponding phase-retrace map. It shows that the cracks are straight and aligned with the edges of the substrate, which are along the [100] and [010] crystal-lattice directions. (d) Low-magnification ADF image of the cross-section of the SMO/STO heterostructure. It displays that cracks are distributed with similar spacing. The depth of the cracks is similar to that extend from the SMO surface to the interface region.

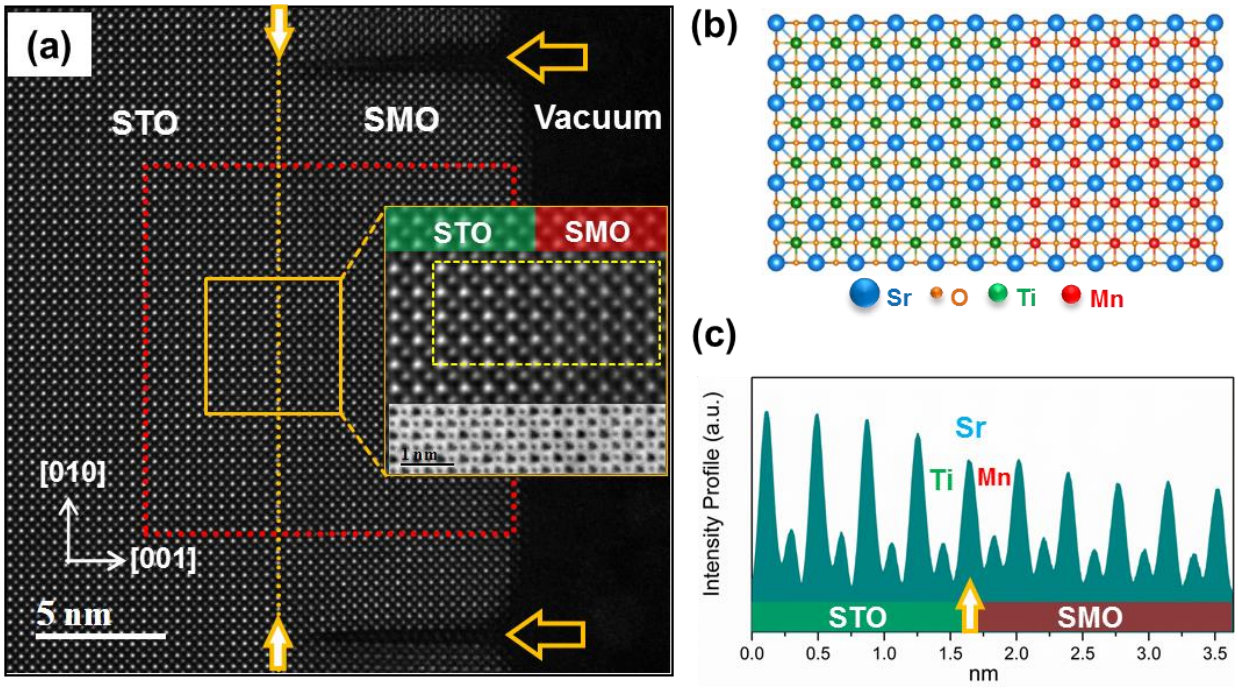

Figure 5-2. The microstructure of an epitaxial SMO thin film grown on the STO substrate. (a) Z-contrast HAADF-STEM image of an SMO/STO sample in cross-sectional orientation, projected along the [100] zone axis. The thickness of the SMO thin film is about 10 nm. The yellow dotted line marks the interface between SMO and STO. Horizontal arrows denote the location of cracks. The yellow box region is magnified and presented in the inset, where the upper part is a HAADF and the bottom part is an ABF image. The red square zone was used for strain analysis presented in Figure 3. (b) The schematic structure model of the SMO/STO interface. (c) Lateral intensity profile of the dotted box region in the inset of image (a), with the interfacial Sr column and the closest Mn and Ti columns marked according to the HAADF intensity variation.

can be obscured by a rough topography. The observed cracks are straight and aligned with the edges of the substrate, which are along the [100] and [010] crystal-lattice directions. A HAADF-STEM image at lower magnification (Figure 5-1(d)) shows several, nearly equidistant cracks in the SMO thin film, which is in good accordance with the above-mentioned AFM observations.

Figure 5-2(a) presents the microstructure of the epitaxial SMO/STO thin film in cross-sectional orientation, projected along the [100] zone axis. Two horizontal arrows denote the cracks appearing in the SMO thin film. The cracks are caused by the relief of epitaxial strain, which occurs during or after cooling the samples.[222] The areas between two cracks display a precise layer-by-layer stacking in the SMO thin film, as shown in HAADF and ABF images simultaneously acquired at higher magnification, where the SMO/STO hetero-interface appears coherent. All atomic columns, including the oxygen ones, are resolved. The corresponding structural model of the SMO/STO interface region is displayed in Fig. 5-2(b). The vertically integrated HAADF signal within the dotted yellow box in the inset of Figure 5-2(a) is presented in Fig 5-2(c). Since the signal intensity (*I*) of a HAADF image is proportional to the atomic number *Z* with $I = Z^{1.7}$,[223, 224] the nominal interface between SMO and STO can be identified accordingly and is marked by vertical arrows in Figure 5-2(a).

Based on the interfacial structural model in Fig. 5-2(b), the QSTEM code was employed to simulate the corresponding HAADF and ABF images in Figure 5-3. All atomic columns, including Sr, Ti, Mn, and O, are clearly shown. It is worth to note that, because of the small difference of the atomic number between Mn (Z=25) and Ti (Z=22), the difference of the contrast between Mn and Ti in Figure 5-3(a) is hard to distinguish by naked eye, which is in good agreement with the above-mentioned experimental results

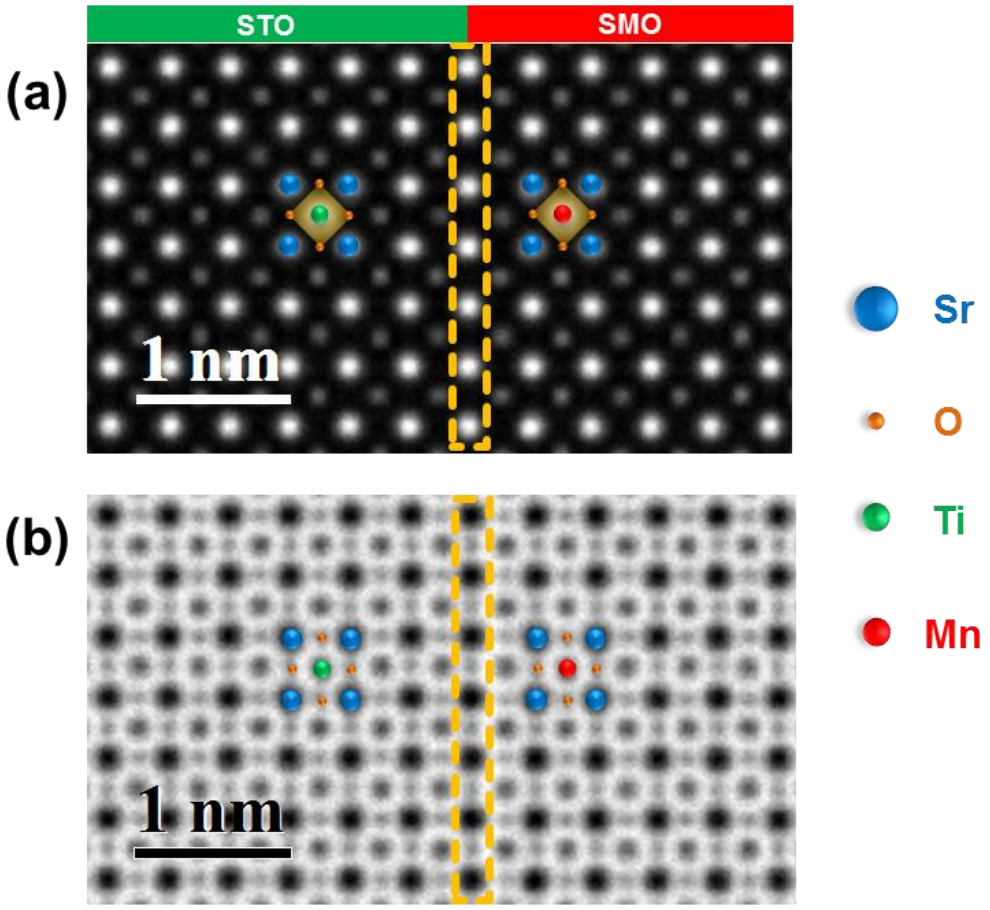

Figure 5-3. STEM-image simulation for the hetero-interface. (a) and (b) are simulated HAADF and ABF images for the schematic structure in Fig. 5-2(b), respectively. The yellow rectangles mark the interfacial Sr-O layer. The atomic columns for Sr, Ti, Mn, and O can be unambiguously distinguished in the simulated images.

(Figure 5-2). Since the interface structure model was not fully relaxed by ab-initio methods due to a too large number of atoms, the simulated images merely provide a good sanity check rather than a quantitative explanation.

5.3.2 Core-loss EELS at $SrMnO_3/SrTiO_3$ interfaces

The electronic structure at the interface was explored by investigating the O-K and Mn-$L_{2,3}$ ELNES of 9 unit cells across the hetero-interface (Figure 5-4). Measured positions are marked in Figure 5-4(a). Spectra 1-4 were acquired from the STO substrate and spectra 5-9 from the SMO thin film. The main maxima of the O-K edge are assigned to peaks *a*, *b* and *c*. Both Ti and Mn are surrounded by 6 O atoms in octahedral symmetry. Peak *a* of the O-K ELNES (Figure 5-4(b)) originates from the excitation of O 1*s* core electrons into unoccupied O p orbitals hybridized with Ti(Mn) 3d orbitals, which is sensitive to the 3*d* band occupancy.[31, 32] Peak *b* and *c* (Figure 5-4(b)) correspond to the hybridization of unoccupied O 2*p* orbitals with Sr 4*d* and Mn/Ti 4*sp* orbitals.[225, 226] Here, the intensity of pre-peak *a* becomes weaker than the one of the bulk SMO (dotted line), when approaching the interface from column 9 to column 5. Furthermore, a gradual decrease of the energy difference between peak *a* and *c* can be observed, while approaching the interface from spectrum 9 to spectrum 5. These observations imply a gradual reduction of the Mn valence due to an increase of the oxygen deficiency near the interface[227, 228, 114], which presumably results from an increased number of Mn 3*d* electrons due to a changed structure and local chemistry around the SMO/STO interface.

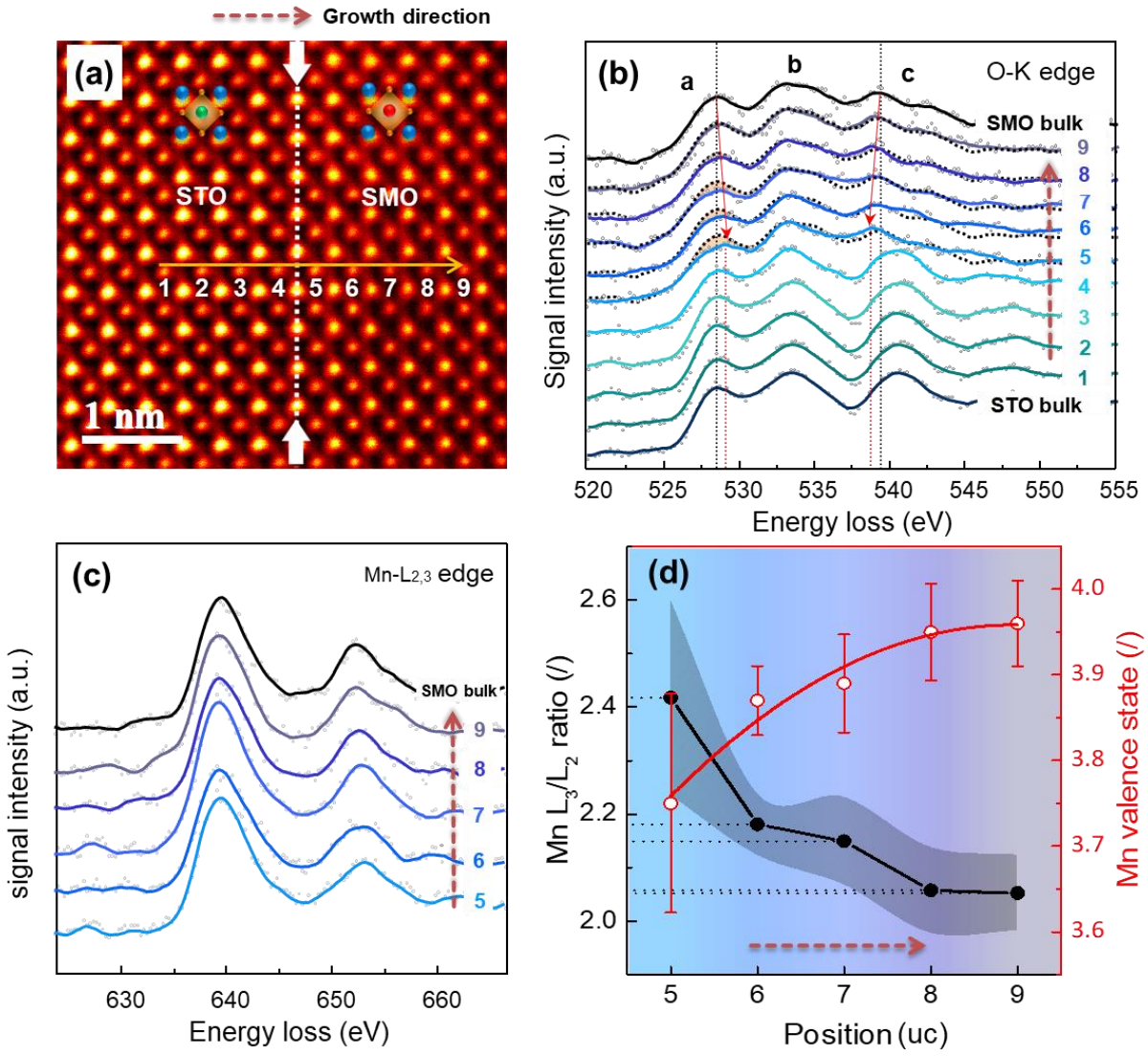

Figure 5-4. EELS fine structure at the hetero-interface. (a) Z-contrast HAADF image of the interface region. Numbers 1 to 9 indicate the Mn (Ti)-O atomic columns across the interface, where EELS spectra were extracted. The vertical arrows mark the interface between SMO and STO. (b) O-K edge spectra for locations 1 to 9 (shown in (a)) across the interface compared with O-K edge spectra from bulk STO and SMO (black dotted lines). The dotted vertical lines mark the positions of the peak a and peak c of O-K edge of the SMO close to the interface (red) and in the bulk state (black). (c) The Mn-$L_{2,3}$ white lines for positions 5 to 9. The dotted spectra in the background represent the raw data. The backgrounds of the O-K and Mn-$L_{2,3}$ spectra have been subtracted using a power law. For removing the noise from the spectrum profiles, the raw data are fitted using a Savitzky-Golay filter with a window size of 3 channels and a 2nd-order polynomial fit. (d) Mn L_3/L_2 intensity ratio (solid black circles) and the corresponding valence state (red open circles) as a function of Mn (Ti) positions (5 to 9 shown in (a)). The shaded region denotes the error bar for Mn L_3/L_2 intensity ratios.

Figure 5-4(c) shows the Mn-$L_{2,3}$ edges of the first 5 monolayers of SMO at the interface. The energy shifts for L_3 and L_2 peaks between different positions are not visible in the spectra, revealing that there could be no energy shift or the energy shift is too small to be resolved. Intensity ratios of the L_3 and L_2 peaks of the Mn-$L_{2,3}$ ELNES are calculated and plotted in Figure 5-4(d). From columns 5 to 9, the intensity ratios progressively decrease from ~2.42 to ~2.08, which are larger than the nominal value 2 for Mn^{4+}.[229] The valence states for Mn are calculated according to the Mn L_3/L_2 white-line intensity ratios[114, 229, 230] and plotted as the red profile in Figure 5-4(d). It shows that the mean Mn valence state gradually decreases when approaching the SMO/STO interface.

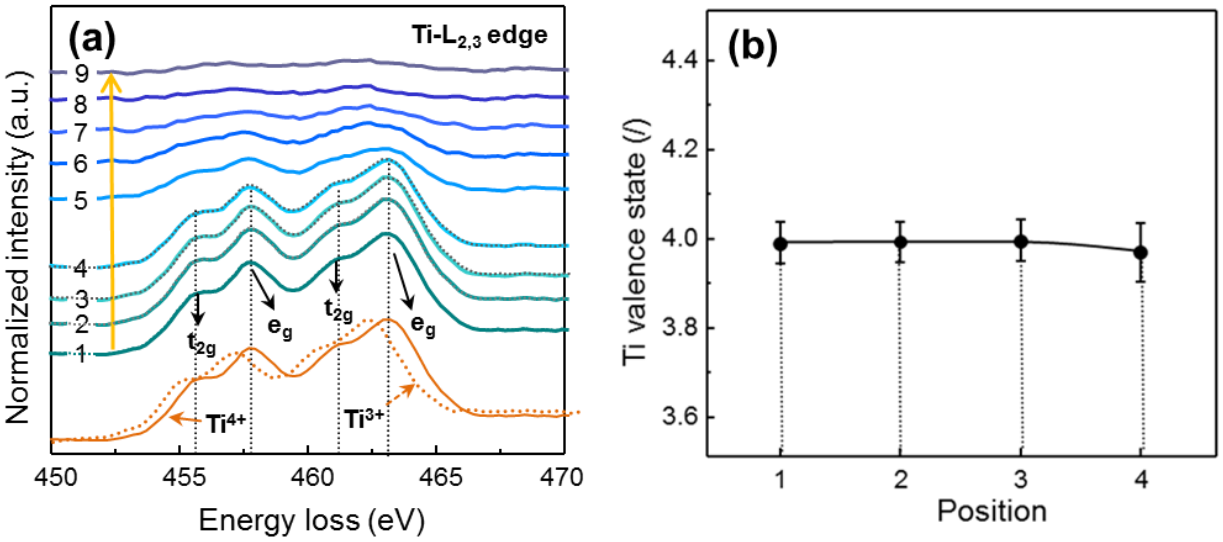

Figure 5-5. EELS analysis of Ti-$L_{2,3}$ edges. (a) The spectra of the Ti-$L_{2,3}$ edge in 9 atomic columns across the interface. (b) Valence states of Ti from columns 1 to 4 obtained by using the multiple linear least squares (MLLS) fitting approach with the reference spectra of Ti^{4+} and Ti^{3+}, indicating that the valence state of Ti remains unchanged on the STO side of the interface.

Figure 5-5(a) shows the Ti-$L_{2,3}$ edges at the SMO/STO interface. The energy shifts for L_3 and L_2 peaks between different positions are not visible. Furthermore, by using the MLLS fitting of the acquired spectra with the reference spectra of Ti^{4+} and Ti^{3+}, we can observe that the valence state of Ti in STO near the interface remains nearly unchanged (Figure 5-5(b,)).

The above-mentioned ELNES analysis of O-K edge, Mn-$L_{2,3}$ edges, Ti-$L_{2,3}$ edges demonstrate that, at the SMO/STO interface, the STO side is neutral and the SMO side is negatively charged. The electronic charges accumulate on the SMO side of the interface with a maximum electronic charge density in column 5. For probing the underlying mechanism for the observed charge accumulation, further investigations regarding the interfacial structure and chemistry will be presented in the following parts.

5.3.3 Strain fields close to $SrMnO_3/SrTiO_3$ interfaces

The misfit strain can dramatically change the charge distribution at the interface, and thus facilitate the emergence of novel phenomena.[231] To study the strain field around the SMO/STO interface, I apply GPA [124] to the atomically resolved HAADF image presented in Figure 5-6(a). Figure 5-6(b) and Figure 5-6(c) shows the 2D strain map along the out-of-plane and in-plane directions, respectively. All strain maps are produced using the g_1=(011) and g_2=($0\bar{1}1$) Fourier components. In the out-of-plane direction (Figure 5-6(b)), the apparent color contrast between the STO substrate and SMO thin film indicates a quick lattice relaxation owing to the free deformation along the growth direction. In contrast, the in-plane strain map in Figure 5-6(c) shows a gradual strain variation. By plotting the vertical-averaged intensity profiles of the 2D maps in Figure 5-6(d), we see that the in-plane strain of the SMO thin film is progressively relaxed with increasing distance from the interface (about 1.7%) towards the SMO surface. However, due to the lateral resolution limit of the GPA-based strain analysis (about 1.2 nm in this work),[125] the exact strain state of unit cells close to the interface is not discriminable anymore.

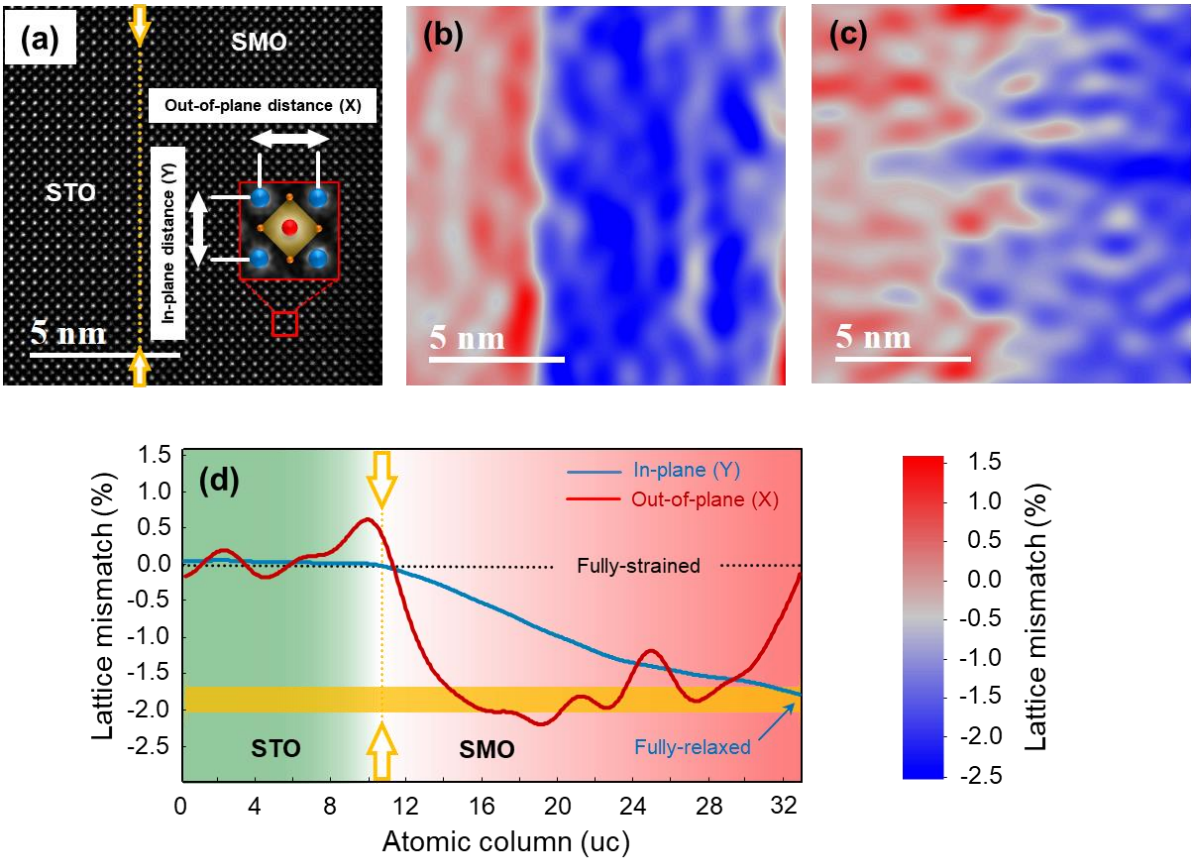

Figure 5-6. The strain state of the SMO thin film. (a) HAADF image of a region between two cracks. The hetero-interface is marked with a yellow dotted line. The box region is taken as the reference for the corresponding strain analysis. The in-plane and out-of-plane directions are defined in the inset. (b) Out-of-plane and (c) in-plane lattice mismatch for (a) with a spatial resolution of about 1.2 nm. The color bar for (b) and (c) is shown on the right side of (d). (d) Lateral intensity profile of the map (b) and (c) with a precision of 10^{-3}.

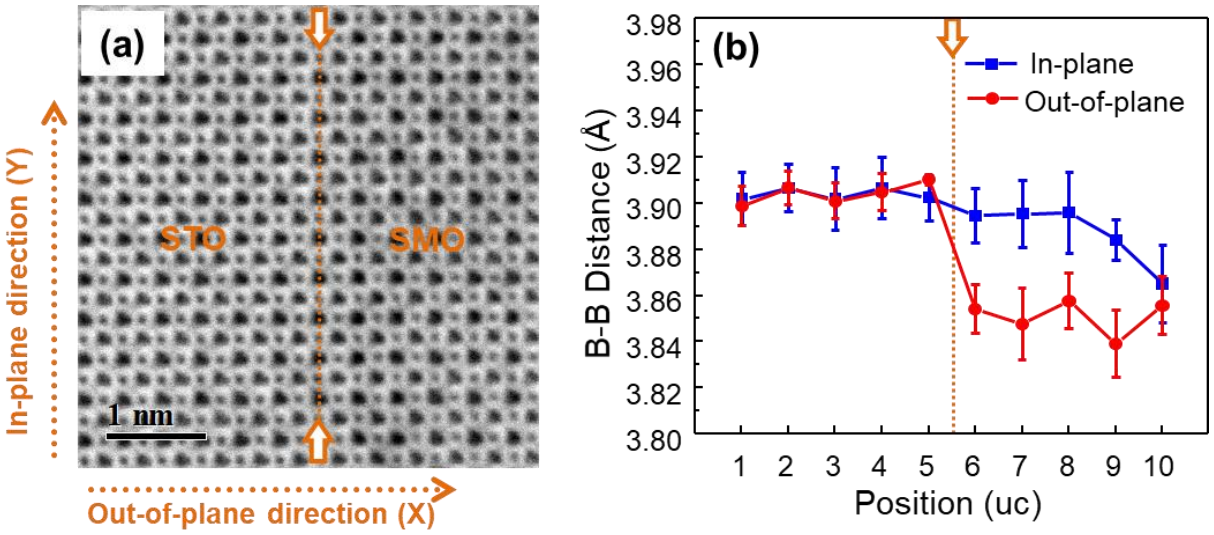

Figure 5-7. Interfacial strain field. (a) Experimental ABF-STEM image of the interface region. Vertical arrows mark the interface between SMO and STO. (b) The corresponding B (Mn/Ti) - B (Mn/Ti) atomic columns spacing along the in-plane and out-of-plane directions.

To obtain the information on the strain at the interface with atomic resolution, I applied 2D Gaussian fitting of atomic columns on high-resolution STEM images and measured the distances between atomic columns.[126] Figure 5-7(a) shows an experimental ABF-STEM image of the interface region. The corresponding coordinates of B atom (Mn/Ti) columns were determined by 2D Gaussian fitting and subsequently used for calculating lattice distances along the out-of-plane (ε_{xx}) and in-plane directions (ε_{yy}). Figure 5-7 (b) displays the in-plane and out-of-plane lattice distances at the interfacial region, showing that the in-plane lattice distances of SMO are similar to that of the STO substrate in the first 3 unit cells close to the interface, but shrink further away from the interface. The SMO lattice is still fully tensile-strained (+1.7 %) along the in-plane biaxial direction in the first 3 unit cells and then gradually relaxed to +0.6 % at unit cell 9. The out-of-plane lattice remains almost unchanged in SMO. According to the Poisson effect, the interfacial SMO lattice in the out-of-plane direction should be compressed due to the intense stretching of the in-plane lattice.[232] However, the corresponding change is absent in Figure 5-7(b), which may be attributed to the presence of ions with a large radius, due to the Mn reduction or/and the elemental mixing between Mn and Ti. Additionally, the thickness of the observed TEM specimen is about 20 nm, and thus the thin foil relaxation effects become prominent.[233-235] The induced lattice relaxation along the beam direction, together with the crack-induced lateral relaxation form a 3-dimensional relaxation, which may account for the absence of out-of-plane compression of the SMO lattice around the heterointerface.

5.3.4 Elemental intermixing at $SrMnO_3/SrTiO_3$ interfaces

The chemical distribution around the interface was studied by 2D STEM-EELS elemental mapping in Figure 5-8. A structural model of the SMO/STO interface in Figure 5-8(a) shows the ideal atomic stacking on both sides of the interface. An experimental ADF-STEM image (Figure 5-8(b)) with corresponding elemental maps using the Ti-$L_{2,3}$ (Figure 5-8(c)), Mn-$L_{2,3}$ (Figure 5-8(d)) and Sr-L_3 (Figure 5-8(e)) edges, and the composite image in Figure 5-8(f) explicitly display the elemental distribution near the interface on

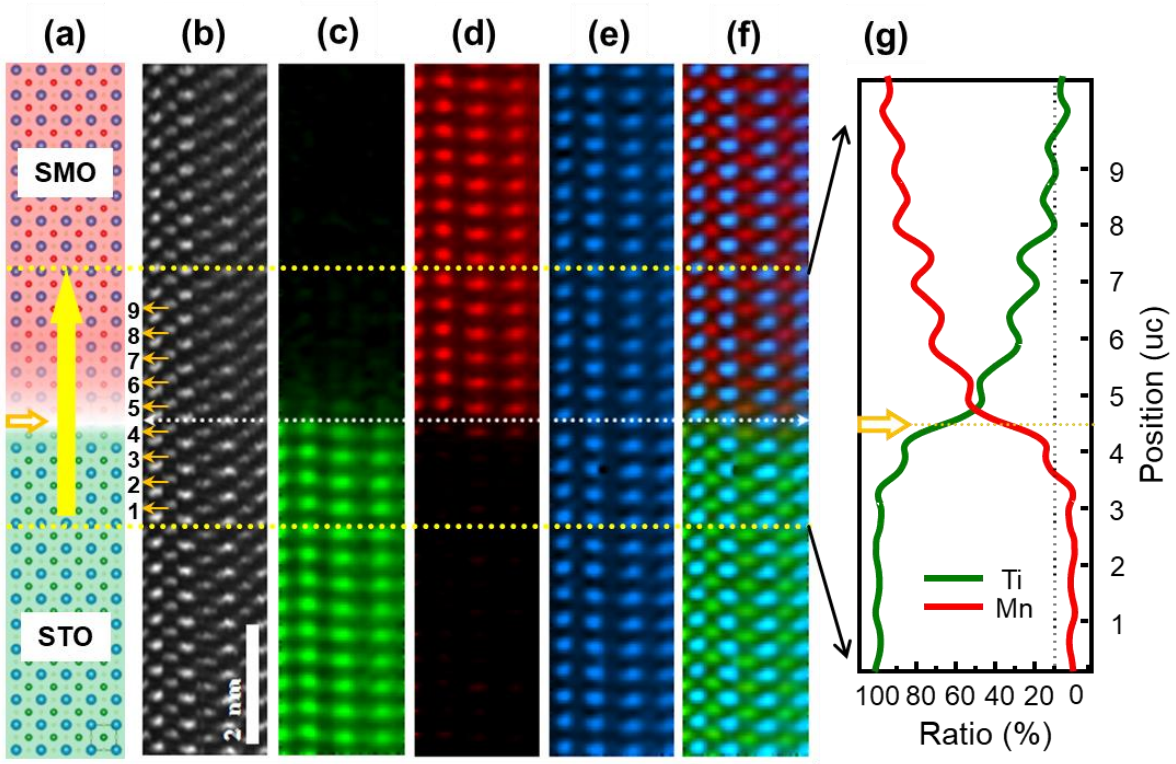

Figure 5-8. Atomically resolved elemental distribution at the hetero-interface determined from STEM-EELS investigations. (a) Schematic of the structure at the hetero-interface. The horizontal arrow marks the interface; the vertical arrow shows the region for elemental signal quantification. (b) Experimental ADF image, wherein 9 unit cells are marked. (c), (d), (e) correspond to Ti-$L_{2,3}$ (green), Mn-$L_{2,3}$ (red), and Sr-L_3 (blue) elemental maps, where black represents zero counts of the signal. (f) Superimposed color-coded image of (c), (d), and (e). (g) Normalized Mn (red) and Ti (green) profile at the B atom position in the vicinity of the hetero-interface. Position 5 is the first Mn column in the SMO thin film at the interface. Note that these maps do not provide the absolute chemical contributions, but merely the relative concentration.

the atomic scale. The Sr-L_3 map shows the homogeneous distribution of Sr around the SMO/STO interface. The Ti-$L_{2,3}$ and Mn-$L_{2,3}$ maps show that the interface is not atomically abrupt, indicating an asymmetric cation intermixing on both sides of the interface. The cationic interfusion between Mn and Ti is more significant on the SMO side than on the STO side.

In order to quantify the cationic intermixing at the interface, the atomic ratio profiles of Mn and Ti are plotted in Figure 5-8(g). The diffusion length for Mn inside the STO substrate is about 1 unit cell, while it is about 4 unit cells for Ti inside the SMO thin film. A strong intermixing between Mn and Ti signals emerges in the first 4 unit cells of the SMO thin film. Nevertheless, the signal spreading shown by STEM-EELS observations does not necessarily originate from the cationic intermixing in the material. The signals may also result from TDS, multiple scattering, and de-channeling effects of electrons, which may cause a deviation of the experimental results from the real elemental distribution in the material.[236] These effects will be discussed now in more detail.

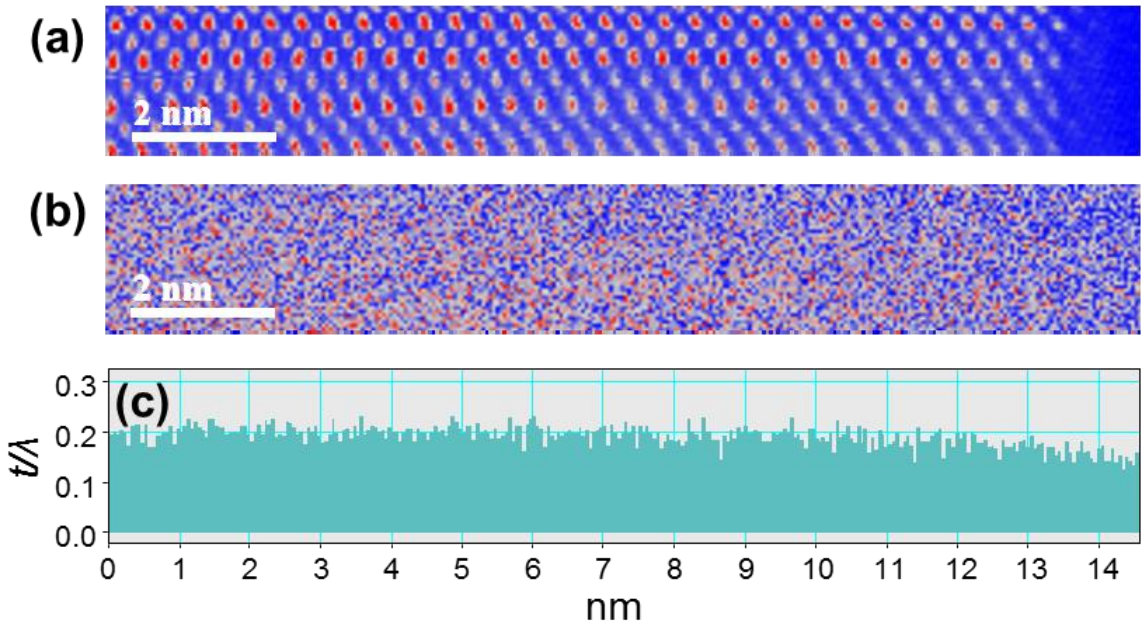

Figure 5-9. EELS thickness map. (a) The colored ADF image of the area for spectrum imaging. (b) Thickness map of the corresponding region using the Fourier log-ratio method. (c) Lateral intensity profile of (b). As is presented in the obtained thickness map, the color distribution among this region is relatively homogeneous, indicating only weak thickness variation. The corresponding intensity profile quantifies the relative thickness of the sample as ~0.20.

The ratio between the sample thickness (t) and the inelastic mean free path (λ) has the main impact on the signal delocalization,[237] which explains that delocalization effects in thin samples will be minimized due to weak multiple inelastic electron scattering. From the simultaneously acquired low-loss map, the sample thickness can be determined *via* the Fourier ratio method.[161] Figure 5-9(a) displays the color-coded ADF image of the same region for EELS spectrum imaging in Figure 5-8. The corresponding thickness map is calculated and presented in Figure 5-9(b). The color code is homogeneous and similar among different regions, revealing that the specimen thickness in this region is almost constant. The vertical-integrated intensity profile of Figure 5-9(b) is shown in Figure 5-9(c). It shows that the thickness is t/λ= 0.20, except for a minor decrease as approaching the surface of the SMO thin film. This decrease results from the tripod polishing procedure during the TEM specimen preparation. At the SMO/STO interface, the thickness is about 20 nm.

To interpret the experimental results and determine the elemental distributions around the interface more accurately, I simulated the EELS spectrum images at the SMO/STO hetero-interface for various sample thicknesses with the μSTEM code, using the model for quantum excitations of phonons.[138, 139] A superstructure with 11×6×64 unit cells corresponding to the same sample thickness studied experimentally was employed for the calculation. The interface was considered to be atomically abrupt. The simulated spectrum image is presented in Figure 5-10(a). The plot shows the intensity profiles of the Ti-$L_{2,3}$ and Mn-$L_{2,3}$ signals across the interface, demonstrating a weak beam spreading of about 1 unit cell on both sides of the interface. Fig. 6(b) displays the spreading of the signal as a function of the sample thickness, indicating an approximately linear relationship. There exists no prominent difference for the signal spreading between Mn and Ti due to their small difference in the atomic number. Therefore, the simulation (Figure 5-10) and the experimental observations (Figure 5-8) substantiate an asymmetric cationic distribution around the interface and verify substantial elemental intermixing at the interface region.

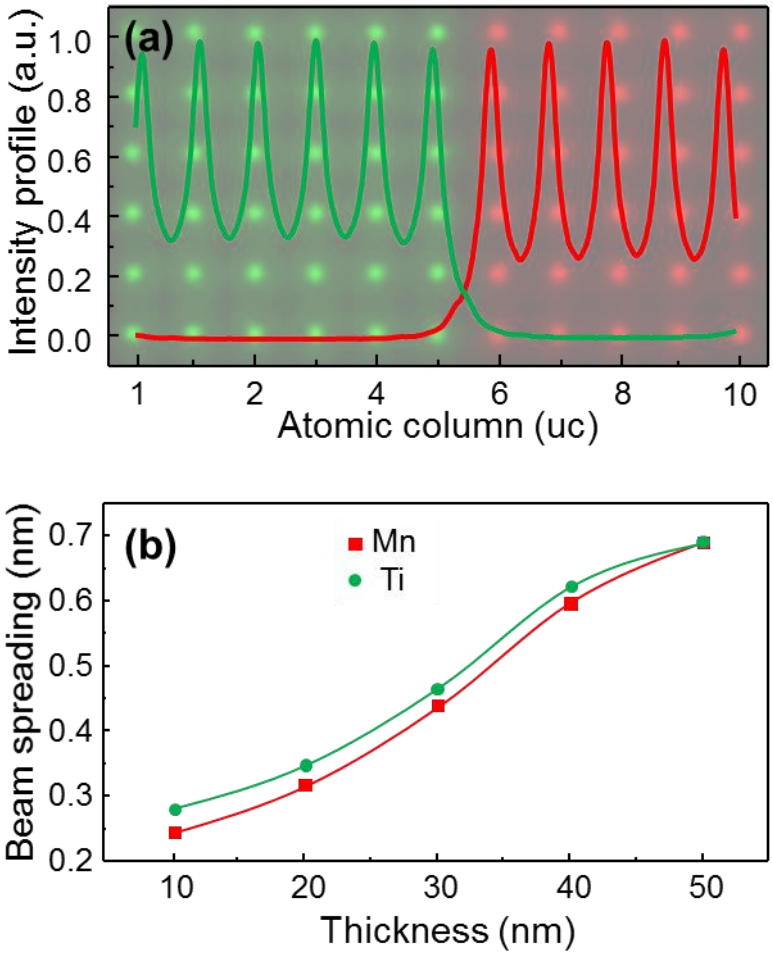

Figure 5-10. Beam spreading effects on the SMO/STO hetero-interface and cation-intermixing-induced formation of oxygen vacancies. (a) Simulated 2D EEL spectrum image for the Ti-$L_{2,3}$ edge (green) and the Mn-$L_{2,3}$ edge (red). This spectrum image was obtained using the thickness of our sample. All other simulation parameters were set according to the experimental conditions during the experimental STEM-EELS investigations. The vertically integrated intensity profiles show a sharp signal variation at the interface. (b) Signal spreading of the Ti-$L_{2,3}$ edge (green) and the Mn-$L_{2,3}$ edge (red) edge as a function of sample thickness.

5.3.5 First-principles calculations of the formation energy of oxygen vacancies

First-principles calculations on the formation energy of oxygen vacancies under different biaxial strain strength were performed by using a 2×2×2 SMO supercell (*i.e.*, $Sr_8Mn_8O_{24}$, $Sr_8Ti_8O_{24}$) and the formation energy of one oxygen vacancy was evaluated (See Appendix B for details of the calculations). Figure 5-11(a) shows the results calculated for SMO under various in-plane biaxial strains, with a = 3.84 Å (the relaxed in-plane lattice parameter at the SMO surface) as the zero-strain state. The oxygen-vacancy formation energy changes approximately linear as a function of the strain and decreases from about 3.3 eV for a compressive strain of 4% to ca. 2.8 eV for a tensile strain of 4%. The decreasing rate in Figure 5-11(a) is, on average, around -0.0625 eV per 1% strain. These results indicate an enhanced formation of oxygen vacancies in the SMO film with an increase of the in-plane biaxial tensile strain. Figure 5-11(a) displays the calculated formation energy of one oxygen vacancy in the STO, with a = 3.905 Å as the zero-strain state. The corresponding formation energy reaches the maximum between the zero-strain and 1% tensile strain and then decreases drastically as the increment of both tensile and compressive strain. This result demonstrates that, in STO, the compressive strain is more effective than the tensile strain on the formation of oxygen vacancies. In contrast, the magnitude of the formation energy of oxygen vacancies in

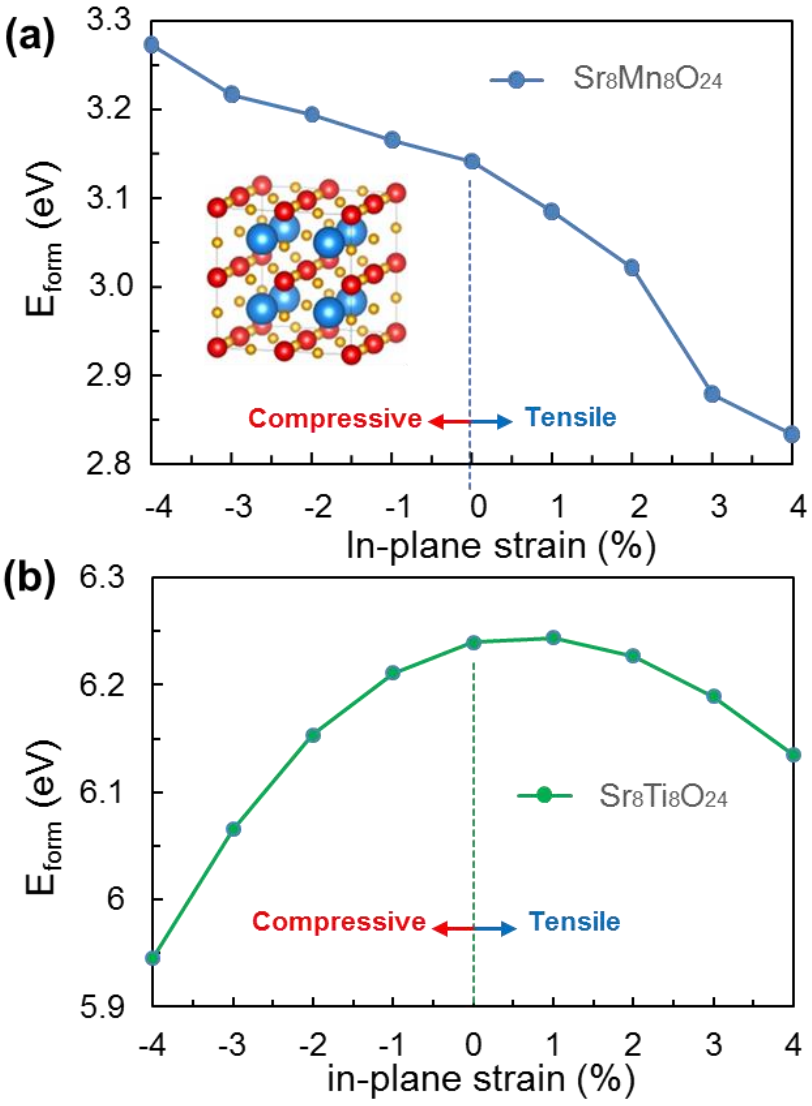

Figure 5-11. The calculated formation energy E_{form} of oxygen vacancies in the pure SMO lattice (a) and pure STO lattice (b) under different in-plane biaxial strain.

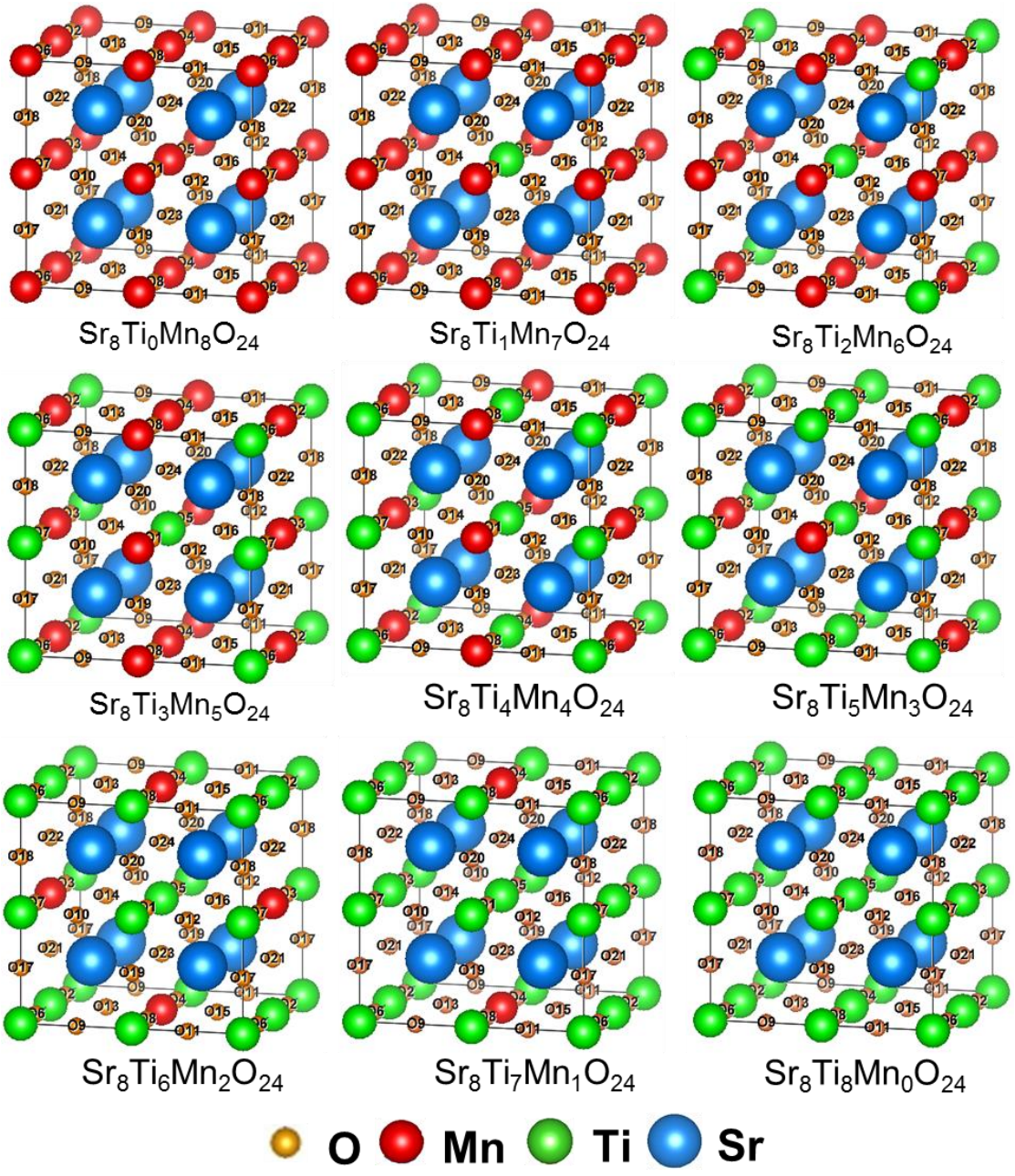

Figure 5-12. 2×2×2 supercell $Sr_8Ti_xMn_{8-x}O_{24}$ (x=0, 1, …, 8) with experimentally measured a=7.81 Å, c=7.68 Å. The number of 24 inequivalent oxygen positions is marked accordingly.

STO is much larger than that of the SMO. It reveals that the formation of oxygen vacancies in STO is more difficult than in SMO under the same conditions.

A previous study suggested that the cation intermixing induces an off-stoichiometry at the interface between the manganite and titanate.[238] Here, first-principles calculations were used to evaluate the influence of cation intermixing on the formation of oxygen vacancies. As a simplified model, a 2×2×2 SMO supercell (*i.e.*, $Sr_8Mn_8O_{24}$) is taken, whose central Mn atom is replaced by the Ti atom from 0 to 8 (see Figure 5-12). The lattice parameters are taken as a = 3.905 Å and c = 3.84 Å, which are the experimentally measured values for the SMO lattice close to the interface. The formation energies for one oxygen vacancy at 24 different oxygen sites in Figure 5-12 are calculated and shown in Figure 5-13(a). It

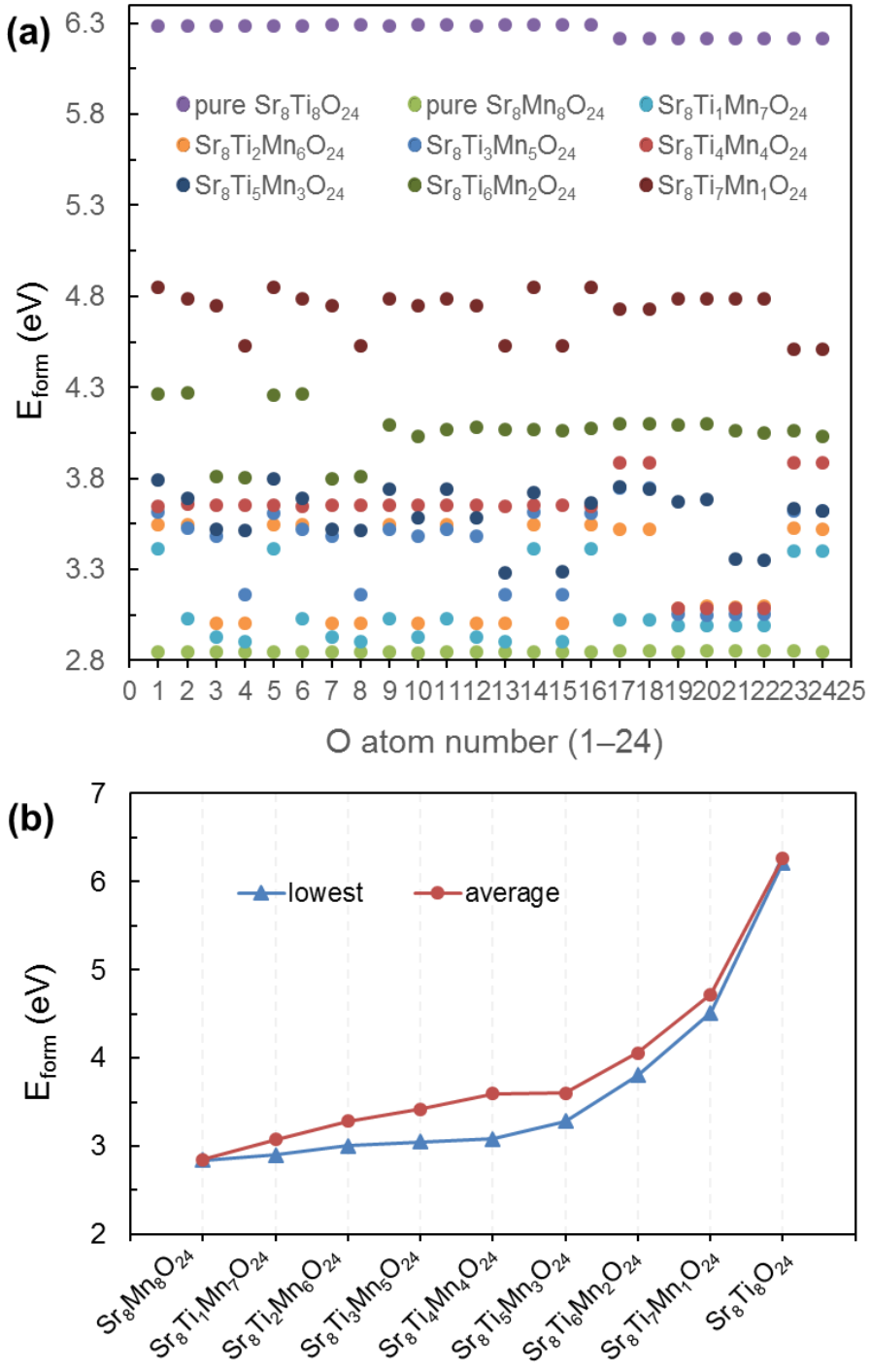

Figure 5-13. The calculated formation energy of one oxygen vacancy in SMO with and without cation intermixing as a function of the oxygen number marked in Figure 5-12. The calculation error is between 1% and 2%. (c) The lowest and average formation energy of an oxygen vacancy obtained by first-principles calculations.

shows that the magnitude of the formation energy is closely linked to the Ti content and usually differing between inequivalent positions. From the lowest formation energy of oxygen vacancy in Figure 5-13(b), we observe that a concentration of 12.5% Ti in SMO slightly increases the oxygen vacancy formation energy by 0.05 eV. Only when Ti substitutes more than 50% of Mn, the formation energy of oxygen vacancies increases sufficiently to exceed that of the pure SMO.

5.3.6 Discussions

The ELNES analysis of the Mn-$L_{2,3}$ and O-K edges (Fig. 5-4 (b, c)) verified the previously observed charge accumulation at the SMO side of the interface, where the charge density attains the maximum (0.13±0.07 e^-/uc) in the first SMO monolayer and becomes smaller farther from the interface (Fig. 5-14). The charge distribution at the hetero-interface caused by a complex mechanism, which may be attributed to multiple effects such as epitaxial strain, charge transfer, interfacial space-charge layer, and cation diffusion. These differences are also strongly intertwined.

Tensile-strain-favored oxygen vacancies. Owing to the lattice mismatch between SMO (3.84 Å) and STO (3.905 Å), the epitaxial SMO film is tensile-strained. In this work, due to the appearance of the cracks, the tensile strain fields are partially relaxed, yielding a strain maximum in the SMO lattice close to the interface. To stabilize the SMO lattice, the electron configurations and chemical composition could be altered in the presence of strain.[35, 239] In this work, on the one hand, since the ionic radius of Mn^{3+} (low spin: 0.58 Å, high spin: 0.65 Å) is larger than Mn^{4+} (high spin: 0.53 Å),[240] the Mn ions tend to be reduced from +4 to +3 to compensate the tensile strain imposed by the STO substrate. This valence decrease may result from the appearance of oxygen vacancies, which was reported to be enhanced by applying tensile strain fields and reduced by applying compressive strain.[241] On the other hand, the magnitude of epitaxial strain was reported to be tunable by changing the concentration of oxygen vacancies in the SMO thin film.[242] Our first-principle calculations show that the in-plane tensile strain lowers the formation energy of oxygen vacancies in SMO (Figure 5-11). This finding is consistent with previous experimental and theoretical studies, [241, 243-245] that rationally attribute the charge accumulation at the interface to the formation of oxygen vacancies.

The interfacial cationic inter-diffusion. STEM-EELS observations and μSTEM calculations unambiguously verified that Mn and Ti intermix in the last one STO monolayer and in the first 3 SMO

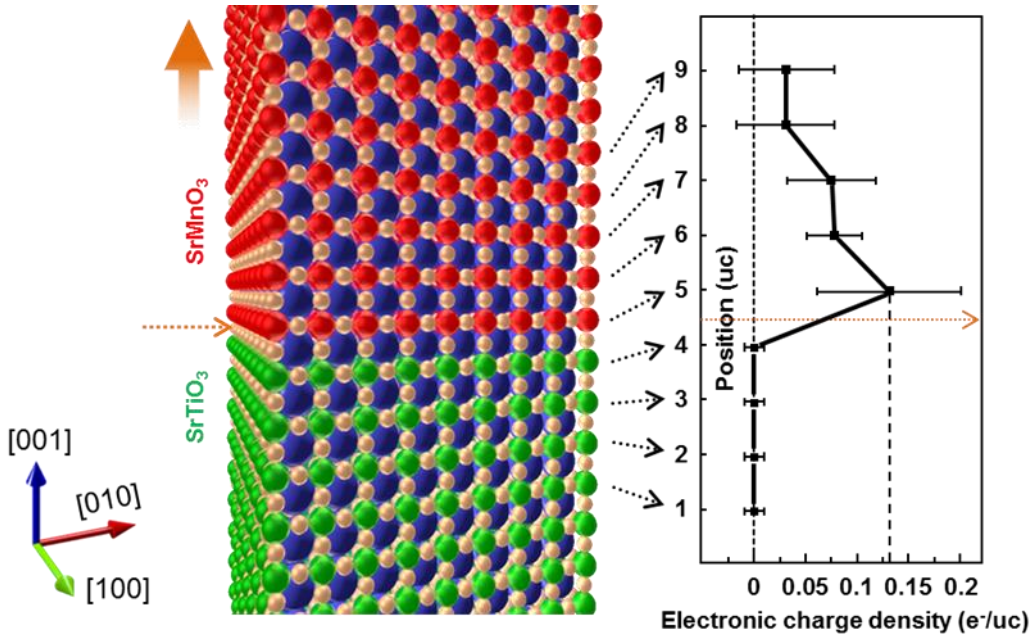

Figure 5-14. The electronic charge density as a function of atomic positions near the interface. The horizontal dotted arrows mark the interface between SMO and STO.

monolayers close to the interface. In this work, the intermixing between Mn and Ti at the interface partially offsets the above-mentioned tensile strain effects on the charge accumulation, because the radius of Ti^{4+} (0.60 Å) exceeds that of Mn^{4+} (0.53 Å).[240] Meanwhile, the calculation results show that the inter-diffusion between Mn and Ti changes the formation energy of oxygen vacancies (Figure 5-13). Interestingly, the cationic intermixing at the interface plays an obstructing role in the charge accumulation on the SMO side of the interface, because the substitution of Mn by Ti in the SMO enhances the formation energy of oxygen vacancies, especially for a high concentration of Ti substitution. Nevertheless, as indicated by the calculation results as well, the inter-diffusion between Mn and Ti could significantly favor the appearance of oxygen vacancies on the STO side of the interface (Figure 5-13), making STO more conductive than naively expected.

The electron transfer from the STO substrate. Charge transfer occurs at the interface when the Fermi levels of the separate materials differ. For the case of the STO/SMO interface, this is relevant, because STO tends to be n-type conducting under the reducing conditions of PLD. This implies that the Fermi level of STO is close to the conduction band. The conduction band of STO is higher than that of SMO [38, 246, 247] and therefore electrons in the conduction band of STO can move to the SMO side of the interface. As indicated by the calculated DOS of $Sr_8(Ti_{8-x}Mn_x)O_{24}$ supercells in Figure 5-15, Mn states are located within the bandgap of STO (note the Mn contribution to the conduction band being at lower energy than the Ti states). If manganese is in the formal 4^+ oxidation state, these states are empty. They become occupied upon the formation of Mn^{3+} under reducing conditions, lifting the Fermi energy to this level, which is, however, still lower than the STO conduction band. Since the Fermi level of STO is close to the conduction band of STO under the reducing conditions during the PLD deposition, the Fermi level is higher in STO than for SMO. Consequently, electron transfer from STO to SMO may occur.

In this work, the measured electronic charge density in the first SMO monolayer is about 0.13 e^-/uc, which corresponds to $0.85 \cdot 10^{14}$ e^-/cm^{-2}. According to the crystal growth conditions, the STO substrate is usually treated as an insulator, which implies that the charge density is supposed to be smaller than $1 \cdot 10^{18}$ cm^{-3}.[248] If one assumes that the charge accumulation originates from the charge transfer from the STO substrate, the accumulation layer needs to collect all charges of the top 0.85 µm of the substrate, indicating that the effect of charge transfer, in this case, can be ignored. However, previous works put forward that the PLD process is remarkably efficient for removing oxygen from the material, especially at a low oxygen pressure, making the STO substrate more conductive than expected.[249, 250] Therefore, the effect of an electron transfer on the observed charge accumulation cannot be ruled out. This illustrates the need to consider the effect of the PLD deposition parameters, when studying the charge distribution at the interface.

Space-charge effects at the interface. Whenever the symmetry of an infinite solid ionic system is broken by introducing interfaces, space charges are a necessary consequence of the chemical difference of anions and cations reflected by different local partial free energies.[251, 252] In ionic materials, the respective transfer of charged ionic defects such as oxygen vacancies can lead to perceptible excess charge densities despite a large bandgap (see, *e.g.,* data for grain boundaries in STO in the reference[253]). Compared to this, electronic interfacial states are of minor importance and are not further considered here. Even though the sign of oxygen vacancies is not observed in the STO substrate from the ELNES of the O-K edge, oxygen vacancies with a density below the detection limit of EELS may exist. If we treat the interface zone as a space-charge region, effective negative charges should appear in SMO to compensate for the positive charges resulting from the oxygen vacancies in STO. However, if the transition from Mn^{4+} to Mn^{3+} is fully compensated by the formation of oxygen vacancies in SMO, both sides of the interface are neutral and no space-charge effect appears.

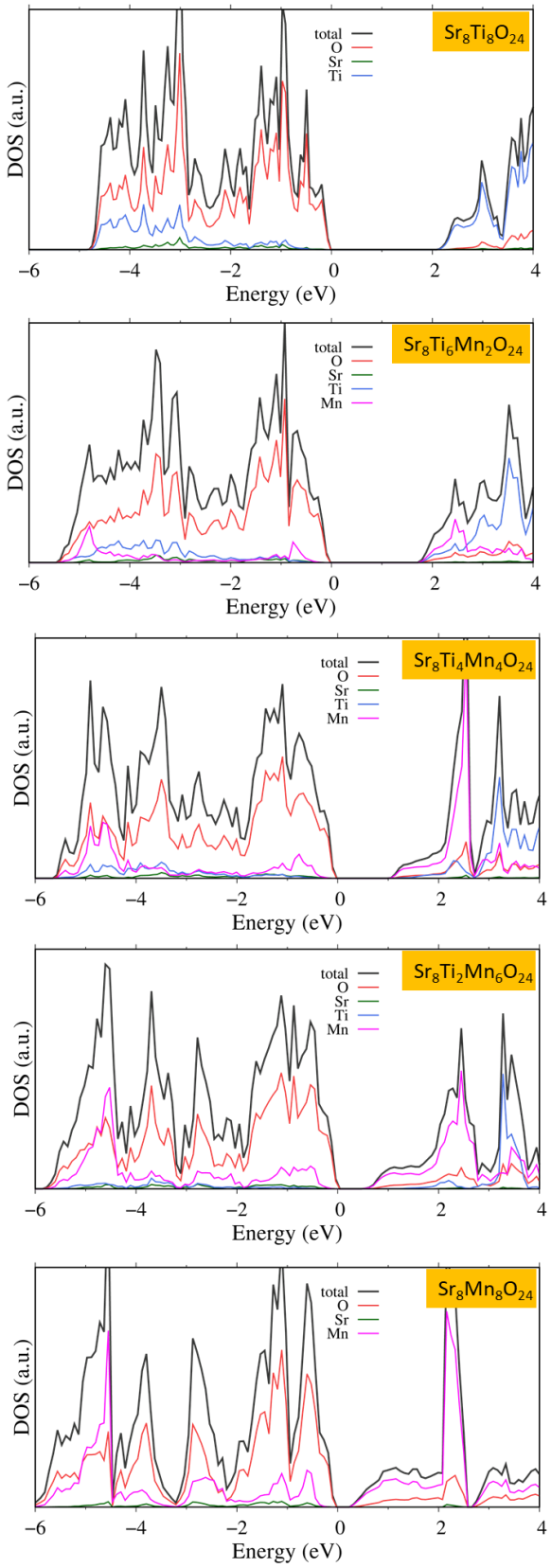

Figure 5-15. The calculated DOS of the $Sr_8(Ti_{8-x}Mn_x)O_{24}$ supercells with x = 0, 2, 4, 6, 8.

5.4 Conclusion

By using spherical-aberration-corrected analytical STEM, this study confirms the electronic charge accumulation on the SMO side of STO/SMO interfaces. The charge density reaches a maximum (0.13±0.07 e^-/uc) at the first SMO monolayer. Through detailed experimental and theoretical investigations, this work provides a comprehensive description of the underlying mechanisms of the charge accumulation, including strain-related effects, cationic intermixing, interfacial charge transfer, and space charge effects. Taken together, our results suggest that the observed charge accumulation at the interface has multiple origins, which need to be interpreted from a comprehensive perspective. While this study focuses on one specific interface, the interface between SMO and STO, its results are of broader relevance. The data evince that the charge distribution at interfaces may well be controlled by a multitude of mechanisms, such as strain fields, local chemistry, charge transfer, and defect formation, which act on different length scales.

Contributions to this chapter:

Hongguang Wang carried out the TEM specimen preparation, TEM characterization and related data processing. H.G. Wang wrote this chapter. Min Yi (TUD) did the first-principle calculations. Xijie Jiang (TUD) performed the AFM measurement and further data analysis. Hans. Boschker (MPI-FKF) grew the SMO thin films. Rotraut Merkle (MPI-FKF) contributed to the discussion part of this chapter. Peter A. van Aken (MPI-FKF), Jochen Mannhart (MPI-FKF) and Robert W. Stark (TUD) supervised and oversaw this work. All authors discussed the results and contributed to this chapter. The work in this chapter also got an insightful discussion with Wilfried Sigle (MPI-FKF), support during TEM sample preparation by Ute Salzberger (MPI-FKF) and Marion Kelsch (MPI-FKF), and the TEM support by Vesna Srot (MPI-FKF), Kersten Hahn (MPI-FKF) and Peter Kopold (MPI-FKF).

Chapter 6. Direct observation of huge flexoelectricity around crack tips*

6.1 Abstract

Flexoelectricity is especially relevant for nanoscale structures and it is expected to be largest at the tip of cracks. In this chapter, direct observations with STEM demonstrate the presence of a huge flexoelectric polarization at crack tips in STO. An averaged polarization of 62 ± 16 $\mu C \cdot cm^{-2}$ is observed in the three-unit cells adjacent to the crack tip, which is one of the largest flexoelectric polarizations ever reported. The polarization is screened by an electron density of 0.7 ± 0.1 e^-/uc localized within one unit cell. These findings reveal the relevance of flexoelectricity for the science of crack formation and propagation.

Graphical abstract: Flexoelectricity around the tip of deep cracks

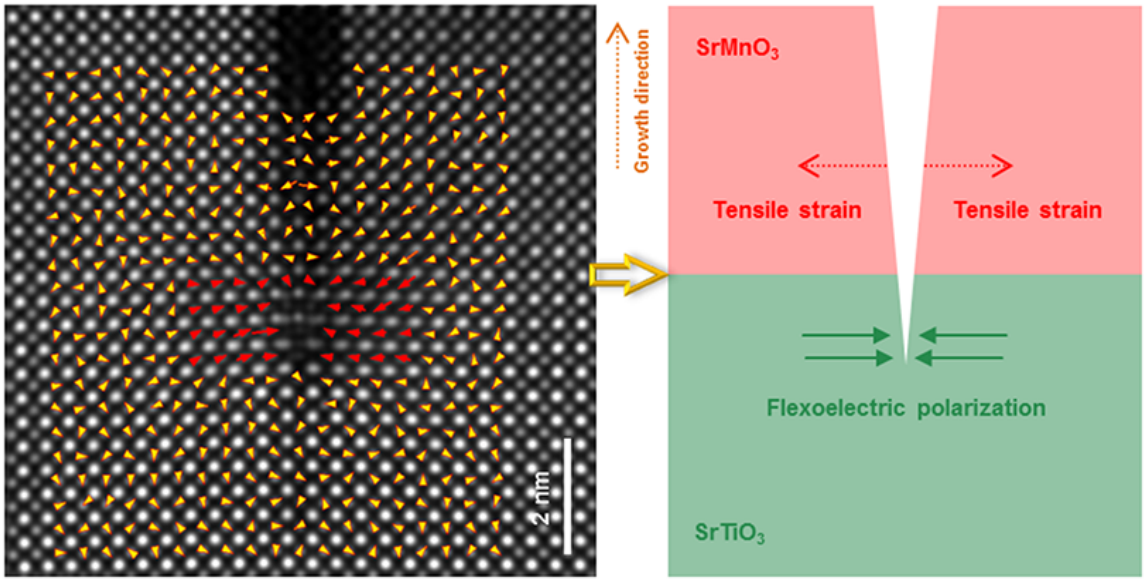

*This chapter has been published in ref.[222]

6.2 Introduction

Flexoelectricity, the electromechanical coupling between strain gradients and polarization, is especially relevant for nanoscale structures [254-258]. The flexoelectric effect is weak in bulk materials, because strain gradients are typically small. In nanoscale structures, however, larger strain gradients are possible, and polarizations comparable to those of ferroelectric materials can be achieved [259-262]. Examples include a huge flexoelectricity observed in bent-core nematic liquid crystals [263] and rotation of polarization away from the ferroelectric polarization axis in twin domains in strained $PbTiO_3$ thin films [264]. Furthermore, flexoelectricity can be used to mechanically write polarization in ferroelectric thin films [265-267], to modulate electrical transport in two-dimensional electron systems [268], and to control tunneling barriers [269]. Flexoelectricity also allows microelectromechanical systems (MEMS) such as cantilevers to be realized without using piezoelectric materials [270, 271].

The largest strain gradients that materials can withstand occur around the tips of cracks. Therefore, flexoelectricity is relevant to the science of crack formation and propagation [72]. Flexoelectricity affects cracks in all materials, because the flexoelectric effect is not limited to polar materials or even to crystalline materials [254]. In polar materials, however, it additionally induces a fracture asymmetry depending on whether the flexoelectric polarization induced by the strain gradients at the crack tip is aligned parallel or anti-parallel to the uniform polarization in the material [272]. The electric fields generated by flexoelectricity at microfracture sites in bone have been suggested to induce osteocyte apoptosis, and thus initiate a crack-healing process [273]. A direct study of the polarization around cracks at the nanoscale, however, has not yet been performed. A recent study investigated polarization around dislocations in STO [274]. The strain fields resulting from these dislocations indeed induce a flexoelectric polarization, and a polarization of ~28 $\mu C \cdot cm^{-2}$ was found at distances smaller than one nm away from the dislocations. These dislocations, however, were formed at high temperatures, and therefore ion diffusion can lead to composition variation and partial strain relief. Here, cracks induced by a non-equilibrium epitaxial strain relief process produce large strain gradients and large flexoelectric polarization.

The SMO/STO epitaxial system was selected for the study, because the flexoelectric effect in both materials is well studied [274-281]. STO is a quantum paraelectric at low temperatures [282]. A large flexoelectric response is expected, because flexoelectric coefficients depend on the dielectric constant of the material. The flexoelectric coefficients of STO indeed scale with its dielectric constant and are therefore strongly temperature-dependent. The bulk coefficients are of the order 10^{-9}–10^{-8} C/m at room temperature [276]. SMO is a paraelectric material close to a ferroelectric transition. Ferroelectricity can be induced by cation substitution [283], large tensile strain [284, 285], or small tensile strain together with structural defects [286]. Furthermore, the flexoelectric rotation of the polarization has been observed in films with vertical strain gradients induced by a gradual distribution of oxygen vacancies [280]. By quantifying the strain gradient and the induced polarization, a longitudinal flexoelectric coefficient of SMO of 4×10^{-7} C/m was found in the ferroelectric phase [280].

SMO grows very well on STO, resulting in a coherent epitaxy at the growth temperature, *i.e.*, 800 °C. The SMO layer is under biaxial tensile strain, which increases with decreasing temperature due to the difference in the thermal expansion coefficients of the materials. The strain in SMO is 1.8% at the growth temperature and 2.0% at 300 K. Therefore, it is possible for such a thin film to have a thickness below the critical thickness for stress relief at high temperatures and above the critical thickness at room temperature. Furthermore, SMO is expected to be oxygen-deficient at high temperatures and to incorporate oxygen during cooling [287]. Upon oxygen incorporation, the lattice shrinks and thus increases the strain. During and after cooling, cracks appear in the film, because the temperature is too low to allow for stress relief by the

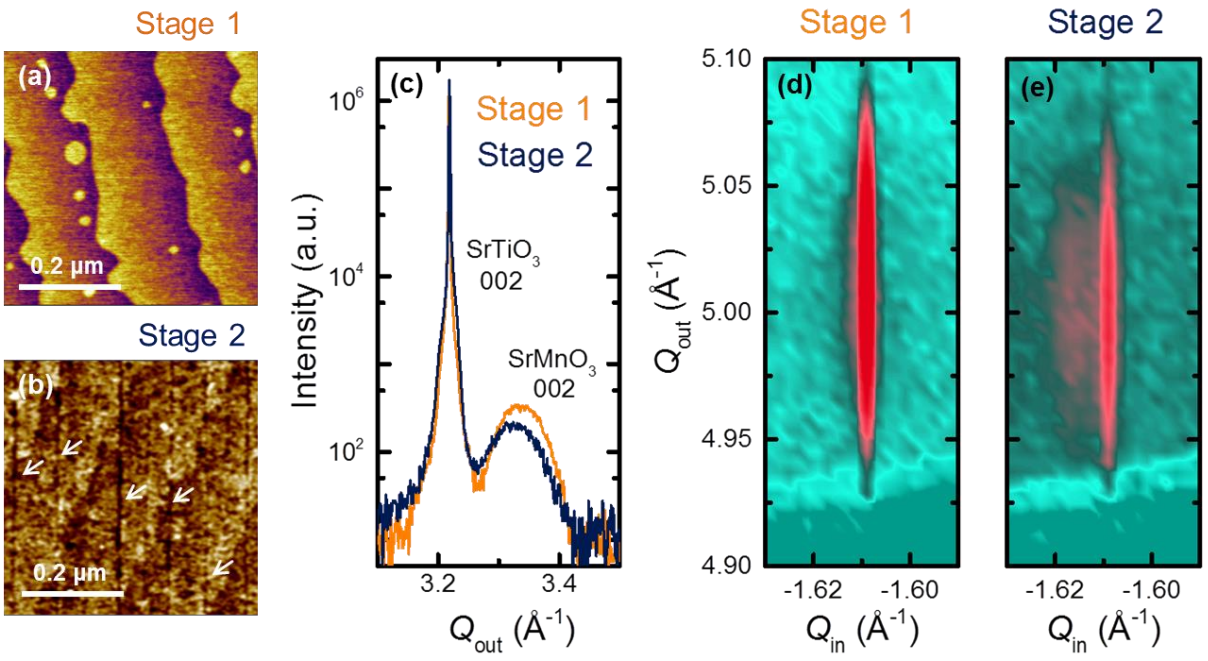

Figure 6-1. (a,b) AFM images of the surface of a SMO film showing the absence and presence of long cracks parallel to the [100] and [010] lattice directions at stage 1 and stage 2, respectively. (c) XRD θ-2θ scan of the sample measured before and after the appearance of the cracks. The out-of-plane lattice parameter of the SMO relaxes after the cracks appear. (d, e) RSMs of the $\bar{1}03$ reflection before and after the appearance of the cracks. At stage 2, a tail of the intensity of the film peak is distributed at higher absolute values of $Q_{in,}$ indicating an in-plane strain relaxation.

creation of dislocations [288, 289]. Evidence for this mechanism was found by the observation of cracks in a SMO layer, but not in a layer capped by an epitaxial overgrown layer [290]. This process is the initial phase of stress relief mechanisms by delamination commonly observed in oxide films [291-293].

6.3 Results and Discussions

6.3.1 Crack formation in thin films

Several SMO film samples with thicknesses of 8–25 nm were grown using PLD, as described in chapter 5. The films were grown in the layer-by-layer growth mode as evidenced by clear RHEED intensity oscillations. Directly after growth (stage 1), the surface morphology of a SMO film with a thickness of 8 nm was investigated with AFM. Smooth terraces with single-unit-cell-high steps can be observed in Figure. 6-1(a). Some large single-unit-cell-high islands were present on the terraces. No cracks appears at this stage. However, when reinvestigating the samples at a later stage (stage 2), cracks had appeared (Figure. 6-1(b)). This timescale for crack formation depends on the thicknesses of the films and ranges from days to several weeks. A large number of cracks are visible in the SEM image of the film surface (see Appendix Figure C-1). The cracks are straight and aligned with the [100] and [010] crystal lattice directions. The average separation of the cracks in the SEM image is ~100 nm and the cracks are continuous for lengths of 100–2000 nm.

In order to investigate, whether the cracks are caused by strain relaxation, XRD measurements were performed. Figure 6-1(c) shows a θ-2θ scan of a SMO film with a thickness of 8 nm. The sample was measured both at stage 1 and at stage 2. The XRD scan shows the STO 002 reflection and the SMO 002 reflection. The latter peak is broad because of the finite thickness effect. Comparing the two measurements,

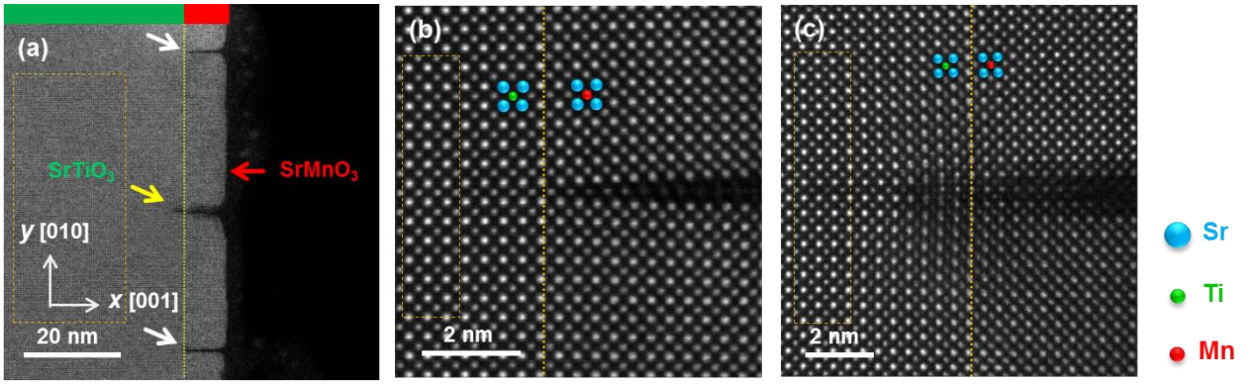

Figure 6-2. Overview of the sample and close-up images of the cracks. (a) HAADF-STEM image of the STO/SMO heterostructure. The yellow dotted line marks the interface, the white arrows mark shallow cracks and the yellow arrow marks a deep crack. (b) HAADF image of a shallow crack. The SMO lattice splits at a MnO_2 plane. (c) HAADF image of a deep crack. An edge dislocation appears at the crack tip. The box region is the reference for the corresponding strain analysis.

the intensity of the film peak at stage 2 is reduced and the maximum of the peak is shifted from Q_{out} = 3.337 Å^{-1} to Q_{out} = 3.326 Å^{-1}. This indicates that the out-of-plane lattice parameter of SMO has changed from 3.766 Å to 3.778 Å, consistent with partial epitaxial stress relief. Figure 6-1(d) and Figure 6-1(e) show RSMs around the $\bar{1}03$ reflection. Here, a decrease in intensity at stage 2 is observed as well, together with a shift of the film peak towards lower Q_{out} values. At stage 1, the peak position along Q_{in} is equal to Q_{in} = 1.609 Å^{-1}, which corresponds to the Q_{in} value of the STO peak, indicating a coherently strained layer. At stage 2, in contrast, only part of the peak intensity is at Q_{in} = 1.609 Å^{-1} and a tail of the intensity is distributed at higher absolute values of Q_{in}. This implies that a part of the film is no longer coherently strained and that strain gradients are therefore present in the sample. Because XRD measurements probe a large area, the stress relief is found to affect most of the film.

6.3.2 STEM imaging of the cracks

To investigate the atomic structure of the sample in detail, atomic-column-resolved STEM was used. Figure 6-2(a) displays the overview of a SMO thin film cross-section by HAADF-STEM imaging along the [100] direction. The yellow dotted line marks the hetero-interface between SMO and STO, which is determined by the corresponding strain analysis (see also Appendix Figure C-2). Cracks are highlighted by arrows. Most cracks terminate at the interface (white arrows), but some cracks also penetrate into the STO (yellow arrow).

In order to study the structure of the cracks in more detail, high magnification images of the cracks were acquired with the HAADF detector. Figure 6-2(b) shows a close-up image of a shallow crack. The crack is centered around a MnO_2 (010) plane. At the apex of the crack, six Mn columns can be identified, which have progressively weaker intensity with increasing distance from the interface. These Mn columns are not displaced along *y* with respect to the underlying STO crystal. No crystalline material is found in the center of the crack at distances larger than six unit cells away from the interface. The Sr columns adjoining these Mn sites move outwards with increasing distance from the interface, thereby increasing the Sr-Sr distance. This separation is approximately 1.5 unit cells at a distance of six unit cells away from the interface. Some of the cracks are wider and penetrate further into the STO substrate. Figure 6-2(c) shows an example of such a crack. The atomic structure of the crack is more disordered compared to the shallow cracks. The crack is centered on the SrO plane. Whereas the Ti and Mn lattices split and the corresponding

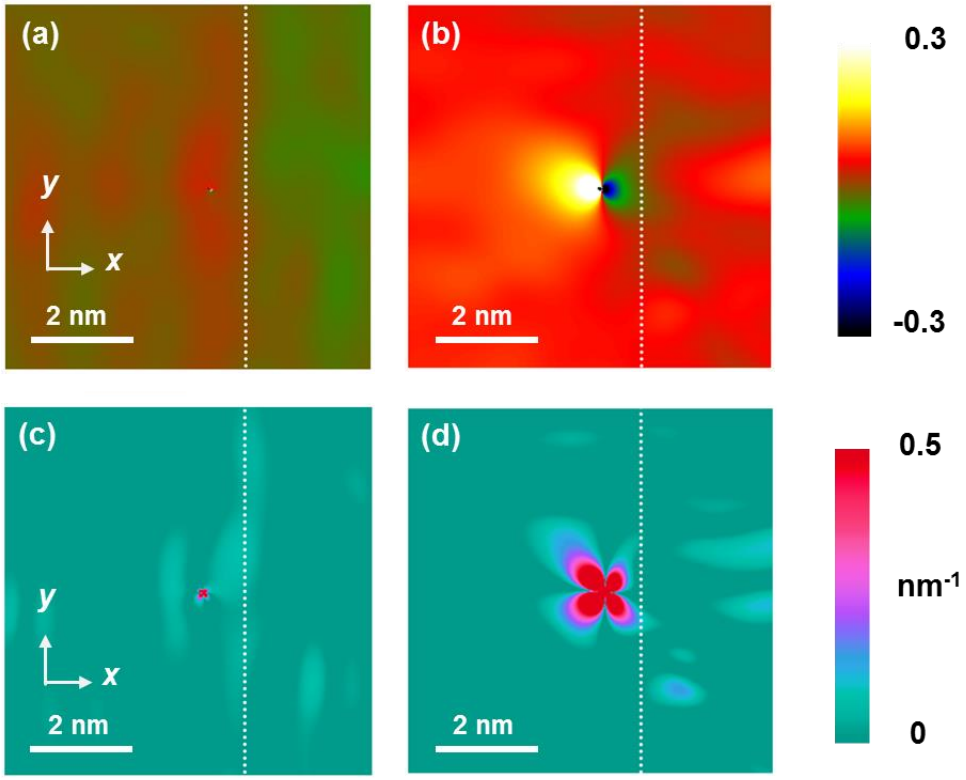

Figure 6-3. Strain analysis of the deep crack. (a) Out-of-plane strain (ε_{xx}) map and (b) in-plane strain (ε_{yy}) map of the deep crack. The large in-plane strain is observed at the tip of the crack. (c, d) Calculated absolute values of strain gradients $d\varepsilon_{xx}/dx$ and $d\varepsilon_{yy}/dy$, respectively. An averaged strain gradient $d\varepsilon_{yy}/dy$ of 0.21 nm^{-1} is present in an area of 3-4 unit cells around the tip of the crack.

atomic planes move apart, the Sr sublattice rearranges and additional Sr columns are found directly at the interface and at the center of the crack. This edge dislocation in the Sr sublattice of the STO has a Burgers vector a[010] and terminates at a SrO plane in the STO. Unlike previous work [294], I do not observe the diffusion of Mn ions into the tip of the deep crack (see also Appendix Figure C-3).

In the following parts, I will focus on the observation of strain gradients and the induced flexoelectric polarization in both kinds of cracks. I will firstly present the study of the tip of deep cracks, because I only observe large strain gradients and induced flexoelectric polarization in deep cracks. A total of 4 deep cracks were investigated, all of which showed consistent results. A detailed analysis of the shallow cracks will be presented as well.

6.3.3 Flexoelectricity around the tip of deep cracks

Results. To analyze the strain fields surrounding the cracks, I apply GPA to the STEM image in Figure 6-2(c). Figures 6-3(a) and 6-3(b) are the corresponding out-of-plane strain (ε_{xx}) and in-plane strain (ε_{yy}) maps of the deep crack, respectively. The ε_{xx} map indicates the position of the interface, showing a strain of 5% around the crack tip. The typical dislocation lobes appear in the ε_{yy} map, indicating the dislocation core in the Sr sublattice of STO. The strain is as high as 20%. The color changes in the ε_{yy} map around the crack tip reveal the inhomogeneous strain distribution. Figures 6-3(c) and Figure 6-3(d) show the calculated absolute values of strain gradients $d\varepsilon_{xx}/dx$ and $d\varepsilon_{yy}/dy$, respectively. Strong strain gradients appear in the $d\varepsilon_{yy}/dy$ map and are confined to within three unit cells around the crack tip. The strain gradients at opposite sides of the crack are of similar magnitude but opposite in sign. The largest strain gradient is observed in

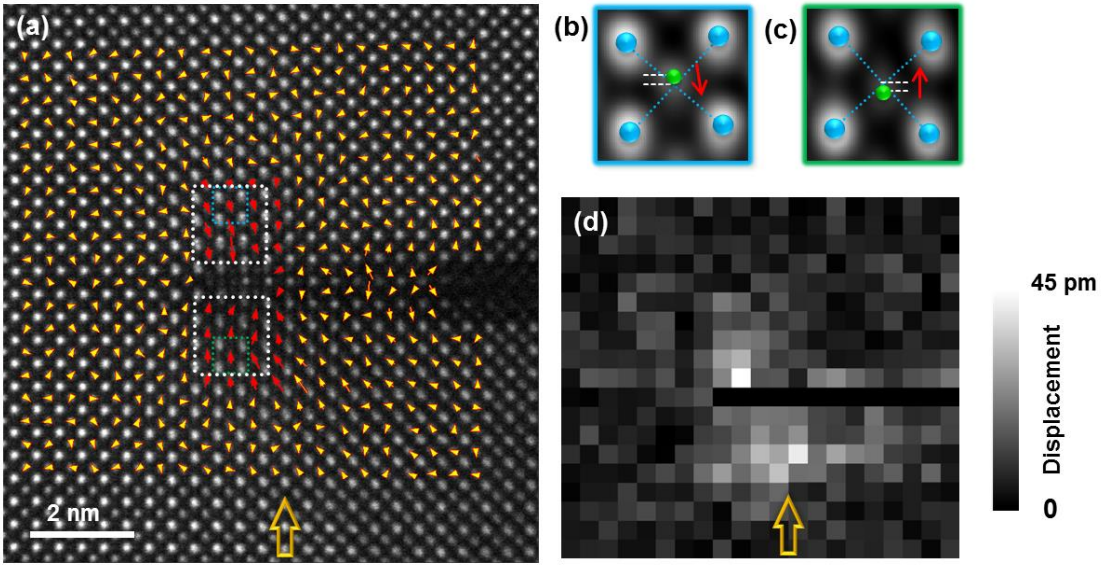

Figure 6-4. Lattice displacement analysis around the deep crack. (a) Displacement vector map between the TiO and Sr columns overlaid with the HAADF image. The big yellow arrow highlights the interfacial SrO plane between SMO and STO. Polarization is observed in a region about 3-4 unit cells surrounding the crack tip (red arrows). (b, c) Schematic images for the relative displacement of TiO columns with respect to the four neighboring Sr columns at the upper side and the lower side of the crack tip. (d) Magnitude map of displacement vectors in the region defined by the red and yellow arrows in (a).

the *y* direction, with a magnitude as high as 3.0 nm^{-1}. The strain gradients $d\varepsilon_{xx}/dy$, $d\varepsilon_{yy}/dx$, $d\varepsilon_{xy}/dx$, $d\varepsilon_{xy}/dy$ are also discussed (see Appendix Figure C-4).

With the quantification of large strain gradients, the electrical polarization around the tip of the deep crack can be estimated. Atomically resolved STEM enables a precise determination of the atomic-column positions, allowing the observation of lattice displacements at a few picometer precision [130]. To minimize sample tilt effects [298], the alignment of the sample to the [100] zone axis was optimized using position-averaged convergent beam electron diffraction (PACBED) (see Appendix Figure C-5). Figure 6-4(a) shows the displacement vector (*D*) map between Ti and neighboring Sr columns for the deep crack. The error of D depends on the quality of the 2-dimensional Gaussian fitting of the atomic column positions. In this work, a Gaussian fitting of atomic columns around the tip of the deep crack is realized, leading to the determination of atomic displacement with high accuracy (See Appendix Figure C-6). The directions of the displacement vectors are aligned at both sides of the crack tip, pointing to the crack tip. The aligned region is about 3-4 unit cells surrounding the crack tip, which correlates well with the location of the strain gradients. The relative position of Ti is shifted upwards for the upper side (Figure 6-4(b)) and downwards for the lower side (Figure 6-4(c)). Away from the tip region, the displacement vectors are randomly oriented, reflecting the measurement uncertainty. Figure 6-4(d) maps the corresponding magnitude of the displacement vector in Figure 6-4(a). It shows that the values close to the crack tip are more significant than those in other regions. Furthermore, HAADF-STEM images of the deep crack region were obtained by scanning the electron beam along different directions, yielding identical results (see Appendix Figure C-7).

For perovskite materials, quantitative mapping of electrical polarization can be performed using cation displacement in *Z*-contrast STEM images [295]. Since the ion charge centers are all collinear, the polarization (*P*) can be determined from the displacement between the position of the Ti atom and the centroid of the neighboring Sr columns mentioned above (Figure 6-4(b) and Figure 6-4(c)). The polarization (*P*) is

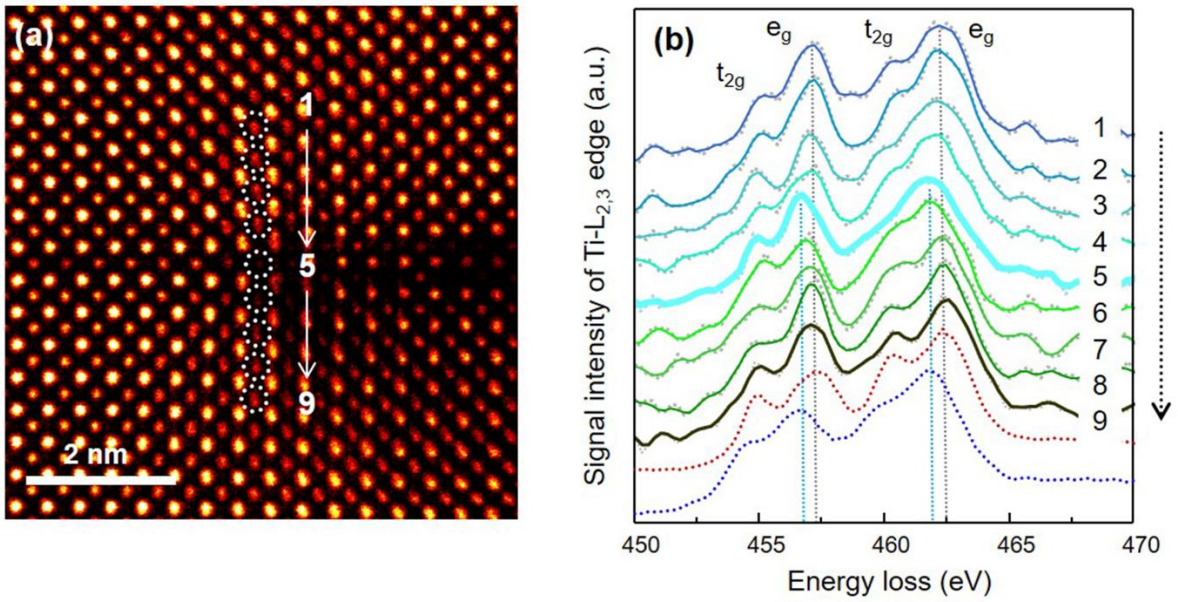

Figure 6-5. STEM-EELS investigation of the deep crack. (a) Colored HAADF image of the deep crack. White circles mark 9 TiO columns placed along the line through the maximum of the polarization field. (b) Ti-$L_{2,3}$ spectra at the different positions marked in (a). The red and blue lines are the reference spectra for Ti^{4+} and Ti^{3+}, respectively. The Ti column at the center of the crack has a reduced valence state of +3.3 ± 0.1 (spectrum 5).

calculated using the formula: $P = -2.5 \cdot D \cdot \mu C \cdot cm^{-2} \cdot pm^{-1}$, where D is the displacement [296]. Because of the linear relation between the cation displacement and the polarization, the electrical polarization increases upon approaching the crack tip. The tip of the deep crack acts as a 180° domain wall with a head-to-head configuration. The averaged magnitude of the spontaneous polarization for the upper side domain is 67 ± 16 $\mu C \cdot cm^{-2}$ and for the lower side it is 56 ± 16 $\mu C \cdot cm^{-2}$. The largest polarization in a single unit cell is 107 ± 16 $\mu C \cdot cm^{-2}$. Here, the noise levels were estimated from the apparent behavior of the non-polar STO substrate.

The observed polarization is expected to be accompanied by electric charges accumulating at the tip of the crack. To study the charge states at the crack tip, EELS measurements are carried out. As indicated in Figure 6-5(a), Ti-$L_{2,3}$ spectra from nine TiO columns around the crack tip were extracted. The Ti-$L_{2,3}$ white lines shifts to lower energy and the splitting between the t_{2g} and e_g peaks becomes less pronounced when approaching the crack tip (Figure 6-5(b)). This indicates a valence change of Ti within one unit cell around the crack tip. The valence state of Ti at the crack tip is +3.3 ± 0.1, as determined by fitting reference Ti-$L_{2,3}$ spectra for Ti^{4+} (STO, red curve) and for Ti^{3+} ($LaTiO_3$, blue curve) at the bottom of Figure 6-5(b) to the Ti-$L_{2,3}$ spectrum at the crack tip (spectrum 5) [42]. The valence state of Ti in the unit cells adjacent to the crack tip is close to +4.0.

Discussion. A high polarization is observed at the cracks that penetrate into the STO. I attribute the polarization to the flexoelectric effect, because (i) the polarization is exclusively observed in regions where the strain gradient $d\varepsilon_{yy}/dy$ is large and (ii) the sign of the polarization matches the sign of the strain gradient. The average polarization of 62 ± 16 $\mu C \cdot cm^{-2}$ is the largest flexoelectric polarization observed so far.

Together with the polarization, a valence state change of +0.7 ± 0.1 of the Ti ions was also observed at the tip of the crack. This valence change is much larger than previously observed polarization-induced valence changes [274]. By analyzing the crack tip as a head-to-head domain wall, the charge density required to screen the average polarization of 62 ± 16 $\mu C \cdot cm^{-2}$ is 0.6 ± 0.15 e^-/uc, in good agreement with the measured charge density. Although composition changes such as O vacancies (See Appendix Figure C-8) or Sr

interstitials cannot be directly ruled out as the cause of the charge density, I attribute the charge density to the flexoelectric polarization, because both its magnitude and its location matches the screening charge expected from the flexoelectric polarization. The main reason the polarization is so large is that the strain gradients at the crack tips are 5 to 1000 times larger than previously investigated nanoscale strain gradients [259, 264, 269, 274]. The longitudinal flexoelectric coefficient μ_{11} is given by $\mu_{11} = P_y / (d\varepsilon_{yy}/dy)$ [254]. The average of the strain gradient in the boxed areas in Figure 6-4(a) is 0.21 nm^{-1}. Therefore, the longitudinal flexoelectric coefficient μ_{11} of STO at the crack tip to be $3 \cdot 10^{-9}$ C/m is observed, in good agreement with bulk measurements [276].

To estimate the importance of the flexoelectric polarization in crack formation and crack propagation processes, the elastic energy density with the electrostatic and flexoelectric energy densities at the crack tip are compared. The former is given by $E_{elas}/V = 0.5Y \cdot \varepsilon^2$, where E_{elas} is the elastic energy, V is the volume, and Y is Young's modulus. Using the average strain and Y = 270 GPa [297], E_{elas}/V is $2.3 \cdot 10^9$ Jm^{-3}. The electrostatic energy density is given by $E_{elec}/V = 0.5\chi^{-1} \cdot P^2$, where E_{elec} is the electrostatic energy, and χ is the dielectric susceptibility. Using the average polarization of the boxes in Figure 6-4(a), and $\chi_{STO} = 300\varepsilon_0$, E_{elec}/V is $7.2 \cdot 10^7$ Jm^{-3}. Here, ε_0 is the permittivity of vacuum. The flexoelectric energy density is given by $E_{flex}/V = 0.5\mu \cdot \chi^{-1} \cdot P \cdot d\varepsilon_{yy}/dy$, where E_{flex} is the flexoelectric energy. Using $\mu = 3 \cdot 10^{-9}$ C/m, E_{flex}/V is $7.4 \cdot 10^7$ Jm^{-3}. Therefore, the flexoelectric and electrostatic energies provide significant contributions to the energy of the crack.

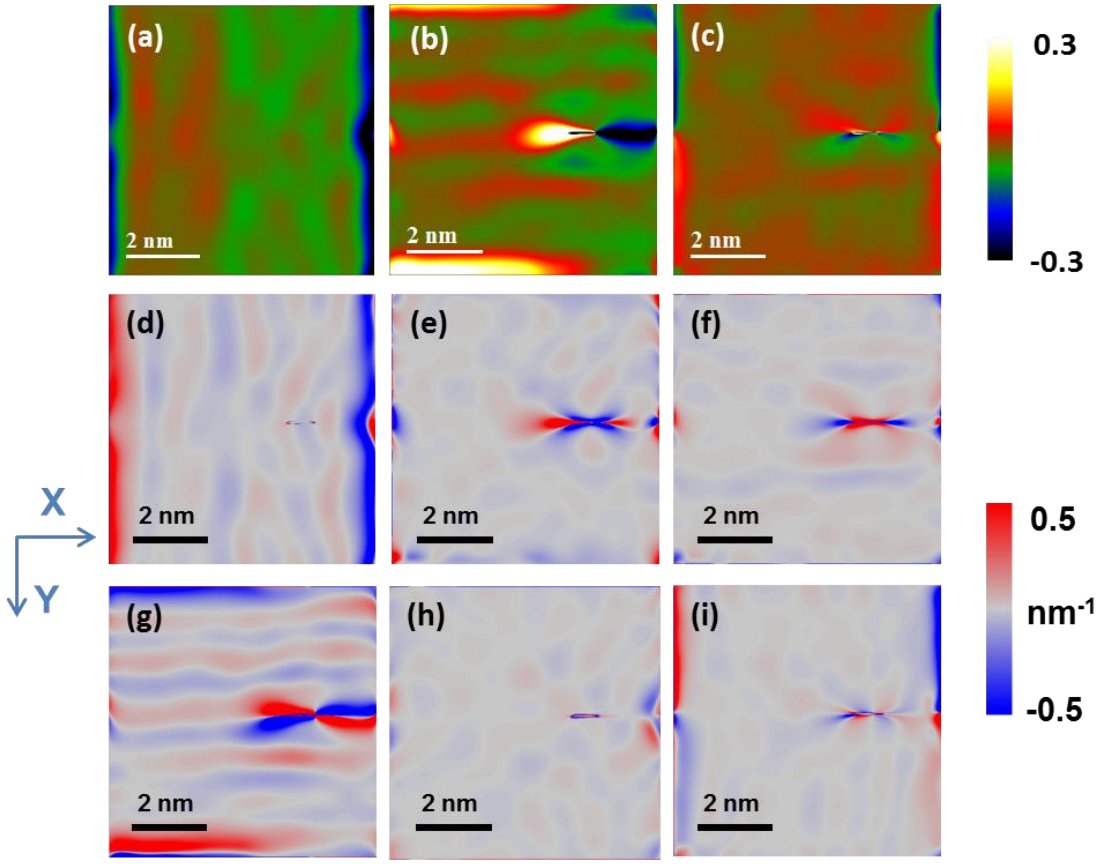

Figure 6-6. Strain fields and derived strain gradients of the shallow crack. (a), (b), and (c) are the out-of-plane strain (ε_{xx}), in-plane strain (ε_{yy}), and shear strain (ε_{xy}) maps of the shallow crack, respectively. (d), (e), (f), (g), (h), (i) correspond to the calculated strain gradients $d\varepsilon_{xx}/dx$, $d\varepsilon_{yy}/dx$, $d\varepsilon_{xy}/dy$, $d\varepsilon_{yy}/dy$, $d\varepsilon_{xx}/dy$, $d\varepsilon_{xy}/dx$, respectively. The coordinate describes the positive strain gradient along with the X and Y directions. The data show that the lattice deformation of the shallow crack mostly emerges in the center unit cell of the crack. There exist no obvious strain gradient fields in the surrounding SMO lattice, implying the absence of flexoelectricity at the shallow crack.

6.3.4 Flexoelectricity around the tip of shallow cracks

A detailed strain analysis for the shallow crack is performed in Figure 6-6. However, obvious lattice deformation takes place in the unit cell region centered by the MnO (010) plane. Therefore, the strain gradient around the shallow crack is rather small, below 0.1 nm^{-1} within one unit cell at both sides of the central MnO plane. This value is 30 times smaller than the strain gradients observed at the deep cracks.

The atomic-displacement map is obtained (Figure 6-7) by using a Gaussian fitting of atomic columns (see Appendix Figure C-9). Hardly any alignment of the displacement vectors is observed, indicating the absence of induced polarization in most of the areas. The only exception is the unit cells directly in the center of the crack, where displacements up to 28 pm are found that are approximately aligned with the plane of the crack. This displacement corresponds to an average polarization of 44 ± 13 $\mu C \cdot cm^{-2}$. At the shallow cracks, valence states of the Ti remain unchanged (Figure 6-8(c)). A red shift of the Mn-$L_{2,3}$ edge in the central MnO plane appears in Figure 6-8(d), indicating a decrease of the Mn valence state. The valence state of Mn at the crack tip is about +3.6 ± 0.1, in reasonable agreement with the presence of the polarization.

The lack of polarization in the bulk of the SMO films implies the films are not ferroelectric, in contrast to previous reports [285, 286]. The absence of ferroelectricity presumably coincides with the formation of cracks in the samples, because a ferroelectric phase would be able to accommodate the strain in the films. Our films may have a lower oxygen vacancy density than the films reported in [286]. Therefore, the oxygen vacancy density cannot stabilize a large strain state, resulting in the formation of cracks instead of uniform ferroelectric polarization.

The polarization is merely observed in the center of the shallow cracks. Here, the strain gradient $d\varepsilon_{yy}/dy$ is zero by symmetry and the strain gradient $d\varepsilon_{xx}/dx$ is very small. Therefore, the polarization cannot be related to the flexoelectric effect. The polarization can be attributed to an induced ferroelectricity. The largest tensile strain is present at the center of the crack and large tensile strain is known to induce

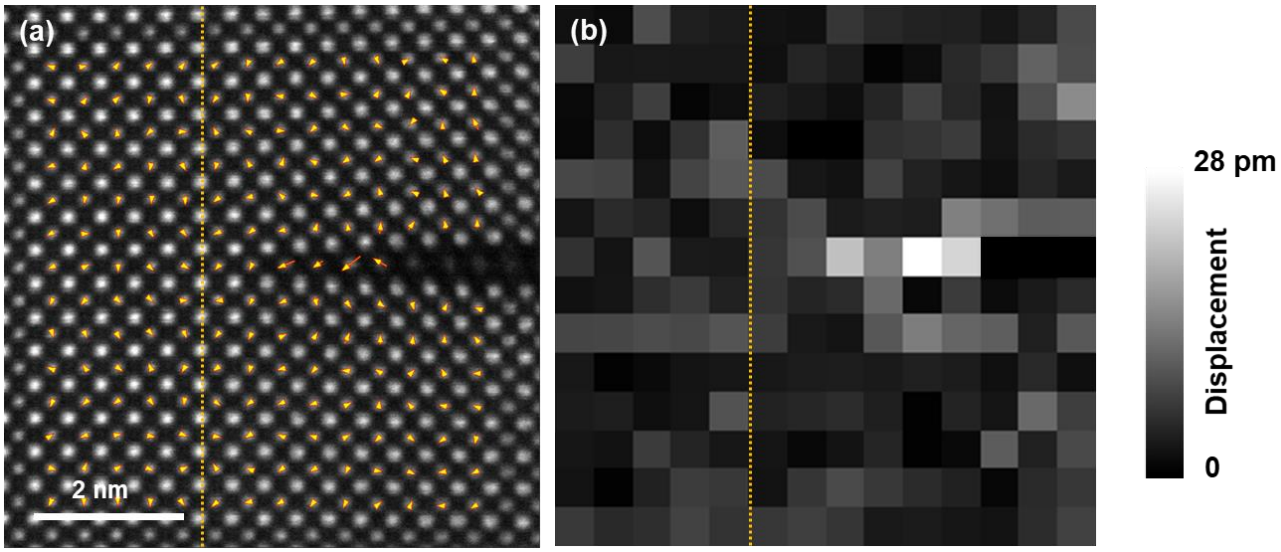

Figure 6-7. Lattice displacement analysis around the shallow crack. (a) Displacement vector map between the TiO and Sr columns overlaid with the HAADF image. The yellow dashed line highlights the interface of SMO and STO. (b) Magnitude map of displacement vectors. The displacement vectors are randomly oriented in the substrate and the SMO lattice surrounding the shallow crack. However, the vectors are aligned at the central unit cell of the shallow crack.

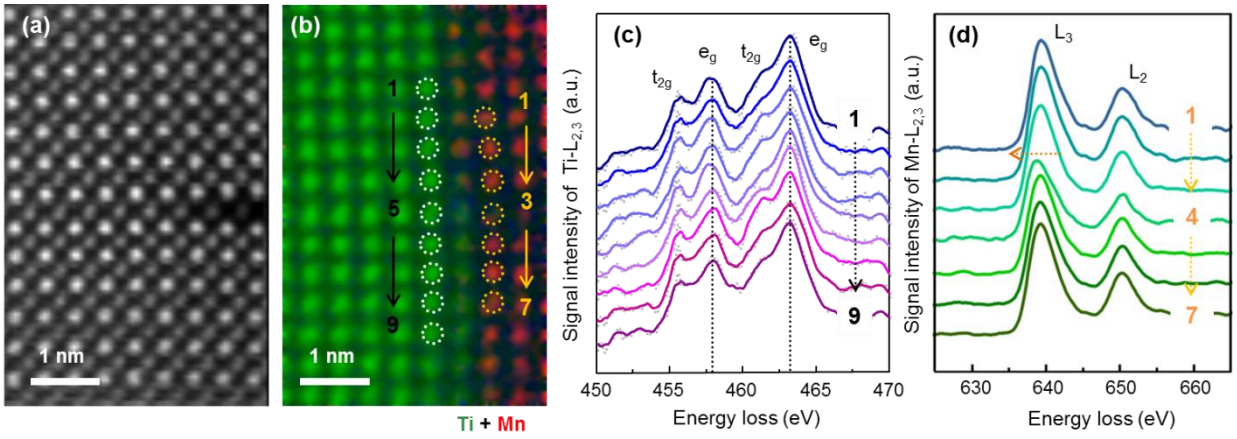

Figure 6-8. STEM-EELS investigations of the shallow crack. (a) HAADF-STEM signal at atomic resolution measured concurrently with EELS. (b) RGB composite image of Mn in red and Ti in green acquired using the Ti-$L_{2,3}$ and Mn-$L_{2,3}$ edges. (c) EELS spectra of the Ti-$L_{2,3}$ edge from position 1 to 9 in (b). (d) EELS spectra of the Mn-$L_{2,3}$ edge from position 1 to 7 in (b). The Mn-$L_{2,3}$ edge shifts to a lower energy loss in the center unit cell (spectrum 4), indicating a reduction of the Mn valence state.

ferroelectricity in SMO [284]. Using the measured strain gradient $d\varepsilon_{yy}/dy$ in the region outside the crack and our noise level in determining the polarization of 13 μC.cm^{-2}, the upper limit for the longitudinal flexoelectric coefficient of SMO is calculated as $1.6 \cdot 10^{-8}$ C/m , which is one order of magnitude smaller than the value observed in ferroelectric SMO [280].

6.4 Conclusion

In summary, I have demonstrated the presence of large flexoelectric polarization at crack tips in STO. Cracks were created in STO by exploiting a thermal-strain relaxation process in SMO thin films. The averaged polarization of 62 ± 16 μC·cm^{-2} around the tip of a deep crack is the largest flexoelectric polarization measured so far. The polarization is screened by an electron density of 0.7 ± 0.1 e^-/uc localized within one unit cell. Both the flexoelectric and electrostatic energy densities were found to be ~3% of the elastic energy. This finding implies that flexoelectricity may influence the processes of crack formation and propagation. Furthermore, unusual electronic and chemical states are presented at crack tips due to large local electronic reconstructions induced by flexoelectric effects.

Contributions to this chapter:

Hongguang Wang carried out the TEM specimen preparation, TEM data acquisition and TEM-related data processing. This chapter has been published in Ref.[220] Hongguang Wang conceived this work, and wrote this chapter. Hans Boschker (MPI-FKF) grew the SMO thin films, did the XRD experiment, and contributed to writing this chapter. Xijie Jiang (TUD) performed the AFM measurement and further data analysis. Yi Wang (MPI-FKF) offered technical support for the determination of atomic displacement around crack tips. Felicitas Predel (MPI-FKF) contributed to the SEM measurement of cracks in the SMO thin film. Peter A. van Aken (MPI-FKF), Jochen Mannhart (MPI-FKF) and Robert W. Stark (TUD) supervised and oversaw this work. All the authors discussed the results and contributed to this chapter.

Chapter 7. Summary and Outlook

This chapter summarizes the research topics and corresponding outcomes in this thesis, and presents an outlook for future studies inspired by related works.

The main objective of this thesis is to study atomic-scale structures and functionalities in quantum matter heterostructures, artificially fabricated with atomic-precise control. For this purpose, epitaxial quantum matter heterostructures of perovskite oxides are grown with atomic layer precision using PLD. STEM and spectroscopy with high spatial resolution are main methods employed to study the lattice structure, local chemistry, and functionality in heterostructures, in particular at the heterointerface, on the atomic scale. High-resolution STEM imaging of heterostructures, in particular at the heterointerface, provides the structural information, including the crystalline quality, misfit strain, and octahedral distortion. Atomically resolved STEM-EELS measurements enable us to analyze the elemental distribution and the bonding environments using ELNES analysis. Based on these techniques, fundamental understanding of quantum matter heterostructures are presented, deciphering the relationship between the structure and behavior of heterostructures.

As summarized in Figure 7-1, this thesis mainly focuses on (i) the optimization of preparing electron-transparent TEM specimen of nano-sized SRO AAs, which is beneficial for high-quality STEM studies, (ii) the linking between magnetic Curie temperature and strain fields of SRO AAs, and the origin of easy axis orientation in terms of lattice anisotropy and octahedral rotation. (iii) Charge distribution at SMO/STO interfaces and underlying mechanisms regarding strain, elemental distribution, oxygen vacancies, and the space-charge effect, *etc.*, and (vi) visualizing the flexoelectricity around crack tips and revealing the role of flexoelectricity during crack propagation.

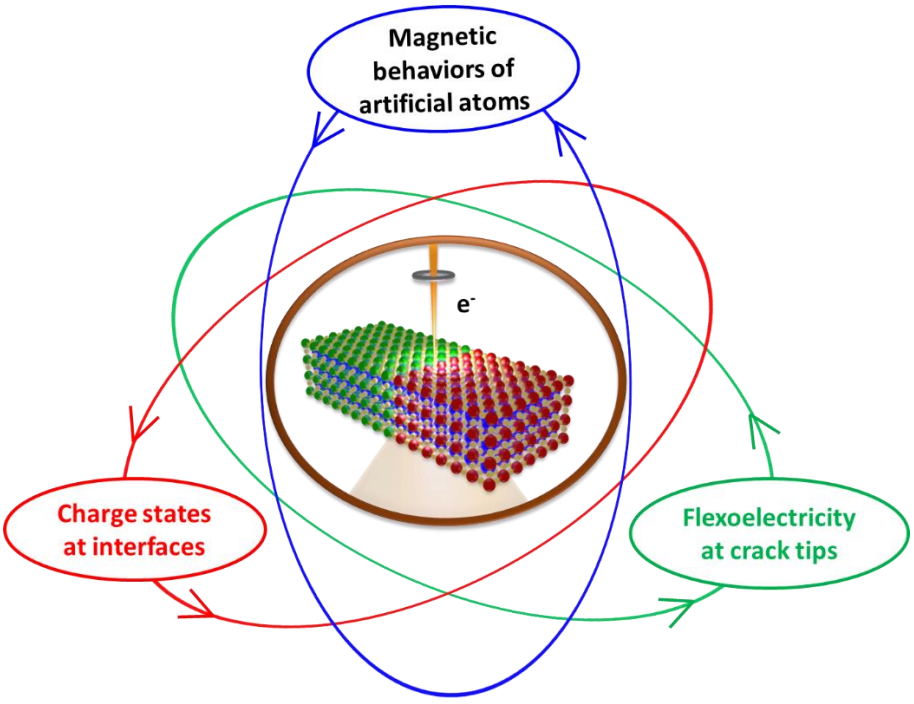

Figure 7-1. Schematic summary of this thesis. The central sketch describes the STEM investigations of electron-transparent TEM specimens prepared by reported methods in chapter 3. The applications of STEM in this thesis are magnetic behaviors of artificial atoms, charge states at interfaces, flexoelectricity at crack tips, which correspond to chapters 4, 5, 6, respectively.

In chapter 1, the motivation of the research in this thesis was firstly introduced, whilst the tremendous advantages of electron microscopy-related techniques were highlighted. Starting from a brief description of the idea of quantum matter heterostructures and its fascinating characteristics, I discussed the unprecedented phenomena at the heterointerface with an emphasis on the effects of epitaxial strain and charge distribution. Next, quantum confinement of the electron system was introduced with a focus on the progress and challenges of quantum confinement of strongly-correlated electron systems. Furthermore, I discussed the nanoscale flexoelectricity and its relation to the cracking process, indicating the necessity of atomic-scale observations. An overview of this dissertation is presented at the end.

In chapter 2, all experimental methodologies applied in this thesis, including sample growth and fabrication techniques, characterization methods, TEM data processing, and corresponding simulation tools, were explained. The schematic illustrations of the PLD growth of thin films and the EBL process are displayed, showing the basic principle and experimental steps. Then, I made a detailed explanation of the aberration-corrected STEM and related techniques, *e.g.*, HAADF and ABF imaging, EELS, and EDS, which are frequently used in this thesis. The working principle for SEM and AFM was briefly depicted. As an essential tool for quantitative analysis of STEM images, strain analysis by GPA and lattice-deformation determination by Gaussian fitting were introduced. QSTEM and μSTEM simulations are also discussed, which are employed to verify the STEM images and STEM-EELS maps in this thesis.

In chapter 3, I presented methods for preparing electron-transparent TEM specimen of heterostructures. This chapter focuses on showing an optimized pathway to address the challenge of TEM specimen preparation of quantum nanostructures. The fabricated AAs in this work are as small as 15 nm with a spacing of about 100 nm, making the TEM sample preparation with traditional TP&IM very challenging. Because AAs cannot be located during the TP&IM process, detecting them in the final TEM lamellae is by mere chance. Furthermore, TEM specimens by TP&IM offer a limited thin region, the possibility of finding a complete quantum dot structure that was sliced through its center is significantly reduced. Through optimizing the experimental procedures, I demonstrated that the combination of FIB&NM has several advantages that can be applied for efficiently preparing high-quality and damage-free TEM specimens consisting of AAs: (i) a FIB lamella thinned into multiple regions enhances the probability of finding a complete dot structure whilst reducing sample bending, (ii) the probability for nanostructures cut through their centers is increased, when cutting the lamella with a certain angle, which depends on the size and spacing of AAs, (iii) the use of the NanoMill enables to make a flat and clean TEM specimen without introducing additional damage.

The optimization of the FIB&NM sample preparation in this chapter establishes a basis for our STEM investigations in chapter 4. I believe that our optimization will also be beneficial for STEM studies of other emerging quantum nanostructures. Moreover, the detailed settings of the used techniques, including TP, IM, FIB, and NM, will be useful for people working in this field.

In chapter 4, using a combination of EBL and dry etching with Ar ions, I succeeded in fabricating SRO AAs as small as 15 nm, which was never achieved before for this class of materials. Both the original SRO thin film and the AAs were demonstrated to have high quality without visible defects. HAADF-STEM and STEM-EELS observations confirmed that the material preserves the original epitaxial quality after patterning, maintaining the structural integrity and interfacial chemical environments. With SQUID measurements, interesting magnetic properties of the patterned array of AAs were found. Firstly, a gradual increase of T_C occurs with shrinking dot size, starting from T_C = 149 ± 1 K in thin films and dots> 200 nm and reaching a maximum of $T_C \approx$ 157 K at a dot size of 35-40 nm. STEM-based GPA was employed to quantify the strain fields of the AAs as a function of the size, revealing a relaxation of compressive strain

with the decrease of the dot size. This strain relaxation has the same trend with T_C variation and thereby leads to the T_C change, which is in good agreement with the literature. Furthermore, the magnetic easy axis tends to reorient toward in-plane with reducing the size of AAs. Quantitative STEM measurements unveiled the lattice anisotropy and rotation of oxygen octahedra in SRO and with decreasing size of AAs, explaining the easy axis rotation.

In this work, I presented interesting characteristics in terms of magnetic properties and structural modifications resulting from the spatial confinement in patterned SRO AAs. For future work, fabricating the AAs with a smaller size down to several nanometers may lead to unprecedented phenomena. Since the interaction between AAs in this work is very weak due to their large spacing with about 100 nm, decreasing their spacing and studying their magnetic interactions would be very interesting as well. Furthermore, many possibilities can be expected, if we fabricate the array into different arrangements or use other material with correlated electron systems. From the perspective of microscopy, to map the magnetic field at low temperature with Lorentz microscopy or 4D-STEM would be very informative to reveal the confined magnetic field in an individual artificial atom and their interaction with each other.

In chapter 5, through studying the heterointerface between epitaxial grown SMO and STO using STEM and spectroscopy, a comprehensive description of the interfacial charge distribution and formation mechanisms at oxide interfaces is provided. As a crucial factor in controlling the interfacial behaviors, the study of interfacial charge distribution has attracted much research attention. However, the understanding of the interfacial charge state is still inadequate owing to the limitation in characterization techniques and the complexity at interfaces.

The epitaxial SMO thin film was grown on TiO_2-terminated (001)-oriented STO substrates with atomic-layer precision using PLD. ELNES analysis of the Mn-$L_{2,3}$, Ti-$L_{2,3,}$ and O-K edges indicate the electronic charge accumulation on the SMO side of STO/SMO interfaces. The charge density reaches a maximum (ca. 0.13±0.07 e^-/uc) at the first SMO monolayer. Quantitative studies of the atomically resolved HAADF-STEM and ABF-STEM images reveal the interfacial strain field, showing that the SMO lattice is fully in-plane strained by the STO substrate in the first 3 unit cells and then gradually relaxes as moving away from the interface. The elemental distribution around the interface was analyzed as well based on STEM-EELS mapping. Combined with μSTEM simulations of the corresponding EELS mapping, I confirmed the asymmetric elemental distribution around the interface, showing conspicuous cationic intermixing between Mn and Ti in the first 3 unit cell of SMO. The role of epitaxial strain and cationic intermixing on the interfacial charge accumulation were evaluated by first-principles calculations. The interfacial tensile strain acts as a driving force by promoting the formation of oxygen vacancies, while the cationic intermixing plays an obstructing role in the charge accumulation by compensating the strain effects and reducing oxygen vacancies. Besides, charge transfer from STO to SMO due to the mismatch of their Fermi level may contribute to the charge accumulation. Furthermore, possible space-charge effects at the interface are also discussed.

Through detailed experimental and theoretical investigations, this work offers an in-depth understanding of fundamental mechanisms of the interface charge accumulation. The ideas are expected to be beneficial for engineering the charge density and distribution to manipulate the interfacial behavior. For example, the role of cationic intermixing on forming oxygen vacancies turn from negative to positive, if we select a proper substrate material. The role of other factors is also tunable by the combination of different materials.

In chapter 6, cracks were created in STO by exploiting a thermal-strain relaxation process in SMO thin films and demonstrated the presence of large flexoelectric polarization at crack tips in. Two types of cracks are found, namely, deep cracks and shallow cracks. Using STEM-based GPA, the strain gradient around

crack tips were analyzed, indicating a huge strain gradient with a magnitude as high as 3.0 nm^{-1} around the tip of deep cracks. Further quantification of atomically resolved HAADF-STEM images identified the electrical polarization around crack tips, where the tip of the deep crack acts as a 180° domain wall with a head-to-head configuration. The averaged polarization of 62 ± 16 $\mu C \cdot cm^{-2}$ around the tip of a deep crack is the largest flexoelectric polarization measured so far. The flexoelectric coefficient of STO at the crack tip is about $3 \cdot 10^{-9}$ C/m, in good agreement with literature data. An electron density of 0.7 ± 0.1 e^-/uc localized within one unit cell screens the flexoelectric polarization, which was evidenced by STEM-EELS measurements. The case of shallow cracks was also studied, showing a weak flexoelectric effect due to a weak strain gradient. Furthermore, the flexoelectric energy density, electrostatic energy density, and the elastic energy density were calculated, respectively. The flexoelectric energy density was found to be ~3% of the elastic energy, implying that flexoelectricity may influence the processes of crack formation and propagation. Since the crack tip presents electric dipole and charge redistribution on the atomic scale, a straightforward 2D mapping of the electric field and charge density around crack tips with 4D-STEM studies would be an exciting topic for future research.

Throughout this thesis, aberration-corrected STEM observations bring us to a fascinating atomic world in quantum matter heterostructures with emergent phenomena. The interaction between degrees of freedom, which host the exotic physical states, are designed and probed at the atomic-scale. This thesis provides an in-depth understanding of the atomic-scale structure-property correlations in quantum matter heterostructures, which is instructive and beneficial for making new electronic devices for emerging technologies.

Appendix

A Interfacial elemental distribution in SRO thin film by STEM-EELS

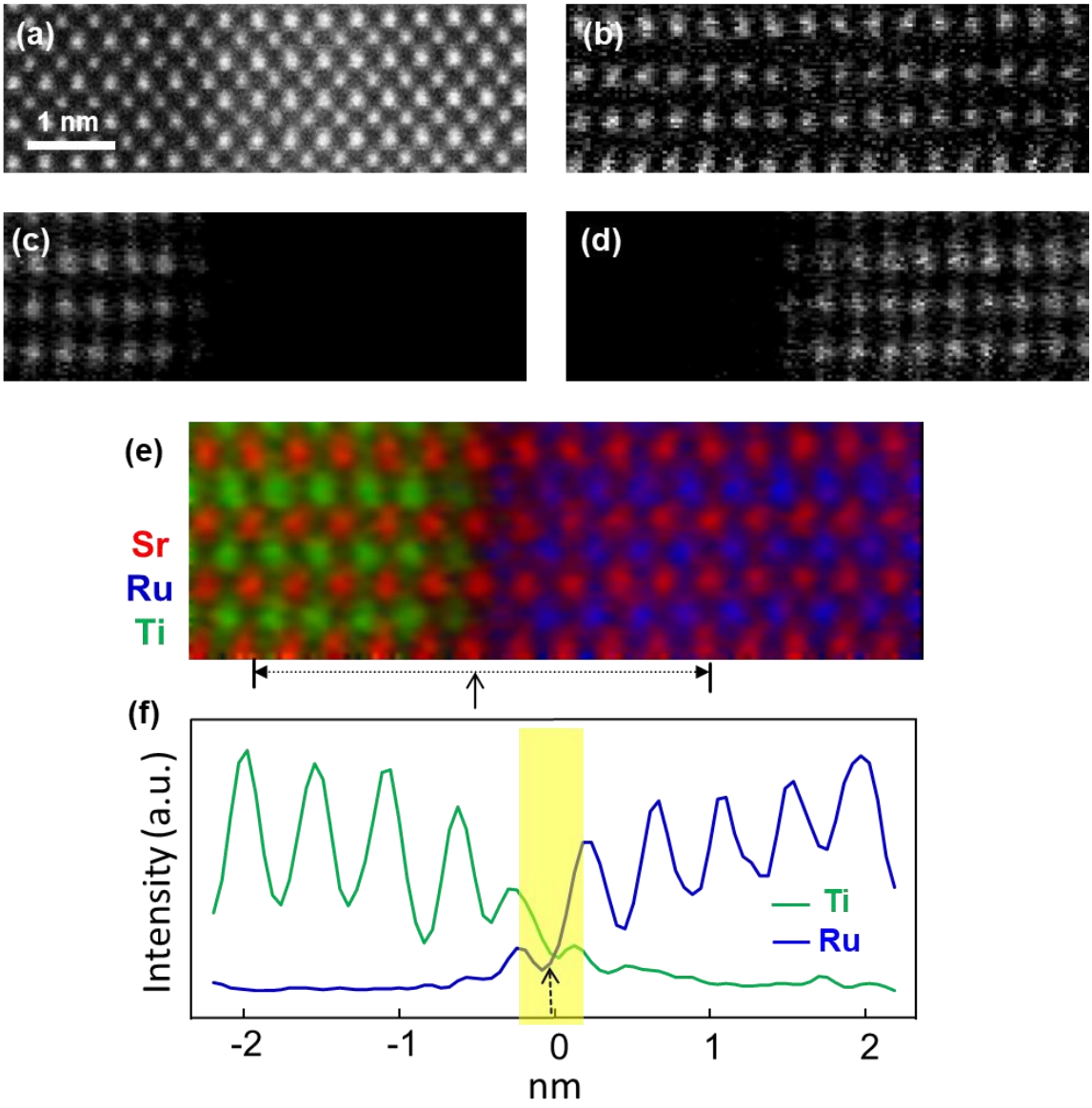

Figure A-1. Elemental distribution at the interface of SRO thin film. (a) the HAADF-STEM image of one region close to the interface. Elemental maps for (b) Sr from Sr-$L_{2,3}$ edge signal, (c) Ti from Ti-$L_{2,3}$ edge signal and (d) Ru from Ru-$L_{2,3}$ edge signal. (e) The composite map with Sr (red), Ru (blue) and Ti (green). (f) The corresponding signal intensity of Ti and Ru in the interfacial region. The yellow shaded region indicates the interdiffusion of the Ti and Ru signals.

STEM-EELS spectrum images in Figure A-1 display the distribution of Sr, Ti, Ru close to the interface in SRO thin films. As shown in Figure A-1(f), the intermixing of Ru and Ti occurs within one unit cell on both sides of the interface, which is in good agreement with that of the patterned AAs. It demonstrates that the local chemistry around the interface remains unchanged during the patterning process.

B First-principles calculations

The formation energy of an oxygen vacancy in the SMO system was calculated using VASP (Vienna *Ab initio* Simulation Package). The generalized gradient approximation (GGA) was employed with the exchange-correlation functional of Perdew-Burke-Ernzerhof (PBE). The cutoff energy was set to 500 eV. The projector augmented wave (PAW) method was used to describe electron-core interactions with Sr ($4s^2$, $4p^6$, $5s^2$), Mn ($3s^2$, $3p^6$, $3d^5$, $4s^2$), Ti ($3s^2$, $3p^6$, $3d^2$, $4s^2$), and O ($2s^2$, $2p^4$) shells treated as valence electrons. For the relaxation calculation, convergence criteria for the maximum force on each atom and the total energy were 0.01 eV/Å and 5×10^{-5} eV, respectively. During the relaxation calculations in the case of in-plane strained SMO, the in-plane lattice parameters (*a* and *b*) are fixed, while the lattice parameter c and internal coordinates of all atoms are fully relaxed. In the relaxation calculations of $Sr_8Ti_xMn_{8-x}O_{24}$ (x=0, 1, …, 8) (as shown in Figure 5-12), the experimentally measured lattice parameters a=7.81 Å and c=7.68 Å are fixed, and the internal coordinates of all atoms are fully relaxed. In the self-consistent calculations of the total energy, an energy convergence criterion of 10^{-5} eV was used. A Coulomb interaction of U=2.7 eV and on-site exchange interaction of J=1.0 eV were used to treat the Mn-*d* electrons.[300] For Ti-*d* electrons, we used U=3.2 eV, J=0.9 eV.[301] All calculations were performed using 2×2×2 supercells constructed from an orthorhombic unit cell with five atoms.[300] The convergence test indicated that the 5×5×5 Γ-centered *k* mesh was sufficient. The oxygen vacancy formation energy E_{form} was computed by $E_{\text{form}} = E^{\text{Vo}} + E^{\text{o}} - E^{\text{noVo}}$, in which E^{Vo}, E^{o}, and E^{noVo} denote the total energy of supercell with one oxygen vacancy, an oxygen atom, and supercell without oxygen vacancy, respectively.

C Supplemental information for the study of cracks

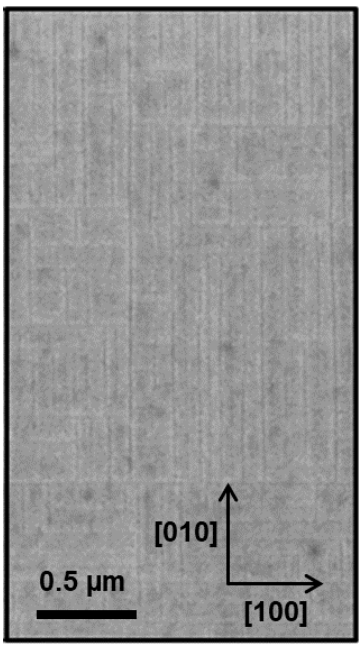

Figure C-1. SEM image of the surface of a SMO film showing the presence of long cracks parallel to the [100] and [010] lattice directions.

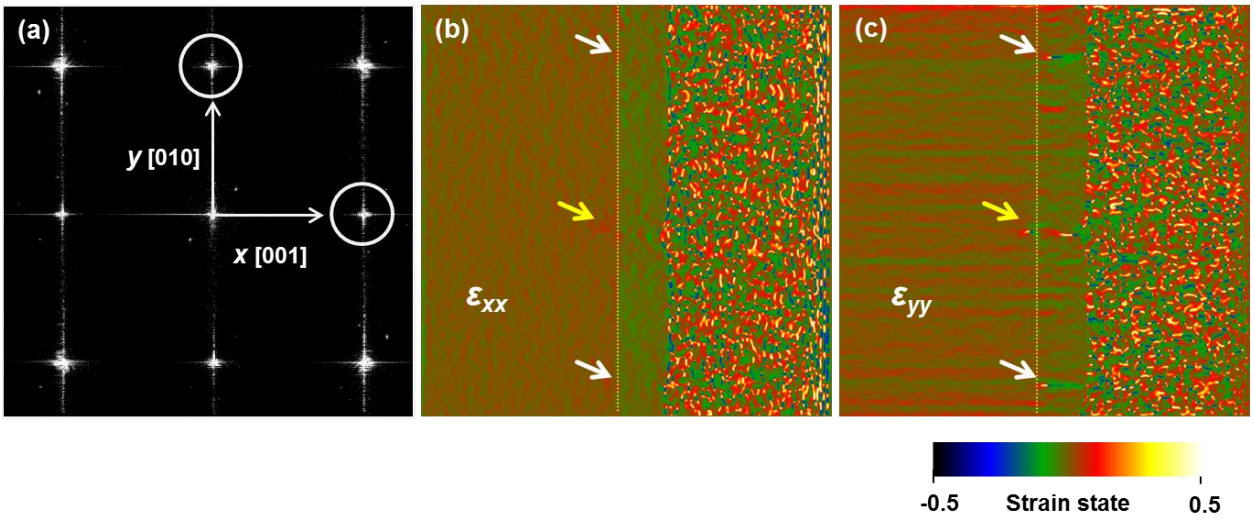

Figure C-2. Strain analysis of the overview image in Figure 2a. **(a)** Corresponding FFT image of the overview image. The selected reflections for strain tensor calculations are marked by white circles. **(b)** and **(c)** are the out-of-plane (ε_{xx}) and in-plane (ε_{yy}) strain components obtained by GPA analysis.

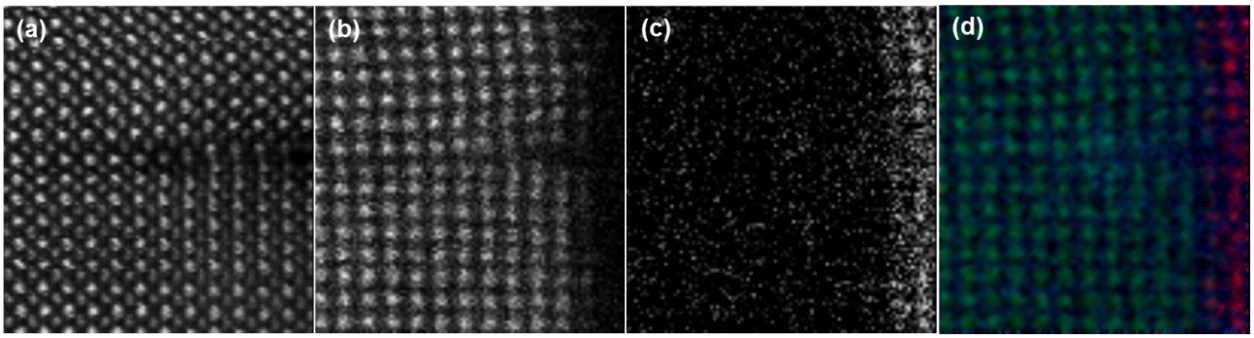

Figure C-3. STEM-EELS spectrum imaging at the deep crack. **(a)** HAADF-STEM signal at atomic resolution measured concurrently with EELS. **(b)** The map of Ti-$L_{2,3}$ edge signal. **(c)** The map of Mn-$L_{2,3}$ edge signal. **(d)** RGB composite image of Mn (red) and Ti (green). I do not observe the diffusion of Mn into the tip of the crack.

Strain gradients. Maps of all strain gradients are presented in Figure A-4. The largest strain gradients are found in $d\varepsilon_{yy}/dx$ and $d\varepsilon_{yy}/dy$. The strain gradients $d\varepsilon_{xy}/dy$ and $d\varepsilon_{xy}/dx$ are slightly smaller and confined to a smaller area. The strain gradients $d\varepsilon_{xx}/dx$ and $d\varepsilon_{xx}/dy$ are negligible. Therefore, I focus on the gradients in ε_{yy}. By symmetry, $d\varepsilon_{yy}/dx$ induces polarization along x, and $d\varepsilon_{yy}/dy$ induces polarization along y. For $d\varepsilon_{yy}/dx$, the largest polarization is expected below the tip of the crack and for $d\varepsilon_{yy}/dy$, the largest polarization is expected on both sides of the tip of the crack. Since I only measure polarization at the sides of the crack and since this polarization is predominantly oriented along y, I attribute the polarization to the flexoelectric effect caused by $d\varepsilon_{yy}/dy$. The absence of polarization aligned along x below the tip of the crack indicates that the μ_{12} component of the flexoelectric tensor is smaller than the μ_{11} component discussed in this chapter. I find $\mu_{12} < 10^{-9}$ C/m.

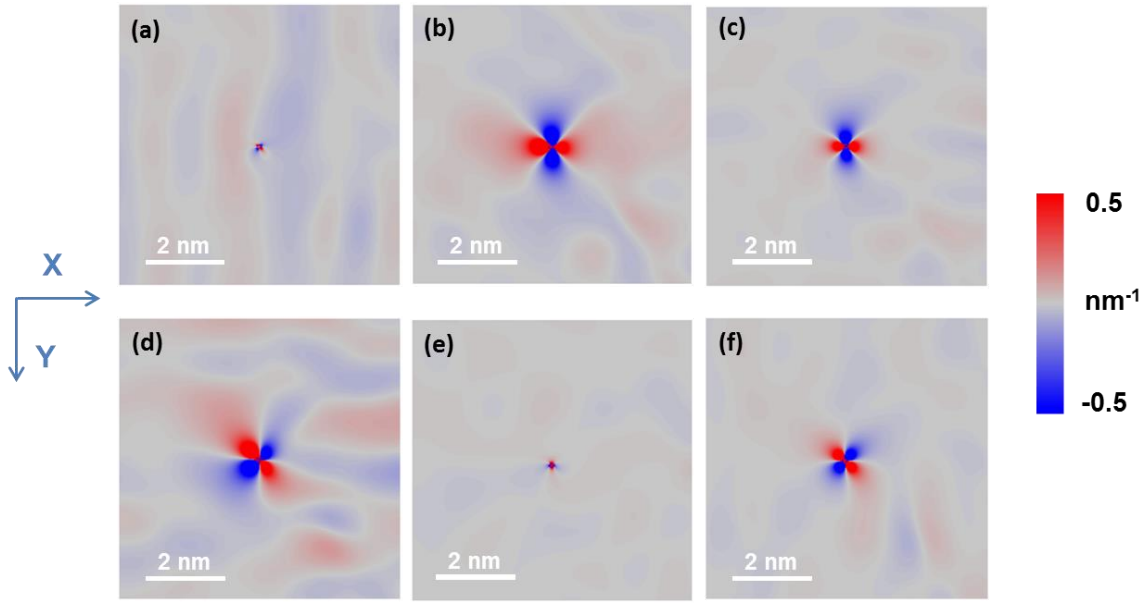

Figure C-4. Calculated strain gradient components for the deep crack. **(a)** $d\varepsilon_{xx}/dx$, **(b)** $d\varepsilon_{yy}/dx$, **(c)** $d\varepsilon_{xy}/dy$, **(d)** $d\varepsilon_{yy}/dy$, **(e)** $d\varepsilon_{xx}/dy$, **(f)** $d\varepsilon_{xy}/dx$. The coordinate describes the positive strain gradient along the X and Y directions.

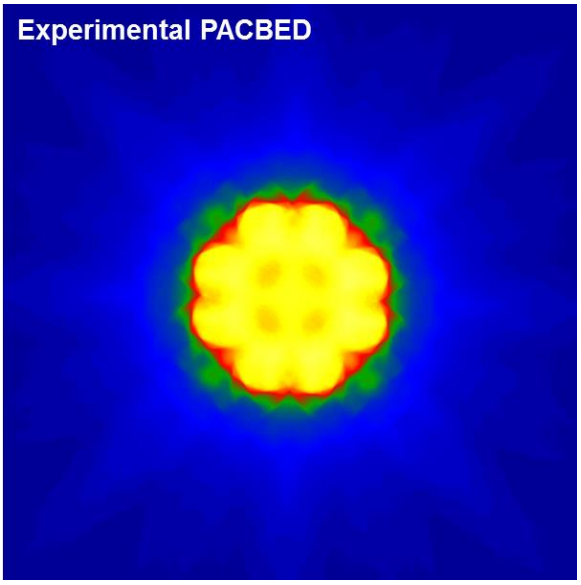

Figure C-5. PACBED pattern of the analyzed area. The highly centrosymmetric pattern indicates the good alignment of the sample during STEM imaging, which is essential for obtaining reliable polarization results.

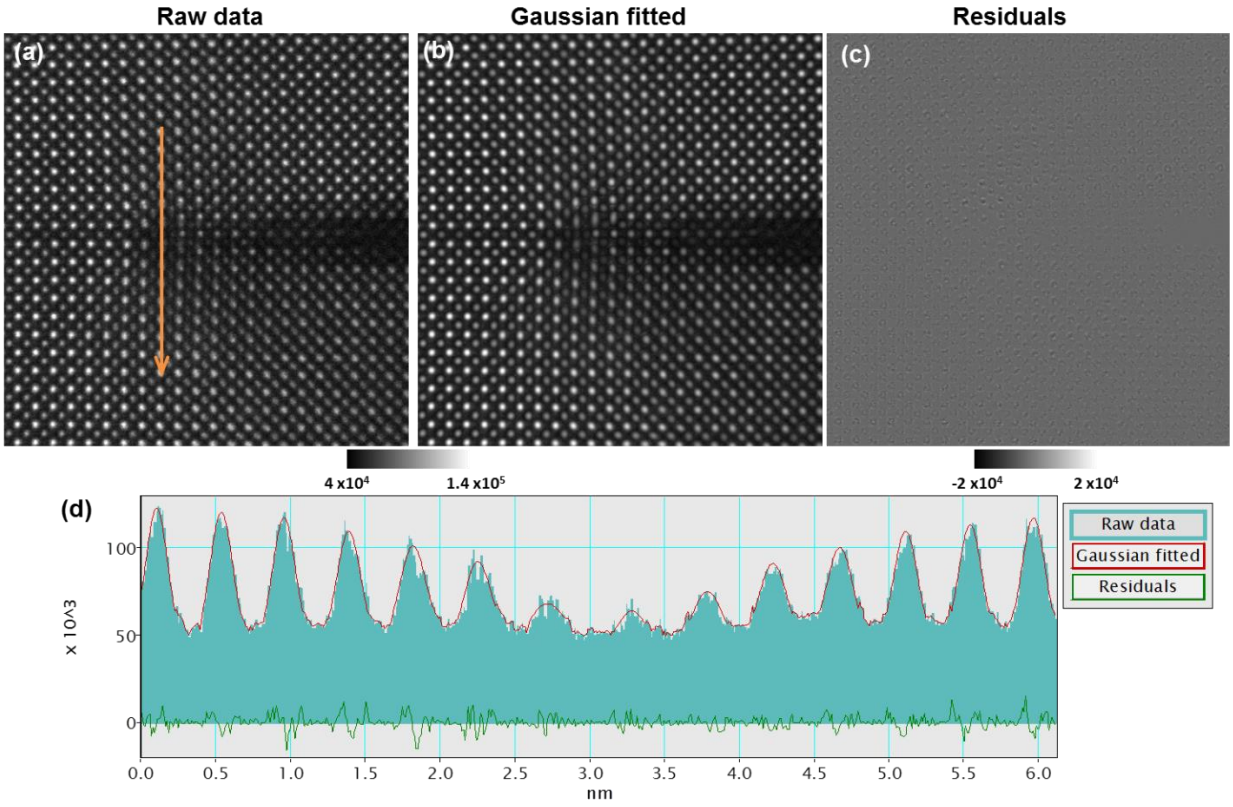

Figure C-6. Gaussian fitting around the deep crack. (a) Experimental HAADF-STEM image of the deep crack from Figure 6-4(a). (b) The Gaussian fitted image. (c) The residuals image, which is the difference between the raw data and the Gaussian fitted image. (d) The intensity profile (blue) of the yellow line marked in (a) with the fitted profile (red) and the profile of residuals (green) after the Gaussian fitting. As can be seen from the line profiles, the intensity of the residuals is one order of magnitude smaller in comparison with the intensity of the raw image. Therefore, the Gaussian fitted image is used to extract the polarization.

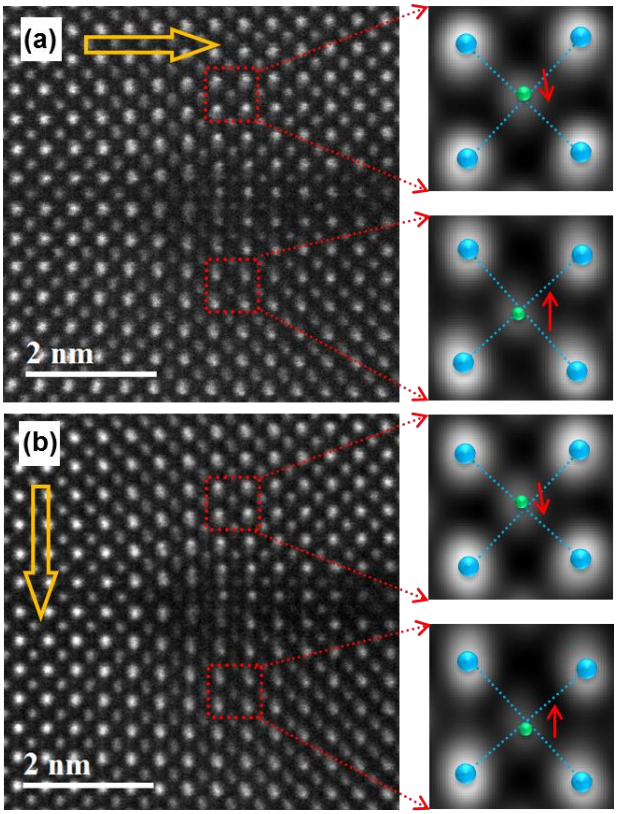

Figure C-7. HAADF-STEM image of one deep crack region obtained by scanning the electron beam along with the horizontal **(a)** and the longitudinal **(b)** directions. The displacements under different scan directions remain unchanged. This result indicates that the atomic displacements are intrinsic to the sample and independent of the scan direction of the electron beam.

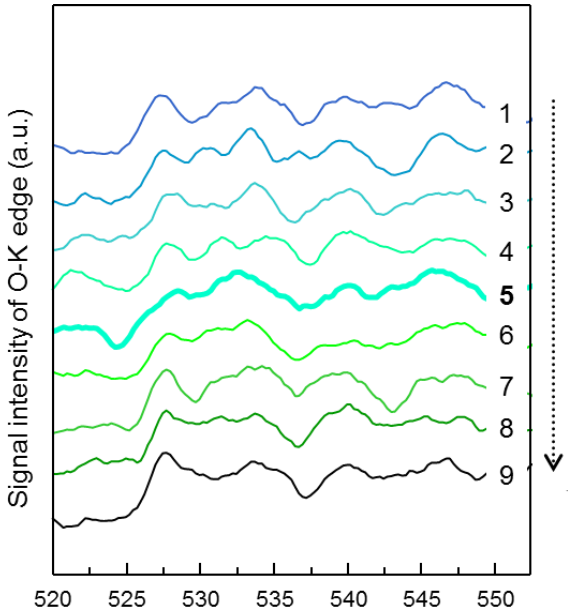

Figure C-8. EELS spectra of the O-K edge from position 1 to 9 in Fig. 5(a) surrounding the deep crack. Position 5 is located at the tip of the deep crack. I can observe changes in the O-K edge pre-peak at the central unit cell of the crack tip (Figure 4 of this reply), indicating that oxygen vacancies may emerge at the crack tip. However, atomic rearrangement leading to exotic coordination states, Ti valence change, and structural defects at the crack tip can be reasons for the variation of the O-K edge pre-peak as well.

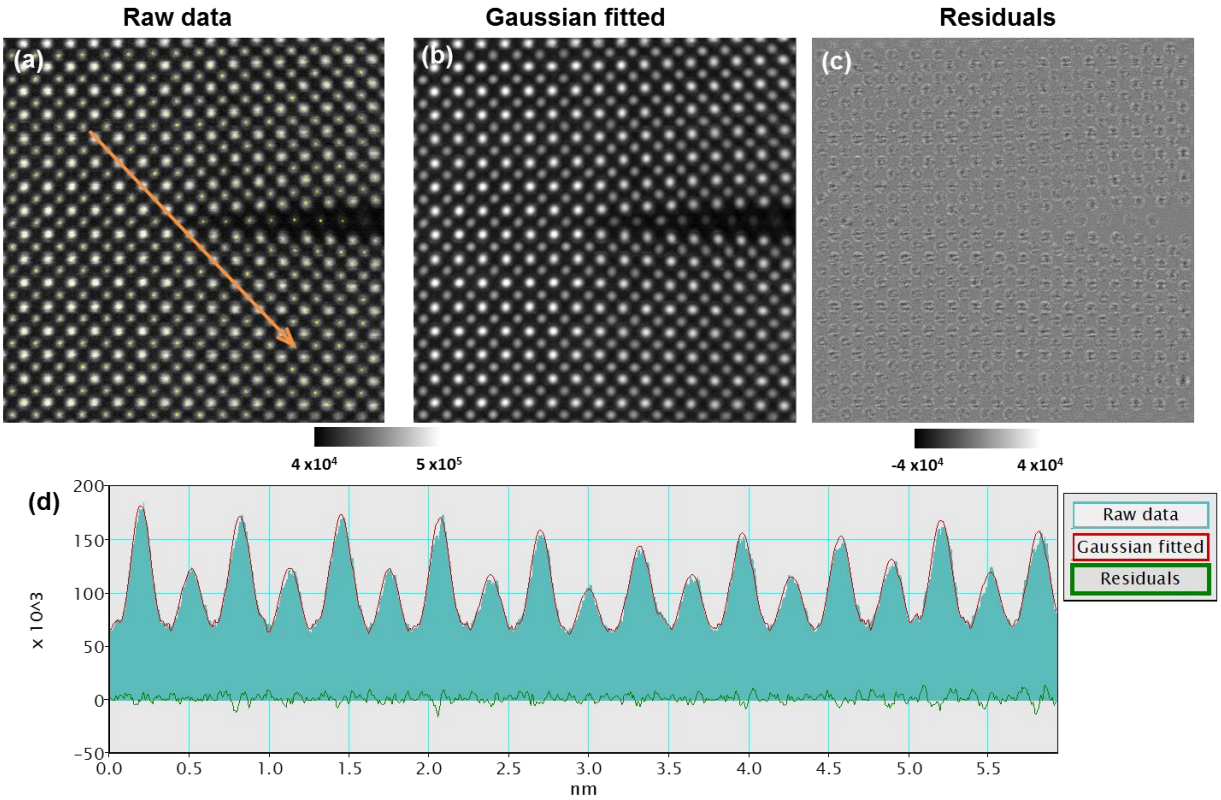

Figure C-9. Gaussian fitting around the shallow crack. (a) Experimental HAADF-STEM image of the shallow crack from Figure 6-7(a). (b) The Gaussian fitted image. (c) The residuals image, which is the difference between the raw data and the Gaussian fitted image. (d) The intensity profile (blue) of the yellow line marked in (a) with the fitted profile (red) and the profile of residuals (green) after the Gaussian fitting.

M.Sc. Hongguang Wang
Heisenbergstr. 1,
70569 Stuttgart

Declaration

Hereby I declare that this thesis titled, "Atomic Scale Investigation of Structures and Functionalities in Quantum Matter Heteroepitaxy" has been independently carried out by me at the Stuttgart Center for Electron Microscopy (StEM), Max Planck Institute for Solid State Research in fulfillment of the requirements for the degree of Doctor of Rerum Naturalium (Dr. rer. nat.) in the Department of Materials and Geosciences at the Technical University of Darmstadt (TU Darmstadt). I certify that the work presented in this thesis is, to the best of my knowledge and belief, original and contains no material previously published or written by another person, except where due reference and permission is made.

Stuttgart

18.09.2020

Hongguang Wang

MAX-PLANCK-GESELLSCHAFT

TECHNISCHE UNIVERSITÄT DARMSTADT

Bibliography

1. Tokura, Y.; Hwang, H. Y., Condensed-matter physics: Complex oxides on fire. *Nature materials* **2008,** *7* (9), 694-695.

2. Gazquez, J.; Sanchez-Santolino, G.; Biskup, N.; Roldan, M. A.; Cabero, M.; Pennycook, S. J.; Varela, M., Applications of STEM-EELS to complex oxides. *Materials Science in Semiconductor Processing* **2017,** *65*, 49-63.

3. Wu, S.; Cybart, S. A.; Yu, P.; Rossell, M.; Zhang, J.; Ramesh, R.; Dynes, R., Reversible electric control of exchange bias in a multiferroic field-effect device. *Nature materials* **2010,** *9* (9), 756-761.

4. Keimer, B.; Moore, J. E., The physics of quantum materials. *Nature Physics* **2017,** *13* (11), 1045-1055.

5. The rise of quantum materials. *Nature Physics* **2016,** *12* (2), 105-105.

6. Ball, P., Quantum materials: Where many paths meet. *MRS Bulletin* **2017,** *42* (10), 698-705.

7. Lu, D.; Vishik, I. M.; Yi, M.; Chen, Y.; Moore, R. G.; Shen, Z.-X., Angle-resolved photoemission studies of quantum materials. *Annual Review of Condensed Matter Physics* **2012,** *3* (1), 129-167.

8. Tokura, Y.; Kawasaki, M.; Nagaosa, N., Emergent functions of quantum materials. *Nature Physics* **2017,** *13* (11), 1056-1068.

9. Boschker, H.; Mannhart, J., Quantum-matter heterostructures. *Annual Review of Condensed Matter Physics* **2017,** *8*, 145-164.

10. Liu, M.; Sternbach, A. J.; Basov, D., Nanoscale electrodynamics of strongly correlated quantum materials. *Reports on Progress in Physics* **2016,** *80* (1), 014501.

11. Zubko, P.; Gariglio, S.; Gabay, M.; Ghosez, P.; Triscone, J. M., Interface physics in complex oxide heterostructures. *Annual Review of Condensed Matter Physics, Vol 2* **2011,** *2* (1), 141-165.

12. Huang, Z.; Ariando; Renshaw Wang, X.; Rusydi, A.; Chen, J.; Yang, H.; Venkatesan, T., Interface engineering and emergent phenomena in oxide heterostructures. *Advanced materials* **2018,** *30* (47), e1802439.

13. Hwang, H. Y.; Iwasa, Y.; Kawasaki, M.; Keimer, B.; Nagaosa, N.; Tokura, Y., Emergent phenomena at oxide interfaces. *Nature materials* **2012,** *11* (2), 103-113.

14. S. Thiel, G. H., Schmehl C, W. Schneider, J. Mannhart, Tunable Quasi–two-dimensional electron gases in oxide heterostructures. *Science* **2006,** *313*.

15. Ohtomo, A.; Hwang, H. Y., A high-mobility electron gas at the $LaAlO_3/SrTiO_3$ heterointerface. *Nature* **2004,** *427* (6973), 423-426.

16. Mannhart, J.; Boschker, H.; Kopp, T.; Valenti, R., Artificial atoms based on correlated materials. *Reports on progress in physics. Physical Society* **2016,** *79* (8), 084508.

17. Zhu, J.; Li, H.; Zhong, L.; Xiao, P.; Xu, X.; Yang, X.; Zhao, Z.; Li, J., Perovskite oxides: preparation, characterizations, and applications in heterogeneous catalysis. *ACS Catalysis* **2014,** *4* (9), 2917-2940.

18. Grabowska, E., Selected perovskite oxides: characterization, preparation and photocatalytic properties—a review. *Applied Catalysis B: Environmental* **2016,** *186*, 97-126.

19. Voorhoeve, R.; Johnson, D.; Remeika, J.; Gallagher, P., Perovskite oxides: materials science in catalysis. *Science* **1977,** *195* (4281), 827-833.

20. Sgourou, E. N.; Panayiotatos, Y.; Davazoglou, K.; Solovjov, A. L.; Vovk, R. V.; Chroneos, A., Self-diffusion in perovskite and perovskite related oxides: Insights from modelling. *Applied Sciences* **2020,** *10* (7), 2286.

21. Goldschmidt, V. M., Die Gesetze der Krystallochemie. *Naturwissenschaften* **1926,** *14* (21), 477-485.

22. Pena, M.; Fierro, J., Chemical structures and performance of perovskite oxides. *Chemical reviews* **2001,** *101* (7), 1981-2018.

23. Kubicek, M.; Bork, A. H.; Rupp, J. L., Perovskite oxides–a review on a versatile material class for solar-to-fuel conversion processes. *Journal of Materials Chemistry A* **2017,** *5* (24), 11983-12000.

24. Fowlie, J., Introduction to Perovskite Oxides. In *Electronic and Structural Properties of $LaNiO_3$-Based Heterostructures*, Springer International Publishing: Cham, 2019; pp 1-8.

25. Tokura, Y.; Nagaosa, N., Orbital physics in transition-metal oxides. *Science* **2000,** *288* (5465), 462-468.

26. Tokura, Y., Critical features of colossal magnetoresistive manganites. *Reports on Progress in Physics* **2006,** *69* (3), 797.

27. Sawada, H.; Terakura, K., Orbital and magnetic orderings in localized t_{2g} systems, $YTiO_3$ and YVO_3: Comparison with a more itinerant e g system $LaMnO_3$. *Physical Review B* **1998,** *58* (11), 6831.

28. Kroemer, H., Nobel Lecture: Quasielectric fields and band offsets: teaching electrons new tricks. *Reviews of modern physics* **2001,** *73* (3), 783.

29. Rondinelli, J. M.; May, S. J., Oxide interfaces: Instrumental insights. *Nature materials* **2012,** *11* (10), 833-834.

30. Nie, Y.; Zhu, Y.; Lee, C.-H.; Kourkoutis, L. F.; Mundy, J. A.; Junquera, J.; Ghosez, P.; Baek, D.; Sung, S.; Xi, X., Atomically precise interfaces from non-stoichiometric deposition. *Nature communications* **2014,** *5* (1), 1-8.

31. Biswas, A.; Jeong, Y. H., Strain effect in epitaxial oxide heterostructures. In *Epitaxy*, IntechOpen: 2017.

32. Zembilgotov, A.; Pertsev, N.; Böttger, U.; Waser, R., Effect of anisotropic in-plane strains on phase states and dielectric properties of epitaxial ferroelectric thin films. *Applied Physics Letters* **2005,** *86* (5), 052903.

33. Haeni, J.; Irvin, P.; Chang, W.; Uecker, R.; Reiche, P.; Li, Y.; Choudhury, S.; Tian, W.; Hawley, M.; Craigo, B., Room-temperature ferroelectricity in strained $SrTiO_3$. *Nature* **2004,** *430* (7001), 758-761.

34. Schlom, D. G.; Chen, L. Q.; Eom, C. B.; Rabe, K. M.; Streiffer, S. K.; Triscone, J. M., Strain tuning of ferroelectric thin films. *Annual Review of Materials Research* **2007,** *37*, 589-626.

35. Becher, C.; Maurel, L.; Aschauer, U.; Lilienblum, M.; Magen, C.; Meier, D.; Langenberg, E.; Trassin, M.; Blasco, J.; Krug, I. P.; Algarabel, P. A.; Spaldin, N. A.; Pardo, J. A.; Fiebig, M., Strain-induced coupling of electrical polarization and structural defects in $SrMnO_3$ films. *Nature nanotechnology* **2015,** *10* (8), 661-665.

36. Jung, C. U.; Yamada, H.; Kawasaki, M.; Tokura, Y., Magnetic anisotropy control of SrRuO3 films by tunable epitaxial strain. *Applied Physics Letters* **2004,** *84* (14), 2590-2592.

37. Takahashi, K. S.; Kawasaki, M.; Tokura, Y., Interface ferromagnetism in oxide superlattices of $CaMnO_3$/$CaRuO_3$. *Applied Physics Letters* **2001,** *79* (9), 1324-1326.

38. Zhong, Z. C.; Hansmann, P., Band alignment and charge transfer in complex oxide interfaces. *Physical Review X* **2017,** *7* (1), 011023.

39. Nishimura, J.; Ohtomo, A.; Ohkubo, A.; Murakami, Y.; Kawasaki, M., Controlled carrier generation at a polarity-discontinued perovskite heterointerface. *Japanese journal of applied physics* **2004,** *43* (8A), L1032.

40. Chen, H.; Kolpak, A. M.; Ismail-Beigi, S., Fundamental asymmetry in interfacial electronic reconstruction between insulating oxides: An ab initio study. *Physical Review B* **2009,** *79* (16), 161402.

41. McCollam, A.; Wenderich, S.; Kruize, M.; Guduru, V.; Molegraaf, H.; Huijben, M.; Koster, G.; Blank, D. H.; Rijnders, G.; Brinkman, A., Quantum oscillations and subband properties of the two-dimensional electron gas at the $LaAlO_3/SrTiO_3$ interface. *APL materials* **2014,** *2* (2), 022102.

42. Ohtomo, A.; Muller, D. A.; Grazul, J. L.; Hwang, H. Y., Artificial charge-modulationin atomic-scale perovskite titanate superlattices. *Nature* **2002,** *419* (6905), 378-380.

43. Willmott, P.; Pauli, S.; Herger, R.; Schlepütz, C.; Martoccia, D.; Patterson, B.; Delley, B.; Clarke, R.; Kumah, D.; Cionca, C., Structural basis for the conducting interface between $LaAlO_3$ and $SrTiO_3$. *Physical review letters* **2007,** *99* (15), 155502.

44. Edvinsson, T., Optical quantum confinement and photocatalytic properties in two-, one-and zero-dimensional nanostructures. *Royal Society open science* **2018,** *5* (9), 180387.

45. Ekimov, A.; Onushchenko, A., Quantum size effect in the optical-spectra of semiconductor micro-crystals. *Soviet Physics Semiconductors-Ussr* **1982,** *16* (7), 775-778.

46. Alivisatos, A. P., Semiconductor clusters, nanocrystals, and quantums dots. *Science* **1996,** *271* (5251), 933-937.

47. Chakraborty, T., Physics of the artificial atoms: Quantum dots in a magnetic field. *Comments Cond. Mat. Phys* **1992,** *16*, 35-68.

48. Kastner, M. A., Artificial atoms. *Physics today* **1993,** *46*, 24-24.

49. Ashoori, R., Electrons in artificial atoms. *Nature* **1996,** *379* (6564), 413-419.

50. Yoffe, A. D., Low-dimensional systems: quantum size effects and electronic properties of semiconductor microcrystallites (zero-dimensional systems) and some quasi-two-dimensional systems. *Advances in Physics* **1993,** *42* (2), 173-262.

51. Yoshimatsu, K.; Horiba, K.; Kumigashira, H.; Yoshida, T.; Fujimori, A.; Oshima, M., Metallic quantum well states in artificial structures of strongly correlated oxide. *Science* **2011,** *333* (6040), 319-322.

52. Mannhart, J.; Schlom, D., Oxide interfaces—an opportunity for electronics. *Science* **2010,** *327* (5973), 1607-1611.

53. Royo, M.; De Luca, M.; Rurali, R.; Zardo, I., A review on III–V core–multishell nanowires: growth, properties, and applications. *Journal of Physics D: Applied Physics* **2017,** *50* (14), 143001.

54. Kiravittaya, S.; Rastelli, A.; Schmidt, O. G., Advanced quantum dot configurations. *Reports on Progress in Physics* **2009,** *72* (4), 046502.

55. Yoshida, H.; Yamashita, Y.; Kuwabara, M.; Kan, H., A 342-nm ultraviolet AlGaN multiple-quantum-well laser diode. *Nature photonics* **2008,** *2* (9), 551.

56. Kagan, C. R.; Lifshitz, E.; Sargent, E. H.; Talapin, D. V., Building devices from colloidal quantum dots. *Science* **2016,** *353* (6302).

57. Kairdolf, B. A.; Smith, A. M.; Stokes, T. H.; Wang, M. D.; Young, A. N.; Nie, S., Semiconductor quantum dots for bioimaging and biodiagnostic applications. *Annual review of analytical chemistry* **2013,** *6*, 143-162.

58. Senellart, P.; Solomon, G.; White, A., High-performance semiconductor quantum-dot single-photon sources. *Nature nanotechnology* **2017,** *12* (11), 1026-1039.

59. Ruzmetov, D.; Seo, Y.; Belenky, L. J.; Kim, D. M.; Ke, X. L.; Sun, H. P.; Chandrasekhar, V.; Eom, C. B.; Rzchowski, M. S.; Pan, X. Q., Epitaxial magnetic perovskite nanostructures. *Advanced materials* **2005,** *17* (23), 2869-2872.

60. Zubko, P.; Catalan, G.; Tagantsev, A. K., Flexoelectric Effect in Solids. *Annual Review of Materials Research* **2013,** *43* (1), 387-421.

61. Mashkevich, V.; Tolpygo, K., Electrical, optical and elastic properties of diamond type crystals. *Soviet Physics JETP* **1957,** *5* (3), 435-439.

62. Tolpygo, K., Long wavelength oscillations of diamond-type crystals including long range forces. *Soviet Physics-Solid State* **1963,** *4* (7), 1297-1305.

63. Tagantsev, A., Theory of flexoelectric effect in crystals. *Zhurnal Eksperimental'noi i Teoreticheskoi Fiziki* **1985,** *88* (6), 2108-22.

64. Shirane, G.; Jona, F., *Ferroelectric crystals*. New-York, Paris: 1962.

65. Nye, J. F., *Physical properties of crystals: their representation by tensors and matrices*. Oxford university press: 1985.

66. Kogan, S. M., Piezoelectric effect during inhomogeneous deformation and acoustic scattering of carriers in crystals. *Soviet Physics-Solid State* **1964,** *5* (10), 2069-2070.

67. Hsueh, C.-H.; Schmauder, S.; Chen, C.-S.; Chawla, K. K.; Chawla, N.; Chen, W.; Kagawa, Y., *Handbook of Mechanics of materials*. Springer: 2019.

68. Nguyen, T. D.; Mao, S.; Yeh, Y. W.; Purohit, P. K.; McAlpine, M. C., Nanoscale flexoelectricity. *Advanced materials* **2013,** *25* (7), 946-974.

69. Molina-Luna, L.; Wang, S.; Pivak, Y.; Zintler, A.; Perez-Garza, H. H.; Spruit, R. G.; Xu, Q.; Yi, M.; Xu, B. X.; Acosta, M., Enabling nanoscale flexoelectricity at extreme temperature by tuning cation diffusion. *Nature communications* **2018,** *9* (1), 4445.

70. Gao, P.; Yang, S.; Ishikawa, R.; Li, N.; Feng, B.; Kumamoto, A.; Shibata, N.; Yu, P.; Ikuhara, Y., Atomic-acale measurement of flexoelectric polarization at $SrTiO_3$ dislocations. *Physical review letters* **2018,** *120* (26), 267601.

71. Catalan, G.; Lubk, A.; Vlooswijk, A. H.; Snoeck, E.; Magen, C.; Janssens, A.; Rispens, G.; Rijnders, G.; Blank, D. H.; Noheda, B., Flexoelectric rotation of polarization in ferroelectric thin films. *Nature materials* **2011,** *10* (12), 963-7.

72. Abdollahi, A.; Peco, C.; Millan, D.; Arroyo, M.; Catalan, G.; Arias, I., Fracture toughening and toughness asymmetry induced by flexoelectricity. *Physical Review B* **2015,** *92* (9).

73. Cordero-Edwards, K.; Kianirad, H.; Canalias, C.; Sort, J.; Catalan, G., Flexoelectric fracture-ratchet effect in ferroelectrics. *Physical review letters* **2019,** *122* (13), 135502.

74. Krebs, H.-U.; Weisheit, M.; Faupel, J.; Süske, E.; Scharf, T.; Fuhse, C.; Störmer, M.; Sturm, K.; Seibt, M.; Kijewski, H., Pulsed laser deposition (PLD)--a versatile thin film technique. In *Advances in Solid State Physics*, Springer: 2003; pp 505-518.

75. Jäger, M.; Teker, A.; Mannhart, J.; Braun, W., Independence of surface morphology and reconstruction during the thermal preparation of perovskite oxide surfaces. *Applied Physics Letters* **2018,** *112* (11), 111601.

76. Rijnders, G. J.; Koster, G.; Blank, D. H.; Rogalla, H., In-situ growth monitoring during PLD of oxides using RHEED at high oxygen pressure. *Materials Science and Engineering: B* **1998,** *56* (2-3), 223-227.

77. Koster, G.; Kropman, B. L.; Rijnders, G. J. H. M.; Blank, D. H. A.; Rogalla, H., Quasi-ideal strontium titanate crystal surfaces through formation of strontium hydroxide. *Applied Physics Letters* **1998,** *73* (20), 2920-2922.

78. Vieu, C.; Carcenac, F.; Pepin, A.; Chen, Y.; Mejias, M.; Lebib, A.; Manin-Ferlazzo, L.; Couraud, L.; Launois, H., Electron beam lithography: resolution limits and applications. *Applied surface science* **2000,** *164* (1-4), 111-117.

79. Goldstein, J. I.; Newbury, D. E.; Michael, J. R.; Ritchie, N. W. M.; Scott, J. H. J.; Joy, D. C., Electron beam—specimen interactions: Interaction volume. In *Scanning Electron Microscopy and X-Ray Microanalysis*, Springer New York: New York, NY, 2018; pp 1-14.

80. Gangnaik, A. S.; Georgiev, Y. M.; Holmes, J. D., New Generation Electron Beam Resists: A Review. *Chemistry of Materials* **2017,** *29* (5), 1898-1917.

81. Wang, X.; Goryll, M., Nanopore patterning using Al_2O_3 hard masks on SOI substrates. *Journal of Micromechanics and Microengineering* **2015,** *25* (7), 075020.

82. Ruska, E., The development of the electron microscope and of electron microscopy. *Reviews of modern physics* **1987,** *59* (3), 627.

83. Knoll, M.; Ruska, E., Beitrag zur geometrischen Elektronenoptik. I. *Annalen der Physik* **1932,** *404* (5), 607-640.

84. Freundlich, M. M., Origin of the electron microscope. *Science* **1963,** *142* (3589), 185-188.

85. von Ardenne, M., Das Elektronen-Rastermikroskop. Praktische Ausführung. *Z. tech, phys.* **1938,** *19*, 407-416.

86. Crewe, A. V.; Isaacson, M.; Johnson, D., A simple scanning electron microscope. *Review of Scientific Instruments* **1969,** *40* (2), 241-246.

87. Hawkes, P., Aberration correction past and present. *Philosophical Transactions of the Royal Society A: Mathematical, Physical and Engineering Sciences* **2009,** *367* (1903), 3637-3664.

88. de Broglie, L.-V., On the theory of quanta. *Thesis, University of Paris* **1924**.

89. Brydson, R., *Aberration-corrected analytical transmission electron microscopy*. John Wiley & Sons: 2011; Vol. 3.

90. David B. Williams, C. B. C., Transmission Electron Microscopy. **2009**.

91. Scherzer, O., Spharische und chromatische korrektur von elektronen-linsen. *Optik* **1947,** *2*, 114-132.

92. Hetherington, C., Aberration correction for TEM. *Materials Today* **2004,** *7* (12), 50-55.

93. Bleloch, A.; Lupini, A., Imaging at the picoscale. *Materials Today* **2004,** *7* (12), 42-48.

94. Rose, H., Correction of aberrations, a promising means for improving the spatial and energy resolution of energy-filtering electron microscopes. *Ultramicroscopy* **1994,** *56* (1), 11-25.

95. Zeitler, E., Stem versus ctem. *Ultramicroscopy* **1978,** *3*, 349-351.

96. Krumeich, F., Properties of electrons, their interactions with matter and applications in electron microscopy.

97. Zhang, Q.-H.; Xiao, D.-D.; Gu, L., Aberration-corrected scanning transmission electron microscopy for complex transition metal oxides. *Chinese Physics B* **2016,** *25* (6), 066803.

98. Pennycook, S. J.; Nellist, P. D., *Scanning transmission electron microscopy: imaging and analysis*. Springer Science & Business Media: 2011.

99. Findlay, S. D.; Shibata, N.; Ikuhara, Y.; Huang, R.; Okunishi, E.; Sawada, H.; Kohno, Y.; Kondo, Y., Annular bright-field scanning transmission electron microscopy: Direct and robust atomic-resolution imaging of light elements in crystalline materials. *Microscopy Today* **2017,** *25* (6), 36-41.

100. Findlay, S. D.; Shibata, N.; Sawada, H.; Okunishi, E.; Kondo, Y.; Ikuhara, Y., Dynamics of annular bright field imaging in scanning transmission electron microscopy. *Ultramicroscopy* **2010,** *110* (7), 903-923.

101. Egerton, R. F., *Electron energy-loss spectroscopy in the electron microscope*. Springer Science & Business Media: 2011.

102. Egerton, R. F., *Physical principles of electron microscopy*. Springer: 2005; Vol. 56.

103. Ernst, F.; Rühle, M., *High-resolution imaging and spectrometry of materials*. Springer Science & Business Media: 2013; Vol. 50.

104. Hage, F.; Radtke, G.; Kepaptsoglou, D.; Lazzeri, M.; Ramasse, Q., Single-atom vibrational spectroscopy in the scanning transmission electron microscope. *Science* **2020,** *367* (6482), 1124-1127.

105. Hage, F. S.; Kepaptsoglou, D. M.; Ramasse, Q. M.; Allen, L. J., Phonon spectroscopy at atomic resolution. *Physical review letters* **2019,** *122* (1), 016103.

106. Malis, T.; Cheng, S.; Egerton, R., EELS log-ratio technique for specimen-thickness measurement in the TEM. *Journal of electron microscopy technique* **1988,** *8* (2), 193-200.

107. Williams, D. B.; Carter, C. B., The transmission electron microscope. In *Transmission electron microscopy*, Springer: 1996; pp 3-17.

108. Guo, S.; Talebi, N.; Sigle, W.; Vogelgesang, R.; Richter, G.; Esmann, M.; Becker, S. F.; Lienau, C.; van Aken, P. A., Reflection and phase matching in plasmonic gold tapers. *Nano letters* **2016,** *16* (10), 6137-6144.

109. Ikeno, H.; Mizoguchi, T., Basics and applications of ELNES calculations. *Microscopy* **2017,** *66* (5), 305-327.

110. Gloter, A.; Badjeck, V.; Bocher, L.; Brun, N.; March, K.; Marinova, M.; Tence, M.; Walls, M.; Zobelli, A.; Stephan, O.; Colliex, C., Atomically resolved mapping of EELS fine structures. *Materials Science in Semiconductor Processing* **2017,** *65*, 2-17.

111. Riedl, T.; Gemming, T.; Gruner, W.; Acker, J.; Wetzig, K., Determination of manganese valency in $La_{1-x}Sr_xMnO_3$ using ELNES in the (S)TEM. *Micron* **2007,** *38* (3), 224-230.

112. Verbeeck, J.; Lebedev, O. I.; Van Tendeloo, G.; Mercey, B., $SrTiO_3(100)/(LaMnO_3)_m(SrMnO_3)_n$ layered heterostructures: A combined EELS and TEM study. *Physical Review B* **2002,** *66* (18), 184426.

113. Kurata, H.; Lefevre, E.; Colliex, C.; Brydson, R., Electron-energy-loss near-edge structures in the oxygen K-edge spectra of transition-metal oxides. *Physical review. B, Condensed matter* **1993,** *47* (20), 13763-13768.

114. Varela, M.; Oxley, M. P.; Luo, W.; Tao, J.; Watanabe, M.; Lupini, A. R.; Pantelides, S. T.; Pennycook, S. J., Atomic-resolution imaging of oxidation states in manganites. *Physical Review B* **2009,** *79* (8), 085117.

115. Mitterbauer, C.; Kothleitner, G.; Grogger, W.; Zandbergen, H.; Freitag, B.; Tiemeijer, P.; Hofer, F., Electron energy-loss near-edge structures of 3*d* transition metal oxides recorded at high-energy resolution. *Ultramicroscopy* **2003,** *96* (3-4), 469-480.

116. Leapman, R. D.; Grunes, L. A., Anomalous L3L2 White-Line Ratios in the 3*d* Transition Metals. *Physical review letters* **1980,** *45* (5), 397-401.

117. Van Aken, P.; Liebscher, B., Quantification of ferrous/ferric ratios in minerals: new evaluation schemes of Fe $L_{2,3}$ electron energy-loss near-edge spectra. *Physics and Chemistry of Minerals* **2002,** *29* (3), 188-200.

118. Song, K. P.; Schmid, H.; Srot, V.; Gilardi, E.; Gregori, G.; Du, K.; Maier, J.; van Aken, P. A., Cerium reduction at the interface between ceria and yttria-stabilised zirconia and implications for interfacial oxygen non-stoichiometry. *APL Materials* **2014,** *2* (3), 032104.

119. Mundy, J. A.; Schaab, J.; Kumagai, Y.; Cano, A.; Stengel, M.; Krug, I. P.; Gottlob, D. M.; Dog Anay, H.; Holtz, M. E.; Held, R.; Yan, Z.; Bourret, E.; Schneider, C. M.; Schlom, D. G.; Muller, D. A.; Ramesh, R.; Spaldin, N. A.; Meier, D., Functional electronic inversion layers at ferroelectric domain walls. *Nature materials* **2017,** *16* (6), 622-627.

120. Cueva, P.; Hovden, R.; Mundy, J. A.; Xin, H. L.; Muller, D. A., Data processing for atomic resolution electron energy loss spectroscopy. *Microscopy and Microanalysis* **2012,** *18* (4), 667-675.

121. Mullejans, H.; Bruley, J., Electron-Energy-Loss Spectroscopy (Eels) - Comparison with X-Ray-Analysis. *J Phys Iv* **1993,** *3* (C7), 2083-2092.

122. Goldstein, J. I.; Newbury, D. E.; Michael, J. R.; Ritchie, N. W.; Scott, J. H. J.; Joy, D. C., *Scanning electron microscopy and X-ray microanalysis*. Springer: 2017.

123. Wang, H.; Srot, V.; Fenk, B.; Laskin, G.; Mannhart, J.; van Aken, P. A., TEM sample preparation of patterned quantum dots. Microscopy and Microanalysis 2019, 25 (S2), 790-791.

124. Hytch, M. J.; Snoeck, E.; Kilaas, R., Quantitative measurement of displacement and strain fields from HREM micrographs. *Ultramicroscopy* **1998,** *74* (3), 131-146.

125. Hytch, M. J.; Minor, A. M., Observing and measuring strain in nanostructures and devices with transmission electron microscopy. *MRS Bulletin* **2014,** *39* (2), 138-146.

126. Wang, Y.; Salzberger, U.; Sigle, W.; Eren Suyolcu, Y.; van Aken, P. A., Oxygen octahedra picker: A software tool to extract quantitative information from STEM images. *Ultramicroscopy* **2016,** *168*, 46-52.

127. De Backer, A.; van den Bos, K. H. W.; Van den Broek, W.; Sijbers, J.; Van Aert, S., StatSTEM: An efficient approach for accurate and precise model-based quantification of atomic resolution electron microscopy images. *Ultramicroscopy* **2016,** *171*, 104-116.

128. Nord, M.; Vullum, P. E.; MacLaren, I.; Tybell, T.; Holmestad, R., Atomap: a new software tool for the automated analysis of atomic resolution images using two-dimensional Gaussian fitting. *Advanced structural and chemical imaging* **2017,** *3* (1), 9.

129. Mukherjee, D.; Miao, L.; Stone, G.; Alem, N., mpfit: a robust method for fitting atomic resolution images with multiple Gaussian peaks. *Advanced Structural and Chemical Imaging* **2020,** *6* (1), 1.

130. Wang, Z.; Tao, J.; Yu, L.; Guo, H.; Chen, L.; Han, M.-G.; Wu, L.; Xin, H.; Kisslinger, K.; Plummer, E., Anomalously deep polarization in $SrTiO_3$ (001) interfaced with an epitaxial ultrathin manganite film. *Physical Review B* **2016,** *94* (15), 155307.

131. Anthony, S. M.; Granick, S., Image analysis with rapid and accurate two-dimensional Gaussian fitting. *Langmuir* **2009,** *25* (14), 8152-8160.

132. Yankovich, A. B.; Berkels, B.; Dahmen, W.; Binev, P.; Sanchez, S. I.; Bradley, S. A.; Li, A.; Szlufarska, I.; Voyles, P. M., Picometre-precision analysis of scanning transmission electron microscopy images of platinum nanocatalysts. *Nature communications* **2014,** *5* (1), 4155.

133. Huyan, H.; Li, L.; Addiego, C.; Gao, W.; Pan, X., Structures and electronic properties of domain walls in $BiFeO_3$ thin films. *National Science Review* **2019,** *6* (4), 669-683.

134. Spurgeon, S. R.; Balachandran, P. V.; Kepaptsoglou, D. M.; Damodaran, A. R.; Karthik, J.; Nejati, S.; Jones, L.; Ambaye, H.; Lauter, V.; Ramasse, Q. M.; Lau, K. K. S.; Martin, L. W.; Rondinelli, J. M.; Taheri, M. L., Polarization screening-induced magnetic phase gradients at complex oxide interfaces. *Nature communications* **2015,** *6*, 6735.

135. Tang, Y.; Zhu, Y.; Hong, Z.; Eliseev, E.; Morozovska, A.; Wang, Y.; Liu, Y.; Xu, Y.; Wu, B.; Chen, L., 3D polarization texture of a symmetric 4-fold flux closure domain in strained ferroelectric $PbTiO_3$ films. *Journal of Materials Research* **2017,** *32* (5), 957-967.

136. Koch, C. T., *Determination of core structure periodicity and point defect density along dislocations*. 2002.

137. Kirkland, E. J., *Advanced computing in electron microscopy*. Springer: 1998.

138. Allen, L. J., Simulation in elemental mapping using aberration-corrected electron microscopy. *Ultramicroscopy* **2017,** *180*, 142-149.

139. Allen, L. J.; AJ, D. A.; Findlay, S. D., Modelling the inelastic scattering of fast electrons. *Ultramicroscopy* **2015,** *151*, 11-22.

140. Wu, R. J.; Mittal, A.; Odlyzko, M. L.; Mkhoyan, K. A., Simplifying Electron Beam Channeling in Scanning Transmission Electron Microscopy (STEM). *Microscopy and microanalysis : the official journal of Microscopy Society of America, Microbeam Analysis Society, Microscopical Society of Canada* **2017,** *23* (4), 794-808.

141. Spurgeon, S. R.; Du, Y.; Chambers, S. A., Measurement error in atomic-scale scanning transmission electron microscopy-energy-dispersive X-Ray spectroscopy (STEM-EDS) mapping of a model oxide interface. *Microscopy and microanalysis: the official journal of Microscopy Society of America, Microbeam Analysis Society, Microscopical Society of Canada* **2017,** *23* (3), 513-517.

142. Boschker, H.; Mannhart, J., Quantum-matter heterostructures. *Annu Rev Conden Ma P* **2017,** *8* (1), 145-164.

143. Harrison, P.; Valavanis, A., *Quantum wells, wires and dots: theoretical and computational physics of semiconductor nanostructures*. John Wiley & Sons: 2016.

144. Laskin, G.; Wang, H.; Boschker, H.; Braun, W.; Srot, V.; van Aken, P. A.; Mannhart, J., Magnetic properties of epitaxially grown $SrRuO_3$ nanodots. *Nano letters* **2019,** *19* (2), 1131-1135.

145. Pennycook, S. J.; Nellist, P. D., Scanning Transmission Electron Microscopy Imaging and Analysis. **2015**.

146. Srot, V.; Gec, M.; van Aken, P. A.; Jeon, J. H.; Ceh, M., Influence of TEM specimen preparation on chemical composition of $Pb(Mg_{1/3}Nb_{2/3})O_3$-$PbTiO_3$ single crystals. *Micron* **2014,** *62*, 37-42.

147. Brydson, R., Aberration-Corrected Analytical Transmission Electron Microscopy. **2011**.

148. Wolfsteller, A.; Geyer, N.; Nguyen-Duc, T. K.; Das Anungo, P.; Zakharov, N. D.; Reiche, M.; Erfurth, W.; Blumtritt, H.; Werner, P.; Gosele, U., Comparison of the top-down and bottom-up approach to fabricate nanowire-based Silicon/Germanium heterostructures. *Thin Solid Films* **2010,** *518* (9), 2555-2561.

149. Voyles, P.; Grazul, J.; Muller, D., Imaging individual atoms inside crystals with ADF-STEM. *Ultramicroscopy* **2003,** *96* (3-4), 251-273.

150. Hudson, M.; Benedict, J.; Flaitz, P., TEM specimen preparation technique for small semiconductor devices. *Microscopy Today* **2004,** *12* (2), 38-41.

151. Wang, Z. M., *FIB nanostructures*. Springer: 2013.

152. Mayer, J.; Giannuzzi, L. A.; Kamino, T.; Michael, J., TEM sample preparation and FIB-induced damage. *MRS Bulletin* **2011,** *32* (5), 400-407.

153. Langford, R.; Petford-Long, A., Preparation of transmission electron microscopy cross-section specimens using focused ion beam milling. *Journal of Vacuum Science & Technology A: Vacuum, Surfaces, and Films* **2001,** *19* (5), 2186-2193.

154. Schaffer, M.; Schaffer, B.; Ramasse, Q., Sample preparation for atomic-resolution STEM at low voltages by FIB. *Ultramicroscopy* **2012,** *114*, 62-71.

155. Drouin, D.; Couture, A. R.; Joly, D.; Tastet, X.; Aimez, V.; Gauvin, R., CASINO V2. 42—a fast and easy-to-use modeling tool for scanning electron microscopy and microanalysis users. *Scanning: The Journal of Scanning Microscopies* **2007,** *29* (3), 92-101.

156. Salzer, R.; Graff, A.; Simon, M.; Altmann, F., Standard free thickness determination of thin TEM samples via backscatter electron image correlation. *Microscopy and Microanalysis* **2009,** *15* (S2), 340-341.

157. Cerchiara, R.; Fischione, P.; Liu, J.; Matesa, J.; Robins, A.; Fraser, H.; Genc, A., Raising the standard of specimen preparation for aberration-corrected TEM and STEM. *Microscopy Today* **2011,** *19* (1), 16-19.

158. Dienstleder, M.; Fisslthaler, E.; Gspan, C.; Kothleitner, G. In *Low energy argon ion sample preparation for HRSTEM analysis*, 7. ASEM workshop of the Austrian Society of Electron Microscopy, 2017.

159. Nowakowski, P.; Bonifacio, C.; Campin, M.; Ray, M.; Fischione, P., Accurate removal of implanted gallium and amorphous damage from TEM specimens after focused ion beam (FIB) preparation. *Microscopy and Microanalysis* **2017,** *23* (S1), 300-301.

160. Giannuzzi, L. A.; Stevie, F. A., A review of focused ion beam milling techniques for TEM specimen preparation. *Micron* **1999,** *30* (3), 197-204.

161. Malis, T.; Cheng, S. C.; Egerton, R. F., EELS log-ratio technique for specimen-thickness measurement in the TEM. *Journal of electron microscopy technique* **1988,** *8* (2), 193-200.

162. Iakoubovskii, K.; Mitsuishi, K.; Nakayama, Y.; Furuya, K., Thickness measurements with electron energy loss spectroscopy. *Microscopy research and technique* **2008,** *71* (8), 626-31.

163. Kouwenhoven, L.; Marcus, C., Quantum dots. *Physics World* **1998,** *11* (6), 35.

164. Wang, Y. B.; Si, B. N.; Lu, S. W.; Liu, E. Z.; Hu, X. Y.; Fan, J., Near-infrared excitation of CdTe quantum dots based on fluorescence resonance energy transfer and their use as fluorescent sensors. *Sensor Actuat B-Chem* **2017,** *246*, 127-135.

165. Wang, H. C.; Bao, Z.; Tsai, H. Y.; Tang, A. C.; Liu, R. S., Perovskite quantum dots and their application in light-emitting diodes. *Small* **2018,** *14* (1), 1702433.

166. A. O. Kosogov; P. Werner; U. Gosele; N. N. Ledentsova; D. Bimberg; V. M. Ustinov; A. Yu. Egorov; A. E. Zhukov; P. S. Kop'ev; N. A. Bert; Alferov, Z. I., Structural and optical properties of InAs–GaAs quantum dots subjected to high temperature annealing. *Appl. Phys. Lett.* **1996,** *69* (30), 3072-3074.

167. Kegel, I. I.; Metzger, T. H.; Lorke, A.; Peisl, J.; Stangl, J.; Bauer, G.; Garcia, J. M.; Petroff, P. M., Nanometer-scale resolution of strain and interdiffusion in self-assembled InAs/GaAs quantum dots. *Physical review letters* **2000,** *85* (8), 1694-7.

168. Puntambekar, A.; Wang, Q.; Miller, L.; Smieszek, N.; Chakrapani, V., Electrochemical charging of CdSe quantum dots: Effects of adsorption versus intercalation. *ACS Nano* **2016,** *10* (12), 10988-10999.

169. Weber, B.; Tan, Y. H.; Mahapatra, S.; Watson, T. F.; Ryu, H.; Rahman, R.; Hollenberg, L. C.; Klimeck, G.; Simmons, M. Y., Spin blockade and exchange in Coulomb-confined silicon double quantum dots. *Nature nanotechnology* **2014,** *9* (6), 430-435.

170. Cen, C.; Thiel, S.; Mannhart, J.; Levy, J., Oxide Nanoelectronics on Demand. *Science* **2009,** *323* (5917), 1026-1030.

171. Cheng, G.; Siles, P. F.; Bi, F.; Cen, C.; Bogorin, D. F.; Bark, C. W.; Folkman, C. M.; Park, J.-W.; Eom, C.-B.; Medeiros-Ribeiro, G., Sketched oxide single-electron transistor. *Nature nanotechnology* **2011,** *6* (6), 343-347.

172. Katine, J.; Ho, M. K.; Ju, Y. S.; Rettner, C., Patterning damage in narrow trackwidth spin-valve sensors. *Applied physics letters* **2003,** *83* (2), 401-403.

173. Koster, G.; Klein, L.; Siemons, W.; Rijnders, G.; Dodge, J. S.; Eom, C. B.; Blank, D. H. A.; Beasley, M. R., Structure, physical properties, and applications of $SrRuO_3$ thin films. *Reviews of Modern Physics* **2012,** *84* (1), 253-298.

174. Chang, Y. J.; Kim, C. H.; Phark, S.-H.; Kim, Y.; Yu, J.; Noh, T., Fundamental thickness limit of itinerant ferromagnetic $SrRuO_3$ thin films. *Physical review letters* **2009,** *103* (5), 057201.

175. Ishigami, K.; Yoshimatsu, K.; Toyota, D.; Takizawa, M.; Yoshida, T.; Shibata, G.; Harano, T.; Takahashi, Y.; Kadono, T.; Verma, V., Thickness-dependent magnetic properties and strain-induced orbital magnetic moment in $SrRuO_3$ thin films. *Physical Review B* **2015,** *92* (6), 064402.

176. Zayak, A. T.; Huang, X.; Neaton, J. B.; Rabe, K. M., Structural, electronic, and magnetic properties of $SrRuO_3$ under epitaxial strain. *Physical Review B* **2006,** *74* (9), 094104.

177. Robinson, I. K., Crystal truncation rods and surface roughness. *Physical Review B* **1986,** *33* (6), 3830.

178. Maria, J.-P.; McKinstry, H. L.; Trolier-McKinstry, S., Origin of preferential orthorhombic twinning in $SrRuO_3$ epitaxial thin films. *Applied Physics Letters* **2000,** *76* (23), 3382-3384.

179. Vailionis, A.; Boschker, H.; Siemons, W.; Houwman, E. P.; Blank, D. H. A.; Rijnders, G.; Koster, G., Misfit strain accommodation in epitaxial ABO_3 perovskites: Lattice rotations and lattice modulations. *Physical Review B* **2011,** *83* (6), 064101.

180. Tian, W.; Haeni, J.; Schlom, D. G.; Hutchinson, E.; Sheu, B.; Rosario, M.; Schiffer, P.; Liu, Y.; Zurbuchen, M. A.; Pan, X., Epitaxial growth and magnetic properties of the first five members of the layered $Sr_{n+1}Ru_nO_{3n+1}$ oxide series. *Applied physics letters* **2007,** *90* (2), 022507.

181. Grutter, A.; Wong, F.; Arenholz, E.; Liberati, M.; Vailionis, A.; Suzuki, Y., Enhanced magnetism in epitaxial $SrRuO_3$ thin films. *Applied Physics Letters* **2010,** *96* (8), 082509.

182. Xia, J.; Siemons, W.; Koster, G.; Beasley, M.; Kapitulnik, A., Critical thickness for itinerant ferromagnetism in ultrathin films of $SrRuO_3$. *Physical Review B* **2009,** *79* (14), 140407.

183. Bern, F.; Ziese, M.; Setzer, A.; Pippel, E.; Hesse, D.; Vrejoiu, I., Structural, magnetic and electrical properties of $SrRuO_3$ films and $SrRuO_3/SrTiO_3$ superlattices. *Journal of physics. Condensed matter : an Institute of Physics journal* **2013,** *25* (49), 496003.

184. Chang, Y. J.; Kim, C. H.; Phark, S.-H.; Kim, Y.; Yu, J.; Noh, T., Fundamental thickness limit of itinerant ferromagnetic $SrRuO_3$ thin films. *Physical review letters* **2009,** *103* (5), 057201.

185. Coey, J.; Venkatesan, M.; Stamenov, P., Surface magnetism of strontium titanate. *Journal of Physics: Condensed Matter* **2016,** *28* (48), 485001.

186. Himpsel, F.; Ortega, J.; Mankey, G.; Willis, R., Magnetic nanostructures. *Advances in physics* **1998,** *47* (4), 511-597.

187. Vasseur, S.; Duguet, E.; Portier, J.; Goglio, G.; Mornet, S.; Hadová, E.; Knížek, K.; Maryško, M.; Veverka, P.; Pollert, E., Lanthanum manganese perovskite nanoparticles as possible in vivo mediators for magnetic hyperthermia. *Journal of magnetism and magnetic materials* **2006,** *302* (2), 315-320.

188. Rong, C. B.; Li, D.; Nandwana, V.; Poudyal, N.; Ding, Y.; Wang, Z. L.; Zeng, H.; Liu, J. P., Size-dependent chemical and magnetic ordering in $L1_0$-FePt nanoparticles. *Advanced materials* **2006,** *18* (22), 2984-2988.

189. Wu, M.; Benckiser, E.; Haverkort, M. W.; Frano, A.; Lu, Y.; Nwankwo, U.; Bruck, S.; Audehm, P.; Goering, E.; Macke, S.; Hinkov, V.; Wochner, P.; Christiani, G.; Heinze, S.; Logvenov, G.; Habermeier, H. U.; Keimer, B., Strain and composition dependence of orbital polarization in nickel oxide superlattices. *Physical Review B* **2013,** *88* (12), 125124.

190. Lee, H.; Campbell, N.; Lee, J.; Asel, T. J.; Paudel, T. R.; Zhou, H.; Lee, J. W.; Noesges, B.; Seo, J.; Park, B.; Brillson, L. J.; Oh, S. H.; Tsymbal, E. Y.; Rzchowski, M. S.; Eom, C. B., Direct observation of a two-dimensional hole gas at oxide interfaces. *Nature materials* **2018,** *17* (3), 231-236.

191. Nakagawa, N.; Hwang, H. Y.; Muller, D. A., Why some interfaces cannot be sharp. *Nature materials* **2006,** *5* (3), 204-209.

192. Boschker, H.; Harada, T.; Asaba, T.; Ashoori, R.; Boris, A. V.; Hilgenkamp, H.; Hughes, C. R.; Holtz, M. E.; Li, L.; Muller, D. A.; Nair, H.; Reith, P.; Wang, X. R.; Schlom, D. G.; Soukiassian, A.; Mannhart, J., Ferromagnetism and conductivity in atomically thin $SrRuO_3$. *Physical Review X* **2019,** *9* (1), 011027.

193. Himcinschi, C.; Singh, R.; Radu, I.; Milenin, A.; Erfurth, W.; Reiche, M.; Gösele, U.; Christiansen, S.; Muster, F.; Petzold, M., Strain relaxation in nanopatterned strained silicon round pillars. *Applied physics letters* **2007,** *90* (2), 021902.

194. Ramesh, V.; Kikuchi, A.; Kishino, K.; Funato, M.; Kawakami, Y., Strain relaxation effect by nanotexturing InGaN/GaN multiple quantum well. *Journal of Applied Physics* **2010,** *107* (11), 114303.

195. Wenisch, J.; Gould, C.; Ebel, L.; Storz, J.; Pappert, K.; Schmidt, M. J.; Kumpf, C.; Schmidt, G.; Brunner, K.; Molenkamp, L. W., Control of magnetic anisotropy in (Ga,Mn)As by lithography-induced strain relaxation. *Physical review letters* **2007,** *99* (7), 077201.

196. Lu, W.; Song, W.; Yang, P.; Ding, J.; Chow, G. M.; Chen, J., Strain engineering of octahedral rotations and physical properties of $SrRuO_3$ films. *Scientific reports* **2015,** *5*, 10245.

197. Gan, Q.; Rao, R. A.; Eom, C. B.; Garrett, J. L.; Lee, M., Direct measurement of strain effects on magnetic and electrical properties of epitaxial $SrRuO_3$ thin films. *Applied Physics Letters* **1998,** *72* (8), 978-980.

198. Thomas, S.; Kuiper, B.; Hu, J.; Smit, J.; Liao, Z.; Zhong, Z.; Rijnders, G.; Vailionis, A.; Wu, R.; Koster, G.; Xia, J., Localized control of Curie temperature in perovskite oxide film by capping-layer-induced octahedral distortion. *Physical review letters* **2017,** *119* (17), 177203.

199. Leslie-Pelecky, D. L.; Rieke, R. D., Magnetic properties of nanostructured materials. *Chemistry of materials* **1996,** *8* (8), 1770-1783.

200. Dagotto, E., When oxides meet face to face. *Science* **2007,** *318* (5853), 1076-1077.

201. Ramesh, R.; Schlom, D. G., Creating emergent phenomena in oxide superlattices. *Nature Reviews Materials* **2019,** *4* (4), 257-268.

202. Chakhalian, J.; Millis, A. J.; Rondinelli, J., Whither the oxide interface. *Nature materials* **2012,** *11* (2), 92-94.

203. Gunkel, F.; Waser, R.; Ramadan, A. H. H.; De Souza, R. A.; Hoffmann-Eifert, S.; Dittmann, R., Space charges and defect concentration profiles at complex oxide interfaces. *Physical Review B* **2016,** *93* (24), 245431.

204. Caprara, S., Oxide interfaces: Spin-to-charge current conversion. *Nature materials* **2016,** *15* (12), 1224-1225.

205. Sata, N.; Eberman, K.; Eberl, K.; Maier, J., Mesoscopic fast ion conduction in nanometre-scale planar heterostructures. *Nature* **2000,** *408* (6815), 946-949.

206. Mannhart, J.; Blank, D. H. A.; Hwang, H. Y.; Millis, A. J.; Triscone, J. M., Two-dimensional electron gases at oxide interfaces. *MRS Bulletin* **2008,** *33* (11), 1027-1034.

207. Brinkman, A.; Huijben, M.; Van Zalk, M.; Huijben, J.; Zeitler, U.; Maan, J. C.; Van der Wiel, W. G.; Rijnders, G.; Blank, D. H. A.; Hilgenkamp, H., Magnetic effects at the interface between non-magnetic oxides. *Nature materials* **2007,** *6* (7), 493-496.

208. Salamon, M. B.; Jaime, M., The physics of manganites: Structure and transport. *Reviews of Modern Physics* **2001,** *73* (3), 583-628.

209. Tokura, Y., Critical features of colossal magnetoresistive manganites. *Reports on Progress in Physics* **2006,** *69* (3), 797-851.

210. Gao, P.; Ishikawa, R.; Feng, B.; Kumamoto, A.; Shibata, N.; Ikuhara, Y., Atomic-scale structure relaxation, chemistry and charge distribution of dislocation cores in $SrTiO_3$. *Ultramicroscopy* **2018,** *184* (Pt A), 217-224.

211. Phillips, P. J.; Rui, X.; Georgescu, A. B.; Disa, A. S.; Longo, P.; Okunishi, E.; Walker, F.; Ahn, C. H.; Ismail-Beigi, S.; Klie, R. F., Experimental verification of orbital engineering at the atomic scale: Charge transfer and symmetry breaking in nickelate heterostructures. *Physical Review B* **2017,** *95* (20), 205131.

212. Mundy, J. A.; Hikita, Y.; Hidaka, T.; Yajima, T.; Higuchi, T.; Hwang, H. Y.; Muller, D. A.; Kourkoutis, L. F., Visualizing the interfacial evolution from charge compensation to metallic screening across the manganite metal-insulator transition. *Nature communications* **2014,** *5*, 3464.

213. Meng, Q.; Xu, G.; Xin, H.; Stach, E. A.; Zhu, Y.; Su, D., Quantification of charge transfer at the interfaces of oxide thin films. *The journal of physical chemistry. A* **2019,** *123* (21), 4632-4637.

214. Song, K.; Ryu, S.; Lee, H.; Paudel, T. R.; Koch, C. T.; Park, B.; Lee, J. K.; Choi, S. Y.; Kim, Y. M.; Kim, J. C.; Jeong, H. Y.; Rzchowski, M. S.; Tsymbal, E. Y.; Eom, C. B.; Oh, S. H., Direct imaging of the electron liquid at oxide interfaces. *Nature nanotechnology* **2018,** *13* (3), 198-203.

215. Zheng, Q.; Schreiber, N. J.; Zheng, H.; Yan, J. Q.; McGuirer, M. A.; Mitchel, J. F.; Chi, M. F.; Sales, B. C., Real space visualization of competing phases in $La_{0.6}Sr_{2.4}Mn_2O_7$ single crystals. *Chemistry of Materials* **2018,** *30* (21), 7962-7969.

216. Savitzky, B. H.; El Baggari, I.; Admasu, A. S.; Kim, J.; Cheong, S. W.; Hovden, R.; Kourkoutis, L. F., Bending and breaking of stripes in a charge ordered manganite. *Nature communications* **2017,** *8* (1), 1883.

217. El Baggari, I.; Savitzky, B. H.; Admasu, A. S.; Kim, J.; Cheong, S. W.; Hovden, R.; Kourkoutis, L. F., Nature and evolution of incommensurate charge order in manganites visualized with cryogenic scanning transmission electron microscopy. *Proceedings of the National Academy of Sciences of the United States of America* **2018,** *115* (7), 1445-1450.

218. Gao, W.; Addiego, C.; Wang, H.; Yan, X.; Hou, Y.; Ji, D.; Heikes, C.; Zhang, Y.; Li, L.; Huyan, H.; Blum, T.; Aoki, T.; Nie, Y.; Schlom, D. G.; Wu, R.; Pan, X., Real-space charge-density imaging with sub-angstrom resolution by four-dimensional electron microscopy. *Nature* **2019,** *575* (7783), 480-484.

219. Cheng, S.; Xu, C.; Deng, S.; Han, M. G.; Bao, S.; Ma, J.; Nan, C.; Duan, W.; Bellaiche, L.; Zhu, Y.; Zhu, J., Interface reconstruction with emerging charge ordering in hexagonal manganite. *Science Advances* **2018,** *4* (5), eaar4298.

220. Garcia-Barriocanal, J.; Bruno, F. Y.; Rivera-Calzada, A.; Sefrioui, Z.; Nemes, N. M.; Garcia-Hernandez, M.; Rubio-Zuazo, J.; Castro, G. R.; Varela, M.; Pennycook, S. J.; Leon, C.; Santamaria, J., "Charge leakage" at $LaMnO_3/SrTiO_3$ interfaces. *Advanced materials* **2010,** *22* (5), 627-632.

221. Ziatdinov, M.; Banerjee, A.; Maksov, A.; Berlijn, T.; Zhou, W.; Cao, H.; Yan, J.-Q.; Bridges, C. A.; Mandrus, D.; Nagler, S. E., Atomic-scale observation of structural and electronic orders in the layered compound α-$RuCl_3$. *Nature communications* **2016,** *7*, 13774.

222. Wang, H.; Jiang, X.; Wang, Y.; Stark, R. W.; van Aken, P. A.; Mannhart, J.; Boschker, H., Direct observation of huge flexoelectric polarization around crack tips. *Nano letters* **2020,** *20* (1), 88-94.

223. Kirkland, E. J.; Loane, R. F.; Silcox, J., Simulation of annular dark field STEM images using a modified multislice method. *Ultramicroscopy* **1987,** *23* (1), 77-96.

224. Langmore, J., The collection of scattered electrons in dark-field electron microscopy. *Optik* **1973,** *38*, 335-350.

225. Tomita, K.; Miyata, T.; Olovsson, W.; Mizoguchi, T., Strong excitonic interactions in the oxygen K-edge of perovskite oxides. *Ultramicroscopy* **2017,** *178*, 105-111.

226. Shah, A. B.; Zhai, X.; Jiang, B.; Wen, J.-G.; Eckstein, J. N.; Zuo, J.-M., Electron energy-loss study of the electronic structure of atomic scale $SrTiO_3$−$SrMnO_3$−$LaMnO_3$ superlattices. *Physical Review B* **2008,** *77* (11), 115103

227. Bagues, N.; Santiso, J.; Esser, B. D.; Williams, R. E. A.; McComb, D. W.; Konstantinovic, Z.; Balcells, L.; Sandiumenge, F., The misfit dislocation core phase in complex oxide heteroepitaxy. *Advanced Functional Materials* **2018,** *28* (8), 1704437.

228. Zhang, Q.; He, X.; Shi, J.; Lu, N.; Li, H.; Yu, Q.; Zhang, Z.; Chen, L.-Q.; Morris, B.; Xu, Q., Atomic-resolution imaging of electrically induced oxygen vacancy migration and phase transformation in $SrCoO_{2.5-\sigma}$. *Nature communications* **2017,** *8* (1), 1-6.

229. Tan, H. Y.; Verbeeck, J.; Abakumov, A.; Van Tendeloo, G., Oxidation state and chemical shift investigation in transition metal oxides by EELS. *Ultramicroscopy* **2012,** *116*, 24-33.

230. Kobayashi, S.; Tokuda, Y.; Mizoguchi, T.; Shibata, N.; Sato, Y.; Ikuhara, Y.; Yamamoto, T., Quantitative analyses of oxidation states for cubic $SrMnO_3$ and orthorhombic $SrMnO_{2.5}$ with electron energy loss spectroscopy. *J Appl Phys* **2010,** *108* (12), 124903.

231. Borisevich, A. Y.; Chang, H. J.; Huijben, M.; Oxley, M. P.; Okamoto, S.; Niranjan, M. K.; Burton, J. D.; Tsymbal, E. Y.; Chu, Y. H.; Yu, P.; Ramesh, R.; Kalinin, S. V.; Pennycook, S. J., Suppression of octahedral tilts and associated changes in electronic properties at epitaxial oxide heterostructure interfaces. *Physical review letters* **2010,** *105* (8), 087204.

232. Zhang, Y.; Shen, L.; Liu, M.; Li, X.; Lu, X.; Lu, L.; Ma, C.; You, C.; Chen, A.; Huang, C., Flexible quasi-two-dimensional $CoFe_2O_4$ epitaxial thin films for continuous strain tuning of magnetic properties. *ACS nano* **2017,** *11* (8), 8002-8009.

233. Clément, L.; Pantel, R.; Kwakman, L. T.; Rouvière, J., Strain measurements by convergent-beam electron diffraction: The importance of stress relaxation in lamella preparations. *Applied physics letters* **2004,** *85* (4), 651-653.

234. Cooper, D.; Denneulin, T.; Bernier, N.; Béché, A.; Rouvière, J.-L., Strain mapping of semiconductor specimens with nm-scale resolution in a transmission electron microscope. *Micron* **2016,** *80*, 145-165.

235. Cherkashin, N.; Denneulin, T.; Hÿtch, M. J., Electron microscopy by specimen design: application to strain measurements. *Scientific reports* **2017,** *7* (1), 1-8.

236. Chu, M. W.; Liou, S. C.; Chang, C. P.; Choa, F. S.; Chen, C. H., Emergent chemical mapping at atomic-column resolution by energy-dispersive x-ray spectroscopy in an aberration-corrected electron microscope. *Physical review letters* **2010,** *104* (19), 196101.

237. Egerton, R.; Yang, Y.-Y.; Chen, F., EELS of "thick" specimens. *Ultramicroscopy* **1991,** *38* (3-4), 349-352.

238. Kourkoutis, L. F.; Song, J. H.; Hwang, H. Y.; Muller, D. A., Microscopic origins for stabilizing room-temperature ferromagnetism in ultrathin manganite layers. *Proceedings of the National Academy of Sciences of the United States of America* **2010,** *107* (26), 11682-5.

239. Maurel, L.; Marcano, N.; Prokscha, T.; Langenberg, E.; Blasco, J.; Guzman, R.; Suter, A.; Magen, C.; Morellon, L.; Ibarra, M. R.; Pardo, J. A.; Algarabel, P. A., Nature of antiferromagnetic order in epitaxially strained multiferroic $SrMnO_3$ thin films. *Physical Review B* **2015,** *92* (2), 024419.

240. Shannon, R. D., Revised effective ionic-radii and systematic studies of interatomic distances in halides and chalcogenides. *Acta Crystallogr A* **1976,** *32* (Sep1), 751-767.

241. Agrawal, P.; Guo, J.; Yu, P.; Hebert, C.; Passerone, D.; Erni, R.; Rossell, M. D., Strain-driven oxygen deficiency in multiferroic $SrMnO_3$ thin films. *Physical Review B* **2016,** *94* (10), 104101.

242. Guzman, R.; Maurel, L.; Langenberg, E.; Lupini, A. R.; Algarabel, P. A.; Pardo, J. A.; Magen, C., Polar-graded multiferroic $SrMnO_3$ thin films. *Nano letters* **2016,** *16* (4), 2221-2227.

243. Nord, M.; Vullum, P. E.; Moreau, M.; Boschker, J. E.; Selbach, S. M.; Holmestad, R.; Tybell, T., Structural phases driven by oxygen vacancies at the $La_{0.7}Sr_{0.3}MnO_3/SrTiO_3$ hetero-interface. *Applied Physics Letters* **2015,** *106* (4), 041604.

244. Chandrasena, R. U.; Yang, W.; Lei, Q.; Delgado-Jaime, M. U.; Wijesekara, K. D.; Golalikhani, M.; Davidson, B. A.; Arenholz, E.; Kobayashi, K.; Kobata, M.; de Groot, F. M.; Aschauer, U.; Spaldin, N. A.; Xi, X.; Gray, A. X., Strain-engineered oxygen vacancies in $CaMnO_3$ thin films. *Nano Letters* **2017,** *17* (2), 794-799.

245. Choi, S. Y.; Kim, S. D.; Choi, M.; Lee, H. S.; Ryu, J.; Shibata, N.; Mizoguchi, T.; Tochigi, E.; Yamamoto, T.; Kang, S. J.; Ikuhara, Y., Assessment of strain-generated oxygen vacancies using $SrTiO_3$ bicrystals. *Nano Letters* **2015,** *15* (6), 4129-4134.

246. Nakamura, M.; Sawa, A.; Fujioka, J.; Kawasaki, M.; Tokura, Y., Interface band profiles of Mott-insulator Nb: $SrTiO_3$ heterojunctions as investigated by optical spectroscopy. *Physical Review B* **2010,** *82* (20), 201101.

247. Chen, Y.; Gan, Y.; Christensen, D. V.; Zhang, Y.; Pryds, N., Effect of Sr-doping of $LaMnO_3$ spacer on modulation-doped two-dimensional electron gases at oxide interfaces. *Journal of Applied Physics* **2017,** *121* (9), 095305.

248. Lin, X.; Bridoux, G.; Gourgout, A.; Seyfarth, G.; Krämer, S.; Nardone, M.; Fauqué, B.; Behnia, K., Critical doping for the onset of a two-band superconducting ground state in $SrTiO_{3-\delta}$. *Physical review letters* **2014,** *112* (20), 207002.

249. Scullin, M. L.; Ravichandran, J.; Yu, C.; Huijben, M.; Seidel, J.; Majumdar, A.; Ramesh, R., Pulsed laser deposition-induced reduction of $SrTiO_3$ crystals. *Acta Materialia* **2010,** *58* (2), 457-463.

250. Schneider, C. W.; Döbeli, M.; Richter, C.; Lippert, T., Oxygen diffusion in oxide thin films grown on $SrTiO_3$. *Physical Review Materials* **2019,** *3* (12), 123401.

251. Maier, J., Ionic-conduction in-space charge regions. *Progress in Solid State Chemistry* **1995,** *23* (3), 171-263.

252. Baiutti, F.; Logvenov, G.; Gregori, G.; Cristiani, G.; Wang, Y.; Sigle, W.; van Aken, P. A.; Maier, J., High-temperature superconductivity in space-charge regions of lanthanum cuprate induced by two-dimensional doping. *Nature communications* **2015,** *6*, 8586.

253. De Souza, R. A., The formation of equilibrium space-charge zones at grain boundaries in the perovskite oxide $SrTiO_3$. *Physical Chemistry Chemical Physics* **2009,** *11* (43), 9939-9969.

254. Zubko, P.; Catalan, G.; Tagantsev, A. K., Flexoelectric effect in solids. In *Annual Review of Materials Research, Vol 43*, Clarke, D. R., Ed. 2013; Vol. 43, pp 387-421.

255. Jiang, X. N.; Huang, W. B.; Zhang, S. J., Flexoelectric nano-generator: Materials, structures and devices. *Nano Energy* **2013,** *2* (6), 1079-1092.

256. Nguyen, T. D.; Mao, S.; Yeh, Y. W.; Purohit, P. K.; McAlpine, M. C., Nanoscale flexoelectricity. *Advanced Materials* **2013,** *25* (7), 946-974.

257. Tagantsev, A. K., Piezoelectricity and flexoelectricity in crystalline dielectrics. *Physical Review B* **1986,** *34* (8), 5883-5889.

258. Yudin, P. V.; Tagantsev, A. K., Fundamentals of flexoelectricity in solids. *Nanotechnology* **2013,** *24* (43), 432001.

259. Lee, D.; Yoon, A.; Jang, S. Y.; Yoon, J. G.; Chung, J. S.; Kim, M.; Scott, J. F.; Noh, T. W., Giant flexoelectric effect in ferroelectric epitaxial thin films. *Physical Review Letters* **2011,** *107* (5), 057602.

260. Lee, D.; Yang, S. M.; Yoon, J. G.; Noh, T. W., Flexoelectric rectification of charge transport in strain-graded dielectrics. *Nano Letters* **2012,** *12* (12), 6436-6440.

261. Catalan, G.; Noheda, B.; McAneney, J.; Sinnamon, L. J.; Gregg, J. M., Strain gradients in epitaxial ferroelectrics. *Physical Review B* **2005,** *72* (2).

262. Majdoub, M. S.; Sharma, P.; Cagin, T., Enhanced size-dependent piezoelectricity and elasticity in nanostructures due to the flexoelectric effect. *Physical Review B* **2008,** *77* (12), 125424.

263. Harden, J.; Mbanga, B.; Eber, N.; Fodor-Csorba, K.; Sprunt, S.; Gleeson, J. T.; Jakli, A., Giant flexoelectricity of bent-core nematic liquid crystals. *Physical Review Letters* **2006,** *97* (15), 157802.

264. Catalan, G.; Lubk, A.; Vlooswijk, A. H. G.; Snoeck, E.; Magen, C.; Janssens, A.; Rispens, G.; Rijnders, G.; Blank, D. H. A.; Noheda, B., Flexoelectric rotation of polarization in ferroelectric thin films. *Nature Materials* **2011,** *10* (12), 963-967.

265. Lu, H.; Bark, C. W.; de los Ojos, D. E.; Alcala, J.; Eom, C. B.; Catalan, G.; Gruverman, A., Mechanical writing of ferroelectric polarization. *Science* **2012,** *336* (6077), 59-61.

266. Park, S. M.; Wang, B.; Das, S.; Chae, S. C.; Chung, J. S.; Yoon, J. G.; Chen, L. Q.; Yang, S. M.; Noh, T. W., Selective control of multiple ferroelectric switching pathways using a trailing flexoelectric field. *Nature Nanotechnology* **2018,** *13* (5), 366-370.

267. Gu, Y. J.; Hong, Z. J.; Britson, J.; Chen, L. Q., Nanoscale mechanical switching of ferroelectric polarization via flexoelectricity. *Applied Physics Letters* **2015,** *106* (2), 022904.

268. Zhang, F.; Lv, P.; Zhang, Y.; Huang, S.; Wong, C.-M.; Yau, H.-M.; Chen, X.; Wen, Z.; Jiang, X.; Zeng, C.; Hong, J.; Dai, J.-y., Modulating the electrical transport in the two-dimensional electron gas at $LaAlO_3/SrTiO_3$ heterostructures by interfacial flexoelectricity. *Physical Review Letters* **2019,** *122* (25), 257601.

269. Das, S.; Wang, B.; Paudel, T. R.; Park, S. M.; Tsymbal, E. Y.; Chen, L.-Q.; Lee, D.; Noh, T. W., Enhanced flexoelectricity at reduced dimensions revealed by mechanically tunable quantum tunnelling. *Nature Communications* **2019,** *10* (1), 537.

270. Bhaskar, U. K.; Banerjee, N.; Abdollahi, A.; Wang, Z.; Schlom, D. G.; Rijnders, G.; Catalan, G., A flexoelectric microelectromechanical system on silicon. *Nature Nanotechnology* **2016,** *11* (3), 263-266.

271. Bhaskar, U. K.; Banerjee, N.; Abdollahi, A.; Solanas, E.; Rijnders, G.; Catalan, G., Flexoelectric MEMS: towards an electromechanical strain diode. *Nanoscale* **2016,** *8* (3), 1293-1298.

272. Cordero-Edwards, K.; Kianirad, H.; Canalias, C.; Sort, J.; Catalan, G., Flexoelectric fracture-ratchet effect in ferroelectrics. *Physical Review Letters* **2019,** *122* (13), 135502.

273. Vasquez-Sancho, F.; Abdollahi, A.; Damjanovic, D.; Catalan, G., Flexoelectricity in bones. *Advanced Materials* **2018,** *30* (9), 1705316.

274. Gao, P.; Yang, S. Z.; Ishikawa, R.; Li, N.; Feng, B.; Kumamoto, A.; Shibata, N.; Yu, P.; Ikuhara, Y., Atomic-scale measurement of flexoelectric polarization at $SrTiO_3$ dislocations. *Physical Review Letters* **2018,** *120* (26), 267601.

275. Ma, W. H.; Cross, L. E., Flexoelectric polarization of barium strontium titanate in the paraelectric state. *Applied Physics Letters* **2002,** *81* (18), 3440-3442.

276. Zubko, P.; Catalan, G.; Buckley, A.; Welche, P. R. L.; Scott, J. F., Strain-gradient-induced polarization in $SrTiO_3$ single crystals. *Physical Review Letters* **2007,** *99* (16), 167601.

277. Hong, J. W.; Catalan, G.; Scott, J. F.; Artacho, E., The flexoelectricity of barium and strontium titanates from first principles. *Journal of Physics-Condensed Matter* **2010,** *22* (11), 112201.

278. Stengel, M., From flexoelectricity to absolute deformation potentials: The case of $SrTiO_3$. *Physical Review B* **2015,** *92* (20), 205115.

279. Li, Q.; Nelson, C. T.; Hsu, S. L.; Damodaran, A. R.; Li, L. L.; Yadav, A. K.; McCarter, M.; Martin, L. W.; Ramesh, R.; Kalinin, S. V., Quantification of flexoelectricity in $PbTiO_3/SrTiO_3$ superlattice polar vortices using machine learning and phase-field modeling. *Nature Communications* **2017,** *8(1), 1-8*.

280. Guzman, R.; Maurel, L.; Langenberg, E.; Lupini, A. R.; Algarabel, P. A.; Pardo, J. A.; Magen, C., Polar-graded multiferroic $SrMnO_3$ thin films. *Nano Letters* **2016,** *16* (4), 2221-2227.

281. Kolhatkar, G.; Nicklaus, M.; Hadj Youssef, A.; Cojocaru, C.; Rivard, M.; Merlen, A.; Légaré, F.; Ruediger, A., Second harmonic generation investigation of symmetry breaking and flexoelectricity induced by nanoindentations in $SrTiO_3$. *Advanced Functional Materials* **2019,** *0* (0), 1901266.

282. Müller, K. A.; Burkard, H., $SrTiO_3$: An intrinsic quantum paraelectric below 4 K. *Physical Review B* **1979,** *19* (7), 3593-3602.

283. Sakai, H.; Fujioka, J.; Fukuda, T.; Okuyama, D.; Hashizume, D.; Kagawa, F.; Nakao, H.; Murakami, Y.; Arima, T.; Baron, A. Q. R.; Taguchi, Y.; Tokura, Y., Displacement-type ferroelectricity with off-center magnetic ions in perovskite $Sr_{1-x}Ba_xMnO_3$. *Physical Review Letters* **2011,** *107* (13), 137601.

284. Lee, J. H.; Rabe, K. M., Epitaxial-strain-induced multiferroicity in $SrMnO_3$ from first principles. *Physical Review Letters* **2010,** *104* (20), 207204.

285. Guo, J. W.; Wang, P. S.; Yuan, Y.; He, Q.; Lu, J. L.; Chen, T. Z.; Yang, S. Z.; Wang, Y. J.; Erni, R.; Rossell, M. D.; Gopalan, V.; Xiang, H. J.; Tokura, Y.; Yu, P., Strain-induced ferroelectricity and spin-lattice coupling in $SrMnO_3$ thin films. *Physical Review B* **2018,** *97* (23), 235135.

286. Becher, C.; Maurel, L.; Aschauer, U.; Lilienblum, M.; Magen, C.; Meier, D.; Langenberg, E.; Trassin, M.; Blasco, J.; Krug, I. P.; Algarabel, P. A.; Spaldin, N. A.; Pardo, J. A.; Fiebig, M., Strain-induced coupling of electrical polarization and structural defects in $SrMnO_3$ films. *Nature Nanotechnology* **2015,** *10* (8), 661-665.

287. Rørmark, L.; Wiik, K.; Stølen, S.; Grande, T., Oxygen stoichiometry and structural properties of $La_{1-x}A_xMnO_{3\pm\delta}$ (A=Ca or Sr and $0\leq x\leq 1$). *Journal of Materials Chemistry* **2002,** *12* (4), 1058-1067.

288. Matthews, J. W.; Mader, S.; Light, T. B., Accommodation of misfit across the interface between crystals of semiconducting elements or compounds. *Journal of Applied Physics* **1970,** *41* (9), 3800-3804.

289. Matthews, J. W.; Klokholm, E., Fracture of brittle epitaxial films under the influence of misfit stress. *Materials Research Bulletin* **1972,** *7* (3), 213-221.

290. Agrawal, P.; Guo, J.; Yu, P.; Hebert, C.; Passerone, D.; Erni, R.; Rossell, M. D., Strain-driven oxygen deficiency in multiferroic $SrMnO_3$ thin films. *Physical Review B* **2016,** *94* (10).

291. Yamada, H.; Kawasaki, M.; Tokura, Y., Epitaxial growth and valence control of strained perovskite $SrFeO_3$ films. *Applied Physics Letters* **2002,** *80* (4), 622-624.

292. Biegalski, M. D.; Fong, D. D.; Eastman, J. A.; Fuoss, P. H.; Streiffer, S. K.; Heeg, T.; Schubert, J.; Tian, W.; Nelson, C. T.; Pan, X. Q.; Hawley, M. E.; Bernhagen, M.; Reiche, P.; Uecker, R.; Trolier-McKinstry, S.; Schlom, D. G., Critical thickness of high structural quality $SrTiO_3$ films grown on orthorhombic (101) $DyScO_3$. *Journal of Applied Physics* **2008,** *104* (11), 114109.

293. Huijben, J., Interfacial phenomena in atomically engineered $LaAlO_3/SrTiO_3$ heterostructures. *PhD thesis, University of Twente* **2018**, https://doi.org/10.3990/1.9789036545242.

294. Chang, C.-P.; Chu, M.-W.; Jeng, H.; Cheng, S.-L.; Lin, J.; Yang, J.-R.; Chen, C., Condensation of two-dimensional oxide-interfacial charges into one-dimensional electron chains by the misfit-dislocation strain field. *Nature communications* **2014,** *5*, 3522.

295. Nelson, C. T.; Winchester, B.; Zhang, Y.; Kim, S. J.; Melville, A.; Adamo, C.; Folkman, C. M.; Baek, S. H.; Eom, C. B.; Schlom, D. G.; Chen, L. Q.; Pan, X., Spontaneous vortex nanodomain arrays at ferroelectric heterointerfaces. *Nano letters* **2011,** *11* (2), 828-834.

296. Abrahams, S. C.; Kurtz, S. K.; Jamieson, P. B., Atomic displacement relationship to Curie temperature and spontaneous polarization in displacive ferroelectrics. *Physical Review* **1968,** *172* (2), 551-553.

297. Bell, R. O.; Rupprecht, G., Elastic constants of strontium titanate. *Physical Review* **1963,** *129* (1), 90-94.

298. Zhou, D.; Müller-Caspary, K.; Sigle, W.; Krause, F. F.; Rosenauer, A.; van Aken, P. A., Sample tilt effects on atom column position determination in ABF–STEM imaging. *Ultramicroscopy* **2016,** *160*, 110-117.

299. Wang, Y.; Huang, M. R. S.; Salzberger, U.; Hahn, K.; Sigle, W.; van Aken, P. A., Atomically Resolved EELS Elemental and Fine Structure Mapping via Multi-Frame and Energy-Offset Correction Acquisition. *Microscopy and Microanalysis* **2018,** *24* (S1), 448-449.

300. Lee, J. H.; Rabe, K. M., Epitaxial-strain-induced multiferroicity in $SrMnO_3$ from first principles. *Physical review letters* **2010,** *104* (20), 207204.

301. Cuong do, D.; Lee, B.; Choi, K. M.; Ahn, H. S.; Han, S.; Lee, J., Oxygen vacancy clustering and electron localization in oxygen-deficient $SrTiO_3$: LDA + U study. *Physical review letters* **2007,** *98* (11), 115503.